Acta Pharmacologica Sinica (2012) 33: 577
 1671-4083/12 $32.00
www.nature.com/aps

Research Highlight

Methylation of FoxO3 regulates neuronal cell death

Wei-guo ZHU[1, 2, *]

Acta Pharmacologica Sinica (2012) 33: 577; doi: 10.1038/aps.2012.48

Oxidative stress plays an essential role in the development of several neurodegenerative disorders[1]. The evolutionally conserved FoxO (FOX family O class) transcription factors, including FoxO1, FoxO3, FoxO4, and FoxO6 in mammals, induce the expression of downstream pro-apoptotic genes, thus act as critical regulators during the oxidative stress-induced neuronal cell death[2, 3].

FoxO family proteins are regulated by a variety of post-translational modifications, such as phosphorylation, acetylation, ubiquitination and arginine methylation[4]. For instance, serine/threonine kinase PKB/Akt is well known FoxO inhibitor. Phosphorylation of FoxO by Akt at three key residues increases its binding activity to 14-3-3 protein and results in its translocation from nucleus to cytoplasm[5]. One the other hand, phosphorylation of FoxO by Hippo/MST1 kinase dampens its binding to 14-3-3 protein and leads to nuclear accumulation of FoxO1/3[3]. Similar to phosphorylation, acetylation/deacetylation of FoxO proteins dynamically regulates thier biological functions through affecting their DNA-binding activity, stability and interaction with other proteins[6].

Recently, Yuan's group of Institute of Biophysics at Chinese Academy of Sciences identified a novel post-translational modification of FoxO3 transcription factor[7]. They found that a lysine methyltransferase, Set9, methylated FoxO3 at lysine 270 that led to inhibition of DNA binding activity and downregulation of transactivation without affecting Akt-mediated phosphorylation. They showed that lysine methylation of FoxO3 reduced oxidative stress-induced neuronal apoptosis in cerebellar granule neurons through transcriptional downregulation of its pro-apoptotic target, *Bim*. In addition, they observed that the lysine methylation of FoxO3 did not affect its protein stability, Akt-mediated phosphorylation and subcellular localization. Interestingly, they showed that oxidative stress reduced the methylation level of FoxO3, indicating that the methylation of FoxO3 might be dynamically regulated even though they failed to identify the demethylase of FoxO3.

In short, Yuan's group identifies a novel modification of FoxO3 and shows that lysine methylation negatively regulates FoxO3-mediated transcription and neuronal cell death, which implicates a variety of neurodegenerative diseases.

[1]*Key laboratory of Carcinogenesis and Translational Research (Ministry of Education), Department of Biochemistry and Molecular Biology, Peking University Health Science Center, Beijing 100191, China;* [2]*Peking University –Tsinghua University Center for Life Sciences, Beijing 100084, China*
Correspondence: Prof Wei-guo ZHU
(zhuweiguo@bjmu.edu.cn)

1 Chong ZZ, Li F, Maiese K. Oxidative stress in the brain: novel cellular targets that govern survival during neurodegenerative disease. Prog Neurobiol 2005; 75: 207–46.
2 Calnan DR, Brunet A. The FoxO code. Oncogene 2008; 27: 2276–88.
3 Lehtinen MK, Yuan Z, Boag PR, Yang Y, Villen J, Becker EB, *et al.* A conserved MST-FOXO signaling pathway mediates oxidative-stress responses and extends life span. Cell 2006; 125: 987–1001.
4 van der Horst A, Burgering BM. Stressing the role of FoxO proteins in lifespan and disease. Nat Rev Mol Cell Biol 2007; 8: 440–50.
5 Brunet A, Bonni A, Zigmond MJ, Lin MZ, Juo P, Hu LS, *et al.* Akt promotes cell survival by phosphorylating and inhibiting a Forkhead transcription factor. Cell 1999; 96: 857–68.
6 Zhao Y, Wang Y, Zhu WG. Applications of post-translational modifications of FoxO family proteins in bioological functions. J Mol Cell Biol 2011; 3: 276–82.
7 Xie Q, Hao Y, Tao L, Peng S, Rao C, Chen H, *et al.* Lysine methylation of FOXO3 regulates oxidative stress-induced neuronal cell death. EMBO Rep 2012; 13: 371–7.

Acta Pharmacologica Sinica (2012) 33: 578–587
 1671-4083/12 $32.00
www.nature.com/aps

Original Article

Asiatic acid, a pentacyclic triterpene in *Centella asiatica*, attenuates glutamate-induced cognitive deficits in mice and apoptosis in SH-SY5Y cells

Min-fang XU[1], Yu-yun XIONG[2], Jian-kang LIU[3], Jin-jun QIAN[4], Li ZHU[5], Jing GAO[1, *]

[1] *School of Pharmacy, Jiangsu University, Zhenjiang 212013, China;* [2] *School of Medical Science and Laboratory Medicine, Jiangsu University, Zhenjiang 212013, China;* [3] *Institute of Mitochondrial Biology & Medicine, The Key Laboratory of Biomedical Information Engineering of Ministry of Education, Xi'an Jiaotong University School of Life Science and Technology, Xi'an 710049, China;* [4] *Department of Neurology, The Forth Affiliated Hospital of Jiangsu University, Zhenjiang 212001, China;* [5] *Department of Neurobiology and Neurochemistry, Institute for Nautical Medicine and Jiangsu Key Laboratory of Neurogeneration, Nantong University, Nantong 226001, China*

Aim: To investigate whether asiatic acid (AA), a pentacyclic triterpene in *Centella asiatica*, exerted neuroprotective effects *in vitro* and *in vivo*, and to determine the underlying mechanisms.
Methods: Human neuroblastoma SH-SY5Y cells were used for *in vitro* study. Cell viability was determined with the MTT assay. Hoechst 33342 staining and flow cytometry were used to examine the apoptosis. The mitochondrial membrane potential (MMP) and reactive oxygen species (ROS) were measured using fluorescent dye. PGC-1α and Sirt1 levels were examined using Western blotting. Neonatal mice were given monosodium glutamate (2.5 mg/g) subcutaneously at the neck from postnatal day (PD) 7 to 13, and orally administered with AA on PD 14 daily for 30 d. The learning and memory of the mice were evaluated with the Morris water maze test. HE staining was used to analyze the pyramidal layer structure in the CA1 and CA3 regions.
Results: Pretreatment of SH-SY5Y cells with AA (0.1–100 nmol/L) attenuated toxicity induced by 10 mmol/L glutamate in a concentration-dependent manner. AA 10 nmol/L significantly decreased apoptotic cell death and reduced reactive oxygen species (ROS), stabilized the mitochondrial membrane potential (MMP), and promoted the expression of PGC-1α and Sirt1. In the mice models, oral administration of AA (100 mg/kg) significantly attenuated cognitive deficits in the Morris water maze test, and restored lipid peroxidation and glutathione and the activity of SOD in the hippocampus and cortex to the control levels. AA (50 and 100 mg/kg) also attenuated neuronal damage of the pyramidal layer in the CA1 and CA3 regions.
Conclusion: AA attenuates glutamate-induced cognitive deficits of mice and protects SH-SY5Y cells against glutamate-induced apoptosis *in vitro*.

Keywords: asiatic acid; glutamate; excitotoxicity; cognitive deficits; hippocampus; apoptosis; mitochondria; PGC-1α; neuroprotection

Acta Pharmacologica Sinica (2012) 33: 578–587; doi: 10.1038/aps.2012.3; published online 26 Mar 2012

Introduction

Human neurodegenerative diseases, including Alzheimer's disease, Parkinson's disease, and amyotrophic lateral sclerosis, are characterized by the progressive dysfunction and loss of neurons induced by particular neurological deficits[1]. Glutamate (Glu)-induced excitotoxicity plays an important role in the pathogenesis of these diseases[2, 3]. Glu-induced neuronal death is initiated by overstimulation of *N*-methyl-*D*-aspartate (NMDA) receptors, resulting in an increase in intracellular free calcium, followed by the activation of catabolic enzymes and leading to an intracellular cascade of cytotoxic events.

Recently, an increasing number of studies has found that mitochondria — organelles that are vitally important for controlling cell life and death — are involved in Glu-induced excitotoxicity because they possess a large capacity for calcium uptake in response, finally resulting in mitochondrial Ca^{2+} overload. Mitochondrial Ca^{2+} overload may activate neuronal cell death through the release of pro-apoptotic factors and increased generation of reactive oxygen species (ROS)[4, 5]. The extent to which ROS and subsequent oxidative stress may play an essential role in Glu toxicity in both acute insults, such as ischemia[6], and chronic neurodegenerative diseases[7] has been

* To whom correspondence should be addressed.
E-mail jinggao@ujs.edu.cn
Received 2011-09-13 Accepted 2012-01-10

investigated. Thus, oxidative damage, destruction of calcium homeostasis and mitochondrial dysfunction are essentially consequences of Glu-induced excitotoxicity. Consistent with these findings, antioxidants and mitochondrial nutrients[8, 9] may be promising candidates for the prevention and treatment of these diseases.

Centella asiatica has long been used in Ayurvedic medicine and traditional Chinese medicine to treat various ailments and to enhance memory. Recent findings suggest that *Centella asiatica* has cognition-enhancing properties through its ability to protect against oxidative stress[10, 11], reduce the extent of mitochondrial damage[12] and increase axonal regeneration and neurite elongation[13]. Asiatic acid (AA) is a pentacyclic triterpene found in *Centella asiatica*. Our previous studies demonstrated that AA could attenuate H_2O_2- or rotenone-induced neural injury due to its protection from mitochondrial membrane depolarization[14]. AA also showed protective effects against Glu- and Aβ-induced neurotoxicity[15, 16]. Moreover, AA may be an effective agent for treating cerebral ischemia[17]. Therefore, AA is interesting as a candidate for potential application in the treatment of neurodegenerative diseases.

In this study, we used an *in vitro* model of Glu-induced excitotoxicity in SH-SY5Y cells and an *in vivo* dementia model of perinatal monosodium glutamate (MSG) exposure[18] to investigate the neuroprotective functions of AA and its possible mechanisms of action.

Materials and methods

Materials

Glu, MSG, AA and MTT were purchased from Sigma (St Louis, MO, USA). Minimum Essential Medium (MEM), Nutrient Mixture Ham's F-12 (F12), nonessential amino acids and trypsin were purchased from Gibco BRL (Grand Island, NY, USA). Fetal bovine serum (FBS) was obtained from Sijiqing Biological Engineering Materials (Hangzhou, China). DCFH-DA and the BCA Protein Quantitative Analysis Kit were purchased from Beyotime (Nantong, China). Anti-β-actin primary antibody was purchased from Abcam (Cambridge, MA, USA). Anti-PGC-1α and anti-Sirt1 antibodies were purchased from Santa Cruz Biotechnology (San Diego, CA, USA), and all secondary antibodies were purchased from Boster Biological Technology (Wuhan, China). All other reagents were purchased from commercial suppliers and were of standard biochemical quality.

Culture of SH-SY5Y Cells

Human neuroblastoma SH-SY5Y cells (a gift from Dr Zun-ji KE, Institute for Nutritional Sciences, Chinese Academy of Sciences, Shanghai, China) were maintained in MEM/F12 medium, supplemented with 1% nonessential amino acids and 10% FBS, 100 U/mL penicillin and 100 U/mL streptomycin at 37 °C in 5 % CO_2. The cells were passaged once every 3 d.

MTT assay

To determine cell viability, the MTT assay was used. SH-SY5Y cells were cultured in 96-well plates at a seeding density of 3000 cells per well. Twenty-four hours later, the cells were treated with AA for 24 h and then exposed to the same fresh medium containing 10 mmol/L Glu for 24 h. Next, 100 μL/well MTT (1 mg/mL) was added to each well, and the cells were incubated for 4 h at 37 °C. After incubation, dimethyl sulfoxide (DMSO, 100 μL) was added to each well to dissolve the precipitate. The absorbance was read with a microplate reader (Molecular Devices, Sunnyvale, CA, USA) at 570 nm.

Flow cytometric analysis

Briefly, following drug treatment, the cells were harvested and washed twice with ice-cold PBS. The presence of apoptotic cells that expose phosphatidylserine on their outside surface was determined by an Annexin V-FITC Apoptosis Kit (Calbiochem, San Diego, CA, USA). Annexin V-FITC (1.25 μL) was added to 500 μL of 1×Annexin V-FITC binding buffer, and the cells were incubated at room temperature for 15 min in the dark. After washing the cells with 1×binding buffer, 10 μL propidium iodide (PI) was added to the binding buffer, and the cells were analyzed with a flow cytometer (Beckman-Coulter MoFLo XDP, Fullerton, CA, USA). The percentages of apoptotic and necrotic cells were estimated for each sample.

Mitochondrial membrane potential (MMP) assay

The MMP were determined with a fluorescent dye, JC-1 (Molecular Probes, Eugene, OR, USA). The cells were seeded in 24-well plates at a density of 3×10^4 cells/mL. The fluorescence intensity was observed immediately following JC-1 staining (2.5 μg/mL of JC-1 at 37 °C for 30 min) with fluorescence spectrometry (Molecular Devices, Sunnyvale, CA, USA; Ex 488/Em 535 for JC-1 green and Ex 488/Em 595 for JC-1 red) and fluorescence microscopy (Nikon TE2000 inverted microscope, Tokyo, Japan).

Hoechst 33342 staining

The cells were cultured in 24-well plates at a density of 3×10^4 cells/mL. The cells were fixed in 4% paraformaldehyde for 30 min at room temperature. After staining with 10 μg/mL Hoechst 33342 for 10 min, the cells were observed under a fluorescence microscope.

Intracellular ROS determination

ROS were measured with the non-fluorescent probe DCFH-DA. The cells were incubated with DCFH-DA at 37 °C for 30 min, and the distribution of DCF fluorescence produced by $1x10^4$ cells was detected with a fluorescence microscope or FACscan cytometer at an excitation wavelength of 488 nm and an emission wavelength of 535 nm.

Western blot analysis

After treatment like describing in MTT assay, 1×10^6 cells were collected and subjected to Western blot analysis. The cell proteins were extracted and quantified with a BCA Protein Quantitative Analysis Kit. After addition of the sample loading buffer, protein samples were electrophoresed using 8%–12%

SDS-PAGE and subsequently transferred to PVDF membranes (Bio-Rad, Hercules, CA, USA). Each membrane was incubated in fresh blocking buffer (0.1% Tween 20 in Tris-buffered saline, pH 7.4, containing 5% nonfat dried milk) at room temperature for 30 min and then probed with anti-PGC-1α, anti-Sirt1 or anti-β-actin antibodies in blocking buffer at 4 °C overnight. The membrane was washed three times for 5 min each using PBST (PBS and 0.1% Tween 20). The membrane was incubated in the appropriate HRP-conjugated secondary antibody at room temperature for 2 h. The immunoreactive protein was visualized using the chemiluminescent reagent ECL (Pierce Biotechnology, Rockford, IL, USA) according to the manufacturer's protocol.

Animals

Neonatal mice at postnatal day (PD) 7 were procured from the Comparative Medicine Center (Yangzhou University, Yangzhou, China) and housed in cages at an ambient temperature of 25 °C with 12 h light/dark cycles. Food and water were freely available.

Drug administration

The animals were randomly assigned to drug or control groups (n=10 in each group), respectively. MSG was dissolved in 0.9% sodium chloride (NaCl). In the drug group, neonatal mice were given MSG subcutaneously (in the neck, 2.5 mg/g body weight) from PD 7 to 13 as previously described[19]. The control pups received equal volumes of 0.9% NaCl. On PD 28, the animals were weaned, and animals of the same sex that had been subjected to the same treatment were housed together. AA was suspended in 0.5% carboxymethylcellulose and administered by oral gavage. The animals were divided into four experimental groups: control, MSG, MSG+50 mg/kg AA and MSG+100 mg/kg AA. The AA doses used in this study were chosen on the basis of previously published experiments[17]. AA was administered after MSG treatment on PD 14 and daily thereafter for 30 d. The mice then performed the Morris water maze. All protocols described were reviewed and approved.

Morris water maze test

The animals were tested with a spatial version of the Morris water maze[20]. It consisted of a circular water tank (90 cm diameter, 50 cm height) that was partially filled with water (25±2 °C). Black ink was used to render the water opaque. Prior to the water maze testing, all mice were habituated to the water by being allowed to swim freely without a platform present. The pool was in the center of a room containing various salient visual cues and was divided virtually into four equal quadrants, labeled N (north), S (south), E (east), and W (west). The cues remained constant throughout the testing process. An escape platform (6 cm diameter) was hidden 1 cm below the water surface in one of the four maze quadrants (the target quadrant). The platform remained in the same quadrant during the entire experiment. The training consisted of 4 trials per day for 4 d with each trial having a time limit of 60 s and with an interval between trials of approximately 60 s. Each mouse had to swim until it climbed onto the submerged platform. After climbing onto the platform, the animal remained there for 30 s before the commencement of the next trial. If the mouse failed to reach the escape platform within the maximally allowed time of 60 s, it was gently placed on the platform and allowed to remain there for 30 s, and the time to reach the platform (latency) was recorded as 60 s. On the fifth day, a spatial probe test was conducted. Each mouse was given one 60 s retention test trial in which the platform had been removed from the tank. The time spent in the target quadrant was recorded. The time spent in the target quadrant indicates the degree of memory consolidation that took place after learning.

Protein, lipid peroxidation, glutathione and superoxide dismutase assays

After completing the Morris water maze test, the animals were sacrificed and their brains were quickly removed to dissect the hippocampus and cerebral cortex. The dissected brains were homogenized in 0.1 mol/L phosphate buffer (PB, pH 7.4). The homogenate was used to estimate the amount of lipid peroxidation, glutathione and superoxide dismutase. The amounts of protein, tissue lipid peroxidation, glutathione and superoxide dismutase were determined using kits (Nanjing Jiancheng Bioengineering Institute, Nanjing, China). The homogenate was centrifuged for 30 min at 3000×g at 4 °C, and the supernatant was used for enzyme assays. Glutathione (GSH) levels were determined using the DTNB-GSH reductase recycling method[21]. The levels of malondialdehyde (MDA), an intermediate product of lipid peroxidation, were determined with the thiobarbituric acid (TBA) reaction[22]. The protein content was measured by the method of Bradford[23] using bovine serum albumin as a standard.

Histological analysis by hematoxylin-eosin (HE) staining

The hippocampi of two mice from each group were chosen for hematoxylin-eosin (HE) staining. The mice were sacrificed and immediately transcardially perfused with 0.1 mol/L phosphate buffer, pH 7.4, followed by freshly prepared 4% paraformaldehyde in 0.1 mol/L phosphate buffer. The brains were removed and fixed in 4% paraformaldehyde in 0.1 mol/L phosphate buffer (pH 7.4) at 4 °C for more than 24 h. Coronal blocks were embedded in paraffin for staining. The hippocampi stained with HE were analyzed under a microscope at 400×magnification.

Statistical analysis

The data were expressed as the mean±SD. The data were analyzed using a one-way factorial analysis of variance (ANOVA). Tukey's test was then performed to compare treated samples, and the differences were considered to be significant when P<0.05.

Results

AA attenuates Glu-induced toxicity in SH-SY5Y cells

The treatment of SH-SY5Y cells with Glu (8 or 10 mmol/L) for 24 h markedly reduced cell viability (Figure 1A). A concentration of 10 mmol/L Glu was chosen for our subsequent experiments. To examine the neuroprotective effects of AA, the cells were preincubated with different concentrations of AA (0.01–100 nmol/L) for 24 h, followed by exposure to 10 mmol/L Glu for 24 h. AA provided protection against Glu-induced injury, and the strongest protective effect was achieved with 10 nmol/L AA (Figure 1B).

Effects of AA on Glu-induced apoptosis

Apoptosis was assessed using Hoechst staining and flow cytometry. As shown in Figure 2A, the exposure of cells to 10 mmol/L Glu resulted in chromatin condensation but not DNA fragmentation. A similar form of chromatin condensation has recently been observed in HT22 cells and cerebellar granule neurons exposed to Glu[24, 25]. Pretreatment with AA alleviated Glu-induced nuclear morphological alterations. The flow cytometry results (Figure 2C) demonstrated that stimulation with 10 mmol/L Glu produced apoptosis in 7.38% of the cells compared with 1.28% of the control group. AA 10 nmol/L treatment reduced the incidence of apoptosis to 2.98%.

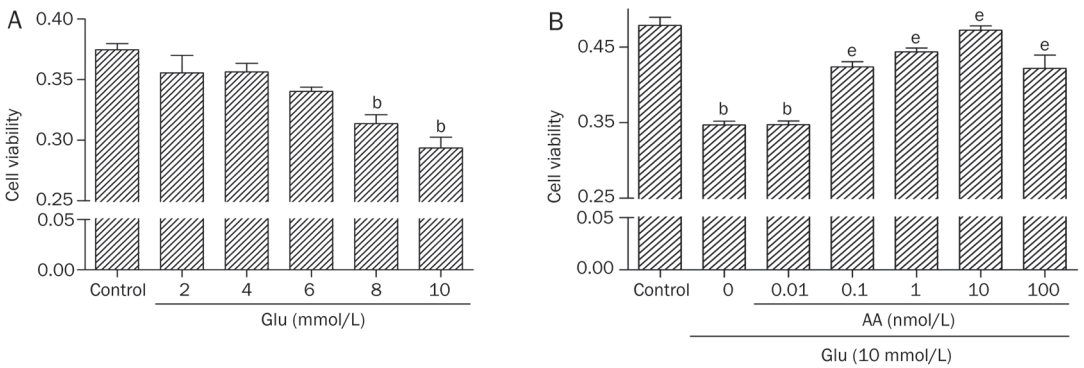

Figure 1. Inhibition by AA of Glu-induced cell death. (A) Cell viability was determined using MTT assay. Cells were exposed to 2–10 mmol/L Glu for 24 h without AA pretreatment. (B) Cells were preincubated with different concentrations of AA for 24 h, and then exposed to 10 mmol/L Glu for 24 h. $^{b}P<0.05$ *vs* control. $^{e}P<0.05$ *vs* Glu. All data are expressed as mean±SD of 5 replicate values in 3 separate experiments.

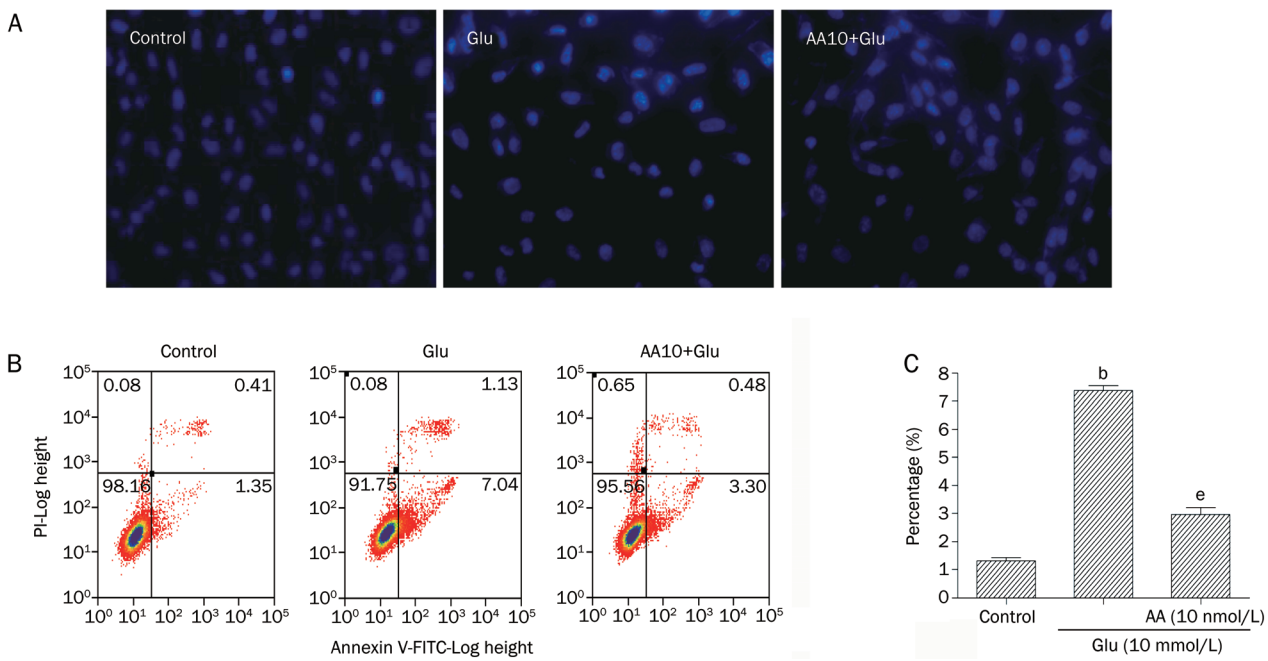

Figure 2. AA pretreatment significantly suppressed Glu-induced cell apoptosis. (A) AA pretreatment significantly decreased Glu-induced nuclear condensation. Apoptosis was determined morphologically by staining with Hoechst 33342 (original magnification 400×). AA10, 10 nmol/L AA. (B) Flow cytometric analyses with Annexin V-FITC and PI labels of cultured SH-SY5Y cells. (C) Percentage of apoptotic cells in total cells (n=3). $^{b}P<0.05$ *vs* control. $^{e}P<0.05$ *vs* Glu.

AA reduces ROS generation and restores the mitochondrial membrane potential (MMP) following Glu stimulation

Previous studies have demonstrated that stimulation by Glu can result in excessive ROS generation and a decrease in the mitochondrial membrane potential[26, 27]. We sought to determine whether AA has the ability to modulate the mitochondrial membrane potential and levels of intracellular ROS following excitotoxic stimulation. As shown in Figure 3B, FACS analysis revealed that 10 mmol/L Glu treatment increased ROS levels compared with the control group, whereas 10 nmol/L AA pretreatment significantly reduced Glu-induced ROS generation. Representative fluorescence photomicrographs (Figure 3A) were consistent with the FACS results. To assess the effect of AA on the changes in the MMP induced by Glu, fluorescence spectrometry and fluorescence microscopy analyses were performed using JC-1 staining. Glu induced a decline in the MMP compared with the control. This decline in MMP was prevented by AA (Figures 3C, 3D). These results indicate that AA may prevent Glu-mediated neurotoxicity partially through a reduction in ROS production and a restoration of MMP.

Effects of AA on the expression of PGC-1α and Sirt1

The silent information regulator 2 family of proteins (sirtuins) are NAD-dependent deacetylases that are believed to regulate survival and longevity[28]. Mammalian species have seven different sirtuin family members with the closest relative to the yeast sirtuin being Sirt1. Its beneficial role in neurodegenerative diseases has been studied extensively, and it holds great potential as a therapeutic target for neurodegeneration[29]. Peroxisome proliferator-activated receptor γ coactivator α (PGC-1α) controls mitochondrial biogenesis and function[30]

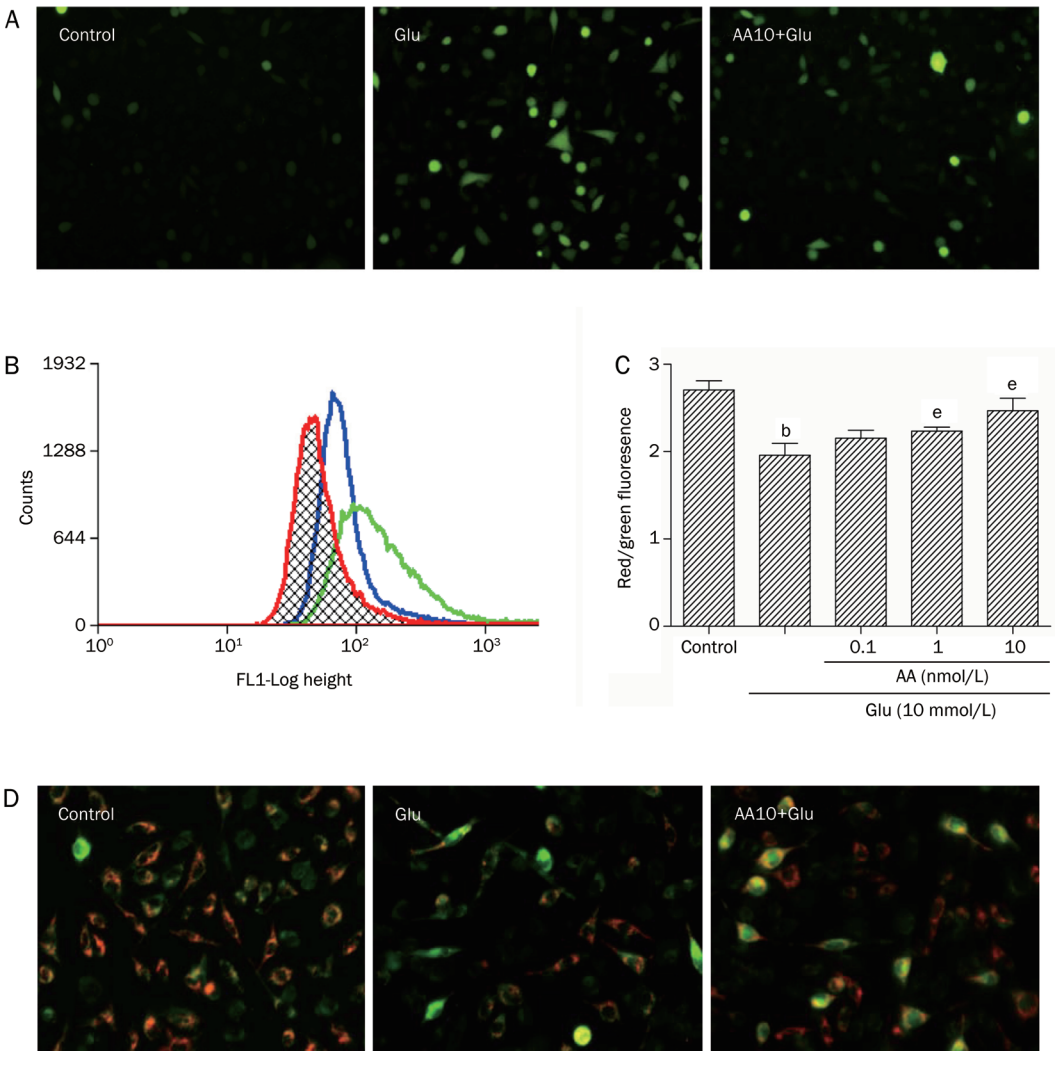

Figure 3. AA reduced ROS generation and restored MMP following Glu stimulus. (A) Cells were exposed to 10 mmol/L Glu with or without 10 nmol/L AA pretreatment. Representative fluorescence photographs (100×). AA10: 10 nmol/L AA. (B) Levels of ROS were analysed by FACS. Representative flow cytometry graph showing the DCF staining (n=3). Red peak: control; green peak: 10 mmol/L Glu; blue peak: 10 nmol/L AA+10 mmol/L Glu. (C) MMP of cells with 24 h Glu stimulus in the absence or presence of AA, determined by fluorescence spectrometry. (D) Representative fluorescence photographs of cellular mitochondrial membrane potential (400×). Mean±SD (n=3) are shown. ^bP<0.05 *vs* control. ^eP<0.05 vs Glu.

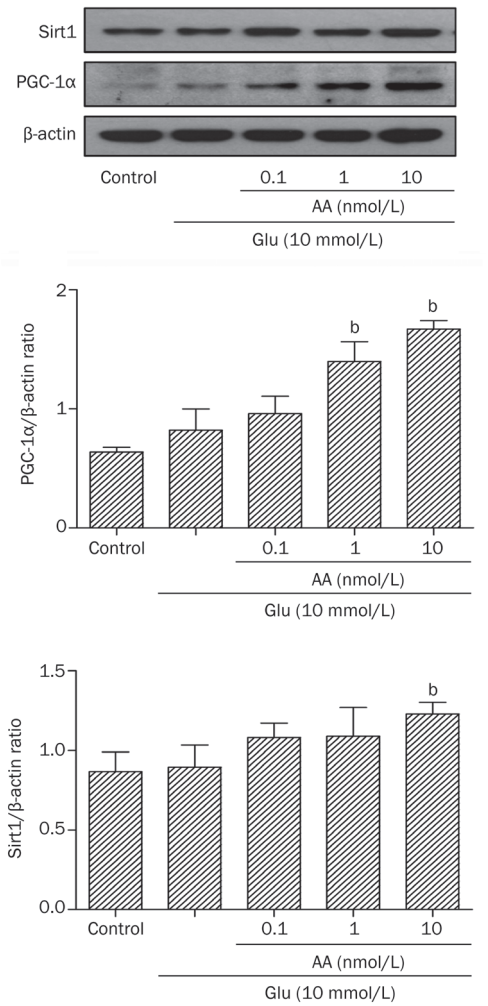

Figure 4. Effects of AA on Glu-stimulated expressions of Sirt1 and PGC-1α. Sirt1 and PGC-1α expressions in cells pretreated with AA (0.1–10 nmol/L). Mean±SD. n=3. ^bP<0.05 *vs* Glu group.

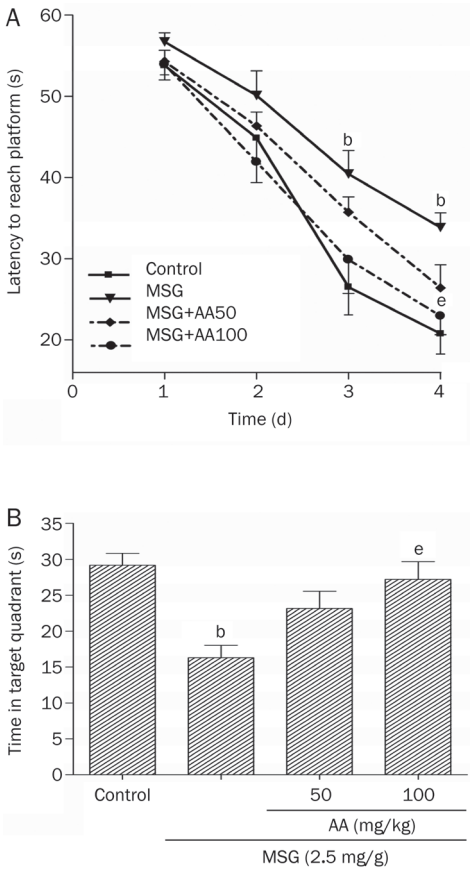

Figure 5. Effects of MSG and treatment with AA on the performance of spatial memory acquisition. (A) Latencies of mice during the 4 d test. (B) Times on d 5 that mice spent in the target quadrant with the platform removed. Mean±SEM. n=10. ^bP<0.05 *vs* control. ^eP<0.05 vs MSG.

and thereby plays an important role in brain energy homeostasis and neurodegenerative diseases[31, 32]. Recently, an increasing number of studies have indicated that Sirt1 can interact with and regulate the activity of PGC-1α[33, 34]. Because of these findings, we examined whether AA affects the expression of Sirt1 or PGC-1α in Glu-treated cells. According to Western blot analysis (Figure 4), cells preincubated with AA showed an upregulation of Sirt1 and PGC-1α compared with the Glu-only group, and this upregulation may have prevented Glu-induced injury in these cells.

Effects of AA on MSG-induced cognitive deficits

The amount of time mice required to find the hidden platform during the acquisition phase of the water maze experiment is presented in Figure 5A. The mean latencies for all groups were similar on the first day; in the following days, controls rapidly improved to locate the hidden platform, whereas the MSG group tended to require more time than controls. The difference in latency to locate the platform between the MSG and control groups was significant by d 3 and 4, whereas improvement of the AA-treated group versus the MSG group became significant on d 4. The MSG-treated animals showed a reduced ability to find the platform, and this poorer performance was partially prevented by chronic treatment with AA. Animals administered the high dose of AA showed a better capacity to reach the platform than those administered the low dose. In the spatial probe on d 5 of the trial, in which the platform was removed and mice were given one 60 s retention test trial, the MSG group spent less time in the platform quadrant than the control group (Figure 5B). In contrast, the mice treated with AA spent a significantly longer time in this quadrant than the MSG group. The 100 mg/kg dose was associated with better memory consolidation.

Effects of AA on MSG-induced oxidative stress

It has been suggested that MSG can induce oxidative stress in the rat brain and that antioxidants may be effective at ameliorating this effect[35]. Therefore, we investigated the levels of lipid peroxidation and the activity of an antioxidant enzyme in the hippocampus and cortex. The MSG-induced lipid peroxidation levels [determined using malondialdehyde (MDA)]

in the hippocampus and cortex of mice increased significantly, whereas glutathione levels and SOD activity decreased. The treatment with AA restored the levels of lipid peroxidation and glutathione and the activity of SOD toward their control values (Table 1).

Table 1. MSG-induced changes in mouse brain oxidative stress parameters and their responses to administration of AA. Values are expressed as mean±SEM. n=8. ^{b}P<0.05 *vs* control. ^{e}P<0.05 vs MSG.

	GSH (mg/g prot)	SOD (U/mg prot)	MDA (nmol/mg prot)
Control	7.22±0.32	402±23	8.44±1.44
MSG	6.72±0.44	365±34	13.68±3.37^{b}
MSG+AA 50 mg/kg	7.71±0.45^{e}	372±24	10.38±0.90^{e}
MSG+AA 100 mg/kg	7.90±0.51^{e}	381±20	8.73±0.91^{e}

Effects of AA on MSG-induced injury of the hippocampus

Neonatal MSG treatment produces degenerative changes in the developing brain; many studies have found that the injury is attributable to the destruction of the hippocampus[36]. In HE-stained sections, neuronal damage was manifested in the MSG group. The pyramidal layered structure disintegrated, and neuronal loss was found in the CA1 region. Neurons with pyknotic or shrunken nuclei were also observed in the CA3 region (Figure 6). These injuries were significantly attenuated by AA treatment.

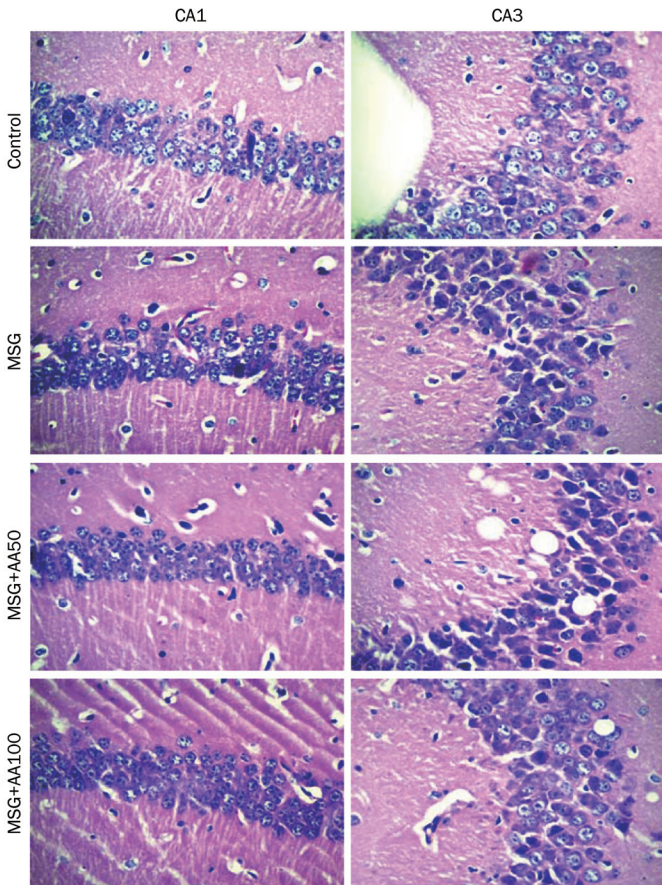

Figure 6. Effect of AA treatment on CA1 and CA3 neuron densities in hippocampus. Representative pictures obtained by HE staining (400×). When compared with the MSG-treated group, CA1 and CA3 neurons appear well preserved in AA-treated mice. MSG, 2.5 mg/g MSG; AA50, 50 mg/kg AA; AA100: 100 mg/kg AA.

Discussion

In the present study, we report that AA protected SH-SY5Y cells from Glu-induced injury *in vitro* and improved learning and memory deficits in the MSG-induced dementia animal model *in vivo*.

First, our data analysis shows that AA significantly protected cells from Glu excitotoxicity (Figure 1), and AA itself caused no conspicuous alterations in the growth of SH-SY5Y cells (data not shown). The neuroprotective effect of AA in the MTT assay paralleled the morphological analyses obtained with Hoechst 33342 staining and the flow cytometry assay. In addition, an important result demonstrated that 0.1–100 nmol/L AA acted against Glu toxicity; however, with increasing concentrations of AA, the protective ability decreased and even showed toxic effects (data not shown). This is because at high doses, AA can induce apoptosis via the activation of caspase-9 and -3 and increased intracellular free Ca^{2+} [37, 38].

The overactivation of glutamate receptors has been reported to induce an excessive influx of Ca^{2+}, following depolarization of the mitochondrial membrane and increased production of ROS[26]. Mitochondria are known to generate ROS due to mitochondrial electron flow in the respiratory chain[39]. Meanwhile, mitochondria themselves are vulnerable to ROS, and excessive ROS can induce mitochondrial damage. This interaction between mitochondrial dysfunction and ROS generation may contribute to an understanding of why AA inhibits cell death during neurotoxicity. On the basis of the above discussion, reducing the intracellular ROS levels and restoring the MMP significantly affects the neuroprotective function of AA. Our data suggest that, at a concentration of 10 mmol/L, Glu increases ROS levels. Pretreatment with AA reduced ROS levels in Glu-injured cells (Figure 3). These results are consistent with those of our previous study, which showed that AA has hydroxyl radical-scavenging activity in cell-free systems[40]. The disruption of the MMP may lead to cytochrome c release and activation of caspases that may lead to cell death. In our experiments, AA attenuated the decline of the MMP induced by Glu. Our data corroborate the results of a previous study, which reported that AA prevents the collapse of the MMP in rotenone-induced neuronal damage[14] and in the oxygen-glucose deprivation (OGD) cell culture model of ischemia[17].

Recently, an increasing number of studies have indicated that the regulation of mitochondrial biogenesis may be beneficial for neuronal recovery and survival in neurodegenerative disorders[32, 41, 42]. PGC-1α has been shown to be a master regulator of mitochondrial biogenesis and cellular energy

metabolism. PGC-1α increases the expression of a major antioxidant enzyme of mitochondria, superoxide dismutase 2 (SOD2)[43], and powerfully suppresses reactive oxygen species (ROS) *in vivo*[32]. Furthermore, PGC-1α knockout mice are much more sensitive to damage by oxidative stress, displaying apoptotic cell death in the dopaminergic cells of the substantia nigra and in hippocampal neurons[32]. From these findings, it seems reasonable that therapeutic agents that activate PGC-1α could successfully treat those neurodegenerative diseases in which mitochondrial dysfunction and oxidative damage play an important pathogenic role. Sirt1—an NAD-dependent deacetylase that has been linked to longevity — interacts with and regulates the activity of PGC-1α[34, 44]. It was reported that Sirt1 can deacetylate transcription factors such as p53 and the forkhead transcription factor (FOXO) family of proteins and thereby reduce p53, FOXO-induced apoptosis[45, 46]. Thus, Sirt1 may be another agent capable of playing a therapeutic role in neurodegenerative disease[29]. Due to the considerable effects that PGC-1α and Sirt1 have on neuronal function, we examined if they mediate the neuroprotective effects of AA. A novel finding is that pretreatment with AA (0.1–10 nmol/L) prior to Glu stimulation dose-dependently increases the expression of PGC-1α and Sirt1 at the same time. This result is consistent with the finding that Sirt1 can regulate PGC-1α as mentioned above. Thus, it is possible that the upregulation of PGC-1α and Sirt1 is responsible for the neuroprotective effects of AA. Another neuroprotective agent, resveratrol, also activates the Sirt1 pathway[47, 48]. Interestingly, we also found that after exposure to Glu alone, the cells show a slight increase in PGC-1α. This change in PGC-1α may reflect the cell's intrinsic response to stressful stimuli, but AA pretreatment largely increased the expression of PGC-1α compared with Glu stimulation alone. This is consistent with a previous report that NMDA can directly induce the expression of PGC-1α in neuronal cells[49].

Furthermore, the neuroprotective function of AA ameliorates MSG-induced cognitive deficits *in vivo*. The neonatal administration of MSG causes cognitive deficits in adult animals[50–52]. The Morris water maze is a commonly used method for evaluating learning and memory. MSG-induced deficits in learning and memory were revealed in the mice, and memory was enhanced by AA. The hippocampus has an important role in spatial learning and memory[53]. Damage to and morphological changes of the CA1 hippocampal structure has been described in MSG-treated animals[36, 54]. Our data confirmed that the CA1 hippocampal structure underwent disintegration. We also found that the CA3 pyramidal neurons became pyknotic or shrunken, and this damage was significantly prevented by simultaneous administration of AA. However, the CA3 hippocampal neurons appear to be less damaged when analyzed in terms of tissue volume and cell numbers instead of morphology[54]. Previous studies have suggested that the oxidative stress induced by MSG might contribute to hippocampal impairment[51, 55]. AA is viewed as a promising antioxidant candidate; it sufficiently abated oxidative stress in MSG-treated rodents by enhancing both GSH levels and SOD activity and by reducing MDA levels. Therefore, it is hypothesized that the attenuation of oxidative stress, following induced hippocampal damage, is responsible for the effects of AA against MSG-induced dementia.

In conclusion, our data support the notion that AA attenuates cognitive deficits in an animal model of MSG-induced dementia. In addition, AA offered beneficial effects in Glu-induced cellular injury by suppressing oxidative stress and protecting mitochondria. Taking these *in vitro* and *in vivo* results together, especially the protection of mitochondria by AA, AA and related compounds may develop into a new therapeutic approach for preventing and/or treating neuronal damage and degenerative disorders.

Acknowledgements

We thank Dr Edward SHARMAN, University of California, Irvine, for his careful reading and editing of this manuscript. This work was supported by the Excellent Young Teachers Program of MOE and grants from Jiangsu University (07JDG012), Jiangsu Natural Sciences Foundation (2008249), and the National Natural Science Foundation of China (31171143).

Author contribution

Min-fang XU and Jing GAO designed the experiments; Min-fang XU and Yu-yun XIONG performed the experiments; Min-fang XU analyzed the data and drafted the manuscript; Jian-kang LIU revised the manuscript and offered valuable advice about all of the experiments; Jin-jun QIAN and Li ZHU offered helpful suggestions and discussion; and Jing GAO revised the paper and supervised the experiments.

References

1 Hague SM, Klaffke S, Bandmann O. Neurodegenerative disorders: Parkinson's disease and Huntington's disease. J Neurol Neurosur Ps 2005; 76: 1058–63.
2 Dumont RJ, Okonkwo DO, Verma S, Hurlbert RJ, Boulos PT, Ellegala DB, *et al*. Acute spinal cord injury, part I: pathophysiologic mechanisms. Clin Neuropharmacol 2001; 24: 254–64.
3 Lankiewicz S, Marc Luetjens C, Truc Bui N, Krohn AJ, Poppe M, Cole GM, *et al*. Activation of calpain I converts excitotoxic neuron death into a caspase-independent cell death. J Biol Chem 2000; 275: 17064–71.
4 Nicholls DG. Mitochondrial calcium function and dysfunction in the central nervous system. BBA-Bioenergetics 2009; 1787: 1416–24.
5 Pivovarova NB, Andrews SB. Calcium-dependent mitochondrial function and dysfunction in neurons. FEBS J 2010; 277: 3622–36.
6 Lazzarino G, Vagnozzi R, Tavazzi B, Pastore FS, Di Pierro D, Siragusa P, *et al*. MDA, oxypurines, and nucleosides relate to reperfusion in short-term incomplete cerebral ischemia in the rat. Free Radic Biol Med 1992; 13: 489–98.
7 Greenamyre JT, Penney JB, Young AB, D'Amato CJ, Hicks SP, Shoulson I. Alterations in *L*-glutamate binding in Alzheimer's and Huntington's diseases. Science 1985; 227: 1496–9.
8 Armstrong JS. Mitochondrial medicine: pharmacological targeting of mitochondria in disease. Br J Pharmacol 2007; 151: 1154–65.
9 Liu JK, Ames BN. Reducing mitochondrial decay with mitochondrial nutrients to delay and treat cognitive dysfunction, Alzheimer's

disease, and Parkinson's disease. Nutr Neurosci 2005; 8: 67–89.
10 Kumar MHV, Gupta YK. Effect of different extracts of *Centella asiatica* on cognition and markers of oxidative stress in rats. J Ethnopharmacol 2002; 79: 253–60.
11 Wattanathorn J, Mator L, Muchimapura S, Tongun T, Pasuriwong O, Piyawatkul N, *et al*. Positive modulation of cognition and mood in the healthy elderly volunteer following the administration of *Centella asiatica*. J Ethnopharmacol 2008; 116: 325–32.
12 Gnanapragasam A, Yogeeta S, Subhashini R, Ebenezar KK, Sathish V, Devaki T. Adriamycin induced myocardial failure in rats: protective role of *Centella asiatica*. Mol Cell Biochem 2007; 294: 55–63.
13 Soumyanath A, Zhong YP, Gold SA, Yu XL, Koop DR, Bourdette D, *et al*. *Centella asiatica* accelerates nerve regeneration upon oral administration and contains multiple active fractions increasing neurite elongation *in-vitro*. J Pharm Pharmacol 2005; 57: 1221–29.
14 Xiong YY, Ding HQ, Xu MF, Gao J. Protective effects of asiatic acid on rotenone- or H_2O_2-induced injury in SH-SY5Y cells. Neurochem Res 2009; 34: 746–54.
15 Lee MK, Kim SR, Sung SH, Lim DY, Kim H, Choi H, *et al*. Asiatic acid derivatives protect cultured cortical neurons from glutamate-induced excitotoxicity. Res Commun Mol Pathol Pharmacol 2000; 108: 75–86.
16 Jew SS, Yoo CH, Lim DY, Kim H, Mook-Jung I, Jung MW, *et al*. Structure-activity relationship study of asiatic acid derivatives against beta amyloid (A beta)-induced neurotoxicity. Bioorg Med Chem Lett 2000; 10: 119–21.
17 Krishnamurthy RG, Senut MC, Zemke D, Min JY, Frenkel MB, Greenberg EJ, *et al*. Asiatic acid, a pentacyclic triterpene from *Centella asiatica*, is neuroprotective in a mouse model of focal cerebral Ischemia. J Neurosci Res 2009; 87: 2541–50.
18 Ishikawa K, Kubo T, Shibanoki S, Matsumoto A, Hata H, Asai S. Hippocampal degeneration inducing impairment of learning in rats: model of dementia? Behav Brain Res 1997; 83: 39–44.
19 Urena-Guerrero ME, Lopez-Perez SJ, Beas-Zarate C. Neonatal monosodium glutamate treatment modifies glutamic acid decarboxylase activity during rat brain postnatal development. Neurochem Int 2003; 42: 269–76.
20 Morris RG, Garrud P, Rawlins JN, O'Keefe J. Place navigation impaired in rats with hippocampal lesions. Nature 1982; 297: 681–3.
21 Anderson ME. Determination of glutathione and glutathione disulfide in biological samples. Methods Enzymol 1985; 113: 548–55.
22 Tzeng WF, Lee JL, Chiou TJ. The role of lipid peroxidation in menadione-mediated toxicity in cardiomyocytes. J Mol Cell Cardiol 1995; 27: 1999–2008.
23 Bradford MM. A rapid and sensitive method for the quantitation of microgram quantities of protein utilizing the principle of protein-dye binding. Anal Biochem 1976; 72: 248–54.
24 Elphick LM, Hawat M, Toms NJ, Meinander A, Mikhailov A, Eriksson JE, *et al*. Opposing roles for caspase and calpain death proteases in *L*-glutamate-induced oxidative neurotoxicity. Toxicol Appl Pharm 2008; 232: 258–67.
25 Bezvenyuk Z, Miettinen R, Solovyan V. Chromatin condensation during glutamate-induced excitotoxicity of celebellar granule neurons precedes disintegration of nuclear DNA into high molecular weight DNA fragments. Mol Brain Res 2003; 110: 140–6.
26 Atlante A, Calissano P, Bobba A, Giannattasio S, Marra E, Passarella S. Glutamate neurotoxicity, oxidative stress and mitochondria. FEBS Lett 2001; 497: 1–5.
27 Ankarcrona M, Dypbukt JM, Bonfoco E, Zhivotovsky B, Orrenius S, Lipton SA, *et al*. Glutamate-induced neuronal death: a succession of necrosis or apoptosis depending on mitochondrial function. Neuron 1995; 15: 961–73.
28 Grubisha O, Smith BC, Denu JM. Small molecule regulation of Sir2 protein deacetylases. FEBS J 2005; 272: 4607–16.
29 Outeiro TF, Marques O, Kazantsev A. Therapeutic role of sirtuins in neurodegenerative disease. Biochim Biophys Acta 2008; 1782: 363–9.
30 Finck BN, Kelly DP. PGC-1 coactivators: inducible regulators of energy metabolism in health and disease. J Clin Invest 2006; 116: 615–22.
31 Cui LB, Jeong H, Borovecki F, Parkhurst CN, Tanese N, Krainc D. Transcriptional repression of PGC-alpha by mutant huntingtin leads to mitochondrial dysfunction and neurodegeneration. Cell 2006; 127: 59–69.
32 St-Pierre J, Drori S, Uldry M, Silvaggi JM, Rhee J, Jager S, *et al*. Suppression of reactive oxygen species and neurodegeneration by the PGC-1 transcriptional coactivators. Cell 2006; 127: 397–408.
33 Lagouge M, Argmann C, Gerhart-Hines Z, Meziane H, Lerin C, Daussin F, *et al*. Resveratrol improves mitochondrial function and protects against metabolic disease by activating SIRT1 and PGC-1 alpha. Cell 2006; 127: 1109–22.
34 Nemoto S, Fergusson MM, Finkel T. SIRT1 functionally interacts with the metabolic regulator and transcriptional coactivator PGC-1 alpha. J Bio Chem 2005; 280: 16456–60.
35 Farombi EO, Onyema OO. Monosodium glutamate-induced oxidative damage and genotoxicity in the rat: modulatory role of vitamin C, vitamin E and quercetin. Hum Exp Toxicol 2006; 25: 251–9.
36 Beas-Zarate C, Perez-Vega MI, Gonzalez-Burgos I. Neonatal exposure to monosodium L-glutamate induces loss of neurons and cytoarchitectural alterations in hippocampal CA1 pyramidal neurons of adult rats. Brain Res 2002; 952: 275–81.
37 Cho CW, Choi DS, Cardone MH, Kim CW, Sinskey AJ, Rha C. Glioblastoma cell death induced by asiatic acid. Cell Biol Toxicol 2006; 22: 393–408.
38 Park BC, Bosire KO, Lee ES, Lee YS, Kim JA. Asiatic acid induces apoptosis in SK-MEL-2 human melanoma cells. Cancer Lett 2005; 218: 81–90.
39 Nicholls DG. Mitochondrial dysfunction and glutamate excitotoxicity studied in primary neuronal cultures. Curr Mol Med 2004; 4: 149–77.
40 Gao J, Tang XH, Dou H, Fan YM, Zhao XN, Xu Q. Hepatoprotective activity of terminalia catappa L leaves and its two triterpenoids. J Pharm Pharmacol 2004; 56: 1449–55.
41 Clark J, Simon DK. Transcribe to survive: transcriptional control of antioxidant defense programs for neuroprotection in Parkinson's disease. Antioxid Redox Signal 2009; 11: 509–28.
42 Thomas B, Beal MF. Mitochondrial therapies for Parkinson's disease. Movement Disord 2010; 25: S155–S60.
43 Valle I, Alvarez-Barrientos A, Arza E, Lamas S, Monsalve M. PGC-1alpha regulates the mitochondrial antioxidant defense system in vascular endothelial cells. Cardiovasc Res 2005; 66: 562–73.
44 Rodgers JT, Lerin C, Haas W, Gygi SP, Spiegelman BM, Puigserver P. Nutrient control of glucose homeostasis through a complex of PGC-1 alpha and SIRT1. Nature 2005; 434: 113–8.
45 Luo J, Nikolaev AY, Imai S, Chen D, Su F, Shiloh A, *et al*. Negative control of p53 by Sir2alpha promotes cell survival under stress. Cell 2001; 107: 137–48.
46 Giannakou ME, Partridge L. The interaction between FOXO and SIRT1: tipping the balance towards survival. Trends Cell Biol 2004; 14: 408–12.
47 Pallas M, Casadesus G, Smith MA, Coto-Montes A, Pelegri C, Vilaplana J, *et al*. Resveratrol and neurodegenerative diseases: activation of SIRT1 as the potential pathway towards neuroprotection. Curr Neurovasc Res 2009; 6: 70–81.

48 Tan L, Yu JT, Guan HS. Resveratrol exerts pharmacological preconditioning by activating PGC-1 alpha. Med Hypotheses 2008; 71: 664–7.
49 Luo Y, Zhu WJ, Jia J, Zhang CY, Xu Y. NMDA receptor dependent PGC-1 alpha up-regulation protects the cortical neuron against oxygen-glucose deprivation/reperfusion injury. J Mol Neurosci 2009; 39: 262–8.
50 Olvera-Cortes E, Lopez-Vazquez MA, Beas-Zarate C, Gonzalez-Burgos I. Neonatal exposure to monosodium glutamate disrupts place learning ability in adult rats. Pharmacol Biochem Behav 2005; 82: 247–51.
51 Narayanan SN, Kumar RS, Paval J, Nayak S. Effect of ascorbic acid on the monosodium glutamate-induced neurobehavioral changes in periadolescent rats. Bratisl Lek Listy 2010; 111: 247–52.
52 Kiss P, Hauser D, Tamas A, Lubics A, Racz B, Horvath Z, *et al*. Changes in open-field activity and novelty-seeking behavior in periadolescent rats neonatally treated with monosodium glutamate. Neurotox Res 2007; 12: 85–93.
53 Compton DM. Behavior strategy learning in rat: effects of lesions of the dorsal striatum or dorsal hippocampus. Behav Processes 2004; 67: 335–42.
54 Gonzalez-Burgos I, Velazquez-Zamora DA, Beas-Zarate C. Damage and plasticity in adult rat hippocampal trisynaptic circuit neurons after neonatal exposure to glutamate excitotoxicity. Int J Dev Neurosci 2009; 27: 741–5.
55 Thomas M, Sujatha KS, George S. Protective effect of piper longum linn on monosodium glutamate induced oxidative stress in rats. Indian J Exp Biol 2009; 47: 186–92.

Acta Pharmacologica Sinica (2012) 33: 588–593
 1671-4083/12 $32.00
www.nature.com/aps

Original Article

Associations between personality changes and nucleus accumbens ablation in opioid addicts

Hai-kang ZHAO[1, #], Chong-wang CHANG[1, #], Ning GENG[1, #], Li GAO[1], Jing WANG[1], Xin WANG[1], Ya-rong WANG[2], Xue-lian WANG[1, *], Guo-dong GAO[1, *]

[1]*Department of Neurosurgery, Tangdu Hospital, the Fourth Military Medical University, Xi'an 710038, China;* [2]*Department of Radiology, Tangdu Hospital, the Fourth Military Medical University, Xi'an 710038, China*

Aim: It has been reported that nucleus accumbens (NAc) lesions can help to prevent relapse in opioid addicts. This article aimed to investigate associations between personality changes and NAc lesions.
Methods: The surgery group consisted of 78 patients who had received bilateral stereotactic lesions of the NAc to treat opioid addiction. Seventy two non-surgery opioid addicts were appropriately paired with the patients of the surgery group as the non-surgery group. All participants were interviewed in person and received urine tests, naloxone provocative tests and hair tests to determine the prevalence of relapse. Eysenck personality questionnaire (EPQ) and the health survey questionnaire (SF-36) were employed to assess personality and functional health, respectively.
Results: In the surgery group, 30 participants relapsed, and the non-relapse rate was 61.5% (48/78). Compared with the Chinese normative data, the neuroticism (N) and psychoticism (P) dimensions of the EPQ in the non-surgery group were significantly higher, whereas the lie (L) dimension was significantly lower. There was no significant difference in all dimensions of the EPQ between the surgery group and the Chinese normative data. The N dimension in the relapse group and the L dimension in the surgery group were significantly lower than those of the non-surgery group. The P dimension in the relapse group was significantly higher than that of the non-relapse group. The extraversion (E) dimension was relatively stable between these groups.
Conclusion: Although the influence of other factors cannot be excluded, it is apparent that surgically induced NAc lesions are associated with lower P and N dimensions for opioid addicts, and a higher P dimension is associated with a tendency to relapse.

Keywords: opiate addiction; relapse; nucleus accumbens lesion; Eysenck personality questionnaire; health survey questionnaire (SF-36); long-term follow-up study

Acta Pharmacologica Sinica (2012) 33: 588–593; doi: 10.1038/aps.2012.10; published online 16 Apr 2012

Introduction

Addictive diseases, including opioid dependence, are a chronic and recurrent cerebropathy (National Institutes of Health, 1998), causing abnormalities in mentality and behavior[1]. The success rate for treating opioid dependence using traditional therapy is approximately 3%–7%[2]. The treatment of opiate addiction remains one of the most challenging problems worldwide. Recently, a large number of animal and clinical studies have suggested that the nucleus accumbens (NAc) is an important part of the dopaminergic (mesocorticolimbic) pathway and plays a key role in drug addiction[3–6].

The Research Center of Functional Cerebropathy of Tangdu Hospital has been attempting to treat opioid addiction via bilateral stereotactic NAc lesions since July 2000. By November 2004, this operation had been performed on a total of 272 opiate addicts, and short-term follow-ups revealed satisfactory results[7, 8]. However, this treatment was halted due to ethical problems associated with irreversible damage to the brain structure and the lack of long-term follow-up data. The current investigation aims to assess the long-term effect of the treatment on the addicts of surgically treated opioid dependence.

# These authors contributed equally to this article.
* To whom correspondence should be addressed.
E-mail tdwxlian@126.com (Xue-lian WANG);
gguodong@fmmu.edu.cn (Guo-dong GAO)
Received 2011-09-30 Accepted 2012-02-01

Materials and methods

Participants

For the surgery group, 100 patients who had received bilateral stereotactic NAc lesions were randomly selected from a total of 272 patients. The non-surgery group was comprised of 72 participants who were selected from the voluntary drug

rehabilitation institution on the basis of their match to the surgery group participants. The pairing of surgery group participants with opiate addicts who had not undergone the operation was performed according to a number of preoperative characteristics: age, gender, education level, place of birth, category of drugs taken pre- or post-operatively, duration of drug abuse, treatment history and personality disorders (Table 1). The exclusion criteria included participants who could not understand the questionnaire items correctly, could not concentrate (*eg*, when completing questionnaires) or failed to complete or attend the follow-up visits. All volunteers gave full consent to participate in the study.

Table 1. Basic information for the surgery group and non-surgery groups.

Items	Surgery group (*n*=72)	Non-surgery group (*n*=72)
Age (Year)		
18–30	25	25
30–40	34	34
40–50	11	11
50–60	2	2
>60	0	0
Male	59 (81.9%)	59 (81.9%)
Years of education		
<6 years	17	17
6–12 years	45	45
>12 years	10	10
Frequent dwelling place		
Rural area	23	23
Town or small city	28	28
City above provincial level	21	21
History of drug addiction		
3–8 years	52	52
8–15 years	16	16
>15 years	4	4
Main addictive drugs		
Heroin	72	72
Occasional combination drugs		
Morphine	4	4
Opium	8	8
Cocaine	5	5
Equivalent weight of heroin daily		
<0.5 g	13	13
0.5–1.0 g	44	44
>1.0 g	15	15
Treatment history		
Drug replacement therapy	28	28
Nonmedicine therapy	44	44
Personality disorder	3	3

Of the 100 patients in the surgery group, 10 did not fully understand the questionnaire items and 12 did not complete the study. The total number of participants in the surgery group was 78 (69 males, 9 females, average age 31.53±9.84 years). The number of years of education was 11.76±5.29. The addictive substances taken by the surgery group were primarily of the opioid drug class. The duration of preoperative opioid addiction was 6.30±4.48 years, and the total preoperative opioid dose was 0.54±0.67 g daily. The follow-up time for the surgery group ranged from 5 to 8 years post-operatively and averaged 5.92±1.33 years. Seventy-two surgery group patients were successfully paired with the non-surgery group (the paired rate was 92%).

The evaluators and data processing staff were blinded to each participant's surgical status. The study ran from December 1, 2009 to January 31, 2010. This study obtained the approval of the Fourth Military Medical University Ethics Committee.

Measurement methods and tools

Non-relapses were defined based on negative results in urine tests, naloxone provocative tests, hair testing and the absence of complaints from patients and family members. A positive result for these test measures was defined as a relapse. The position of lesion foci in the surgery group participants was re-examined using post-operative magnetic resonance imaging (MRI).

The investigation included personal interviews and self-assessment scales. Screening for mental diseases and personality disorders was performed by two psychiatrists in accordance with the International Classification of Diseases (ICD-10).

Eysenck personality questionnaire (EPQ)

The EPQ is comprised of scales for 4 dimensions of personality: extraversion (E), wherein higher scores represent greater extroversion; neuroticism (or nervosity, N), wherein higher scores reflect less stable emotions; psychoticism (P), wherein higher scores indicate higher psychoticism; and lie (L), wherein higher scores are associated with a greater tendency to lie. The EPQ Chinese Revised Edition was used to provide the normative data for this study[9].

Short form-36 health survey questionnaire (SF-36)

The SF-36 includes 8 dimensions of functional health: physical functioning (PF), role-physical (RP), bodily pain (BP), general health (GH), vitality (VT), social functioning (SF), role-emotional (RE) and mental health (MH). A higher score in each of these dimensions is indicative of better health.

Statistical analysis

Descriptive statistics (mean±SD) were calculated for all questionnaire items. The statistical analysis was performed using SPSS 12.0 software. The statistical analyses included paired sample *t*-tests, independent sample *t*-tests, relative analysis, and the χ^2 test. A significance level of $P<0.05$ was considered to be statistically significant.

Results

Re-examination of the ablation locus and relapse rate for the surgery group

The positions of lesion foci in the surgery patients were located

accurately and the errors of the foci were within the normal range. MRIs taken preoperatively, 1 week postoperatively and 5 years postoperatively are shown in Figures 1 and 2. The non-relapse rate for the surgery group was 61.5% (48/78).

Comparison of personality (EPQ) differences

As shown in Table 2, the N and P dimensions for the non-surgery group were higher (P<0.05), and the L dimension for the non-surgery group was lower (P<0.05) compared with the normative data. The L dimension for the surgery group was lower than the normative data (n=78, P<0.05). Compared with the normative data, the P dimension for the relapse group was higher (P<0.05), and the L dimension for the relapse group was lower (P<0.05). The non-relapse group showed no significant differences compared with the normative data in all the dimensions of the EPQ. The N and P dimensions for the

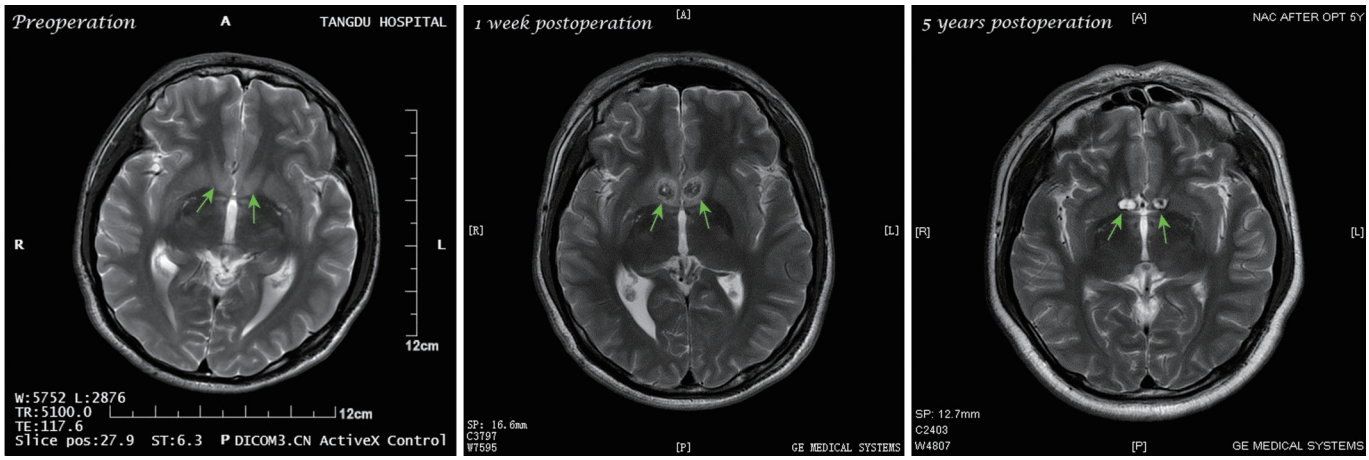

Figure 1. The exial view MRI of the surgery opiates-dependent patients. The place marked by the arrow is the proximal NAc.

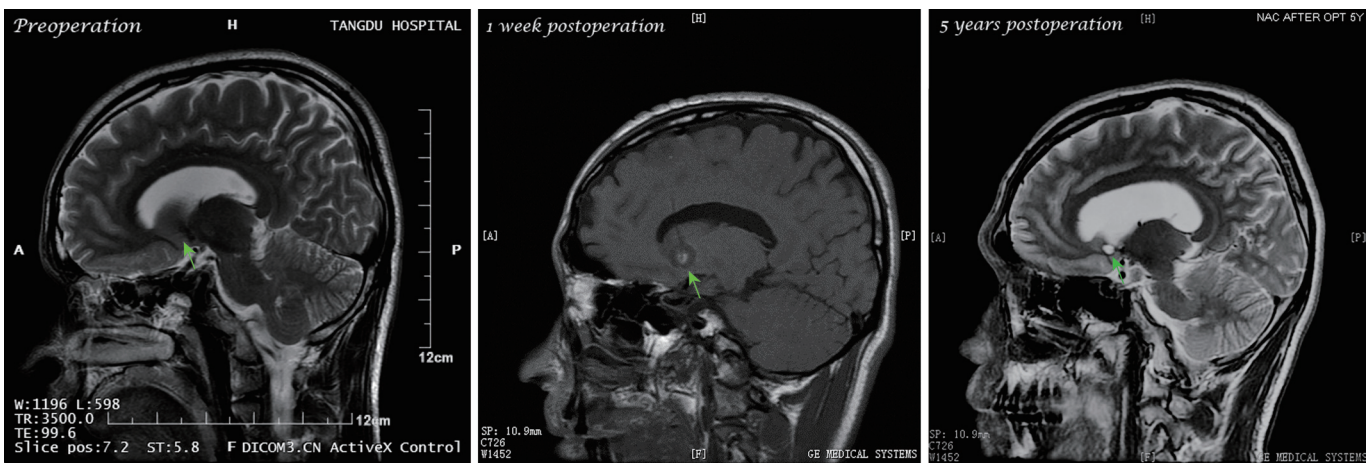

Figure 2. The sagittal view MRI of the surgery opiates-dependent patients. The place marked by the arrow is the proximal NAc.

Table 2. Differences of EPQ dimensions for the groups.

Dimensions	Chinese normative (n=1388)	Non-surgery group (n=72)	Surgery group (n=72)	Surgery group (n=78)	Non-relapse group (n=48)	Relapse group (n=30)
P	5.96±2.84	8.85±3.03[h]	7.10±3.57[b]	6.96±3.64	6.21±3.33[e]	8.17±3.86[h]
E	10.63±4.44	10.53±3.51	10.40±5.44	10.48±5.26	10.31±5.34	10.77±5.20
N	12.17±3.17	16.19±4.63[h]	12.21±5.04[b]	12.12±5.20	11.58±5.55	12.97±4.54[b]
L	11.26±4.26	9.13±3.58[h]	9.47±4.46[h]	9.55±4.50[h]	10.16±4.64	8.57±4.16[h]

[b]P<0.05 *vs* non-surgery group; [e]P<0.05 *vs* the relapsers; [h]P<0.05 *vs* Chinese normative.

surgery group (n=72) and the non-relapse group were lower (P<0.05) than those for the non-surgery group. The N dimension for the relapse group was lower than for the non-surgery group (P<0.05). The P dimension for the non-relapse group was lower than that for the relapse group (P<0.05).

Differences in functional health (SF-36)

As shown in Table 3, there were no significant differences for the RE dimension between the surgery group and the non-surgery group, whereas the other 7 dimensions of the SF-36 were more favorable for the surgery group (P<0.05). The PF and BP dimensions for the relapse group were higher than those of the non-surgery group (P<0.05). Compared with the relapse group, the PF dimension for the non-relapse group was not significantly different, whereas the other seven dimensions of the SF-36 were more favorable for the non-relapse group (P<0.05).

Correlations between personality or functional health and patients with or without surgery or relapse

As shown in Table 4, with or without surgery was negatively correlated with the P and N dimensions (P<0.05); the P and N dimension scores were lower for the surgery group. With or without surgery was not correlated with RE but was positively correlated (P<0.05) with the other 7 dimensions of the SF-36. The functional health of the surgery group was better than that of the non-surgery group. With or without relapse was negatively correlated with the P and N dimensions (P<0.05); the P and N scores were higher for the relapse group. The non-relapse groups were not correlated with the RE and GH but were positively correlated with the other 6 dimensions of the SF-36 (P<0.05). The functional health of the non-relapse group was better than that of the relapse group.

Table 4. Correlations between surgery/relapse and personality/health functioning (Spearman rank correlation). ^{b}P<0.05, ^{c}P<0.01.

Items	Non-surgery=1 Surgery=2 (n=150)	Non-relapse=1 Relapse=2 (n=78)
E	0.012	0.019
P	-0.268^{c}	-0.188^{b}
N	-0.390^{c}	-0.341^{c}
L	0.042	-0.008
PF	0.445^{c}	0.378^{c}
RP	0.335^{c}	0.257^{c}
BP	0.475^{c}	0.386^{c}
GH	0.201^{c}	0.119
VT	0.269^{c}	0.195^{b}
SF	0.255^{c}	0.168^{b}
RE	0.133	0.039
MH	0.279^{c}	0.202^{b}

Discussion

All the participants within the surgery group were patients who had received bilateral stereotactic NAc lesions 5 to 8 years prior to this study. The non-relapse rate was 61.5% (minimum) at 5 years after the surgery. In addition, the functional health of the surgery group was significantly better on all of the SF-36 dimensions except the RE. The results indicate that the bilateral stereotactic NAc lesions were associated with a relapse rate of only 38.5% for the opioid addiction patients and improved the functional health of both non-relapse and relapse patients.

The results showed that only the L dimension was significantly lower in the surgery group relative to the Chinese normative data. Notably, the personalities of the non-relapse patients within the surgery group were not different from those of the Chinese normative data. However, the P dimension was significantly higher and the L dimension was significantly lower for the relapse group compared to the Chinese normative data. The difference in the L dimension for the surgery group was probably attributable to the relapse patients. The personalities of the relapse patients showed a higher tendency toward psychoticism and a lower tendency to lie.

Unfortunately, this study lacked preoperative data for the EPQ. As a feasible means of redress, a matched non-surgery group was included in this study. It has been reported that opiate addicts have specific personality characteristics, including an unstable personality with a tendency to be sensitive, suspicious, anxious, changeable, curious, impulsive, aggres-

Table 3. Average values and differences for the health survey questionnaire (SF-36).

Items	Non-surgery group (n=72)	Surgery group (n=72)	t	P	Non-relapse group (n=48)	Relapse group (n=30)	t	P
PF	63.61±27.38	87.12±13.08	6.62	0.000	89.17±12.26	83.83±13.88^{b}	1.78	0.080
RP	45.49±39.43	72.12±37.79	4.22	0.000	79.17±33.55	60.83±41.88^{e}	2.13	0.036
BP	59.32±23.56	79.23±16.35	5.97	0.000	83.08±12.61	73.07±19.71^{b}	2.74	0.008
GH	47.72±18.84	57.50±27.14	2.58	0.011	63.21±27.23	48.37±24.78^{e}	2.42	0.018
VT	49.51±15.79	59.87±23.47	3.19	0.002	64.38±23.35	52.67±22.20^{e}	2.20	0.031
SF	66.36±25.77	78.78±21.13	3.24	0.001	83.57±19.17	71.11±22.15^{e}	2.63	0.010
RE	50.46±41.86	61.97±40.82	1.70	0.091	72.92±37.45	44.44±40.43^{e}	3.17	0.002
MH	54.06±15.86	65.33±21.90	3.63	0.000	69.33±21.35	58.93±21.58^{e}	2.09	0.040

^{b}P<0.05 *vs* non-surgery group, ^{e}P<0.05 *vs* non-relapse group.

sive, poorly self-controlled, hedonistic, excitement-seeking and antisocial[10–13]. The results for the non-surgery group were similar to those reported above, with participants having higher P and N dimensions and a lower L dimension than the Chinese normative data. Compared to the non-surgery group, the P and L dimensions were notably lower for the surgery group.

The N dimension was significantly lower for the relapse group compared to the non-surgery group, whereas no differences between these groups were revealed in the other 3 dimensions of the EPQ. All participants in this comparison were opiate addicts. The difference among the groups was that the relapse patients had received bilateral stereotactic NAc lesions at least 5 years previously with a minimum time difference of 5 years (*ie*, the relapse patients had taken opiates for a minimum of 5 more years than the non-surgery patients). As a result, it is suggested that the difference for the N dimension may have been due to the surgery and/or the time difference.

When the non-relapse group was compared with the relapse group, the P dimension of the non-relapse group was significantly lower, while no differences were revealed in the other 3 dimensions of the EPQ. As all participants in this comparison had received the bilateral stereotactic NAc lesions, it is possible that the difference for the P dimension was mainly associated with relapse. In other words, a higher P score or a longer duration of opioid use (minimum 5 years) led to a greater risk of relapse.

The EPQ, developed by Eysenck, is a personality inventory based on the personality theory of physiological psychology[14–16]. According to Eysenck, the physiological principle of the E dimension is the excitability level of the cortex. Low excitability levels of the cortex are thought to be associated with extroverted personality traits, whereas high excitability levels of the cortex are associated with introverted personality traits. The ability to form conditioned reflexes was believed to be relative to the E and N dimensions. The formation of strong, conditioned reflexes was associated with introverted personality traits and more stable emotions, whereas a weak reflex ability was associated with extroverted personality traits and less stable emotions. The concepts of emotionality and drive, which are influenced by the balance of the function between the sympathetic and parasympathetic nervous systems, are related mainly to the N dimension and only partly to the E dimension. If the sympathetic nervous system is dominant, highly unstable emotions prevail. Eysenck thought that the P dimension, which he added at a later stage, was relative to increased androgen levels[15].

The concepts cited by Eysenck have been explored using laboratory examinations. Research indicates that the vital brain centers of emotional processing include the hypothalamus, septal area, amygdaloid nucleus, hippocampus, limbic cortex, prefrontal cortex and temporal lobes[16].

The NAc neurons are implicated in behaviors that are elicited by reward-predictive sensory cues[4, 17, 18]. The anatomical characteristics and functional associations of the NAc indicate that it may play an important role in the development of euphoric feelings and other forms of positive reinforcement. Furthermore, it is possible that the NAc influences the formation of learned conditioned reflexes, the functioning of the sympathetic and parasympathetic nervous systems, and the secretion of androgen.

If the difference in the N dimension between the relapse group and the non-surgery group was caused by the bilateral NAc lesions, this indicates that the NAc might contribute to the formation of learned conditioned reflexes and the functional harmonization of the sympathetic and parasympathetic nervous systems. However, this difference in the N dimension might also be attributable to the additional 5 years of drug abuse in the non-surgery group compared with the relapse group. The difference in the P dimension between the relapse and non-relapse groups might be associated with the personality factors of the participants themselves. The participants with a higher P score tended to relapse more easily, but this effect on personality may be the result of drug use. According to Eysenck's theory, one could interpret the results in terms of androgen secretion: high levels of androgen secretion might be associated with the risk of relapse, or the frequency/duration of drug taking may facilitate androgen secretion. The lack of a significant difference for the E dimension between the surgery group and the Chinese normative data, the surgery and non-surgery groups, the non-surgery and relapse groups, and the non-relapse and relapse groups indicates that the surgery did not influence the E dimension. This result suggests that NAc lesions have little influence on cortical excitability.

Overall, the results show a reduction in the P and N dimensions for the opioid addicts, which may be attributable to the bilateral NAc lesions in the surgery group; however, the influence of other factors cannot be excluded.

Although the study design limits the conclusions that can be drawn, the phenomena we observed highlight a number of avenues for future research. For instance, future studies could address how the personalities of opiate addicts are affected by opioid dosage changes or prolonged drug abstinence. Questions remain regarding the possibility that a lesion to a specific region of the NAc may improve the ability to form learned conditioned reflexes. Further investigation is necessary to determine if there is a change in the balance between sympathetic and parasympathetic nervous system activity following NAc lesions and whether NAc lesions affect the secretion of androgen. Although the NAc lesion operation used to treat drug addiction was discontinued because of ethical concerns, our investigation highlights a number of important factors associated with the surgery. Subsequent research will focus on long-term observations of the postoperative patients to re-evaluate the operation.

Acknowledgements

This work was supported by a grant from the Project of Reevaluation to Clinical Therapy of Existing Relapse Prevention Therapy under the National "Eleventh Five-year" Technology Supporting Plan (No 2007BA107B03).

Author contribution

Guo-dong GAO and Xin WANG were responsible for the conception and design of the study; Hai-kang ZHAO and Chong-wang CHANG contributed to the data acquisition; Ning GENG was responsible for data analysis, the interpretation of findings and the drafting of the manuscript; other authors participated in collecting data; and all authors critically reviewed the content and approved the final version for publication.

References

1 Wang XL, He SM, Heng LJ, Li WX, Liang QC, Li J, *et al*. Analysis on follow-up results of bilateral nucleus accumbens ablation for ablating drug dependence. Chin J Neurosurg 2005; 21: 579–84.
2 Flynn PM, Joe GW, Broome KM, Simpson DD, Brown BS. Recovery from opioid addiction in DATOS. J Subst Abuse Treat 2003; 25: 177–86.
3 Volkow ND, Fowler JS, Wang GJ. The addicted human brain: insights from imaging studies. J Clin Invest 2003; 111: 1444–51.
4 Nicola SM. The nucleus accumbens as part of a basal ganglia action selection circuit. Psychopharmacology (Berl) 2007; 191: 521–50.
5 Lecca D, Piras G, Driscoll P, Giorgi O, Corda MG. A differential activation of dopamine output in the shell and core of the nucleus accumbens is associated with the motor responses to addictive drugs: a brain dialysis study in Roman high- and low-avoidance rats. Neuropharmacology 2004; 46: 688–99.
6 Cardinal RN, Howes NJ. Effects of lesions of the nucleus accumbens core on choice between small certain rewards and large uncertain rewards in rats. BMC Neurosci 2005; 6: 37.
7 Gao GD, Wang XL, He SM, Li WX, Wang QF, Liang QC, *et al*. Clinical study for alleviating opiate drug psychological dependence by a method of ablating the nucleus accumbens with stereotactic surgery. Stereotact Funct Neurosurg 2003; 81: 96–104.
8 He F, Guan H, Zhao ZJ, Miao XF, Zhou Q, Li LH, *et al*. Evaluation of short-term psychological functions in opiate addicts after ablating the nucleus accumbens via stereotactic surgery. Stereotact Funct Neurosurg 2008; 86: 320–9.
9 Gong YX. Eysenck personality questionnaire (Chinese revision). Changsha. Hunan Map Press; 1984. p45.
10 Wills TA, Windle M, Cleary SD. Temperament and novelty seeking in adolescent substance use: convergence of dimensions of temperament with constructs from Cloninger's theory. J Pers Soc Psychol 1998; 74: 387–406.
11 Sarramon C, Verdoux H, Schmitt L, Bourgeois M. Addiction and personality traits: sensation seeking, anhedonia, impulsivity. Encephale 1999; 25: 569–75.
12 Franques P, Auriacombe M, Tignol J. Addiction and personality. Encephale 2000; 26: 68–78.
13 Kozlov AA, Rokhlina ML. "Addictive" personality. Zh Nevrol Psikhiatr Im S S Korsakova 2000; 100: 23–7.
14 von Gunten A, Pocnet C, Rossier J. The impact of personality characteristics on the clinical expression in neurodegenerative disorders — A review. Brain Res Bull 2009; 80: 179–91.
15 Eysenck HJ. Biological dimensions of personality. In: LA Pervin (Ed), Handbook of personality: Theory and research. New York: Guilford 1990; 244–76.
16 Shen Z, Lin SZ. Physiological psychology. Beijing: Peking University Press 1993: 233.
17 Cardinal RN, Parkinson JA, Hall J, Everitt BJ. Emotion and motivation: the role of the amygdala, ventral striatum, and prefrontal cortex. Neurosci Biobehav Rev 2002; 26: 321–52.
18 Humphries MD, Prescott TJ. The ventral basal ganglia, a selection mechanism at the crossroads of space, strategy, and reward. Prog Neurobiol 2010; 90: 385–417.

Acta Pharmacologica Sinica (2012) 33: 594–605
 1671-4083/12 $32.00
www.nature.com/aps

Original Article

Lowering glucose level elevates $[Ca^{2+}]_i$ in hypothalamic arcuate nucleus NPY neurons through P/Q-type Ca^{2+} channel activation and GSK3β inhibition

Yu CHEN[1], Jun ZHOU[1], Na XIE[1, 2, 3], Chao HUANG[1], Jun-qi ZHANG[1], Zhuang-li HU[1, 2, 3], Lan NI[1], You JIN[1], Fang WANG[1, 2, 3], Jian-guo CHEN[1, 2, 3], Li-hong LONG[1, 2, 3, *]

[1]Department of Pharmacology, Tongji Medical College, Huazhong University of Science and Technology, Wuhan 430030, China; [2]Key Laboratory of Neurological Diseases, Huazhong University of Science and Technology, Ministry of Education of China, Wuhan 430030, China; [3]Institutes of Biomedcine and Drug Discovery, Huazhong University of Science and Technology, Wuhan 430030, China

Aim: To identify the mechanisms underlying the elevation of intracellular Ca^{2+} level ($[Ca^{2+}]_i$) induced by lowering extracellular glucose in rat hypothalamic arcuate nucleus NPY neurons.
Methods: Primary cultures of hypothalamic arcuate nucleus (ARC) neurons were prepared from Sprague-Dawley rats. NPY neurons were identified with immunocytochemical method. $[Ca^{2+}]_i$ was measured using fura-2 AM. Ca^{2+} current was recorded using whole-cell patch clamp recording. AMPK and GSK3β levels were measured using Western blot assay.
Results: Lowering glucose level in the medium (from 10 to 1 mmol/L) induced a transient elevation of $[Ca^{2+}]_i$ in ARC neurons, but not in hippocampal and cortical neurons. The low-glucose induced elevation of $[Ca^{2+}]_i$ in ARC neurons depended on extracellular Ca^{2+}, and was blocked by P/Q-type Ca^{2+} channel blocker ω-agatoxin TK (100 nmol/L), but not by L-type Ca^{2+} channel blocker nifedipine (10 μmol/L) or N-type Ca^{2+} channel blocker ω-conotoxin GVIA (300 nmol/L). Lowering glucose level increased the peak amplitude of high voltage-activated Ca^{2+} current in ARC neurons. The low-glucose induced elevation of $[Ca^{2+}]_i$ in ARC neurons was blocked by the AMPK inhibitor compound C (20 μmol/L), and enhanced by the GSK3β inhibitor LiCl (10 mmol/L). Moreover, lowering glucose level induced the phosphorylation of AMPK and GSK3β, which was inhibited by compound C (20 μmol/L).
Conclusion: Lowering glucose level enhances the activity of P/Q type Ca^{2+} channels and elevates $[Ca^{2+}]_i$ level in hypothalamic arcuate nucleus neurons via inhibition of GSK3β.

Keywords: hypothalamic arcuate nucleus; NPY neurons; glucose; calcium imaging; P/Q type Ca^{2+} channel; GSK3β; AMPK; whole-cell patch clamp

Acta Pharmacologica Sinica (2012) 33: 594–605; doi: 10.1038/aps.2012.17; published online 16 Apr 2012

Introduction

The prevalence of obesity, an important risk factor for the development of type 2 diabetes, is increasing dramatically, and the number of obese individuals worldwide is now projected to reach as many as 1.1 billion by 2030[1, 2]. Currently, however, the behavioral and physiological cues leading to imbalanced food intake and energy expenditure remains poorly defined.

Hypothalamic neuropeptide Y and agouti-related peptide (NPY/AgRP) neurons are critical in food intake and energy homeostasis[3–5], especially in glucose homeostasis[6] and it has been reported that a decrease in extracellular glucose concentration increases the intracellular calcium signals in neurons isolated from arcuate nucleus (ARC) of rat, and 94% of them are immunoreactive for NPY[7]. Thus ARC-NPY neurons are closely related to obesity and diabetes[5, 8]. Glucose sensing in hypothalamic NPY/AgRP neurons needs the activation of AMP-activated protein kinase (AMPK)[9–12]. AMPK is activated when the AMP-to-ATP ratio increases[9, 13]. The knockout of mice AMPKα2 induces the responses to changes in extracellular glucose levels in NPY neurons[13]. The change in action potential can be stimulated by AMPK activator AICAR and blocked by AMPK inhibitor compound C[14–16]. Decreased glucose activates AMPK and elevates $[Ca^{2+}]_i$ in NPY neurons[15]. The similar process is also observed by administration of many metabolic hormones, such as leptin, insulin and

* To whom correspondence should be addressed.
E-mail long_lilly03@yahoo.com.cn
Received 2011-12-05 Accepted 2012-02-08

ghrelin to ARC NPY neurons[17]. Our previous study showed that leptin, which inhibits AMPK in central nervous system[12], can decrease the peak amplitude of high voltage-activated calcium currents in the isolated neurons from ARC[18]. Therefore, the activation of AMPK is crucial in the change in excitability of ARC-NPY neurons. However, the possible role of AMPK activation in the regulation of ion channels in NPY neurons remains to be elucidated.

Calcium ions are probably the most widely used intracellular messengers, and voltage-gated calcium channels (VGCCs) play key role in regulating intracellular calcium concentration during depolarization[19]. Being a state of energy deficit, decrease in extracellular glucose levels induces membrane depolarization and increases the firing rate of action potential in NPY neurons[13]. But the underlying mechanism of glucose decrease induced intracellular elevation is still uncertain[7]. Furthermore, the inhibition of AMPK-mediated GSK3β inhibition has been found both in hepatic and cortical neuronal cells[20–22]. In our previous study, it was found that GSK3β phosphorylated P/Q-type calcium channel in hippocampal neurons[23]. It is possible that AMPK may be involved in the depolarization due to calcium influx through VGCCs. However, little is known about the subtype of VGCC which contributes to the calcium elevation in ARC-NPY neurons.

In the present study, using calcium imaging to determine the source of glucose decrease induced $[Ca^{2+}]_i$ elevation and the signaling pathway, we provide evidence that AMPK activation increases glucose decrease-induced $[Ca^{2+}]_i$ response in ARC-NPY neurons via regulation of P/Q-type calcium channel by GSK3β inhibition.

Materials and methods

Chemicals

DMEM/F12, Neurobasal and B27 supplement were obtained from Gibco Invitrogen Corporation (Carlsbad, CA, USA). Fura-2 AM was obtained from biotium (Hayard, CA). Other general agents were available commercially. All the drugs were prepared as stock solutions. AICAR, compound C and Fura-2 AM were dissolved in dimethylsulfoxide (DMSO). These stock solutions were diluted to the final concentrations with the HEPES-buffered solution before application. The final concentration of DMSO or ethanol did not exceed 0.1%. No detectable effects of the vehicles were found in our experiments.

Preparation of single neurons from ARC

The research was conducted in accordance with the Declaration of Helsinki and with the Guide for Care and Use of Laboratory Animals as adopted and promulgated by the United States National Institutes of Health. All experimental protocols were approved by the Review Committee for the Use of Human or Animal Subjects of Huazhong University of Science and Technology. Primary cultures of ARC neurons were prepared as previously described with some modifications[24]. Briefly, Sprague-Dawley rats, 2–4 d postnatal, were humanely killed by decapitation. After decapitation, brain slices containing the entire ARC were prepared, and entire ARC was excised from the left and right sides. The dissected tissues were removed and transferred to PBS-buffered solution containing (in mmol/L) 135 NaCl, 5 KCl, 1 $CaCl_2$, 1 $MgCl_2$, pH 7.3 and finely chopped. The tissues were then treated with 0.125% trypsin in PBS-balanced salt solution for 20 min at 37 °C and gently triturated using flame-polished Pasteur pipettes. Cell suspension was centrifuged for 7 min at 1000×*g*. Then, the cell pellets were resuspended in the Dulbecco's modified Eagle's medium (DMEM) and F-12 supplement (1:1) with 10% fetal bovine serum before plating onto glass-bottomed dishes (MatTek) coated with poly-L-lysine (20 μg/mL for 1–2 h) and kept at 37 °C in 5% CO_2 incubator. After overnight incubation in DMEM, the medium was changed to neurobasal medium (Gibco) containing 15 mmol/L glucose supplemented with 2% B27, 2 mmol/L glutamine, 10 μg/mL penicillin, and 10 μg/mL streptomycin. The ARC neurons were fed with fresh medium every 48 h. Microscopically, glial cells were not apparent in ARC neurons employing this protocol. The neurons were maintained for 7–10 d in primary culture until used for calcium imaging.

Immunocytochemical identification of single ARC neurons

The immunocytochemical identification of ARC neurons was prepared as previously reported with slight modifications[25]. ARC neurons were fixed with 4% paraformaldehyde in 0.1 mol/L PBS overnight immediately after calcium imaging. They were pretreated with H_2O_2 in methanol for 1 h. Nonspecific binding sites were then blocked with 10% goat serum in 0.1 mol/L PBS for 1 h at room temperature. Cells were incubated overnight at 4 °C with primary antiserum to NPY diluted 1:1000 in PBS containing 1.5% normal goat serum. Cells were subsequently incubated with biotinylated goat anti-rabbit IgG secondary antibody for 1 h at room temperature. The secondary antibody was then rinsed, and the sections were labeled with avidin-peroxidase complex reagent (ABC kit; Vector) for 1 h. The sections were developed with 3,3-diaminobenzidine (DAB). In control sections, the primary antibodies were replaced by the corresponding nonspecific IgG and processed in parallel.

Ca^{2+} measurements

For $[Ca^{2+}]_i$ measurements, cultured ARC, hippocampus and cortical neurons were rinsed three times with HEPES-buffered solution containing (in mmol/L) 140 NaCl, 5 KCl, 1 $MgCl_2$, 2 $CaCl_2$, 10 glucose and 10 HEPES (pH 7.3). Then, cells were incubated with 2 μmol/L Fura-2 AM for 30 min at 37 °C and subsequent washed three times with HEPES to remove the excess extracellular Fura-2 AM. Coverslips of every group were mounted on a recording chamber after they were pretreated with corresponding tool agent (MK801, D-APV, CNQX, Nifedipine, ω-conotoxin GVIA, ω-agatoxin TK, Compound C, LiCl) of each group at final concentration for five minutes. Then, experiments were performed at room temperature. At the beginning of experiments, coverslips were perfused with HEPES-buffered solution with 10 mmol/L

glucose using a peristaltic pump at a rate of 3 mL/min till baseline was stable. After that, low glucose HEPES-buffered solution containing corresponding tool agent (the blocker of AMPA, NMDA, VGSC, and VGCCs) was administrated $[Ca^{2+}]_i$ changes were measured by a Ratio Vision digital fluorescence microscopy system (TILL Photonics GmbH, Germany). Fura-2 AM loaded cells were illuminated at 340 nm for 150 ms and 380 nm for 50 ms at 1 s intervals using a TILL Polychrome monochromator. Fura-2 fluorescence emission was imaged at 510 nm by an intensified cooled charge coupled device (TILL Photonics GmbH). F_{340}/F_{380} fluorescence ratios were generated by TILL VISION 4.0 software. The contours of a single neuron were used to define a region of interest (ROI) from which the mean fluorescence was measured. Paired F_{340}/F_{380} fluorescence ratio images of ROI were acquired every second. The intracellular free calcium concentration was presented as the ratio of the fluorescence signals obtained (340/380 nm). All experiments were repeated three times using different batches of cells.

Western blot analysis

The protocol of Western blot refers to our previous articles. Cultures were treated as described in results; 30 mg of intracellular proteins were loaded in each lane for comparison with β-actin as loading control. Following SDS-PAGE, the proteins were transferred to polyvinylidene difluoride membrane. Immunodetection was performed overnight at 4 °C using rabbit polyclonal antibodies against each protein below: anti-phospho-AMPKα (Thr172; 1:1000; CST, USA), anti-AMPKα (1:1000; CST, USA). Monoclonal antibody (mAb) against total GSK-3β (1:1000 for Western blotting, Abcam, Cambridge, UK), polyclonal antibody (pAb) against phosphorylated GSK-3β at Ser9 (1:1000 for Western blotting, Abcam, Cambridge, UK), anti-β-actin (1:5000; Santa Cruz, CA, USA). Membranes were then incubated with a horseradish peroxidase-conjugated secondary antibody (anti-rabbit 1:10 000; Jackson Immunoresearch) for 1 h at room temperature before signals were visualized using the SuperSignal West Pico ECL kit (Thermo Scientific, Rockford, IL, USA). Quantification was performed using Scion Image software (Fredrick, MD, USA). Results are presented as percentage of control after normalization to β-actin. The effect of experimental manipulations on AMPK phosphorylation was determined using one-way ANOVA.

Whole-cell patch-clamp recording

The procedures for whole-cell patch-clamp recording were according to previous research[26, 27] and as what described in our previous reports with minor modification[18, 28]. The bath solution for recording high-voltage activated calcium current (I_{HVA}) contained (in mmol/L): Choline-Cl 110, $MgCl_2$ 2, $CaCl_2$ 10, TEA-Cl 20, HEPES 10, glucose 10, and the pH was adjusted to 7.4 with Tris base. Glass pipettes were used with a resistance of about 2–4 MΩ when filled with the following solution (in mmol/L): CsF 64, CsCl 64, $CaCl_2$ 0.1, $MgCl_2$ 2, EGTA 10.0, HEPES 10.0, Tris-ATP 5.0, and the pH was adjusted to 7.2 with Tris base. After establishing a whole-cell configuration, the adjustment of capacitance compensation and series resistance compensation were done before recording. The current signals were acquired at a sampling rate of 10 kHz and filtered at 3 kHz. Whole-cell patch-clamp recordings were carried out using an EPC-10 amplifier (HEKA, Lambrecht, Germany) driven by Pulse/PulseFit software (HEKA, Southboro, Germany). Drug actions were measured only after steady-state conditions were reached, which were judged by the amplitudes and time courses of currents remaining constant. All the recordings were made at room temperature (20–22 °C). All experiments were repeated three times using different batches of cells and at least three to four dishes with cells were used for recording in different batches of cells.

Statistical analysis

The amplitude of $[Ca^{2+}]_i$ transient represents the difference between baseline concentration and the transient peak response to the stimulation. This amplitude is expressed in the percentage (%) change of F_{340}/F_{380} and calculated by (R_{peak}–R_{basal}) divided by R_{basal}. Statistical significance between the multiple groups was determined using one-way ANOVA followed by *post hoc* comparisons (SPSS 11.5 software). Data are presented as mean±SEM. Differences at the $P<0.05$ level were considered statistically significant.

Results

Morphological features of ARC-NPY neurons

The cells were fixed for immunocytochemical identification of NPY neurons immediately after the calcium imaging records were finished with the method as described before[18, 29]. The NPY neurons are typically small and medium neurons with triangular or spindle-shaped perikaryons. Most of them have one to three slender, poorly ramified primary dendrites (Figure 1), which are consistent with the observations by van den[25] (2004) and our previous work [18, 29] (2008 and 2010).

Decreased extracellular glucose elevates $[Ca^{2+}]_i$ in ARC-NPY neurons

We first tested the effect of glucose decrease on intracellular Ca^{2+} mobilization in ARC-NPY neurons. Primary cultured rat ARC NPY neurons were loaded with Fura-2 AM and monitored by fluorescence imaging with excitation wavelengths of 340 and 380 nm. We found that a decrease in glucose concentration from 10 mmol/L to 1 mmol/L induced a transient increase in intracellular Ca^{2+} (Figure 2A) in 25% control neurons (37 of 146, Figure 2E). In contrast, this elevation can not be observed in cultured cortical and hippocampal neurons (Figure 2B and Figure 2C). Thus, our following research focused on these positive-reaction ARC-NPY neurons.

The decreased glucose-induced $[Ca^{2+}]_i$ response is extracellular calcium-dependent but not receptor-operated calcium channels (ROCC) dependent

We firstly applied the Ca^{2+}-free external solution to investigate the involvement of extracellular Ca^{2+} in this $[Ca^{2+}]_i$ elevation. Removal of extracellular Ca^{2+} suppressed the $[Ca^{2+}]_i$ to basal

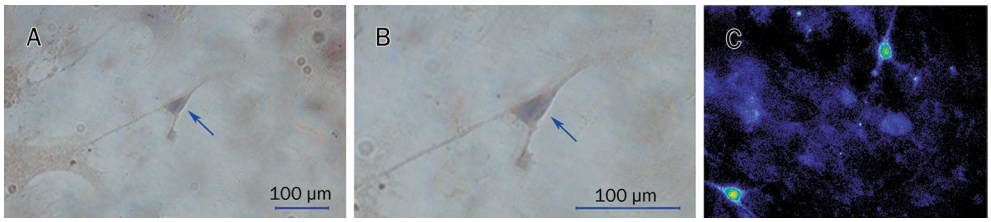

Figure 1. The morphological features of NPY neurons in cultured ARC neurons. A and B are the immunocytochemical identification of morphological features of NPY neurons in cultured ARC neurons. C is morphological features in calcium imaging. The arrows point at a typical NPY neuron. A, C original magnification ×40; B original magnification ×100.

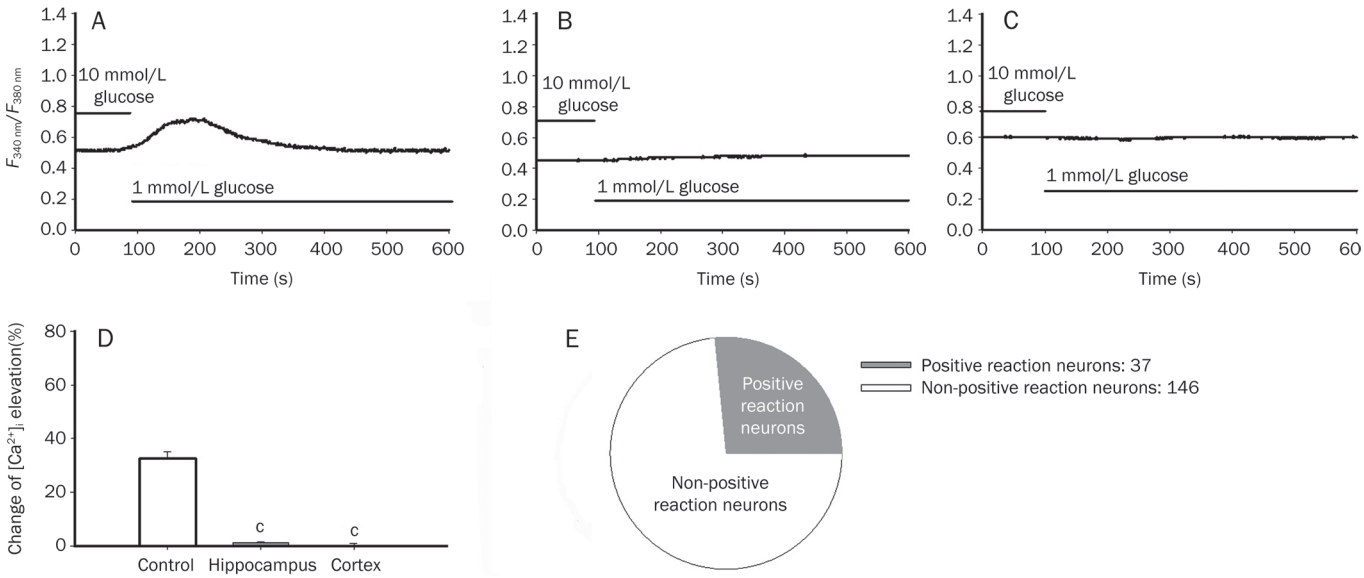

Figure 2. Decreased extracellular glucose-induced $[Ca^{2+}]_i$ elevation is hypothalamic specific effect. (A) An acute decrease in extracellular glucose concentration from 10 to 1 mmol/L induced an elevation of $[Ca^{2+}]_i$ in ARC-NPY neurons. (B) The similar $[Ca^{2+}]_i$ change could not be observed in hippocampal neurons. (C) The similar $[Ca^{2+}]_i$ change could not be observed in cortical neurons. (D) Histogram summarizes the effect of glucose decrease on arcuate nucleus-neuropeptide Y(ARC-NPY) neurons hippocampal neurons and cortical neurons. Mean±SEM. F value is 53,676, $^cP<0.01$ *vs* control. (E) 25.2% (37/146) ARC-NPY neurons responded to the decreased glucose concentration. PRN, positive response neurons.

levels (Figure 3B), indicating an extracellular calcium-dependent mechanism.

To determine whether receptor-operated calcium channels (ROCC) are involved in decreased glucose concentration-induced $[Ca^{2+}]_i$ response, we used NMDA receptor blocker MK801, D-APV and specific AMPA receptor blocker CNQX. After pretreated with one of the three blockers for 5 min, the ARC-NPY neurons were perfused with HEPES-buffered low glucose (1 mmol/L) in the presence of blockers. The basal level of $[Ca^{2+}]_i$ was elevated by 32.8%±3.6% in MK801 (10 μmol/L)-treated group (n=16, Figure 3C), 39.2%±7.6% in D-APV (20 μmol/L)-treated group (n=9, Figure 3D) and 28.7%±1.6% in CNQX (50 μmol/L)-treated group (n=29, Figure 3E), respectively. There are no significant difference between control group and those groups (Figure 3F), suggesting that neither NMDA receptor nor AMPA receptor mediates the reduction of glucose concentration-induced $[Ca^{2+}]_i$ increase in ARC-NPY neurons.

The amplitude of HVA current, not LVA current, is augmented by glucose decrease

Next we want to know whether action potential is involved in glucose decrease induced calcium influx. We firstly used voltage-gated sodium channel blocker tetrodotoxin (TTX) to identify this possibility. We found that glucose decrease induced $[Ca^{2+}]_i$ increase could not be observed when TTX (5 μmol/L) existed (Figure 4A, 4B, and 4C). Thus, this glucose decrease induced $[Ca^{2+}]_i$ increase is probably related to the change of membrane potential. Therefore, we used patch clamp to identify the effect of glucose decrease on VGCC currents.

In the whole-cell patch-clamp recording for I_{HVA}, the cells were stepped from the holding potential of -80 mV to -40 mV (50 ms), and then depolarized to +10 mV (200 ms) after briefly hyperpolarized to -45 mV for 10 ms. I_{HVA} was activated by the second depolarization. The protocol was applied about every 40 s. Extracellular glucose decrease from 10 mmol/L to 1 mmol/L significantly augmented I_{HVA} amplitude in NPY

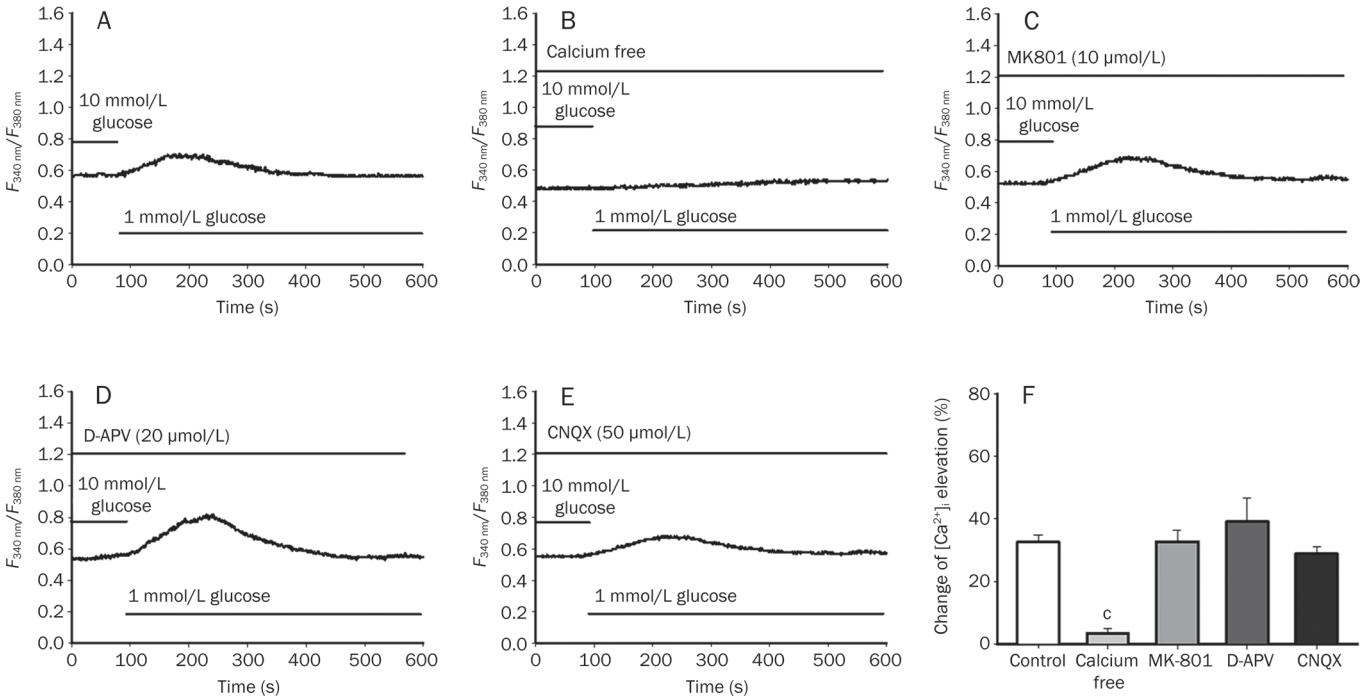

Figure 3. The $[Ca^{2+}]_i$ elevation in ARC-NPY neurons is extracellular calcium-dependent and is not via ROCC. (A) Representative experiment showing glucose decrease induced $[Ca^{2+}]_i$ elevation in ARC-NPY neurons. (B) $[Ca^{2+}]_i$ elevation of ARC-NPY neurons was inhibited in a Ca^{2+}-free external solution. (C) $[Ca^{2+}]_i$ elevation in ARC-NPY neurons could not be blocked by NMDA receptor blocker MK801 (10 μmol/L). (D) $[Ca^{2+}]_i$ elevation in ARC-NPY neurons could not be blocked by NMDA receptor blocker D-APV (20 μmol/L). (E) $[Ca^{2+}]_i$ elevation in ARC-NPY neurons could not be blocked by AMPA receptor blocker CNQX (50 μmol/L). (F) Histogram summarizes the effect of external calcium, MK801, D-APV, and CNQX on the amplitude of glucose decrease-induced $[Ca^{2+}]_i$ elevation in ARC-NPY neuron. Mean±SEM. *F* value is 15.006, $^c P<0.01$ *vs* control.

neurons (Figure 4D, 4E, and 4H). The amplitude was about 1.44±0.20 times (n=15, P<0.05) compared to control groups.

In the whole-cell patch-clamp recording for I_{LVA}, the cell membrane voltage was held at -90 mV, and whole cell currents were recorded in response to step pulses at different test potentials. I_{LVA} were elicited by voltage steps to -20 mV from a holding potential of -90 mV, and the amplitude of the peak current was measured for analysis. Extracellular glucose decrease from 10 mmol/L to 1 mmol/L did not significantly alter I_{LVA} amplitude in NPY neurons (Figure 4F, 4G, and 4H).

Blockade of P/Q-type calcium channel, not T-type, L-type, and N-type calcium channel, inhibits the decreased glucose-induced $[Ca^{2+}]_i$ response in ARC-NPY neurons

To identify which kind of VGCC is involved in the glucose decrease-induced $[Ca^{2+}]_i$ elevation, specific calcium channel blockers were used as described before[27, 30–32]. Mibefradil (5 μmol/L), the blocker of T-type calcium channel, could not block the the glucose decrease-induced $[Ca^{2+}]_i$ elevation. The amplitude of $[Ca^{2+}]_i$ elevation was 39.0%±5.8% (n=8, Figure 5B). Neither L-type calcium channel blocker nifedipine (10 μmol/L) nor N-type calcium channel blocker ω-conotoxin GVIA (300 nmol/L) inhibited the glucose decrease-induced $[Ca^{2+}]_i$ elevation. The basal level was increased by 31.8%±6.3% (n=6) and 26.1%±2.9% (n=17), respectively (Figure 5C and 5D). On the contrast, P/Q-type calcium channel blocker ω-agatoxin TK (100 nmol/L) completely depressed $[Ca^{2+}]_i$ elevation in ARC-NPY neurons (n=8, Figure 5E, P<0.01 *vs* control). There is no significant difference between control group and those groups except ω-agatoxin TK group (Figure 5F). Thus, glucose decrease-induced $[Ca^{2+}]_i$ influx is via P/Q-type calcium channel.

AMPK activation contributes to $[Ca^{2+}]_i$ increase induced by decreased glucose in ARC-NPY neurons

To identify whether AMPK is activated in glucose decrease, the time dependent AMPK activation is tested 1, 2, and 5 min after glucose reduction in NPY neurons. By Western blot analysis, we found that decreasing glucose concentration from 10 to 1 mmol/L remarkably increased AMPKα-subunit phosphorylation in primary ARC neurons to 142%±5.9% (n=3, P<0.05) and 118%±1.2% (n=3, P<0.05 *vs* 10 mmol/L glucose) by 2 min and 5 min glucose decrease; and this increased phosphorylation could be abolished by pretreatment with Compound C (20 μmol/L), the AMPK inhibitor (n=3, P<0.05 *vs* 1 mmol/L glucose). However there was no significant difference between each group by 1 min treatment (Figure 6A, 6B, n=3). It suggests that AMPK is activated 2 min and 5 min after glucose decrease.

Using calcium imaging, we next determined whether AMPK activation mediated the $[Ca^{2+}]_i$ elevation induced by decreased glucose in ARC-NPY neurons. As shown in Figure 6D and

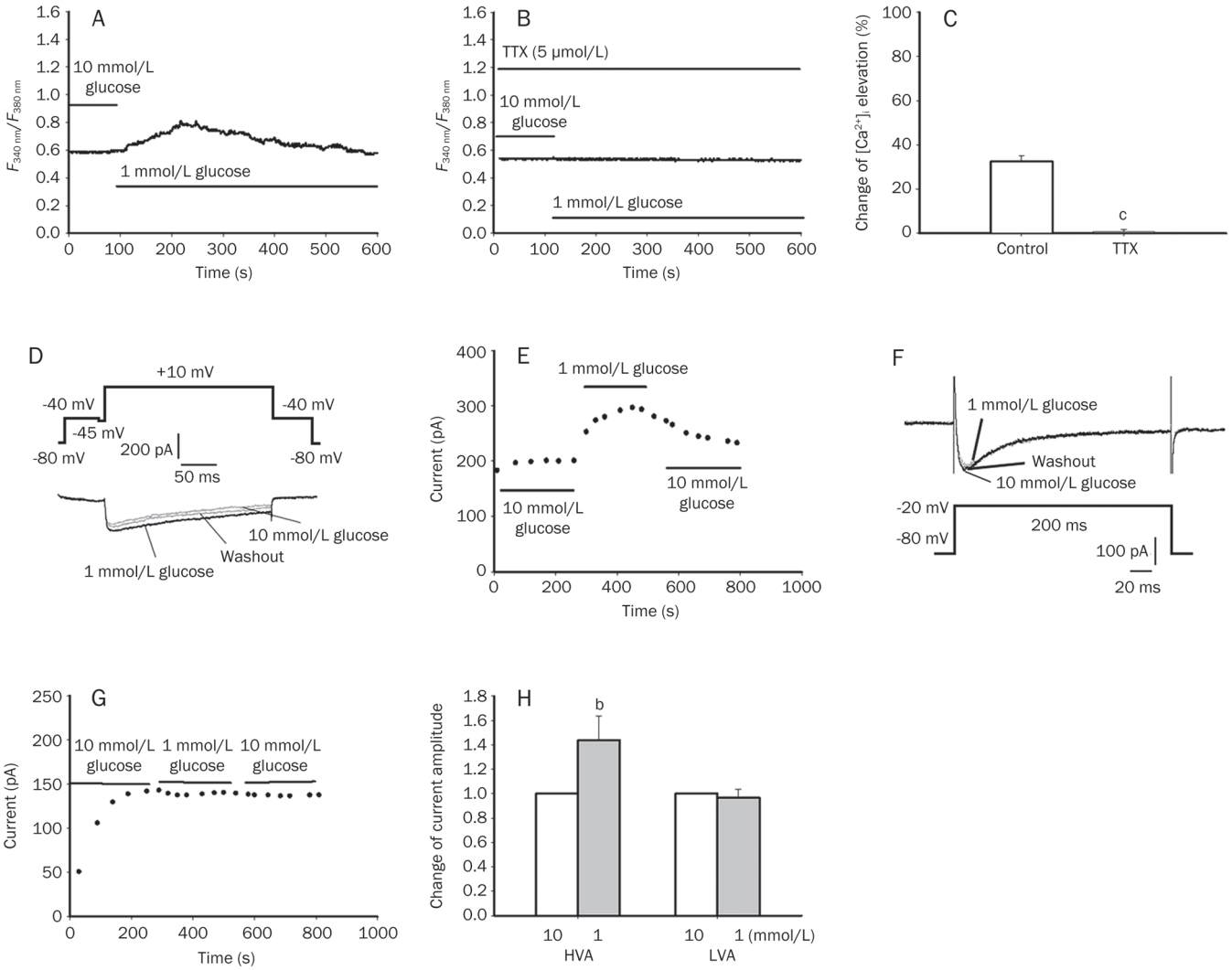

Figure 4. The amplitude of HVA current, not LVA current, is augmented by glucose decrease from 10 mmol/L to 1 mmol/L in ARC-NPY neurons. (A, B) $[Ca^{2+}]_i$ elevation of ARC-NPY neurons was inhibited by TTX (5 μmol/L). (C) Histogram summarizes the effect of TTX on the amplitude of glucose decrease-induced $[Ca^{2+}]_i$ elevation in ARC-NPY neuron. Mean±SEM. $^cP<0.01$ *vs* control. (D) Representative traces of I_{HVA} under control, glucose decrease and washout. I_{HVA} were evoked by the protocol shown on the top. (E) Time-course curve of I_{HVA} before, during and after 1 mmol/L glucose, corresponding to the neuron showed in Figure 4D. (F) Representative traces of I_{LVA} under control, glucose decrease and washout. I_{LVA} were evoked by the protocol shown on the top. (G) Time-course curve of I_{LVA} before, during and after 1 mmol/L glucose, corresponding to the neuron showed in Figure 4F. (H) Histogram summarizes the amplitude change of currents induced by glucose decrease. (Mean±SEM. I_{HVA}, n=15; I_{LVA}, n=10, $^bP<0.05$ *vs* control).

6E compound C (20 μmol/L) largely depressed $[Ca^{2+}]_i$ elevation from 28.7%±1.6%(n=37, Figure 6C) to 16.9%±2.5% (n=14, $P<0.05$ *vs* control). It indicates that AMPK activation is essential in glucose decrease induced $[Ca^{2+}]_i$ increase.

The inhibition effect of AMPK activation on GSK3β mimics the glucose decrease induced $[Ca^{2+}]_i$ elevation in primary cultured ARC-NPY neurons

AMPK activation inhibits the activity of GSK3β in the liver and epithelial cells[20, 33, 34], next we want to reveal whether this inhibition also exists in the hypothalamus. After cultured ARC-NPY neurons were treated with AICAR (200 μmol/L), an AMPK activator for 2 min, the phosphorylation of GSK3β was significantly increased (n=3, $P<0.01$ *vs* control); and this effect could be blocked by compound C (20 μmol/L) (n=3, $P<0.01$ *vs* AICAR group, Figure 7A and 7B). Our previous study has shown that GSK3β can regulate P/Q-type calcium channel via phosphorylation[23]. Therefore, we investigated whether decreased glucose concentration from 10 to 1 mmol/L remarkably increased GSK3β phosphorylation in primary ARC neurons by 1, 2, and 5 min treatment (Figure 7C). Similar to the result of AMPK phosphorylation, p-GSK3β was significantly increased by 77.4%±8.9% and 67.4%±2.5% by 2 min and 5 min after glucose decrease (n=3, $P<0.05$ *vs* 10 mmol/L glucose, Figure 7D). There was no significant difference after 1 min treatment (Figure 7D, n=3). Additionally, inhibition of AMPK by compound C (20 μmol/L) could depress the increased p-GSK3β induced by glucose decrease (n=3, $P<0.05$ *vs* 1

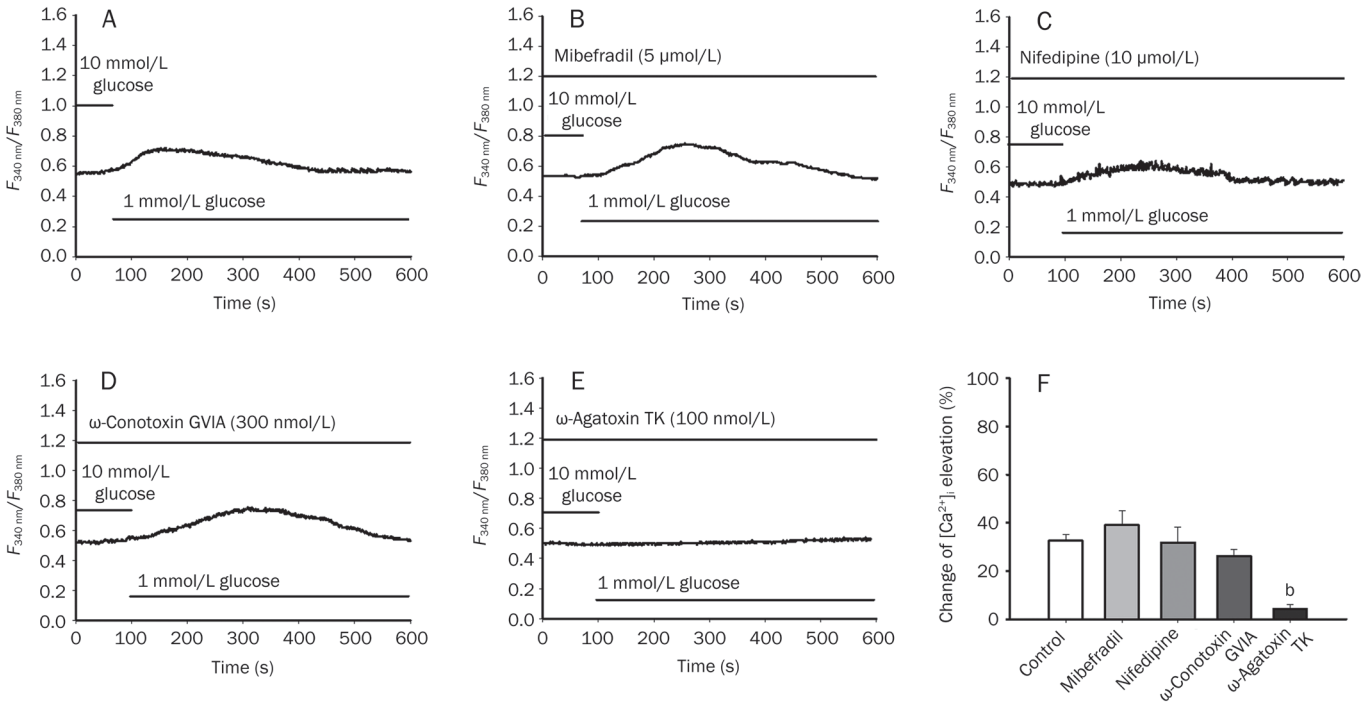

Figure 5. The $[Ca^{2+}]_i$ elevation of ARC-NPY neurons is mediated by P/Q-type calcium channel. (A) Representative trace of control group. (B) $[Ca^{2+}]_i$ elevation of ARC-NPY neurons could not be blocked by selective T-type calcium channel blocker Mibefradil (5 μmol/L). (C) $[Ca^{2+}]_i$ elevation of ARC-NPY neurons could not be blocked by selective L-type calcium channel blocker nifedipine (10 μmol/L). (D) $[Ca^{2+}]_i$ elevation of ARC-NPY neurons could not be blocked by N-type calcium channel blocker ω-conotoxin GVIA (300 nmol/L). (E) Selective P/Q-type calcium channel blocker ω-agatoxin TK (100 nmol/L) completely blocked the $[Ca^{2+}]_i$ elevation of ARC-NPY neurons. (F) Histogram summarizes the effect of VGCC blockers on the amplitude of glucose decrease-induced $[Ca^{2+}]_i$ elevation in ARC-NPY neuron. Mean±SEM. F value is 12.825. $^bP<0.05$ *vs* control.

mmol/L glucose, Figure 7C and 7D). Thus we can find that GSK3β is inhibited 2 min and 5 min after glucose decrease; furthermore AMPK activation is required in the inhibition of GSK3β in this process.

Considering that glucose decrease induced GSK3β inhibition, we therefore investigated whether AMPK activation contributed to GSK3β inhibition in glucose decrease-induced $[Ca^{2+}]_i$ change in ARC-NPY neurons. Lithium chloride can often be used to inhibit GSK 3β activity. In our experiment lithium (10 mmol/L) obviously increased $[Ca^{2+}]_i$ from 28.7%±1.6% (n=37, Figure 7E) to 45.3%±14.6% (n=8, Figure 7F). It suggests that AMPK activation contributes to GSK3β inhibition in glucose decrease-induced $[Ca^{2+}]_i$ change in ARC-NPY neurons (Figure 7G).

Discussion

In this study, it was demonstrated that P/Q-type calcium channel contributed to glucose decrease-induced $[Ca^{2+}]_i$ elevation via an AMPK-dependent manner, and GSK3β inhibition facilitated P/Q-type calcium channel activity. Decreased glucose concentration activated cellular energy sensor AMPK, and, in turn, phosphorylated GSK3β. Thus, phosphorylated GSK3β alleviated its inhibition on P/Q-type calcium channel and induced $[Ca^{2+}]_i$ elevation in ARC-NPY neurons.

Using $[Ca^{2+}]_i$ as a marker of neuronal excitability, our data shows that $[Ca^{2+}]_i$ in hypothalamic NPY neurons increases when extracellular glucose concentration decreases from 10 mmol/L to 1 mmol/L, and up to 25% of all ARC neurons were excited and induced $[Ca^{2+}]_i$ elevation by decreasing concentrations of glucose. In contrast, neither hippocampal nor cortical neurons responded to decreased glucose over the same concentration range and induce the increase of $[Ca^{2+}]_i$, which shows that the effect is specific in glucose sensing neurons in hypothalamus. This is concordant with the previous report that the activity of cortical neurons becomes silent when glucose is reduced from 5 mmol/L to 0 mmol/L[35].

In addition, this $[Ca^{2+}]_i$ elevation can be abolished via a Ca^{2+} free extracellular fluid perfusion. This result suggests an extracellular calcium-dependent mechanism. Thus, concerning depolarization of ARC-NPY induced by glucose decrease[16, 36], we wondered that whether action potential is associated with this $[Ca^{2+}]_i$ elevation. The administration of TTX verified the $[Ca^{2+}]_i$ elevation is related to the change of membrane potential. Therefore, we hypothesized VGCC as a source of glucose decrease-induced $[Ca^{2+}]_i$ elevation in NPY neuron. Using whole cell patch clamp, we found that when extracellular glucose concentration decreases from 10 mmol/L to 1 mmol/L, the amplitude of $I_{HVA,}$ but not I_{LVA}, was significantly augmented in ARC NPY neurons. Some previous studies demonstrate that N-type calcium channel may be involved in the regulation of hormones on rat arcuate nucleus[37, 38]; our present results showed that P/Q-type calcium channel con-

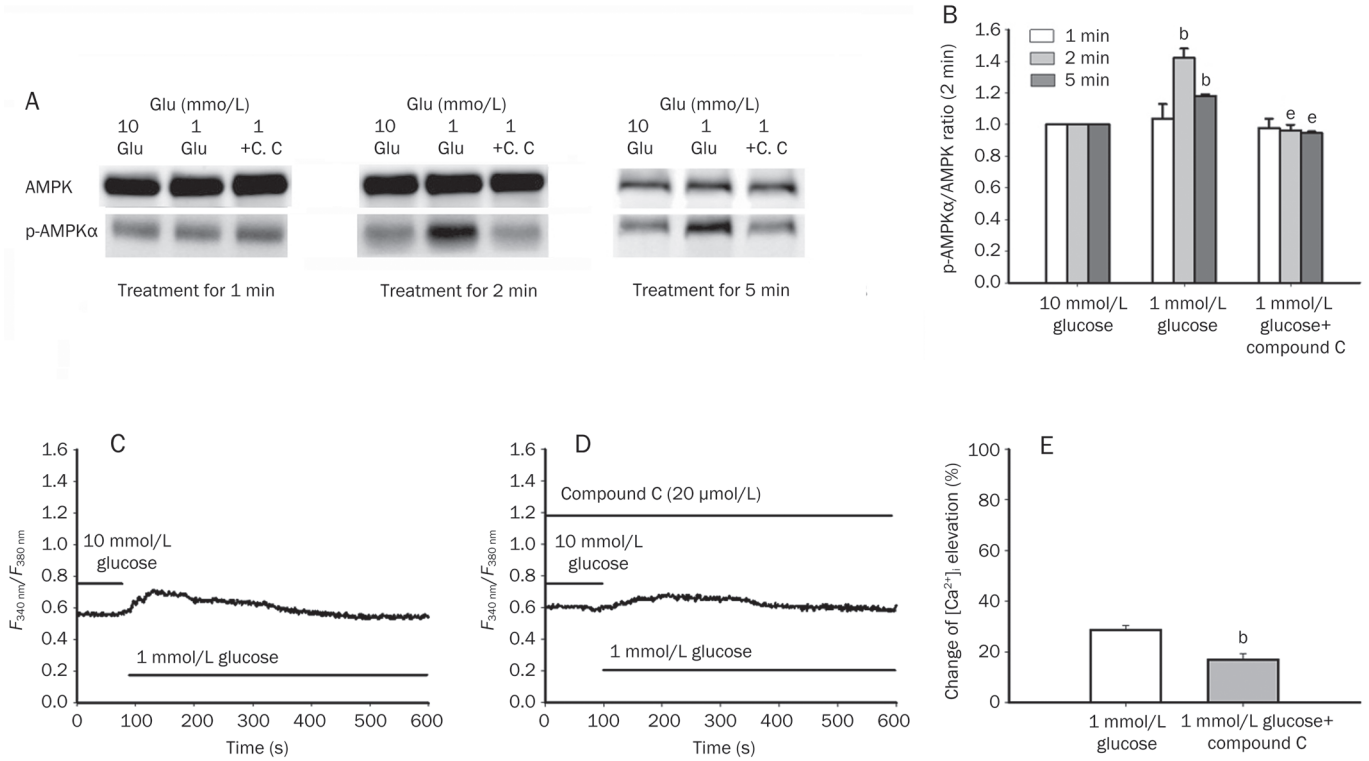

Figure 6. The effect of AMPK activation mediates the elevation of $[Ca^{2+}]_i$ induced by glucose decrease in ARC-NPY neurons. (A) Representative immunoblot of total AMPK, and p-AMPKα in primary cultured ARC-NPY neurons after 1, 2, and 5 min treatment. p-AMPKα increased after 2 min treatment and this effect could be inhibited by compound C (20 μmol/L). This change could not be observed after 1 min treatment. (B) The difference of p-AMPKα between each group was not significant when neurons were treated for 1 min (n=3). There was significant difference between 1 mmol/L glucose group and other group after 2 min treatment, while the difference between control group and compound C group was not significant. Immunoblots of p-AMPKα were measured using image J. The n of each group is 3, F value of 1 min is 2.461; 2 min, 7.005; 5 min, 4.673. ^bP<0.05 *vs* 10 mmol/L glucose. ^eP<0.05 *vs* 1 mmol/L glucose. (C) Representative trace of control group. (D) The response of NPY neuron to glucose decrease was largely depressed by compound C (20 μmol/L). (E) The amplitude of $[Ca^{2+}]_i$ elevation of control (28.7%±8.5%, n=37) is different from compound C (16.9%±9.3%, n=14), ^bP<0.05 *vs* control.

tributed to the response of glucose decrease-induced effect. Subsequently, the $[Ca^{2+}]_i$ elevation will influence the downstream signaling molecules, such as CaMKK2, and finally regulate food intake[39].

It has been reported that AMPK activation can simulate the effect of glucose decrease in NPY neurons[14]. Since extracellular glucose concentrations decrease, the rate of glucose uptake[40] and metabolism[41] will fall. Then, the resultant increase in the AMP to ATP ratio is expected to activate AMPK[42], which will in turn promote ATP synthesis and restore the AMP to ATP ratio. AMPK is activated when cells undergo an energy stress and it has been hypothesized that glycogen synthesis would be shut down by energy consuming processes through activation of AMPK in skeletal muscle[43]. The later study provides evidence for GSK-3β inhibition by AMPK activator, AICAR[44]. In addition, AMPK can inactivate downstream GSK3β through Ser^9 phosphorylation both in direct[20] and indirect[45] ways. p-AMPK is elevated and GSK3β is also inhibited via phosphorylation in ARC-NPY neurons facing glucose decrease. Although previous researches have reported the inhibitory effect of p-AMPK on GSK3β, it is intriguing to observe this hypothalamic regulation of glucose decrease on $[Ca^{2+}]_i$ of ARC-NPY neurons through this signaling pathway, and reveal the potential involvement of the inhibition effect of p-AMPK on GSK3 in food intake and energy homeostasis.

Lithium is used to inhibit GSK-3β activity[46]. And calcium imaging showed that lithium could largely enhance $[Ca^{2+}]_i$ elevation in ARC-NPY neurons, which evidenced a GSK3β-dependent mechanism. As illustrated above, this glucose decrease-dependent $[Ca^{2+}]_i$ elevation is probably related to P/Q-type calcium channels. While in recent report, GSK3β can phosphorylate the intracellular loop-connecting domains of P/Q-type calcium channels, which leads to a decrease of $[Ca^{2+}]_i$ elevation through the P/Q-type voltage-dependent calcium channel[23]. Therefore, it is reasonable to attribute $[Ca^{2+}]_i$ elevation to de-inactivation of P/Q-type calcium channel (Figure 8). Compare to the relatively slow time-course change of Western blot, $[Ca^{2+}]_i$ elevation happened very fast (approximately 20–40 s), according calcium imaging, after lowering the glucose concentration. Although it seems complex, the glucose decrease induced $[Ca^{2+}]_i$ elevation may be the directly initiated by the

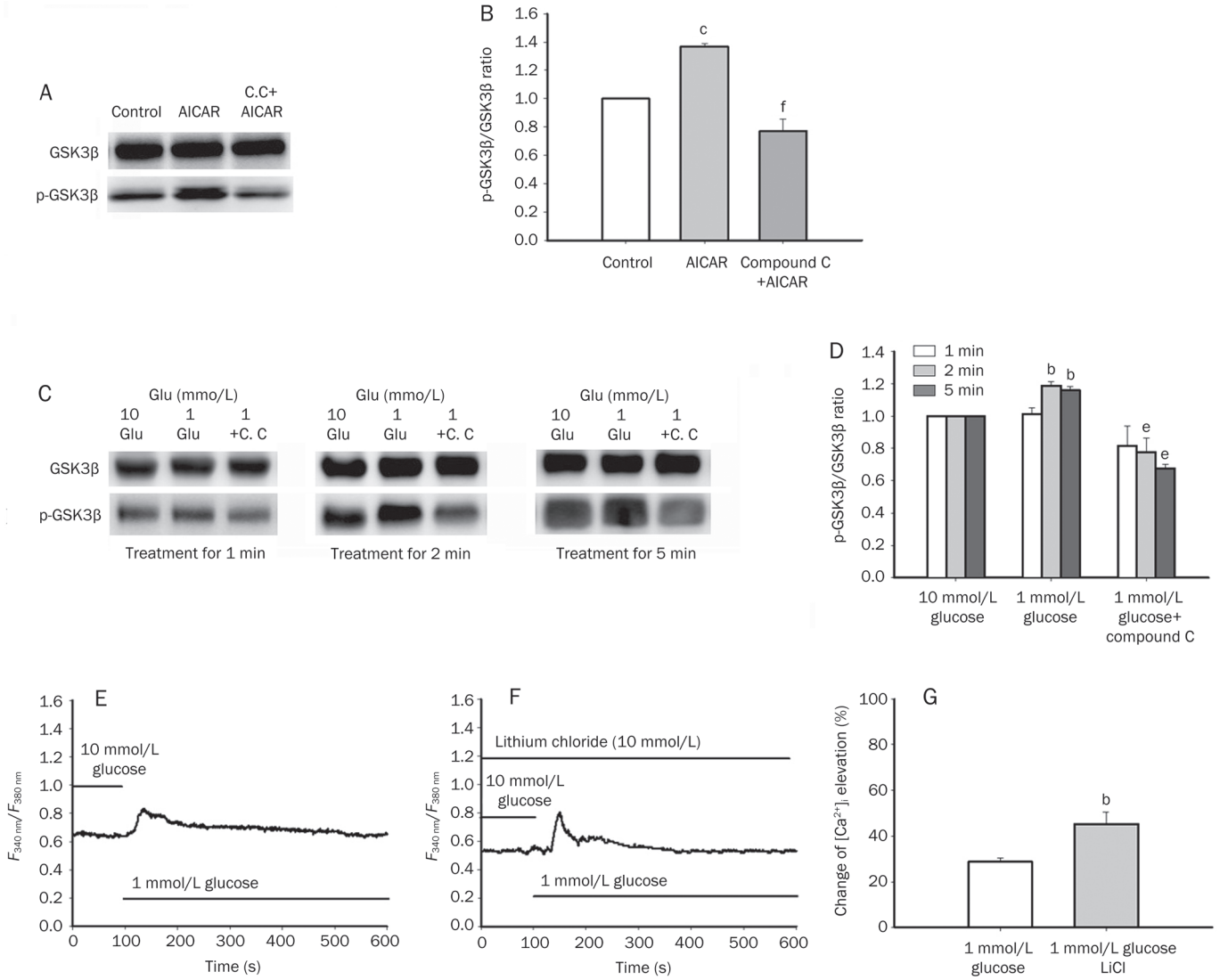

Figure 7. The inhibition effect of AMPK activation on GSK3β mimics the glucose decrease induced $[Ca^{2+}]_i$ elevation in primary cultured ARC-NPY neurons. (A) Representative immunoblot of total GSK3β, p-GSK3β in primary cultured ARC-NPY neurons 2 min after treated with AICAR (200 μmol/L). (B) The statistic of pGSK3β after AMPK activation. The level of p-GSK3β could be promoted by direct activation of AMPK by AICAR; and this effect could be blocked by compound C (20 μmol/L). n=3, F value of 1 min group is 30.27; 2 min, 38.82; 5 min, 33.08. ^{c}P<0.01 *vs* control, ^{f}P<0.01 *vs* AICAR group. (C) Representative immunoblot of total GSK3β, p-GSK3β in primary cultured ARC-NPY neurons by 1, 2, and 5 min treatment separately. The level of p-GSK3β can be inhibited by compound C and can be promoted by glucose decrease after 2 min treatment. (D) The statistic of p-GSK3β at 1, 2, and 5 min time points. There is significant difference between the level of p-GSK3β of control group and other groups after 2 min treatment. Immunoblots of p-GSK3β and GSK3β were measured using image J. ^{b}P<0.05 *vs* 10 mmol/L glucose. ^{e}P<0.05 *vs* 1 mmol/L glucose. (E) Representative trace of control group. (F) The response of NPY neuron to glucose decrease was enhanced by lithium chloride. (G) The amplitude of $[Ca^{2+}]_i$ elevation of control (28.7%±8.5%, n=37) is different from lithium (45.3%±14.6%, n=8). ^{b}P<0.05 *vs* control.

depolarization of neurons and the subsequent AMPK activation can be the potent promoter of P/Q-type calcium channel opening.

The increase of $[Ca^{2+}]_i$ reflects the excitation of neuron. Glucose-inhibited neurons are always excited when glucose concentration decrease to a certain level. In previous report, the *in vivo* glucose concentration to which hypothalamic glucose-inhibited neurons are exposed is still controversial. In early studies about hypothalamic glucose-sensing, the extracellular glucose levels in the brain were measured at different plasma glucose concentrations. The brain glucose level varies from 1 to 2.5 mmol/L when the plasma glucose is altered from 5 to 8 mmol/L in normoglycemia[47]. When plasma glucose level is at 15–17 mmol/L in hyperglycemia, brain concentrations are at 4.5 mmol/L[48]. While all those researches focused on glucose-excited neuron to illustrate a mechanism of glucose-increase excitation. Therefore, in most hypothalamic neuron culture protocol, neurons were cultured in a relatively high glucose surroundings depending on different medium used in experiments[15, 49]. Moreover, it has been argued that the hypo-

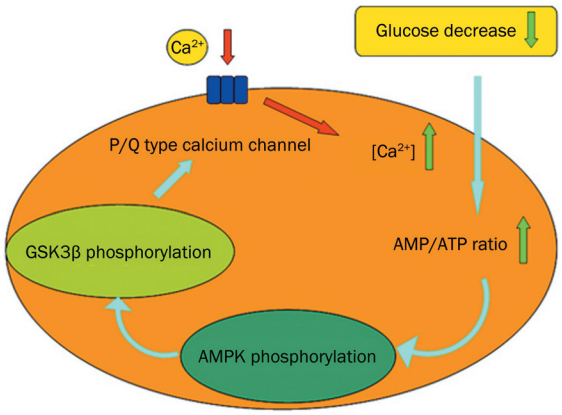

Figure 8. The summary diagrams of current studies and proposed model. Schematic of glucose decrease induced hypothalamic ARC-NPY neurons intracellular calcium elevation. The activation of AMPK inhibited GSK3β, and subsequently alleviated the inhibition of GSK3β on P/Q type calcium channel and lastly increased calcium influx through P/Q type calcium channel.

thalamic blood-brain barrier is deficient to allow hormones pass[50], so that hypothalamus might be exposed to the levels closer to those measured in the plasma. Therefore, to avoid the disturbance of a dramatic change of extracellular fluid on neurons which are to be tested, we used a relatively acceptable glucose level of 10 mmol/L for incubation and the low limit of perfusion fluid is 1.0 mmol/L in the range as reported[48, 51, 52].

To maintain the glucose concentration in a certain scale, the regulation of daily change of glucose concentration is important. Therefore, the regulation of ARC-NPY excitability is crucial, which underlies the mechanism of food intake regulation and energy homeostasis[25, 53]. As a feature of central neurons, electrophysiology activity is an intrinsic character of hypothalamic ARC-NPY neurons. Therefore, their excitation is undoubtedly regulated by ion channel especially calcium channels. And calcium is important for ARC-NPY neurons' activity as a second messenger[37] . Thus, we focused on calcium channels to illustrate their role in hypothalamic metabolism homeostasis. In our results, GSK3β and P/Q-type calcium channel integrate energy sensing signaling to hypothalamic electrophysiology activity. Although this P/Q-type calcium channel-based mechanism contributes to the glucose-decrease dependent $[Ca^{2+}]_i$ increase, we still can't exclude the possibility of calcium-induced calcium release. Accordingly, it will be the next step for us to identify the intracellular mechanism.

Conclusion

In summary, we showed that P/Q-type calcium channel contributes to glucose-decrease induced $[Ca^{2+}]_i$ increase in hypothalamic ARC-NPY neurons. This process is dependent on the activation of AMPK, and its inhibitory effect on GSK3β contributes to the attenuation of the blockade on P/Q-type calcium channels. These results directly link VGCCs to glucose sensing. Our work opens up the possibility of using modulators of ion channels to control energy homeostasis and the conditions of aberrant food intake such as obesity and diabetes.

Acknowledgements

This work was supported by the grants from the National Basic Research Program of China (973 Program) (No 2007CB507404), the Chang Jiang Scholar Program of the Ministry of Education of China, the Key Project of NSFC (No 30930104) to Dr Jian-guo CHEN, and NSFC (No 30801390) to Dr Li-hong LONG. It was also supported by the Program for New Century Excellent Talents in Universities of China (NCET-08-0225) to Dr Fang WANG.

Author contribution

Yu CHEN and Li-hong LONG designed research; Yu CHEN, Jun ZHOU, Chao HUANG, and Jun-qi ZHANG performed research; Lan NI and You JIN contributed new reagents or analytic tools; Yu CHEN, Na XIE, and Zhuang-li HU analyzed data; Yu CHEN and Li-hong LONG wrote the paper; Fang WANG and Jian-guo CHEN critically revised the manuscript.

References

1 Grundy SM, Hansen B, Smith SC Jr, Cleeman JI, Kahn RA. Clinical management of metabolic syndrome: report of the American Heart Association/National Heart, Lung, and Blood Institute/American Diabetes Association conference on scientific issues related to management. Circulation 2004; 109: 551–6.
2 Kelly T, Yang W, Chen CS, Reynolds K, He J. Global burden of obesity in 2005 and projections to 2030. Int J Obes (Lond) 2008; 32: 1431–7.
3 Shimada M, Tritos NA, Lowell BB, Flier JS, Maratos-Flier E. Mice lacking melanin-concentrating hormone are hypophagic and lean. Nature 1998; 396: 670–4.
4 Bewick GA, Gardiner JV, Dhillo WS, Kent AS, White NE, Webster Z, *et al.* Post-embryonic ablation of AgRP neurons in mice leads to a lean, hypophagic phenotype. FASEB J 2005; 19: 1680–2.
5 Patel HR, Qi Y, Hawkins EJ, Hileman SM, Elmquist JK, Imai Y, *et al.* Neuropeptide Y deficiency attenuates responses to fasting and high-fat diet in obesity-prone mice. Diabetes 2006; 55: 3091–8.
6 Belgardt BF, Okamura T, Bruning JC. Hormone and glucose signalling in POMC and AgRP neurons. J Physiol 2009; 587: 5305–14.
7 Muroya S, Yada T, Shioda S, Takigawa M. Glucose-sensitive neurons in the rat arcuate nucleus contain neuropeptide Y. Neurosci Lett 1999; 264: 113–6.
8 Briggs DI, Enriori PJ, Lemus MB, Cowley MA, Andrews ZB. Diet-induced obesity causes ghrelin resistance in arcuate NPY/AgRP neurons. Endocrinology 2010; 151: 4745–55.
9 Kahn BB, Alquier T, Carling D, Hardie DG. AMP-activated protein kinase: ancient energy gauge provides clues to modern understanding of metabolism. Cell Metab 2005; 1: 15–25.
10 Kim MS, Lee KU. Role of hypothalamic 5′-AMP-activated protein kinase in the regulation of food intake and energy homeostasis. J Mol Med 2005; 83: 514–20.
11 Xue B, Kahn BB. AMPK integrates nutrient and hormonal signals to regulate food intake and energy balance through effects in the hypothalamus and peripheral tissues. J Physiol 2006; 574: 73–83.
12 Minokoshi Y, Alquier T, Furukawa N, Kim YB, Lee A, Xue B, *et al.* AMP-kinase regulates food intake by responding to hormonal and nutrient

signals in the hypothalamus. Nature 2004; 428: 569–74.
13 Claret M, Smith MA, Batterham RL, Selman C, Choudhury AI, Fryer LG, *et al.* AMPK is essential for energy homeostasis regulation and glucose sensing by POMC and AgRP neurons. J Clin Invest 2007; 117: 2325–36.
14 Canabal DD, Song Z, Potian JG, Beuve A, McArdle JJ, Routh VH. Glucose, insulin, and leptin signaling pathways modulate nitric oxide synthesis in glucose-inhibited neurons in the ventromedial hypothalamus. Am J Physiol Regul Integr Comp Physiol 2007; 292: R1418–28.
15 Mountjoy PD, Bailey SJ, Rutter GA. Inhibition by glucose or leptin of hypothalamic neurons expressing neuropeptide Y requires changes in AMP–activated protein kinase activity. Diabetologia 2007; 50: 168–77.
16 Murphy BA, Fioramonti X, Jochnowitz N, Fakira K, Gagen K, Contie S, *et al.* Fasting enhances the response of arcuate neuropeptide Y-glucose-inhibited neurons to decreased extracellular glucose. Am J Physiol Cell Physiol 2009; 296: C746–56.
17 Kohno D, Sone H, Minokoshi Y, Yada T. Ghrelin raises $[Ca^{2+}]_i$ via AMPK in hypothalamic arcuate nucleus NPY neurons. Biochem Biophys Res Commun 2008; 366: 388–92.
18 Wang JH, Wang F, Yang MJ, Yu DF, Wu WN, Liu J, *et al.* Leptin regulated calcium channels of neuropeptide Y and proopiomelanocortin neurons by activation of different signal pathways. Neuroscience 2008; 156: 89–98.
19 Catterall WA. Structure and function of voltage-gated ion channels. Annu Rev Biochem 1995; 64: 493–531.
20 Horike N, Sakoda H, Kushiyama A, Ono H, Fujishiro M, Kamata H, *et al.* AMP-activated protein kinase activation increases phosphorylation of glycogen synthase kinase 3beta and thereby reduces cAMP-responsive element transcriptional activity and phosphoenolpyruvate carboxykinase C gene expression in the liver. J Biol Chem 2008; 283: 33902–10.
21 Greco SJ, Sarkar S, Casadesus G, Zhu X, Smith MA, Ashford JW, *et al.* Leptin inhibits glycogen synthase kinase-3beta to prevent tau phosphorylation in neuronal cells. Neurosci Lett 2009; 455: 191–4.
22 Shin SM, Cho IJ, Kim SG. Resveratrol protects mitochondria against oxidative stress through AMP-activated protein kinase-mediated glycogen synthase kinase-3beta inhibition downstream of poly(ADP-ribose)polymerase-LKB1 pathway. Mol Pharmacol 2009; 76: 884–95.
23 Zhu LQ, Liu D, Hu J, Cheng J, Wang SH, Wang Q, *et al.* GSK-3 beta inhibits presynaptic vesicle exocytosis by phosphorylating P/Q-type calcium channel and interrupting SNARE complex formation. J Neurosci 2010; 30: 3624–33.
24 Muroya S, Funahashi H, Yamanaka A, Kohno D, Uramura K, Nambu T, *et al.* Orexins (hypocretins) directly interact with neuropeptide Y, POMC and glucose-responsive neurons to regulate Ca^{2+} signaling in a reciprocal manner to leptin: orexigenic neuronal pathways in the mediobasal hypothalamus. Eur J Neurosci 2004; 19: 1524–34.
25 van den Top M, Lee K, Whyment AD, Blanks AM, Spanswick D. Orexigen-sensitive NPY/AgRP pacemaker neurons in the hypothalamic arcuate nucleus. Nat Neurosci 2004; 7: 493–4.
26 Kawabata A, Ishiki T, Nagasawa K, Yoshida S, Maeda Y, Takahashi T, *et al.* Hydrogen sulfide as a novel nociceptive messenger. Pain 2007; 132: 74–81.
27 Okubo K, Takahashi T, Sekiguchi F, Kanaoka D, Matsunami M, Ohkubo T, *et al.* Inhibition of T-type calcium channels and hydrogen sulfide–forming enzyme reverses paclitaxel-evoked neuropathic hyperalgesia in rats. Neuroscience 2011; 188: 148–56.
28 Chen J, Daggett H, De Waard M, Heinemann SH, Hoshi T. Nitric oxide augments voltage-gated P/Q-type $Ca^{(2+)}$ channels constituting a putative positive feedback loop. Free Radic Biol Med 2002; 32: 638–49.
29 Yang MJ, Wang F, Wang JH, Wu WN, Hu ZL, Cheng J, *et al.* PI3K integrates the effects of insulin and leptin on large-conductance Ca^{2+}-activated K^+ channels in neuropeptide Y neurons of the hypothalamic arcuate nucleus. Am J Physiol Endocrinol Metab 2010; 298: E193–201.
30 Adams DJ, Trequattrini C. Opioid receptor-mediated inhibition of omega-conotoxin GVIA-sensitive calcium channel currents in rat intracardiac neurons. J Neurophysiol 1998; 79: 753–62.
31 Lenz RA, Wagner JJ, Alger BE. N- and L-type calcium channel involvement in depolarization-induced suppression of inhibition in rat hippocampal CA1 cells. J Physiol 1998; 512: 61–73.
32 Shankar S, Teyler TJ, Robbins N. Aging differentially alters forms of long-term potentiation in rat hippocampal area CA1. J Neurophysiol 1998; 79: 334–41.
33 Choi SH, Kim YW, Kim SG. AMPK-mediated GSK3beta inhibition by isoliquiritigenin contributes to protecting mitochondria against iron–catalyzed oxidative stress. Biochem Pharmacol 2010; 79: 1352–62.
34 Zhang L, Jouret F, Rinehart J, Sfakianos J, Mellman I, Lifton RP, *et al.* AMP-activated protein kinase (AMPK) activation and glycogen synthase kinase-3beta (GSK-3beta) inhibition induce Ca^{2+}-independent deposition of tight junction components at the plasma membrane. J Biol Chem 2011; 286: 16879–90.
35 Mobbs CV, Kow LM, Yang XJ. Brain glucose-sensing mechanisms: ubiquitous silencing by aglycemia vs. hypothalamic neuroendocrine responses. Am J Physiol Endocrinol Metab 2001; 281: E649–54.
36 Song Z, Levin BE, McArdle JJ, Bakhos N, Routh VH. Convergence of pre- and postsynaptic influences on glucosensing neurons in the ventromedial hypothalamic nucleus. Diabetes 2001; 50: 2673–81.
37 Kohno D, Gao HZ, Muroya S, Kikuyama S, Yada T. Ghrelin directly interacts with neuropeptide-Y-containing neurons in the rat arcuate nucleus: Ca^{2+} signaling via protein kinase A and N-type channel-dependent mechanisms and cross-talk with leptin and orexin. Diabetes 2003; 52: 948–56.
38 Sahu A, Crowley WR, Kalra SP, Kalra PS. Role of multiple voltage-sensitive calcium channels in depolarization-induced release of neuropeptide y and luteinizing hormone-releasing hormone from rat median eminence-arcuate nucleus. Mol Cell Neurosci 1993; 4: 492–8.
39 Anderson KA, Ribar TJ, Lin F, Noeldner PK, Green MF, Muehlbauer MJ, *et al.* Hypothalamic CaMKK2 contributes to the regulation of energy balance. Cell Metab 2008; 7: 377–88.
40 Kang L, Routh VH, Kuzhikandathil EV, Gaspers LD, Levin BE. Physiological and molecular characteristics of rat hypothalamic ventromedial nucleus glucosensing neurons. Diabetes 2004; 53: 549–59.
41 Dunn-Meynell AA, Routh VH, Kang L, Gaspers L, Levin BE. Glucokinase is the likely mediator of glucosensing in both glucose–excited and glucose-inhibited central neurons. Diabetes 2002; 51: 2056–65.
42 Hardie DG, Carling D, Carlson M. The AMP-activated/SNF1 protein kinase subfamily: metabolic sensors of the eukaryotic cell. Annu Rev Biochem 1998; 67: 821–55.
43 Wojtaszewski JF, Nielsen JN, Jorgensen SB, Frosig C, Birk JB, Richter EA. Transgenic models — a scientific tool to understand exercise-induced metabolism: the regulatory role of AMPK (5′-AMP-activated protein kinase) in glucose transport and glycogen synthase activity in skeletal muscle. Biochem Soc Trans 2003; 31: 1290–4.
44 Fediuc S, Gaidhu MP, Ceddia RB. Inhibition of insulin-stimulated glycogen synthesis by 5-aminoimidasole-4-carboxamide-1-beta-d-ribofuranoside-induced adenosine 5′-monophosphate-activated

protein kinase activation: interactions with Akt, glycogen synthase kinase 3-3alpha/beta, and glycogen synthase in isolated rat soleus muscle. Endocrinology 2006; 147: 5170–7.

45 King TD, Song L, Jope RS. AMP-activated protein kinase (AMPK) activating agents cause dephosphorylation of Akt and glycogen synthase kinase-3. Biochem Pharmacol 2006; 71: 1637–47.

46 Klein PS, Melton DA. A molecular mechanism for the effect of lithium on development. Proc Natl Acad Sci U S A 1996; 93: 8455–9.

47 Silver IA, Erecinska M. Glucose-induced intracellular ion changes in sugar–sensitive hypothalamic neurons. J Neurophysiol 1998; 79: 1733–45.

48 Silver IA, Erecinska M. Extracellular glucose concentration in mammalian brain: continuous monitoring of changes during increased neuronal activity and upon limitation in oxygen supply in normo-, hypo-, and hyperglycemic animals. J Neurosci 1994; 14: 5068–76.

49 O'Malley D, Reimann F, Simpson AK, Gribble FM. Sodium-coupled glucose cotransporters contribute to hypothalamic glucose sensing. Diabetes 2006; 55: 3381–6.

50 Ganong WF. Circumventricular organs: definition and role in the regulation of endocrine and autonomic function. Clin Exp Pharmacol Physiol 2000; 27: 422–7.

51 Murphy BA, Fakira KA, Song Z, Beuve A, Routh VH. AMP-activated protein kinase and nitric oxide regulate the glucose sensitivity of ventromedial hypothalamic glucose-inhibited neurons. Am J Physiol Cell Physiol 2009; 297: C750–8.

52 de Vries MG, Arseneau LM, Lawson ME, Beverly JL. Extracellular glucose in rat ventromedial hypothalamus during acute and recurrent hypoglycemia. Diabetes 2003; 52: 2767–73.

53 Wang R, Liu X, Hentges ST, Dunn-Meynell AA, Levin BE, Wang W*, et al.* The regulation of glucose-excited neurons in the hypothalamic arcuate nucleus by glucose and feeding-relevant peptides. Diabetes 2004; 53: 1959–65.

Acta Pharmacologica Sinica (2012) 33: 606–614
 1671-4083/12 $32.00
www.nature.com/aps

Original Article

Breviscapine inhibits high glucose-induced proliferation and migration of cultured vascular smooth muscle cells of rats via suppressing the ERK1/2 MAPK signaling pathway

Meng HE, Zhi-min XUE, Juan LI, Bin-quan ZHOU*

The Department of Cardiology, Biomedical Research (Therapy) Center, Sir Run Run Shaw Hospital, College of Medicine, Zhejiang University, Hangzhou 310016, China

Aim: To investigate the influences of breviscapine, a flavonoid extracted from Erigeron breviscapus, on the proliferation and migration of vascular smooth muscle cells (VSMCs) cultured in a high glucose medium and the underlying mechanisms.
Methods: VSMCs were isolated from thoracic aortas of male Sprague-Dawley rats and cultured *in vitro*. Cell proliferation was evaluated using Counting Kit-8 cell viability assay. Cell migration was evaluated using transwell migration assay and *in vitro* scratch assay. The expression and activity of protein kinase C-β2 (PKC-β2), extracellular signal-regulated kinase 1/2 (ERK1/2), p38 mitogen-activated protein kinase (p38), and JNK mitogen-activated protein kinase (JNK) were measured with Western blotting.
Results: Exposure of VSMCs to a high glucose (25 mmol/L) medium significantly increased the proliferation and migration potential as compared to the control group. Pretreatment with breviscapine (65 μmol/L and 108 μmol/L) attenuated high glucose-enhanced proliferation and migration of VSMCs. Exposure of VSMCs to the high glucose medium activated both the PKC-β2 and ERK1/2 MAPK, but not the p38 and JNK MAPK. Pretreatment with breviscapine (65 μmol/L and 108 μmol/L) blocked high glucose-induced increase of the ERK1/2 activity, but not that of the PKC-β2 activity.
Conclusion: Our study demonstrated that breviscapine ameliorates high glucose-induced proliferation and migration of VSMCs via inhibiting ERK1/2 MAPK signaling.

Keywords: breviscapine; vascular smooth muscle cells; cell proliferation; cell migration; protein kinase C; MAP kinase

Acta Pharmacologica Sinica (2012) 33: 606–614; doi: 10.1038/aps.2012.6; published online 2 Apr 2012

Introduction

The global prevalence of diabetes mellitus has increased dramatically in recent years and is projected to affect 4.4% of the world's population by 2030[1]. Cardiovascular complications, such as atherosclerosis, are the primary cause of mortality and morbidity among patients with type 2 diabetes[2]. In diabetics, atherosclerosis presents earlier and progresses more rapidly than in the equivalent healthy population[3].

The development of atherosclerosis involves a series of complex pathophysiological steps, including the migration of hyperplastic vascular smooth muscle cells (VSMCs) into the intima and the transformation of these VSMCs from a non-motile, contractile phenotype into a proliferative, secretory phenotype. Many cytokines, such as platelet-derived growth factor (PDGF), transforming growth factor-β (TGF-β), interferon γ (IFN γ) and monocyte chemotactic protein 1 (MCP-1), are secreted, which contributes to furthering the process of atherosclerosis[4–6].

Hyperglycemia has been suspected of accelerating atherosclerosis in type 2 diabetes[7, 8]. The effect of high glucose levels on the risk of cardiovascular events starts at glucose concentrations below the non-diabetic glucose range (<6.1 mmol/L), and glucose continues to exert its effects within the diabetic glucose range (>11.1 mmol/L) in an exponential fashion[2].

High glucose levels regulate structural and functional changes in the vessels involved in diabetic atherosclerosis by activating several signal transduction pathways. Previous studies have demonstrated that VSMCs that are cultured under hyperglycemic conditions displayed enhanced proliferative and migratory responses compared to cells that are

* To whom correspondence should be addressed.
E-mail benzhou@hotmail.com
Received 2011-11-08 Accepted 2012-01-13

cultured under euglycemic conditions, and it has been suggested that protein kinase C (PKC) signal transduction may play an important role in this effect[7, 9, 10]. Other studies have shown that activation of the mitogen-activated protein kinase (MAPK) pathway may contribute to the increased proliferation and migration of VSMCs in response to hyperglycemia[10, 11].

Breviscapine ($C_{21}H_{18}O_{12}$) is a flavonoid that is extracted from *Erigeron breviscapus*, the essential active ingredient of which is flavone. Its pharmacological actions, which include dilating micro-blood vessels, reducing blood viscosity and improving microcirculation, have been demonstrated in a large number of experimental studies and clinical observations. Breviscapine has been demonstrated to inhibit PKC and provide a protective effect against diabetic nephropathy in recent years[12–14]. Furthermore, it has been shown that the inhibitory effect of breviscapine on cardiac hypertrophy was mediated by disrupting PKC-α-dependent ERK1/2 and PI3K/AKT signaling[15]. Our previous studies have also indicated that breviscapine ameliorated the cardiac hypertrophy that was induced by high glucose in diabetic rats through inhibiting the PKC signaling pathway[16, 17]. Other studies have demonstrated that breviscapine inhibited the proliferation and collagen production by cardiac fibroblasts that were induced by angiotensin II through the suppression of the p38 and ERK1/2 MAPK signaling pathways[18]. In addition, breviscapine has been shown to potentially have a protective effect against atherosclerosis in rats[19]. Despite a preponderance of data, little is known about the underlying mechanisms of breviscapine. In this study, we investigated the influence of breviscapine on the high glucose-induced proliferation and migration of VSMCs and the underlying molecular mechanisms of breviscapine.

Materials and methods

Experimental animals

All of the procedures were approved by the Ethics Committee for the Use of Experimental Animals at Zhejiang University. All of the experiments followed the institution's instructions for animal care and usage. Male Sprague-Dawley rats [5–8 weeks old; body weight, 160.62±10.26 g; total range, 147–183 g; Grade II; certificate number: SYXK (Zhe) 2010–0149] provided by the experimental animal center at Zhejiang University were used to obtain cells for cell culture *in vitro*.

Drugs and chemicals

Breviscapine ($C_{21}H_{18}O_{12}$, purity>98%) was purchased from Shanghai RongHe Bioengineering Company (Shanghai, China). The PKC inhibitor Ro-31-8220, the MEK1/2 inhibitor PD 98059 and FITC-conjugated monoclonal anti-α-smooth muscle actin antibody were obtained from Sigma Chemical Company (St Louis, MO, USA). Trypsin, fetal calf serum and Dulbecco's modified Eagle's medium (DMEM) were purchased from Gibco Chemical Company (Grand Island, NY, USA). A Bio-Rad DC protein assay kit II (Bio-Rad, Hercules, USA) was used to quantitate proteins. Primary antibodies, including rabbit anti-p-PKC-β2, rabbit anti-p-ERK1/2, rabbit anti-p-p38, rabbit anti-p38, rabbit anti-p-JNK, and rabbit anti-JNK antibodies, and goat anti-rabbit secondary antibody, were obtained from Cell Signaling Technology (Beverly, MA, USA). Other primary antibodies, such as rabbit anti-PKC-β2 and rabbit anti-ERK antibodies, were obtained from Santa Cruz Biotechnology (CA, USA). A Cell Counting Kit-8 was purchased from Dojindo Molecular Technologies (Rockville, MD, USA). Cell migration was evaluated using a 24-well transwell plate that contained polycarbonate 8-μm pore membrane filters (Millipore, Bedford, MA, USA).

Cell culture

Rat vascular smooth muscle cells were isolated from the thoracic aorta and cultured *in vitro* as previously described[20]. Briefly, male Sprague-Dawley rats (5–8 weeks old) were injected with muscle relaxant and anesthetic before being sacrificed, and then their thoracic aortas were isolated. The connective outer layer of tissue was removed, and the outer membrane was stripped using microforceps. The endomembrane was removed by scraping the inner surface of the vessel gently with forceps. Next, the tunica media was cut into 1 mm^3 chips and spread evenly in a 25 cm^2 culture bottle. The resultant vascular smooth muscle cells were cultured in DMEM that was supplemented with 10% fetal bovine serum (FBS) at 37 °C with 5% CO_2. Differential attachment purification was used to obtain a purer population of VSMCs. Only VSMCs from passages 4–6 were used for the experiments. Immunofluorescent staining with monoclonal anti-α-smooth muscle actin antibody was used for the identification and characterization of VSMCs.

Division of cultured VSMCs

After an initial 24 h of culture in serum-free medium, the VSMCs were divided into groups as follows: (1) normal glucose group (NG group; 5 mmol/L, corresponding to a blood glucose level of 91 mg/dL); (2) high glucose group (HG group; 25 mmol/L, corresponding to a blood glucose level of 455 mg/dL); (3) high glucose plus breviscapine group (HG+breviscapine group; breviscapine: 65 and 108 μmol/L); (4) high glucose plus the PKC inhibitor Ro-31-8220 group (HG+RO group; Ro-31-8220: 3 μmol/L); and (5) high glucose plus the MEK1/2 (MEK1/2 is the activator that is upstream of ERK1/2) inhibitor PD 98059 group (HG+PD group; PD 98059: 25 μmol/L). The VSMCs were pretreated with the indicated drugs for 1 h before high glucose treatment.

Cell viability assay

After the initial 24 h of serum-free culture, cells were seeded at 4000 cells per well in 96-well culture plates. After being treated with a high concentration of glucose or a high concentration of glucose supplemented with the indicated drugs for 48 h, the reagent was added to VSMCs, and the cells were incubated for 3.5 h at 37 °C according to the manufacturer's instructions. The absorbance was measured at a wavelength of 450 nm.

Transwell migration assay

Cell migration was determined using a 24-well transwell plate

that contained polycarbonate 8-μm pore membrane filters. VSMCs that were harvested using 0.25% trypsin were seeded in the upper wells (1×10^5 cells in 200 μL of serum-free DMEM containing 1% FBS), whereas the lower wells were filled with DMEM containing 10% FBS. High glucose medium and the experimental drugs were added to the upper wells. The cells were allowed to migrate across the porous filters for 12 h at 37 °C. After staining them with DAPI (1.4 μmol/L) and scraping the upper surface of the filter, the number of cells that had migrated to the lower side of the filter was determined using wide-field fluorescent microscopy (Zeiss).

In vitro scratch assay

VSMCs were grown to confluence on 6-well plates. The confluent monolayers were scratched with 200-μL pipette tips. The cells were rinsed twice, and the denuded surface was measured. Next, VSMCs were incubated with serum-free DMEM containing different experimental drugs and high glucose for 24 h. After incubation, the area of the cells that had migrated across the denuded area was determined. To ensure that the same zone was measured throughout the experiments, black spots were drawn to serve as benchmarks. The result was expressed as the percentage of recolonization in the denuded zone.

Western blot analysis

VSMCs in 6-well plates were washed with PBS three times and incubated on ice in lysis buffer [50 mmol/L Tris-HCl (pH 7.5), 150 mmol/L NaCl, 1% Nonidet P-40, 0.5% sodium deoxycholate, 0.1% SDS, and 1 mmol/L EDTA] that was supplemented with a protease inhibitor cocktail containing 1 mmol/L PMSF, 1 mmol/L Na_3VO_4 and 10 mmol/L NaF for 20 min. The lysates were scraped from the 6-well plate, and the proteins were collected. Proteins were quantified with a Bio-Rad DC protein assay kit II. Next, samples containing equal amounts of total protein were separated on 10% SDS-polyacrylamide gels and transferred to PVDF membranes. The membranes were blocked with 5% nonfat milk in Tris-buffered solution (TBS) for 1 h at room temperature and then incubated with primary antibodies (1:1000 dilution) overnight at 4 °C. After being washed three times with TBST (TBS containing 0.1% Tween 20) for 15 min each, the membranes were incubated with horseradish peroxidase-conjugated secondary antibodies (1:10 000 dilution) for 1 h, followed by three washes with TBST for 15 min each. Finally, the membranes were incubated with enhanced chemiluminescence (ECL) reagent (Amersham, Haemek, Israel), and following the reaction, the images were captured on the image reader LAS-4000 system (Fujifilm, Tokyo, Japan). The band densities were determined using Multi-Gauge imaging software (Fujifilm, Tokyo, Japan).

Statistical analysis

All of the experiments were performed a minimum of three times, and all of the data are presented as the mean±SEM. The statistical analysis was performed by one-way analysis of variance for multiple comparisons with SPSS, version 16.0 (SPSS Inc, Chicago, IL, USA). A value of $P<0.05$ was considered statistically significant.

Results

Identification and characterization of VSMCs

Rat vascular smooth muscle cells were isolated from the thoracic aorta and cultured *in vitro*. As shown in Figure 1A, few cells had grown on the bottom of the culture flask after 5–7 days, but by 10–12 d after plating, the vascular smooth muscle cells had developed into peaked clusters. The purity of the VSMCs was determined by immunofluorescent staining with monoclonal anti-SM-α-actin antibody. The purity of the cultured VSMCs was greater than 98% after 3 passages, as shown in Figure 1B.

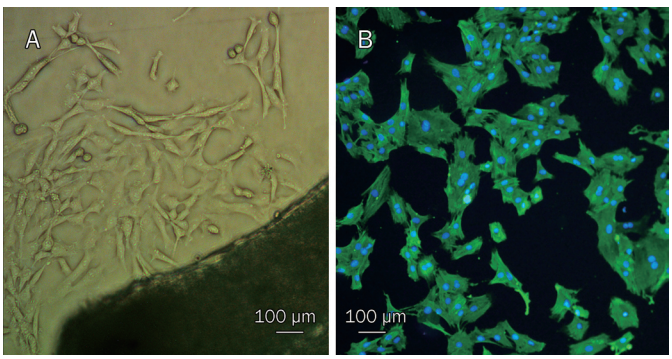

Figure 1. VSMCs were cultured *in vitro* and identified by immunofluorescence staining with FITC monoclonal anti-α-smooth muscle actin antibody (×100). (A) Primary cells and the organization blocks; (B) VSMCs combined with FITC monoclonal anti-α-smooth muscle actin antibody gave off green lights. Other cells could not give off green lights. The nuclei of all the cells stained with DAPI displayed blue color.

Breviscapine inhibited high glucose-induced proliferation of VSMCs

To examine the role of breviscapine in the high glucose-induced proliferation of VSMCs, we first investigated the effect of hyperglycemia on VSMC proliferation. The results showed that VSMCs cultured under hyperglycemic conditions (25 mmol/L) displayed an enhanced proliferative capability compared to VSMCs cultured under normal glucose levels (5 mmol/L) over a 48-h period. This effect was not simply the result of a change in osmolarity, as incubation with 25 mmol/L mannitol had no effect on VSMC proliferation.

Breviscapine was dissolved in dimethyl sulfoxide (DMSO) medium for the *in vitro* studies, and the VSMCs were pretreated with breviscapine (65 or 108 μmol/L) for 1 h and subsequently treated with high glucose for 48 h. We noticed that the high glucose-enhanced proliferation of VSMCs was inhibited by breviscapine, while the solvent alone (DMSO) showed no effect. The inhibitory effect was more obvious using the higher concentration of breviscapine (108 μmol/L). The results are shown in Table 1.

Table 1. Breviscapine inhibited high-glucose-induced proliferation of VSMCs. Cell Counting Kit-8 was used to evaluate cell proliferation and absorbance values were used to compare differences between groups. The results were represented as means±SEM of three independent experiments. [a]*P*>0.05, [c]*P*<0.01 *vs* normal glucose (5 mmol/L) group. [d]*P*>0.05 *vs* high glucose (25 mmol/L) group. [i]*P*<0.01 *vs* high glucose+DMSO group. [k]*P*<0.05 *vs* high glucose+65 μmol/L breviscapine group.

	Absorbance value
Normal Glucose (5 mmol/L)	0.460±0.027
Normal Glucose+Mannitol (25 mmol/L)	0.453±0.022[a]
High Glucose (25 mmol/L)	0.674±0.029[c]
High Glucose+DMSO	0.670±0.031[d]
High Glucose+Breviscapine65	0.541±0.025[i]
High Glucose+Breviscapine108	0.452±0.020[ik]
Normal Glucose+Breviscapine108	0.455±0.023[a]

Breviscapine inhibited high glucose-induced migration of VSMCs

A transwell migration assay and an *in vitro* scratch assay were used to assess the migratory capability of the VSMCs. As shown in Figure 2A–2D, the number of cells that migrated to the lower side of the porous membrane in the transwell chambers increased under high glucose (25 mmol/L) conditions compared to the normal glucose (5 mmol/L) group over a 12-h period. Therefore, high glucose induced VSMC migration. In contrast, breviscapine decreased high glucose-enhanced migration in a dose-dependent manner (65 or 108 μmol/L). This effect was also observed in an *in vitro* scratch assay. Incubation with high glucose (25 mmol/L) promoted the closure of a linear scratch line compared to the normal glucose group (5 mmol/L). The migration rate was evaluated and used to compare differences between the groups. The results showed that high glucose-induced migration of VSMCs was attenuated by co-incubating cells with breviscapine (65 or 108 μmol/L). The results of the *in vitro* scratch assay are shown in Figure 3.

Exposure of VSMCs to high glucose-activated PKC-β2 and ERK1/2 MAPK signaling

We examined several signal transduction pathways to investigate the mechanism by which breviscapine abrogated the functional impairment of VSMCs that was induced by high glucose. The VSMCs were incubated with high glucose (25 mmol/L) after 24 h of serum starvation. The results showed that exposure of VSMCs to high glucose increased PKC-β2 and ERK1/2 MAPK signaling compared to the normal glucose (5 mmol/L) group. The effects were reflected by a higher ratio of p-PKC-β2 to PKC-β2 than was observed in the control group, as well as a higher proportion of p-ERK1/2 to ERK1/2. However, no changes in p38 and JNK MAPK activity were detected. The results are shown in Figure 4A–4D.

The PKC inhibitor Ro 31-8220 and the MEK1/2 inhibitor PD 98059 both inhibited the high glucose-induced proliferation and migration of VSMCs

To determine whether the PKC and ERK1/2 MAPK signaling pathways are involved in the high glucose-induced proliferation and migration of VSMCs, we examined the effect of a PKC inhibitor and a MEK1/2 inhibitor on the proliferation and migration of VSMCs cultured in high glucose medium. The VSMCs were pretreated with the PKC inhibitor Ro-31-8220 (3 μmol/L) or the MEK1/2 inhibitor PD 98059 (25 μmol/L) at the indicated concentrations for 1 h before high glucose treatment. In our study, the PKC inhibitor Ro-31-8220 and the MEK1/2

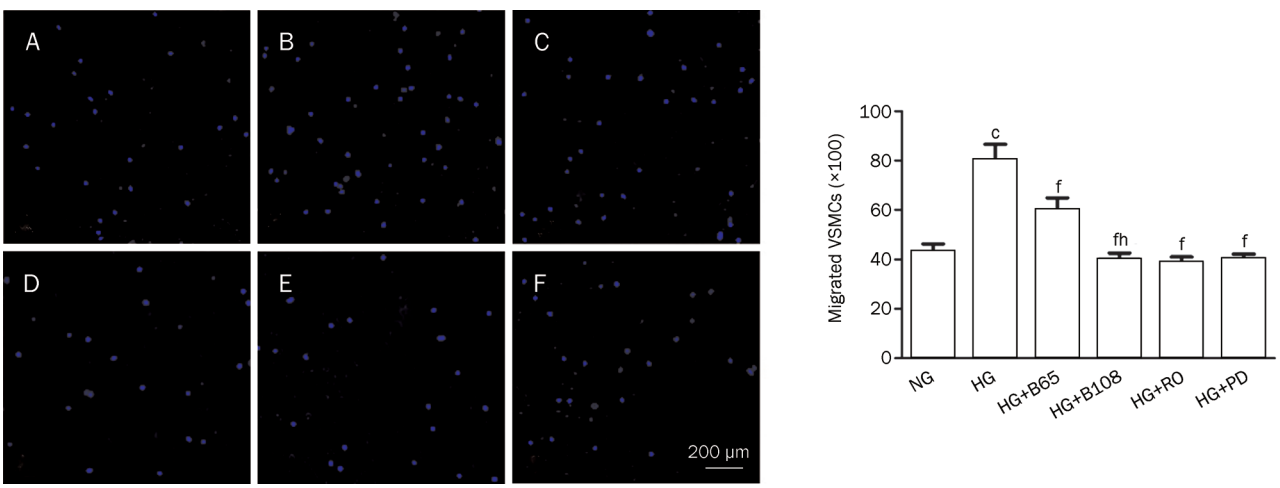

Figure 2. Breviscapine, Ro-31-8220, and PD 98059 inhibited high-glucose-induced migration of VSMCs in the transwell migration assay. Five visual fields were chosen randomly in each assay (×100). The results were presented as mean±SEM of three independent experiments. (A) Normal glucose (5 mmol/L) group; (B) High glucose (25 mmol/L) group; (C) High glucose+65 μmol/L breviscapine group; (D) High glucose+108 μmol/L breviscapine group; (E) High glucose+Ro-31-8220 (3 μmol/L) group; (F) High glucose+PD 98059 (25 μmol/L) group. NG: normal glucose; HG: high glucose; B30: 65 μmol/L breviscapine; B50: 108 μmol/L breviscapine; RO: Ro-31-8220; PD: PD 98059. [c]*P*<0.01 *vs* normal glucose group. [f]*P*<0.01 *vs* high glucose group. [h]*P*<0.05 *vs* high glucose+65 μmol/L breviscapine group.

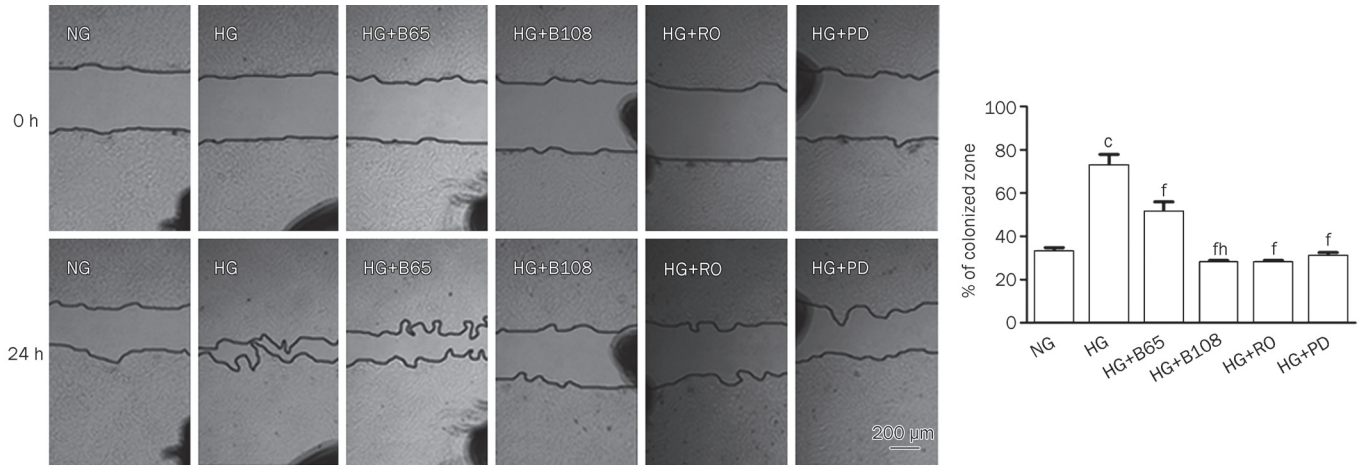

Figure 3. Breviscapine, Ro-31-8220 and PD 98059 inhibited high-glucose-induced migration of VSMCs in the wound healing assay. Black spots serving as benchmarks were drawn to ensure the capture of the same zone throughout experiments. The percentages of colonized zones were evaluated and used to compare differences between groups (×40). The results were presented as mean±SEM of three independent experiments. $^{c}P<0.01$ *vs* normal glucose group. $^{f}P<0.01$ *vs* high glucose group. $^{h}P<0.05$ *vs* high glucose+65 μmol/L breviscapine group.

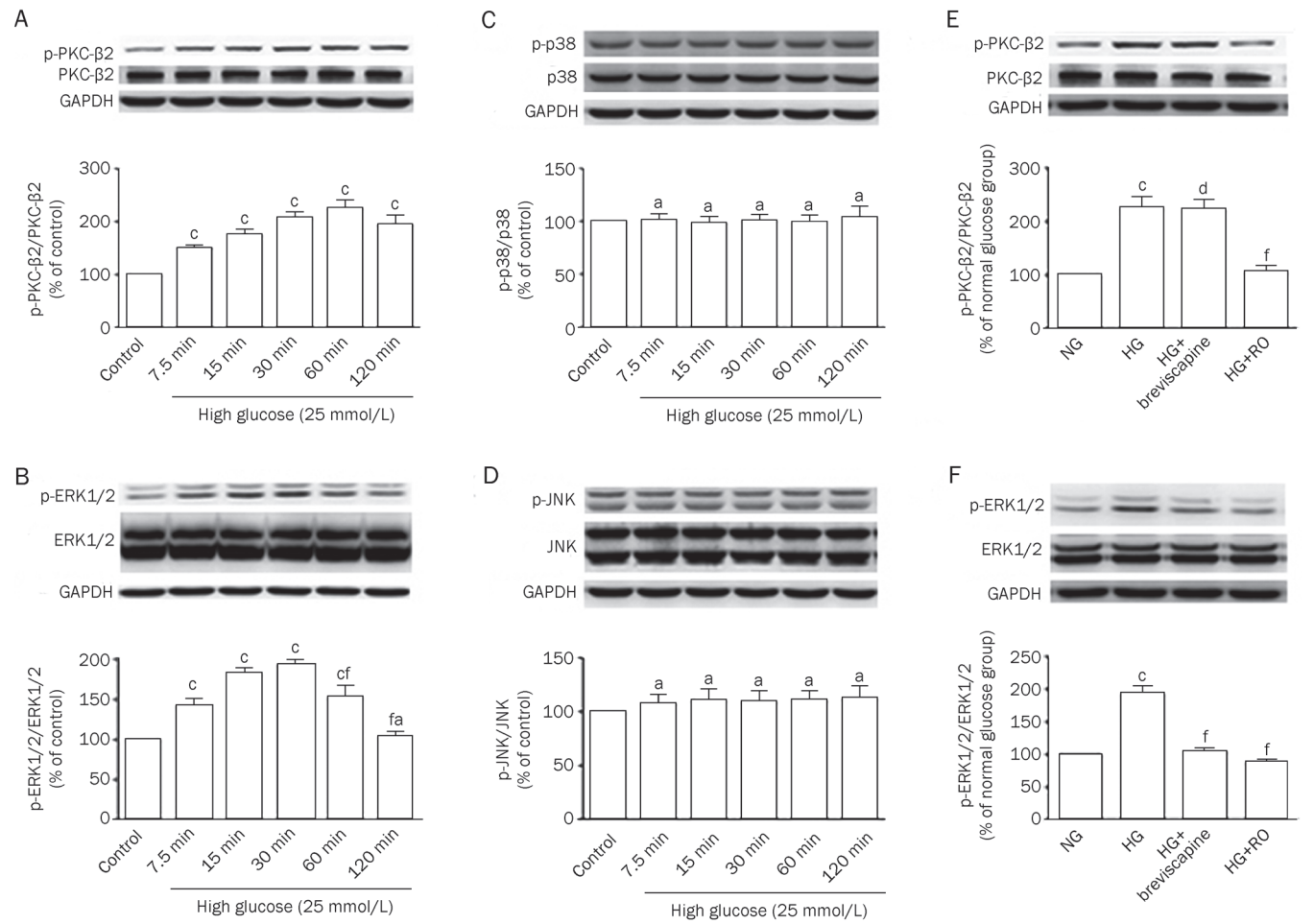

Figure 4. (A–D) Exposure of VSMCs with high glucose activated PKC-β2 and ERK1/2 MAPK signaling pathways, whereas p38 and JNK MAPK were not activated by high glucose. Data were expressed as mean±SEM of three independent experiments. Control: normal glucose (5 mmol/L). (A) $^{c}P<0.01$ *vs* control group; (B) $^{a}P>0.05$, $^{c}P<0.01$ *vs* control group. $^{f}P<0.01$ *vs* 30 min high glucose treatment group; (C–D) $^{a}P>0.05$ *vs* control group; (E–F) ERK1/2 MAPK played a role in 108 μmol/L breviscapine-mediated protective effects on functional impairment of VSMCs induced by high glucose. $^{c}P<0.01$ *vs* normal glucose group. $^{d}P>0.05$, $^{f}P<0.01$ *vs* high glucose group.

inhibitor PD 98059 both abrogated the high glucose-enhanced proliferation and migration of VSMCs. The results are shown in Table 2 and Figure 2 and 3.

Table 2. Both Ro-31-8220 and PD 98059 inhibited high-glucose-induced proliferation of VSMCs. [a]*P*>0.05, [c]*P*<0.01 *vs* normal glucose (5 mmol/L) group. [f]*P*<0.01 *vs* high glucose (25 mmol/L) group.

	Absorbance value
Normal Glucose (5 mmol/L)	0.442±0.021
High Glucose (25 mmol/L)	0.669±0.025[c]
High Glucose+Breviscapine (108 μmol/L)	0.441±0.025[af]
High Glucose+Ro-31-8220 (3 μmol/L)	0.385±0.026[af]
High Glucose+PD 98059 (25 μmol/L)	0.453±0.020[af]
Normal Glucose+Ro-31-8220 (3 μmol/L)	0.391±0.022[a]
Normal Glucose+PD 98059 (25 μmol/L)	0.449±0.021[a]

Breviscapine inhibited high glucose-induced ERK1/2 MAPK signaling

The activation of PKC-β2 and ERK1/2 MAPK signaling in VSMCs was measured to investigate whether the protective effect of breviscapine is related to the PKC-β2 or ERK1/2 MAPK signaling pathways. After 24 h of serum starvation, the VSMCs were pretreated with breviscapine, the PKC inhibitor Ro-31-8220 or the MEK1/2 inhibitor PD 98059 for 1 h and subsequently treated with high glucose for 1 h (for Western blot analysis of the PKC-β2 signaling pathway) or 30 min (for Western blot analysis of the ERK1/2 MAPK signaling pathway). As shown in Figure 4E and 4F, breviscapine inhibited the high glucose-enhanced activity of ERK1/2 MAPK (108 μmol/L), whereas no inhibition of the high glucose-enhanced activity of PKC-β2 was observed.

Under normal glucose conditions, breviscapine, the PKC inhibitor Ro-31-8220 and the MEK1/2 inhibitor PD 98059 had no effect on the proliferation and migration of VSMCs or on PKC-β2 and ERK1/2 MAPK signaling.

To determine whether breviscapine, Ro-31-8220 or PD 98059 had an effect on VSMCs cultured under normal glucose conditions, extra control groups with breviscapine, Ro-31-8220 or PD 98059 alone were included. The results indicated that none of the 3 reagents had an effect on the proliferation or migration of VSMCs cultured under normal glucose conditions. Furthermore, breviscapine and Ro-31-8220 did not affect the activity of PKC-β2 in normal glucose medium; likewise, breviscapine and PD 98059 did not inhibit the activity of ERK1/2 MAPK under normal glucose conditions (Figure 5).

Discussion

Atherosclerosis is one of the most prevalent cardiovascular

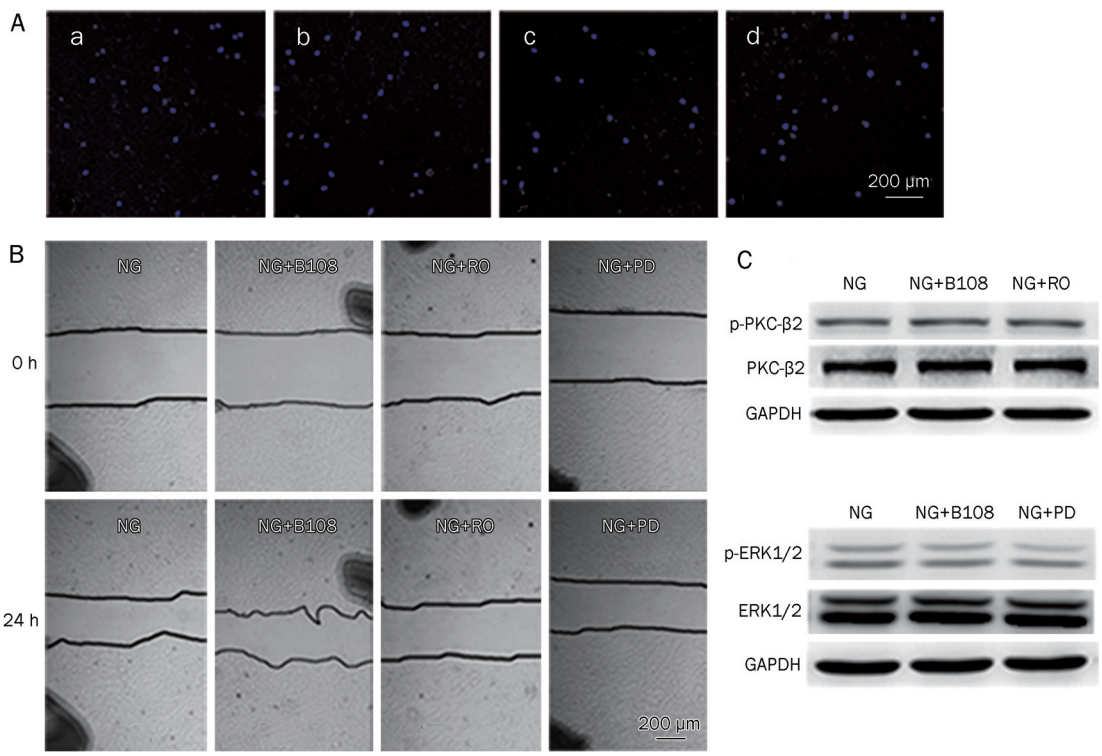

Figure 5. Breviscapine (108 μmol/L), Ro-31-8220, and PD 98059 had no effect on migration of VSMCs cultured in normal-glucose conditions (A and B), as well as activities of PKC-β2 and ERK1/2 MAPK (C). (a) Normal glucose (5 mmol/L) group; (b) Normal glucose+108 μmol/L breviscapine group; (c) Normal glucose+Ro-31-8220 (3 μmol/L) group; (d) Normal glucose+PD 98059 (25 μmol/L) group.

complications of diabetes mellitus and has become a major cause of morbidity and mortality in diabetic patients[21]. Rupture of an atherosclerotic plaque may result in myocardial infarction, stroke or peripheral vascular disease[22, 23]. Atheroma formation involves endothelial damage, oxidized low density lipoprotein (LDL) infiltration, macrophage activation, collagen deposition, a change in the phenotype of VSMCs, as well as an increase in proliferative and migratory capability of VSMCs[4, 5, 24].

Previous studies have indicated that hyperglycemia is an important causative factor in the development of diabetic atherosclerosis, and high glucose levels appeared to be an important contributor to the functional impairment of VSMCs[2, 5, 25, 26]. In the present study, we demonstrated that VSMCs that are cultured in a high concentration of glucose had an increased capacity to proliferate and migrate compared to cells that were cultured under normal glucose conditions, which correlates well with previous studies. The typical pathological changes that are induced by high glucose aggravate the impairment of the vessel wall and contribute to furthering the process of atherosclerosis[4].

However, the exact mechanisms by which high glucose induces functional changes in VSMCs are not clear. Several signal transduction pathways, including the PKC pathway and the MAPK pathway, are activated in response to a variety of external stimuli and have been demonstrated to be involved in a wide variety of cellular responses such as growth, differentiation, gene expression, and angiogenesis[27–30]. In VSMCs, the PKC-β2 isoform, but not PKC-α, has been shown to be activated in response to hyperglycemia. Previous studies have also indicated that activation of the MAPK pathway could potentially result in increased proliferation and migration of VSMCs under high glucose conditions[7, 9–11, 25, 31]. Our results are consistent with previous reports that PKC-β2 and ERK1/2 MAPK were dramatically activated by high glucose. No changes in p38 or JNK MAPK activity were observed. Li *et al* reported that age differentially influenced the activation of the MAPK signaling pathway in VSMCs that were exposed to high glucose[32]. In their study, there was no significant effect of high glucose on p38 activation in VSMCs, which is consistent with our results. Therefore, age or other environmental factors may modulate the activation of MAPK signaling pathways in VSMCs that are exposed to high glucose.

To identify whether activation of the PKC or MAPK pathway is responsible for the high glucose-induced proliferation and migration of VSMCs, VSMCs that were pretreated with the PKC inhibitor Ro-31-8220 or the MEK1/2 inhibitor PD 98059 were cultured in high glucose. As previously reported[7, 10, 11, 25], both the PKC inhibitor Ro 31-8220 and the MEK1/2 inhibitor PD 98059 abrogated the high glucose-enhanced proliferation and migration of VSMCs. Thus, the PKC and MAPK pathways were both responsible for mediating the proliferative- and migratory-promoting response of VSMCs in high glucose medium.

Breviscapine, a traditional Chinese medicine, has potent protective effects on the cardiovascular system. Previous studies have demonstrated that breviscapine ameliorated cardiac hypertrophy that was induced by high glucose or angiotensin II. Studies have also reported that breviscapine had a protective effect against diabetic cardiomyopathy in diabetic rats[15–17]. However, little is known about whether breviscapine has a protective role in diabetic atherosclerosis, which is a common complication of diabetes mellitus that is independent of diabetic cardiomyopathy. A previous study demonstrated that breviscapine potentially had a protective effect on atherosclerosis and caused a significant reduction in the atherogenic index in rat atherosclerotic models[19]. However, whether breviscapine's anti-atherogenic effect resolves the functional impairments of VSMCs remains to be determined. In this study, we aimed to investigate the influence and mechanism of breviscapine's effects on the high glucose-enhanced proliferation and migration of VSMCs. We found that the high glucose-induced proliferation and migration of VSMCs were markedly attenuated by breviscapine treatment. These findings suggested that breviscapine had a protective effect on high glucose-induced dysfunction in VSMCs, which might contribute to its protective effect against diabetic atherosclerosis.

However, further studies were required to uncover the underlying mechanisms behind the effects of breviscapine treatment. A number of reports have demonstrated that breviscapine possessed a strong inhibitory effect on PKC-α and PKC-β2 activation that contributed to its protective roles in cerebral ischemia, hepatic injury during brain death and cardiac hypertrophy[13, 15–17, 33]. To investigate whether the protective effect of breviscapine on VSMCs is related to PKC, PKC-β2 activation was evaluated in VSMCs. Unexpectedly, we did not observe any obvious inhibition of high glucose-induced activation of PKC-β2 by breviscapine. This result suggested that the PKC-β2 signaling pathway might not be responsible for the protective role of breviscapine in VSMCs that are impaired by high glucose.

Many studies have focused on breviscapine in recent years, so its effects on other signaling molecules were also evaluated. In a recent report, breviscapine inhibited the proliferation and collagen production of cardiac fibroblasts that is induced by angiotensin II, as well as angiotensin II-induced phosphorylation of p38 and ERK1/2 MAPK[19]. Because the ERK1/2 MAPK pathway was activated in response to hyperglycemia and was involved in the high glucose-induced proliferation and migration of VSMCs, we tried to establish whether the MAPK pathway plays a role in the protective effect of breviscapine against VSMC functional impairment under high glucose conditions. Our study showed that breviscapine markedly decreased the high glucose-enhanced activation of ERK1/2 MAPK, indicating that disruption of ERK1/2 MAPK signaling contributed to the protective effect of breviscapine.

These data indicate that breviscapine could be an effective and safe therapeutic candidate for the prevention of diabetic atherosclerosis. Further animal experiments and clinical trials are required to prove the new potential clinical therapeutic use of breviscapine.

Conclusion

We provide the first experimental evidence that breviscapine can ameliorate the high glucose-enhanced proliferation and migration of VSMCs. We also demonstrate for the first time that the ERK1/2 MAPK signaling pathway, but not the PKC-β2 signaling pathway, may be involved in the protective effect of breviscapine against the functional impairments of VSMCs that are induced by high glucose. Therefore, breviscapine could be an effective and safe therapeutic candidate for preventing diabetic atherosclerosis through suppression of the ERK1/2 MAPK signaling pathway.

Acknowledgements

We thank the Department of Cardiovascular Disease at Sir Run Run Shaw Hospital in the College of Medicine at Zhejiang University for the use of test instruments and equipment.

Author contribution

Bin-quan ZHOU designed the research, and Meng HE performed most of the research and wrote the paper. Zhi-min XUE contributed new analytic tools and analyzed the data, and Juan LI performed some of the research.

References

1 Wild S, Roglic G, Green A, Sicree R, King H. Global prevalence of diabetes: estimates for the year 2000 and projections for 2030. Diabetes Care 2004; 27: 1047–53.
2 Laakso M. Hyperglycemia and cardiovascular disease in type 2 diabetes. Diabetes 1999; 48: 937–42.
3 Nishimura H. [Diabetes mellitus and atherosclerosis]. Nihon Rinsho 2011; 69: 131–7.
4 Doran AC, Meller N, McNamara CA. Role of smooth muscle cells in the initiation and early progression of atherosclerosis. Arterioscler Thromb Vasc Biol 2008; 28: 812–9.
5 Yasunari K, Kohno M, Kano H, Yokokawa K, Minami M, Yoshikawa J. Antioxidants improve impaired insulin-mediated glucose uptake and prevent migration and proliferation of cultured rabbit coronary smooth muscle cells induced by high glucose. Circulation 1999; 99: 1370–8.
6 Chen WJ, Lin KH, Lai YJ, Yang SH, Pang JH. Protective effect of propylthiouracil independent of its hypothyroid effect on atherogenesis in cholesterol-fed rabbits: PTEN induction and inhibition of vascular smooth muscle cell proliferation and migration. Circulation 2004; 110: 1313–9.
7 Yasunari K, Kohno M, Kano H, Yokokawa K, Minami M, Yoshikawa J. Mechanisms of action of troglitazone in the prevention of high glucose-induced migration and proliferation of cultured coronary smooth muscle cells. Circ Res 1997; 81: 953–62.
8 Griffin E, Re A, Hamel N, Fu C, Bush H, McCaffrey T, *et al*. A link between diabetes and atherosclerosis: Glucose regulates expression of CD36 at the level of translation. Nat Med 2001; 7: 840–6.
9 Lee IK, Koya D, Ishi H, Kanoh H, King GL. d-Alpha-tocopherol prevents the hyperglycemia induced activation of diacylglycerol (DAG)-protein kinase C (PKC) pathway in vascular smooth muscle cell by an increase of DAG kinase activity. Diabetes Res Clin Pract 1999; 45: 183–90.
10 Panchatcharam M, Miriyala S, Yang F, Leitges M, Chrzanowska-Wodnicka M, Quilliam LA, *et al*. Enhanced proliferation and migration of vascular smooth muscle cells in response to vascular injury under hyperglycemic conditions is controlled by beta3 integrin signaling. Int J Biochem Cell Biol 2010; 42: 965–74.
11 Natarajan R, Scott S, Bai W, Yerneni KK, Nadler J. Angiotensin II signaling in vascular smooth muscle cells under high glucose conditions. Hypertension 1999; 33: 378–84.
12 Zhou H, Chen S, Wang L, He Q, Fan X. [Regulation of the expression of pulmonary arterial collagen by protein kinase C and breviscapine in chronic hypoxic rats]. Zhonghua Jie He He Hu Xi Za Zhi 2002; 25: 347–51.
13 Zhang SJ, Song Y, Zhai WL, Shi JH, Feng LS, Zhao YF, *et al*. Breviscapine alleviates hepatic injury and inhibits PKC-mRNA and its protein expression in brain-dead BA-Ma mini pigs. Hepatobiliary Pancreat Dis Int 2007; 6: 604–9.
14 Qi XM, Wu GZ, Wu YG, Lin H, Shen JJ, Lin SY. Renoprotective effect of breviscapine through suppression of renal macrophage recruitment in streptozotocin–induced diabetic rats. Nephron Exp Nephrol 2006; 104: e147–57.
15 Yan L, Huang H, Tang QZ, Zhu LH, Wang L, Liu C, *et al*. Breviscapine protects against cardiac hypertrophy through blocking PKC-alpha-dependent signaling. J Cell Biochem 2010; 109: 1158–71.
16 Wang M, Zhang WB, Zhu JH, Fu GS, Zhou BQ. Breviscapine ameliorates hypertrophy of cardiomyocytes induced by high glucose in diabetic rats via the PKC signaling pathway. Acta Pharmacol Sin 2009; 30: 1081–91.
17 Wang M, Zhang WB, Zhu JH, Fu GS, Zhou BQ. Breviscapine ameliorates cardiac dysfunction and regulates the myocardial Ca(2+)-cycling proteins in streptozotocin-induced diabetic rats. Acta Diabetol 2010; 47: 209–18.
18 Pan Z, Zhao W, Zhang X, Wang B, Wang J, Sun X, *et al*. Scutellarin alleviates interstitial fibrosis and cardiac dysfunction of infarct rats by inhibiting TGFbeta1 expression and activation of p38-MAPK and ERK1/2. Br J Pharmacol 2011; 162: 688–700.
19 Li Q, Wu JH, Guo DJ, Cheng HL, Chen SL, Chan SW. Suppression of diet-induced hypercholesterolemia by scutellarin in rats. Planta Med 2009; 75: 1203–8.
20 Chamley-Campbell J, Campbell GR, Ross R. The smooth muscle cell in culture. Physiol Rev 1979; 59: 1–61.
21 Farmer JA. Diabetic dyslipidemia and atherosclerosis: evidence from clinical trials. Curr Diab Rep 2008; 8: 71–7.
22 Glass CK, Witztum JL. Atherosclerosis. The road ahead. Cell 2001; 104: 503–16.
23 Goldschmidt-Clermont PJ, Creager MA, Losordo DW, Lam GK, Wassef M, Dzau VJ. Atherosclerosis 2005: recent discoveries and novel hypotheses. Circulation 2005; 112: 3348–53.
24 Huang CN, Chan KC, Lin WT, Su SL, Wang CJ, Peng CH. Hibiscus sabdariffa inhibits vascular smooth muscle cell proliferation and migration induced by high glucose — a mechanism involves connective tissue growth factor signals. J Agric Food Chem 2009; 57: 3073–9.
25 Campbell M, Trimble ER. Modification of PI3K- and MAPK-dependent chemotaxis in aortic vascular smooth muscle cells by protein kinase CbetaII. Circ Res 2005; 96: 197–206.
26 Zhu L, Sun G, Zhang H, Zhang Y, Chen X, Jiang X, *et al*. PGC-1alpha is a key regulator of glucose-induced proliferation and migration in vascular smooth muscle cells. PLOS ONE 2009; 4: e4182.
27 Dempsey EC, Newton AC, Mochly-Rosen D, Fields AP, Reyland ME, Insel PA, *et al*. Protein kinase C isozymes and the regulation of diverse cell responses. Am J Physiol Lung Cell Mol Physiol 2000; 279: L429–38.
28 Anjum R, Blenis J. The RSK family of kinases: emerging roles in cellular signalling. Nat Rev Mol Cell Biol 2008; 9: 747–58.
29 Wagner EF, Nebreda AR. Signal integration by JNK and p38 MAPK pathways in cancer development. Nat Rev Cancer 2009; 9: 537–49.
30 Min L, He B, Hui L. Mitogen-activated protein kinases in hepato-

cellular carcinoma development. Semin Cancer Biol 2011; 21: 10–20.

31 Kunisaki M, Bursell SE, Umeda F, Nawata H, King GL. Normalization of diacylglycerol-protein kinase C activation by vitamin E in aorta of diabetic rats and cultured rat smooth muscle cells exposed to elevated glucose levels. Diabetes 1994; 43: 1372–7.

32 Li M, Mossman BT, Kolpa E, Timblin CR, Shukla A, Taatjes DJ, *et al*. Age-related differences in MAP kinase activity in VSMC in response to glucose or TNF-alpha. J Cell Physiol 2003; 197: 418–25.

33 Xu W, Zha RP, Wang WY, Wang YP. Effects of scutellarin on PKCgamma in PC12 cell injury induced by oxygen and glucose deprivation. Acta Pharmacol Sin 2007; 28: 1573–9.

Acta Pharmacologica Sinica (2012) 33: 615–624
 1671-4083/12 $32.00
www.nature.com/aps

Original Article

Non-genomic vasorelaxant effects of 17β-estradiol and progesterone on rat aorta are mediated by L-type Ca^{2+} current inhibition

Elisa CAIRRÃO*, Ezequiel ALVAREZ, João Miguel CARVAS, Antonio Jose SANTOS-SILVA, Ignacio VERDE

Centro de Investigação em Ciências da Saúde, Universidade da Beira Interior, Av Infante D Henrique s/n 6200–506 Covilhã, Portugal

Aim: The sex hormones 17β-estradiol (βES) and progesterone (PRG) induce rapid non-genomic vasodilator effects which could be protective for the cardiovascular system. The purpose of this study was to analyze the mechanisms underlying their vasodilator effect in rat aortic smooth muscle preparations.
Methods: Endothelium-denuded aorta artery rings were prepared from male Wistar rats and incubated in an organ bath. The contractions of the preparation were recorded through isometric transducers. The effects of the hormones on K^+ current and L-type Ca^{2+} current (LTCC) were analyzed by using the whole cell voltage-clamp technique in A7r5 cells.
Results: Both βES and PRG (1–100 μmol/L) concentration-dependently relaxed the endothelium-denuded aortic rings contracted by (–)-Bay K8644 (0.1 μmol/L) or by KCl (60 mmol/L). The IC_{50} values of the two hormones were not statistically different. The K_V channel blocker 4-aminopyridine (2 mmol/L), BK_{Ca} channel blocker tetraethylammonium (1mmol/L) and K_{ATP} channel blocker glibenclamide (10 μmol/L) did not significantly modify the relaxant effect of the hormones. On the other hand, the blockage of the intracellular βES and PRG receptors with estradiol receptor antagonists ICI 182,780 (1 μmol/L) and PRG receptor antagonist mifepristone (30 μmol/L), respectively, did not significantly modify the relaxant action of the hormones. In A7r5 cells, both the hormones (1–100 μmol/L) rapidly and reversibly inhibited the basal and BAY-stimulated LTCC. However, these hormones had no effect on the basal K^+ current.
Conclusion: The vasorelaxant effects of βES and PRG are due to the inhibition of LTCC. The K^+ channels are not involved in the effects.

Keywords: female sex hormone; 17β-estradiol; progesterone; non-genomic action; vasorelaxant effect; Ca^{2+} channel; K^+ channel; rat aorta artery ring; A7r5 cel

Acta Pharmacologica Sinica (2012) 33: 615–624; doi: 10.1038/aps.2012.4; published online 2 Apr 2012

Introduction

Cardiovascular diseases are one of the most common causes of death in western countries and there are different degrees of incidence of these diseases between both sexes[1]. Concerning the role of sex hormones in these diseases, it was reported that estrogen replacement therapy can reduce the risk of coronary and cerebrovascular diseases in postmenopausal women[2, 3]. Also, the results of distinct observational and clinical studies suggested that female and male sex hormones can modulate the vascular function[4, 5]. Nevertheless, the molecular mechanisms underlying the effects of these hormones remain undefined due to controversial data and to relatively small number of experimental studies undertaken.

According to the classic theory to explain the steroid hormones effects, these signalling molecules modulate gene transcription due to the interaction with intracellular receptors. However, these hormones can also induce rapid (seconds to minutes) non-genomic effects which are reversible and insensible to transcription and protein synthesis inhibitors[1, 6, 7]. Non-genomic effects of sex hormones include vasodilatation, one of the most relevant and promising action of sex steroids. Different pathways have been proposed to explain this effect. Progesterone (PRG) and 17beta-estradiol (βES) may activate endothelium-dependent vasorelaxant pathways, including pathways mediated by nitric oxide, prostacyclin and hyperpolarizing factors[1, 8, 9]. However, these steroids can also relax arterial smooth muscle via endothelium-independent mechanisms, mainly involving modulation of membrane ionic flux[10, 11]. This direct vasodilator effect of PRG and βES has been observed in different arteries from different species such as aorta[12, 13], coronary arteries[8, 10, 14], cerebral arteries[15], omental artery[16], tail artery[17] and mesenteric artery[9, 18, 19].

The inhibition of Ca^{2+} channels and the activation of K^+ channels was suggested as a leading cause of the sex hor-

* To whom correspondence should be addressed.
E-mail ecairrao@fcsaude.ubi.pt
Received 2011-11-03 Accepted 2012-01-05

mones' effect. The extracellular Ca^{2+} can enter into the smooth muscle cells through different types of Ca^{2+} channels such as store-operated Ca^{2+} channels, voltage-operated Ca^{2+} channels (VOCCs), Ca^{2+}-permeable non-selective cation channels and the controversial receptor-operated Ca^{2+} channels[20]. Some authors showed that the inhibition of Ca^{2+} channels is associated to the vasodilatation mediated by estrogens[21–23] and PRG[24, 25]. The effects of βES and PRG on VOCCs were the objective of some studies. Zhang *et al* have reported that in A7r5 cells estradiol inhibits two types of VOCCs: L- and T-type Ca^{2+} channels (LTCC and TTCC respectively)[26]. Nakajima *et al*, using tight-seal whole cell clamp technique, observed that βES inhibits LTCC, but failed to affect Ca^{2+}-permeable non-selective cation currents evoked by endothelin or vasopressin[21]. In addition, these authors also observed that PRG and testosterone fail to inhibit calcium channels[21]. Other authors observed that environmental estrogenic pollutants and βES induced a rapid and endothelium-independent relaxation by inhibiting LTCC in vascular smooth muscle cells[27]. Activation of K^+ channels by PRG and by βES in vascular smooth muscle may induce repolarization of plasma membrane, which will close the VOCCs and contribute to the vascular relaxation[27–30]. This mechanism does not appear to be very important for PRG[29], but the opening of Ca^{2+}-activated K^+ (BK_{Ca}) channels by βES has been observed in human coronary artery smooth muscle cells[30] and rat aorta A7r5 cells[27]. The activation of K^+ channels was suggested to be involved in the vasodilatation induced by βES in arteries from different species[8, 31] and could also be important to prevent or reduce hypertension[32, 33]. On the contrary, K^+ currents can be attenuated by 17alpha-estradiol or βES, an effect that could be mediated by estrogen-induced proteasomal degradation of these channels. These sex hormones specific bind to K^+ channels and induce proteasome-dependent proteolytic degradation. This action can be elicited independently of the activation of the nuclear estradiol receptors or the accessory β1-subunit, but in the presence of β1-subunits, specific binding of estradiol to BK_{Ca} channels is significantly increased[34].

In summary, PRG and βES have vascular non-genomic actions which include vasodilatation. Although the mechanistic pathways implicated in this effect are still unknown, some studies have reported, regardless of the specific site of action, the involvement of an ionic-related transduction mechanism. The purpose of this study was to analyse the mechanisms implicated in the vasodilator effect of these hormones in rat aortic smooth muscle. The relaxation induced by these hormones in endothelium-denuded rat aorta was analysed. Also, the whole cell configuration of the patch-clamp technique was used to analyse the effects of sex hormones on voltage-dependent Ca^{2+} current (I_{Ca}) and on the K^+ current (I_K) in A7r5 cells.

Materials and methods

Contractility experiments in isolated rat thoracic aorta rings

Male adult Wistar rats (Charles-River, Barcelona, Spain) weighing 400–500 g were housed and acclimatized with light cycles of 12 h light: 12 h dark and food and water *ad libitum* for at least one week before performing the experiments. The rats were used in accordance with the European regulations about protection of animals (Directive 86/609) and the Guide for the Care and Use of Laboratory Animals promulgated by the US National Institutes of Health (NIH Publication No 85–23, revised 1996).

The rats were sacrificed by decapitation and, after thoracotomy, the thoracic aortas were removed, placed in a thermostatized (37 °C) Krebs' modified solution and the fat and connective tissue was cleaned. Also, the vascular endothelium was mechanically removed by gentle rubbing with a cotton bud introduced through the arterial lumen. The rat aorta artery rings were placed in an organ bath (LE01.004, Letica) containing Krebs-bicarbonate solution at 37 °C continuously gassed with carbogen. The composition of the Krebs' modified solution was (mmol/L): NaCl 119, KCl 5, $CaCl_2 \cdot 2H_2O$ 0.5, $MgSO_4 \cdot 7H_2O$ 1.2, KH_2PO_4 1.2, $NaHCO_3$ 25, EDTA-Na_2 0.03, *L*-(+)-ascorbic acid 0.6 and glucose 11 (pH 7.4). The rings were suspended by two parallel stainless steel wires and tension measurement was performed using isometric transducers (TRI201, Panlab SA, Spain), amplifier (ML118/D Quad Bridge, ADInstruments), interface PowerLab/4SP (ML750, ADInstruments), interface PowerLab/4SP (ML750, ADInstruments), and computerised system with Chart5 PowerLab software (ADInstruments). During the resting periods, the organ bath solution was changed every 15 min.

Initially, the rings were equilibrated for 60 minutes until a resting tension of 1.0 g. After the equilibration period, aortic rings were firstly contracted with high isosmotic KCl (60 mmol/L) and the absence of endothelium functionality was confirmed by the lack of relaxant response to acetylcholine (1 μmol/L). After that, the arteries were washed many times for at least 45 min before the next stimuli. The rings were contracted using KCl (60 mmol/L) or (–)-Bay K 8644 (BAY; 0.1 μmol/L) and vasorelaxation induced by βES and PRG (1–100 μmol/L) on these contractions was analysed.

The contraction induced by BAY (0.1 μmol/L; specific LTCC activator) was performed to observe the direct effect of these sex hormones o LTCC. The contractions induced by BAY were obtained in presence of KCl 10 mmol/L.

In some experiments, specific antagonists for the intracellular hormonal receptor were used in order to analyse the involvement of these receptors in the vasorelaxant effects of βES and PRG. In these cases, after a stable contraction with KCl (60 mmol/L), the arteries were incubated for 15 min with ICI 182,780 (1 μmol/L; a specific antagonist for the classical estradiol receptor) or with mifepristone (30 μmol/L; a specific antagonist for the classical progesterone receptor). After this incubation the vasorelaxation induced by βES or PRG in the presence of this specific antagonist was analysed.

To analyse the role of K^+ channels in the effects of these sex hormones, different inhibitors of these channels were used: tetraethylammonium (TEA; 1 mmol/L), that inhibits of large-conductance Ca^{2+}-activated potassium (BK_{Ca}) channel; glybenclamide (Gly; 10 μmol/L), that inhibits ATP-sensitive potas-

sium (K_{ATP}) channel; and 4-aminopyridine (4-AP; 1 mmol/L), that inhibits voltage-sensitive potassium (K_V) channels. In these cases, after a stable contraction with KCl (60 mmol/L), the arteries were incubated 15 min with the potassium channel inhibitors. After this incubation the effect of the sex hormones was analysed. Control experiments were performed using ethanol, the vehicle used to dissolve the channel inhibitors.

Cell culture of vascular smooth muscle cells

The A7r5 cell line, used in this study, is a commercial vascular smooth muscle cell line obtained from embryonic rat aorta (Promochem, Spain). The cells were grown in culture medium Dulbecco's modified Eagle's medium/Nutrient Mixture F-12 Hams (DMEF-F12; Sigma-Aldrich, Portugal) supplemented with $NaHCO_3$ (1.2 μg/L), L-ascorbic acid (20 mg/L; Sigma-Aldrich), bovine serum albumin (0.5%; Sigma-Aldrich), heat-inactivated foetal bovine serum (FBS; 10%; Biochrom), and a mixture of penicillin (100 U/mL), streptomycin (100 g/mL), and amphotericin B (250 ng/mL) (Sigma-Aldrich). The cells were kept in culture at 37 °C in a humidified atmosphere with 5% CO_2 in air. After confluence, the cells were placed in culture medium without FBS (FBS-free culture medium) for 24–48 h. Trypsinization was made using a solution of trypsin (0.3%) in Ca^{2+}-Mg^{2+}-free phosphate buffered solution with EDTA (0.025%). Subsequently, the cells were kept at 4 °C in FBS-free medium until the realisation of the electrophysiological experiments.

Electrophysiology experiments

The whole cell configuration of patch clamp technique was used to analyse the L-type calcium current ($I_{Ca,L}$) and the K^+ current (I_K). To analyse the $I_{Ca,L}$, the control external solution contained (mmol/L): NaCl 124.0, $CaCl_2$ 5.0, HEPES 5.0, tetraethylammonium sodium salt (TEA) 10.0, KCl 4.7 and glucose 6.0, pH 7.4 adjusted with NaOH. Patch electrodes (2–4 MΩ) were filled with internal solution (mmol/L): CsCl 119.8, $CaCl_2$ 0.06, $MgCl_2$ 4.0, Na-ATP 3.1, Na-GTP 0.4, EGTA 5.0, HEPES 10.0 and TEA 10.0, pH 7.3 adjusted with CsOH. The presence of Cs^+ instead of K^+ in the solutions blocked the potassium currents. The cells were maintained at a holding potential of -80 mV and routinely depolarised every 8 s to 0 mV test potential during 500 ms to measure $I_{Ca,L}$.

To analyse the I_K, the control external solution contained (mmol/L): NaCl 134.3, $CaCl_2$ 1.0, HEPES 5.0, KCl 5.4 and glucose 6.0, pH 7.4 adjusted with NaOH. Patch electrodes (2–4 MΩ) were filled with internal solution (mmol/L): KCl 125.0, $MgCl_2$ 1.0, Na-ATP 5.0, Na-GTP 0.5, EGTA 0.1, HEPES 20.0 and glucose 10.0, pH 7.3 adjusted with KOH. For I_K analysis we used the same holding potential and depolarizations to 60 mV for 300 ms were performed every 8 s.

Basal $I_{Ca,L}$ and I_K were measured 3–5 min after patch break to allow the equilibration between pipette and intracellular solutions. Currents were not compensated for capacitance and leak currents. All experiments were done at room temperature (21–25 °C) and the temperature did not vary by more than 1 °C in a given experiment. The cells were voltage clamped using the patch-clamp amplifier Axopatch 200B (Axon instruments, USA). Currents were sampled at a frequency of 10 kHz and filtered at 0.1 kHz using the analog-digital interface Digidata 1322A (Axon Instruments, USA) connected to a compatible computer with the Pclamp8 software (Axon Instruments, USA). The external solution was applied to the cell proximity by placing the cell at the opening of a 250 μm inner diameter capillary tube flowing at a rate of 20 μL/min. The basal and BAY-stimulated (10 nmol/L) $I_{Ca,L}$ were studied in the presence of different concentrations of βES (1–100 μmol/L) and of PRG (1–100 μmol/L) dissolved in the external solution.

Drugs

All drugs were purchased from Sigma-Aldrich Química (Sintra, Portugal), except 4-aminopyridine and PRG that purchased from Biogen Cientifica (Madrid, Spain).

Mifepristone, ICI 182,780, BAY, nifedipine, βES and PRG were initially dissolved in ethanol. 4-Aminopyridine, glibenclamide, apamin and tetraethylammonium were initially dissolved in deionised water. Appropriate dilutions in Krebs' modified solution or in the corresponding electrophysiology external solution were prepared every day before the experiment. Final concentration of ethanol never exceeded 0.1% in the experiments.

Statistical analysis

Statistical treatment of data was performed using the SigmaStat Statistical Analysis System, version 1.00 (1992). Results are expressed as mean±SEM of *n* experiments. Comparison among multiple groups was analysed by using a one-way ANOVA followed by Dunnet's or Tukey *post hoc* test to determine significant differences among the means. Comparison between two groups was analysed by using Students *t*-test. Probability levels lower than 5% were considered significant ($P<0.05$).

In the contractility experiments, the relaxant responses induced by βES and PRG are expressed as a percent of the maximal contraction (E_{max}=100%) produced by each vasoconstrictor agent. In these experiments, sigmoidal concentration-response curves for the vasorelaxant effects were fitted and IC_{50} values (*ie* concentrations inducing 50% of relaxation) of βES and PRG were estimated for KCl- or BAY-induced contractions. The antagonist of classical progesterone receptors, mifepristone, relaxed by itself the arteries contracted by KCl, and in this case the maximal effect used to perform the concentration-response curves was the tension obtained in presence of mifepristone.

The $I_{Ca,L}$ amplitudes were automatically calculated between the maximum current peak and the stable current plateau near the final of the every 8 s pulse. The $I_{Ca,L}$ variations induced by the different drugs used are expressed as a percent of the basal or BAY-stimulated $I_{Ca,L}$. The I_K variations are expressed as a percent of the basal I_K obtained by depolarization in the absence of any drug.

Results

Vasorelaxant effects of female sex hormones on rat isolated aorta

The rat aortic rings without endothelium were contracted by depolarisation with isosmotic KCl (60 mmol/L) solution or by the calcium channel opener BAY (0.1 μmol/L). The maximal contractions elicited by KCl and BAY, 1134.3±39.9 mg (n=52) and 1222.8±83.1 mg (n=20) respectively, were not significantly different (P<0.05, Student's t-test). These contractile effects were reversible after washing out with Krebs' solution.

Afterwards, the effect of βES or PRG (1–100 μmol/L) on the contraction induced by KCl and Bay were analysed. Increasing concentrations of both hormones were administered and, at higher concentrations, almost completely relaxed the contractions induced by KCl and BAY (Figure 1A and 1B). The vasorelaxation induced by each dose of βES or PRG was observed 10–15 min after the application. The effect of the hormones was reversible because, after washing out, a second administration of the contractile agents elicited similar contractile effects than the previous one (P>0.05, data not shown). The maximal relaxation induced by βES and by PRG was similar in arteries contracted by KCl or BAY. However, the vasorelaxant effect induced by PRG 10 μmol/L in the arteries contracted with BAY is lower that the induced by βES at the same concentration (Figure 1B). Also, in the arteries contracted with KCl the vasorelaxant effect induced by βES 10 μmol/L is lower that the induced by PRG at the same concentration, and similar to the control arteries (Figure 1A).

The IC_{50} values corresponding to the relaxant effects of βES or PRG on KCl-induced contraction were almost similar, being βES slightly more effective than PRG, although this difference was not significant (P>0.05; Student's t-test; Table 1). Similarly, in BAY-contracted arteries, the vasorelaxant effect of βES seems to be slightly more effective than that of PRG, as revealed the IC_{50} values obtained in both cases (Table 1). However, there are no significant differences between the IC_{50} values of βES and PRG, independently of the contractile agent (KCl or BAY) (P>0.05; Student's t-test; Table 1). Thus, in general, the vasorelaxant effect induced by βES and by PRG was similar.

Influence of K^+ channels on the vasorelaxant effects of the female sex hormones

The effects of three K^+ channels inhibitors (Gli, 4-AP, and TEA) were investigated to analyse the involvement of these channels in the female sex hormones-associated relaxant mechanism. Initially, after contraction with KCl 60 mmol/L, rat aorta rings were exposed for 15 min to glibenclamide (Gli; 10 μmol/L), 4-aminopyridine (4-AP; 1 mmol/L), and tetraethylammonium (TEA; 1mmol/L), either together or separately, and these inhibitors did not have a significant effect on the contraction induced by KCl 60 mmol/L (data not shown). After that, the administration of cumulative concentrations of βES or PRG induced the total relaxation of the contracted aortic rings. None of the K^+ channel inhibitors tested modified significantly the relaxant effect of these hormones (Figure 2) (P>0.05, one-way ANOVA with Dunnet's *post hoc* test). The relaxant IC_{50} values for βES and PRG in the presence of any one of the K^+ channels inhibitors did not differ significantly from the IC_{50} values calculated in the absence of them (P>0.05; Student's t-test. Table 1). Thus, the inhibition of K_V, BK_{Ca}, and K_{ATP} channels did not reduce the relaxing effect of βES or PRG.

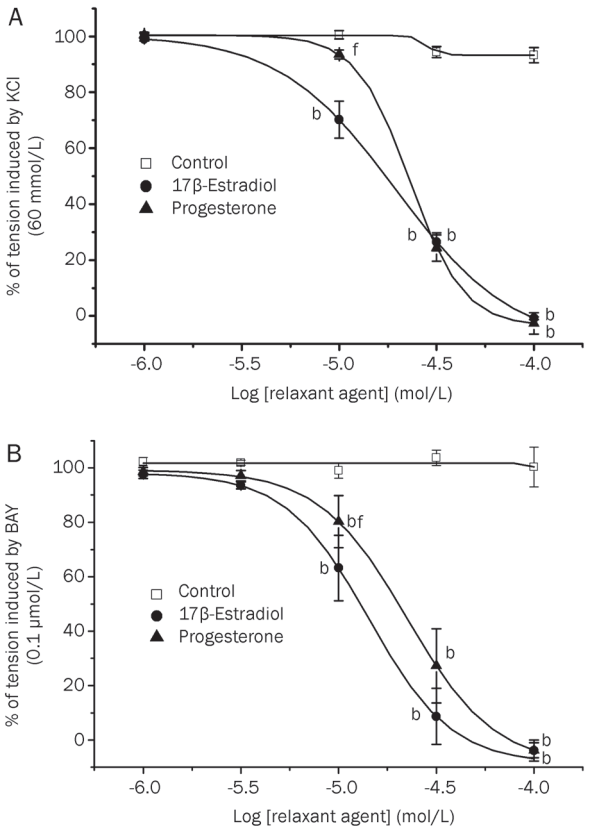

Figure 1. Relaxant effect of different concentrations of βES and PRG (1–100 μmol/L) on contractions of endothelium-denuded rat aortic rings induced by KCl (60 mmol/L) (A) or by BAY (0.1 μmol/L after KCl 10 mmol/L) (B). Each point represents the mean value and the vertical lines indicate SEM of at least 5 experiments. Control experiments were performed using with ethanol, the vehicle used to dissolve the hormones. ^bP<0.05 versus control. ^fP<0.01 βES versus PRG. One-way ANOVA followed by with Tukey *post hoc* test.

Implication of βES and PRG intracellular receptor in the vasorelaxant effects of these hormones

To analyse if the vasorelaxant effects of βES and PRG are mediated by the activation of the intracellular receptors, we used specific antagonists for these receptors. The arteries were contracted by KCl or BAY, after reaching a plateau of contraction the antagonists were administered and increasing concentrations of βES or PRG were added to test the relaxant effect of these hormones in these conditions. The ICI 182,780 (1 μmol/L) was used to block βES receptors and mifepristone (30 μmol/L) was employed for the receptors of PRG.

When administrated alone, mifepristone induced a significant relaxation of the contracted rat aortic rings (53.9%±3.1%).

Table 1. Values of IC_{50} (μmol/L) for the relaxant effect of 17β-estradiol and progesterone on rat aortic contractions induced by BAY (10 nmol/L) and with KCl (60 mmol/L). The influence of potassium channel inhibitors was analysed using the following drugs: the K_V channel blocker 4-aminopyridine (4-AP; 2 mmol/L); the BK_{Ca} channel blocker tetraethylammonium (TEA; 1 mmol/L); and the K_{ATP} channel blocker glibenclamide (GLI; 10 μmol/L). The influence of the blockage of intracellular hormone receptors was analysed using the estradiol receptor antagonists ICI 182,780 (ICI; 1 μmol/L) and the progesterone receptor antagonists mifepristone (30 μmol/L). Each value represents the mean±SEM from the number of experiments shown in brackets.

AGENTS	17β-Estradiol	Progesterone
BAY	14.24±0.05 (*n*=6)	22.33±0.30 (*n*=5)
KCl	19.54±1.15 (*n*=9)	23.04±0.02 (*n*=9)
KCl+TEA	22.66±2.76 (*n*=4)	20.25±1.11 (*n*=6)
KCl+4-AP	17.14±1.33 (*n*=7)	22.60±1.06 (*n*=6)
KCl+GLI	30.44±2.43 (*n*=3)	18.79±2.01 (*n*=4)
KCl+ICI	16.97±1.26 (*n*=6)	
KCl+Mifepristone		24.49±1.35 (*n*=8)

4-AP, 4-aminopyridine; BAY, (−)-Bay K8644; GLI, glibenclamide; TEA, tetraethylammonium sodium salt; ICI, ICI 182,780.

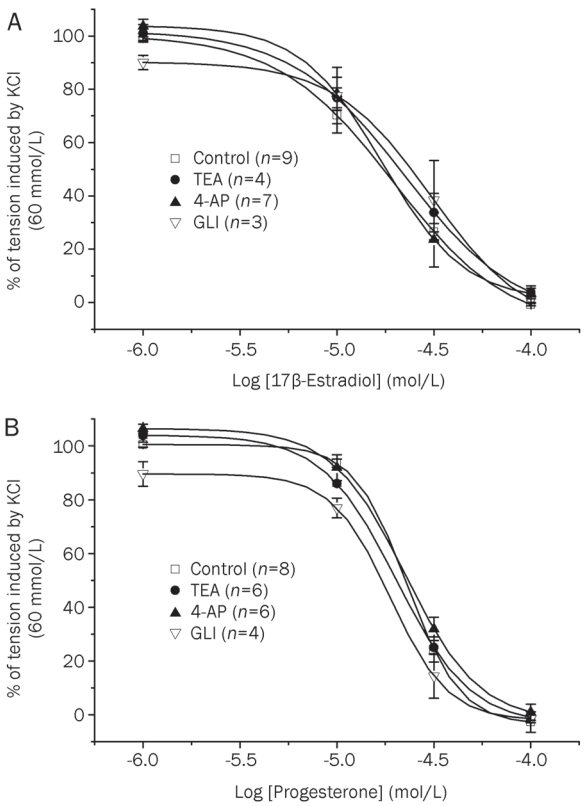

Figure 2. Relaxant effect of different concentrations of 17β-estradiol (A) and progesterone (B) on KCl-contracted arteries in presence or absence of the following different potassium channel inhibitors: glibenclamide (GLI; 10 μmol/L); 4-aminopyridine (4-AP; 1 mmol/L); and tetraethylammonium (TEA; 1 mmol/L). Each point represents the mean value±SEM (indicated in vertical bars) from the number of experiments shown in brackets.

However, mifepristone and ICI 182,780 did not alter the relaxant effects of PRG or βES, respectively, because the IC_{50} values obtained in the absence and in the presence of these antagonist were similar (P>0.05, Student's t-test; Table 1). These results indicated that the vasorelaxant effects of βES and PRG are not mediated by classical hormonal receptor activation.

Effects of βES and PRG on $I_{Ca,L}$ in A7r5 cells

The whole-cell patch clamp technique was used to analyse calcium current through the LTCC ($I_{Ca,L}$) in A7r5 cells. The mean value of basal $I_{Ca,L}$ density was of 0.90±0.05 pA/pF (n=70). The application of BAY (10 nmol/L; specific stimulator of LTCC) significantly stimulated the calcium current by 97.7%±8.3% (n=17) above the basal level. On the contrary, nifedipine (0.1 μmol/L; LTCC inhibitor) significantly reduced the basal $I_{Ca,L}$ until a level of 24.3%±4.5% (n=7) of the basal activity (P<0.05). The effects of BAY and/or nifedipine were completely reversible upon washout of the drug (data not shown). These results indicate that the current measured was due to the LTCC.

Like a proposed vasodilatation mechanism of the female sex hormones is the inhibition of LTCC, we tested the effect of βES or PRG on the $I_{Ca,L}$. The Figure 3A shows a typical experiment in which different concentrations of βES (1–100 μmol/L) inhibited the basal $I_{Ca,L}$ in a reversible manner. Concerning PRG, Figure 3B shows a typical experiment in which PRG (1–100 μmol/L) almost completely inhibits the basal $I_{Ca,L}$. The data obtained in this type of experiments demonstrate that PRG (1–100 μmol/L) inhibits the basal $I_{Ca,L}$. Thus, PRG seems to have similar effects with βES on basal $I_{Ca,L}$ (P>0.05, Student's

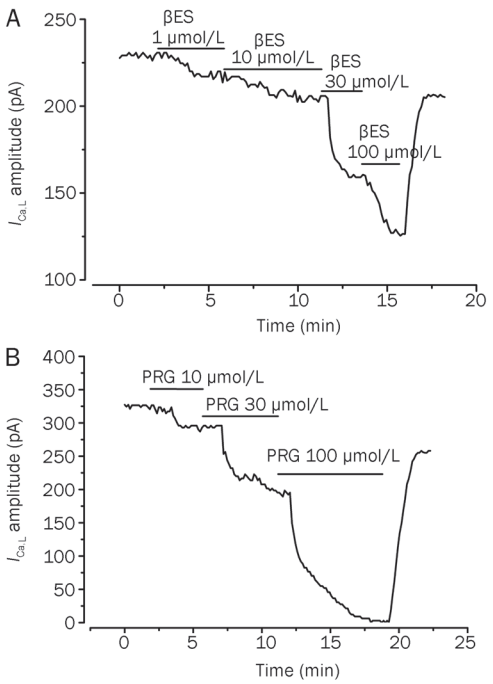

Figure 3. Original records showing the effect of increasing concentrations of 17β-estradiol (A) and progesterone (B) on basal $I_{Ca,L}$ amplitudes measured in patch-clamp experiments performed with A7r5 cells.

t-test).

To further characterize the effect of βES on these channels, we analyse their effect on the BAY-stimulated $I_{Ca,L}$. Figure 4A shows a typical experiment in which βES reversibly inhibited the $I_{Ca,L}$ stimulated by BAY (10 nmol/L) and this inhibitory effect was dependent on the concentration. The maximal effect of βES was an inhibition of 53.8%±11.8% on the BAY-stimulated $I_{Ca,L}$ (Figure 5B). Concerning PRG effect, we also analyse its effect on the $I_{Ca,L}$ stimulated by BAY (Figure 4B). PRG also inhibited BAY-stimulated $I_{Ca,L}$. At a concentration of 100 μmol/L, PRG almost completely inhibited the stimulation of BAY and reduced the $I_{Ca,L}$ below the basal level (Figure 5B).

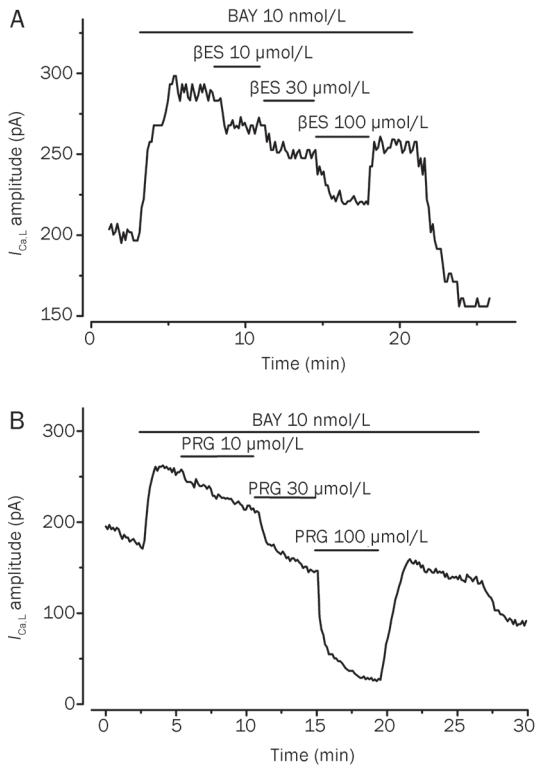

Figure 4. Original records showing the effect of increasing concentrations of 17β-estradiol (A) and progesterone (B) on BAY-stimulated $I_{Ca,L}$ amplitudes measured in patch-clamp experiments performed with A7r5 cells.

A comparison between the effects of both hormones showed that the effects of βES and PRG on BAY-stimulated $I_{Ca,L}$ are similar (P>0.05, Student's *t*-test). On the other hand, ethanol (0.001%–0.1%), the vehicle used to dissolve βES and PRG did not affect basal or stimulated $I_{Ca,L}$ (data not shown).

Effects of βES and PRG on I_K in A7r5 cells

The whole-cell patch clamp technique was used to analyse potassium current (I_K) in A7r5 cells. The mean value of basal I_K density was of 6.1±0.7 pA/pF (n=37). In order to determine the types of K^+ channels that were responsible for the total potassium current measured, we used selective blockers of different channels. The K_V channel blocker 4-AP reduced basal I_K by 37.4%±2.5% at +60 mV. TEA (1 mmol/L), which is used as a BK_{Ca} channel blocker, reduced net current by 38.3%±3.9% at +60 mV (Figure 6). We also tested the presence of the low conductance K_{Ca} channels using the selective blocker apamin (10 μmol/L), which induced a small reduction on the basal I_K (11.7%±3.8%, n=9). Glibenclamide, usually used as a K_{ATP} channel blocker also induced a small reduction on the I_K (8.3%±0.7%, n=6) (Figure 6). The effects of the K^+ channels blockers used were completely reversible upon washout of the drug. Thus, our data suggest that the potassium current measured is mainly constituted by potassium exit through K_V and BK_{Ca} channels.

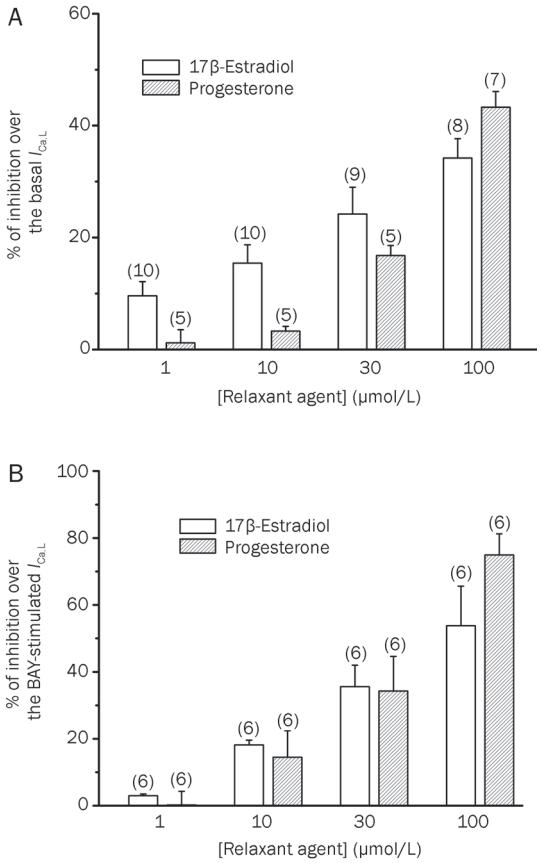

Figure 5. Inhibitory effect (% of reduction) of 17β-estradiol and progesterone on basal $I_{Ca,L}$ (A) and BAY-stimulated (10 nmol/L) (B) $I_{Ca,L}$ in A7r5 cells. Each column represents the mean value±SEM (indicated in vertical bars), in percent of the basal (A) or BAY-stimulated (B) $I_{Ca,L}$ from the number of experiments shown in brackets.

Discussion

In the present study, we analyzed the vascular responses

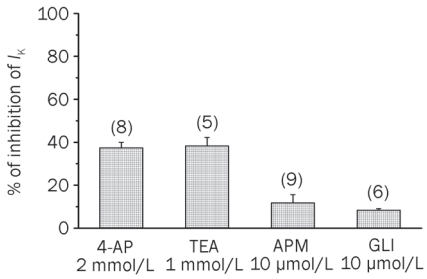

Figure 6. Inhibition of I_K (% of reduction) induced by different potassium channel inhibitors in A7r5 cells. The bars represent the effect on I_K of the following potassium channel blockers: the K_V channel blocker 4-aminopyridine (4-AP; 2 mmol/L); the BK_{Ca} channel blocker tetraethylammonium (TEA; 1 mmol/L); the low conductance K_{Ca} channels blocker apamin (APM, 10 μmol/L); and the K_{ATP} channel blocker glibenclamide (GLI; 10 μmol/L). Each column represents the mean value±SEM (indicated in vertical bars), in percence of the inhibition of I_K from the number of experiments shown in brackets.

Table 2. Inhibitory effect of the basal potassium current (% of basal I_K) induced by 17β-estradiol and progesterone (1–100 μmol/L) on A7r5 cells. Each value represents the mean of the % of variation of basal I_K±SEM from the number of experiments shown in the brackets.

Concentration	17 β-Estradiol	Progesterone
1 μmol/L	2.1%±2.4% (*n*=5)	-1.4%±3.8% (*n*=8)
10 μmol/L	-1.1%±5.7% (*n*=6)	1.8%±3.1% (*n*=7)
30 μmol/L	-3.7%±2.8% (*n*=5)	-0.9%±4.3% (*n*=5)
100 μmol/L	-2.1%±3.2% (*n*=5)	-3.8%±0.8% (*n*=5)

of βES and PRG in endothelium-denuded aorta from male adult rats and their effects on the $I_{Ca,L}$ and I_K measured by whole cell voltage-clamp in A7r5 cells. The female hormones (1–100 μmol/L) equally relaxed, in a rapid and concentration-dependent manner, the aortic rings contracted with KCl or BAY, suggesting an inhibitory effect on voltage-dependent Ca^{2+} influx currents. These voltage-dependent slow inactivated inward currents were measured in A7r5 cells and were characterised electrophysiologically and pharmacologically as $I_{Ca,L}$. The sex hormones studied, βES and PRG, inhibited the basal and BAY-stimulated $I_{Ca,L}$. On the other hand, the vasorelaxant effects of βES and PRG on rat aorta were not mediated by classic hormone receptors or by K^+ channels opening. This data, obtained performing contractility experiments, were also confirmed using the whole cell configuration of the patch clamp, which show that βES and PRG failed to stimulate I_K in A7r5 cells. Therefore, altogether, our results demonstrated a non-genomic inhibitory effect induced by βES and PRG on LTCC that seems to be the responsible for the endothelium-independent vasorelaxant effect of these hormones.

The vasorelaxant effects of βES and PRG on aortic rings contracted with KCl were dose-dependent (1 and 100 μmol/L) and the maximal relaxation achieved with the hormones was 100%. Because we studied the effect of these hormones at the smooth muscle level, the vascular endothelium was previously removed. Previous studies have shown the vasorelaxant effect of the female sex hormones in rat aorta, but there is no consensus about the mechanistic pathway involved in this action. Some authors defended a main role of the endothelium in the relaxant effects of these hormones[1, 9]. Our results demonstrate that there is a relaxant effect independent of the endothelium. These data agree with the that obtained by Perusquia *et al* using PRG in rat thoracic aorta[35]. Also, Unemoto *et al* described a vasorelaxant effect of βES and PRG on agonist-induced contractions in the aorta of Wistar-Kyoto and spontaneously hypertensive rats[12]. For these authors, the vasorelaxant effect of βES seemed to be more gifted than PRG, however they did not find statistical differences between the IC_{50} values calculated for the inhibitory action of the female hormones. In opposition, Rodriguez *et al* showed that 17α-estradiol, but not βES, relaxes calcium-dependent contractions in rat aortic strip[36]. On the other hand, we previously showed that testosterone and cholesterol also relax rat aorta by inhibiting LTCC[37]. Thus, in the sense, the vasodilator effect of cholesterol, testosterone, βES and PRG seems to be similar.

The relaxant effect induced by βES and PRG on the contractions induced by KCl or by BAY is similar, which, attending to the mode of action of both drugs, suggests that these hormones inhibit Ca^{2+} influx into vascular smooth muscle cells. High extracellular KCl concentrations induce plasmatic membrane depolarization, which activates the Ca^{2+} entry by VOCCs (mainly LTCC) and this leads to muscle contraction. BAY directly and specifically opens LTCC and induces vascular smooth muscle contraction also due to intracellular Ca^{2+} elevation. Thus, βES and PRG inhibited KCl and BAY-induced contractions and presumably inhibit Ca^{2+} influx through LTCC. This hypothesis was also supported by other investigators that studied the sex steroids effects in rat aorta[12, 38] and in other arteries[15, 23, 39].

Activation of K^+ channels in vascular smooth muscle may induce repolarization of the plasma membrane, which leads to close VOCCs and contributes to vascular relaxation. To test the possible implication of this pathway in the vascular effects of βES and PRG we used inhibitors of these channels: TEA (BK_{Ca} channels inhibitor), glibenclamide (K_{ATP} channels inhibitor) and 4-aminopyridine (K_V channel inhibitor). None of them significantly modified the rat aorta relaxant effects of βES or PRG, suggesting that potassium channel opening is not involved in the vascular action of these hormones. This conclusion may not surprise for PRG because its vascular effects were never associated to the potassium channel activation[12, 29]. However, in rat cerebral arteries, βES seems to enhance nitric oxide production from vascular endothelium and, by this way, activate BK_{Ca}[40]. According to Unemoto *et al*, the relaxation induced by βES in aortas from spontaneously hypertensive rats is, at least partially, mediated via K_{ATP} and K_V channels stimulation in addition to Ca^{2+} influx blockage[12]. Nevertheless, these authors suggest that the K^+ channels stimulation by βES does not occur in aorta of Wistar rats. Other authors dem-

onstrate that βES can activate BK_{Ca} channels and induce artery relaxation in human coronary artery smooth muscle cell[31] and in rat coronary arteries[8]. On the contrary, potassium currents can be attenuated in transfected HEK293 cells by 17alpha-estradiol or by βES, an effect that could be mediated by estrogen-induced proteasomal degradation of the channels[34]. To further investigate the effect of βES and PRG on the K^+ channels, we performed patch clamp studies in A7r5 cells. The potassium current measured was significantly inhibited by the K_V channel blocker (4-AP) and by the BK_{Ca} channel blocker (TEA), but the SK_{Ca} (low conductance) channel blocker (apamine) and the K_{ATP} channel blocker (glibenclamide) did not have a significant effect on the potassium current measured. In agreement with previous data[37], our study show that the potassium current measured in A7r5 cells is mainly due to K_V and BK_{Ca} channels. On the other hand, for the first time our study also demonstrates that βES and PRG fail to stimulate I_K in A7r5 cells. These data confirm the contractility data and demonstrate that K^+ channels are not implicated in the vasorelaxant effect of βES and PRG in rat aorta.

The blockage of the intracellular receptors for βES and PRG did not modify significantly the vasorelaxant action of these hormones, demonstrating that their intracellular receptors are not involved in the vascular effects induced by these hormones. This fact was previously observed by other authors[23, 38]. On the contrary, it has been described that the antiprogestin mifepristone reduced the PRG-induced relaxation on human placental arteries and veins, suggesting a classic receptor-activated mechanism for PRG in these vessels[41]. Furthermore, Han *et al* showed that βES activates K^+ channels is due to the activation of the intracellular alpha receptor for estradiol[31]. On the other hand, the relaxation induced by mifepristone on KCl-contracted arteries was never referred by other authors. However, a similar effect in rat aorta was described for flutamide, a specific antagonist of the intracellular testosterone receptor[42, 43]. To explain this effect of flutamide, Iliescu *et al* suggested the involvement of the NO-cGMP pathway activation[42]. Also, Ba *et al* also observed this effect in rat arteries and a bigger relaxation in arteries from males than from females, suggesting a sex dependent mechanism for the flutamide effect[43].

To further investigate the effects of the female sex hormones on calcium channels, we performed patch clamp studies in A7r5 cells. The characterisation of the I_{Ca} was made by analysing the effect of BAY, a known agonist of this type of channels, which clearly stimulate the basal I_{Ca}, and nifedipine, a selective antagonist of LTCC, that significantly blocked either basal or BAY-stimulated calcium current. These data confirm that calcium current measured is due to calcium entry through LTCC ($I_{Ca,L}$). Concerning the βES and PRG effects in the calcium currents, our results revealed a rapid concentration-dependent inhibitory effect on basal $I_{Ca,L}$, which indicates that these sex hormones have the ability to block LTCC. These results agree with previously report by Zhang *et al*, that showed an inhibitory effect of βES on the basal $I_{Ca,L}$ in A7r5 cells[26]. Nakagima *et al* determined that, while βES (10 μmol/L) inhibited basal $I_{Ca,L}$ in A7r5 cells, PRG (30 μmol/L) failed to affect these current[21]. In agreement with our results, these authors indicated that the inhibitory effect of βES on LTCC was already significant at a concentration of 10 μmol/L. Our results showed a more powerful effect of PRG than βES at high concentrations (100 μmol/L). The inhibition of LTCC current by PRG in A7r5 cells is here reported for the first time, although Zhang *et al* observed in rat tail vascular smooth muscle cells that PRG reduced the LTCC[25]. We already studied the effect of PRG and βES on the BAY-stimulated $I_{Ca,L}$. We show for the first time that PRG and βES inhibit BAY-stimulated $I_{Ca,L}$, confirming the inhibitory properties of these hormones on rat aorta LTCC.

The action of sex steroids on the genetic protein expression is due to diffusion of these molecules across the cell membrane that, afterwards, bind to specific intracellular receptors that regulate this expression as genetic transcription factors[44]. Therefore, this action needs some time to produce physiological effects. On the contrary, the inhibitory effects of βES and PRG observed in this study were rapid and reversible, because the effects disappeared after drug washing. Some author already described the existence of a non-genomic mechanism for some sex steroids through which the hormones can regulate the vascular tone[45, 46]. Our study also demonstrates that the effects of βES and PRG are mediated by a non-genomic pathway. Furthermore, the vasodilator effects of these female hormones are not mediated by their intracellular receptors and further investigations are needed to identify the pathway involved in this effect. In these sense, recent data have suggested that the sex steroids receptors are distributed at the membrane surface, throughout the cytosol, in the mitochondria and in the nucleus of the cells. However there is controversy regarding the exact characterization of membrane estrogen receptors. Some studies suggested the activation of the membrane surface receptors, for example, the receptor GPR30, that may activate multiple effects, including adenylate cyclase, Scr and spingosine kinases[47–49]. Other authors suggested a direct modulation of the ionic channels by steroids[1]. In this sense, further studies must be done to clarify the mechanism of non-genomic action of sex hormones on vascular tissue.

In summary, our results showed for the first time an inhibition on $I_{Ca,L}$ induced by βES and PRG in vascular smooth muscle cells, which supports and confirms the observed vasorelaxant effects of these hormones in rat aortic rings. These sex steroids inhibit basal and BAY-stimulated $I_{Ca,L}$. This blockage of LTCC will reduce intracellular free Ca^{2+} concentration and is responsible of the rat aorta relaxation. Our data also correlate with the idea of a rapid relaxant effect of βES and PRG through a mechanism independent of the endothelium and not mediated by intracellular receptors or by potassium channel activation.

The results of this study help to further understand the non-genomic vasodilator mechanism of sex hormones. Moreover, the accumulating evidences about the cardiovascular effects of sex hormones provide promising data about their role in preventing and retaining the progression of cardiovascular diseases.

Acknowledgements

We thank the FCT (Fundação para a Ciência e a Tecnologia) which supported the fellowships SFRH/BPD/14458/2003 and SFRH/BDE/15532/2004.

Author contribution

Ezequiel ALVAREZ: designed research, performed research, analyzed data; João Miguel CARVAS: performed research; Antonio Jose SANTOS-SILVA: contributed; Ignacio VERDE: designed research, wrote the paper.

Abbreviations

BAY, (–)-Bay K8644; βES, 17β-estradiol; BK_{Ca}, large conductance Ca^{2+}-activated K^+ channels; FBS, foetal bovine serum; I_{Ca}, voltage-dependent Ca^{2+} current; LTCC, L-type Ca^{2+} channels; PRG, progesterone; VOCCs, voltage-operated Ca^{2+} channels.

References

1 Miller VM. Sex-based differences in vascular function. Womens Health (Lond Engl) 2010; 6 : 737–52.
2 Masood DE, Roach EC, Beauregard KG, Khalil RA. Impact of sex hormone metabolism on the vascular effects of menopausal hormone therapy in cardiovascular disease. Curr Drug Metab 2010; 11: 693–714.
3 Davis SR, Panjari M, Stanczyk FZ. Clinical review: DHEA replacement for postmenopausal women. J Clin Endocrinol Metab 2011; 96: 1642–53.
4 Liu PY, Death AK, Handelsman DJ. Androgens and cardiovascular disease. Endocr Rev 2003; 24 : 313–40.
5 Kim JK, Levin ER. Estrogen signaling in the cardiovascular system. Nucl Recept Signal 2006; 4: e013.
6 Orshal JM, Khalil RA. Gender, sex hormones, and vascular tone. Am J Physiol Regul Integr Comp Physiol 2004; 286: R233–49.
7 Edwards DP. Regulation of signal transduction pathways by estrogen and progesterone. Annu Rev Physiol 2005; 67: 335–76.
8 Santos RL, Marin EB, Goncalves WL, Bissoli NS, Abreu GR, Moyses MR. Sex differences in the coronary vasodilation induced by 17 beta-oestradiol in the isolated perfused heart from spontaneously hypertensive rats. Acta Physiol (Oxf) 2010; 200: 203–10.
9 Lekontseva O, Chakrabarti S, Jiang Y, Cheung CC, Davidge ST. Role of neuronal nitric oxide synthase in estrogen-induced relaxation in rat resistance arteries. J Pharmacol Exp Ther 2011; 339: 367–75.
10 Crews JK, Khalil RA. Antagonistic effects of 17-estradiol, progesterone, and testosterone on Ca^{2+} entry mechanisms of coronary vasoconstriction. Arterioscler Thromb Vasc Biol 1999; 19: 1034–40.
11 Barbagallo M, Dominguez LJ, Licata G, Shan J, Bing L, Karpinski E, *et al*. Vascular effects of progesterone : role of cellular calcium regulation. Hypertension 2001; 37: 142–7.
12 Unemoto T, Honda H, Kogo H. Differences in the mechanisms for relaxation of aorta induced by 17beta-estradiol or progesterone between normotensive and hypertensive rats. Eur J Pharmacol 2003; 472: 119–26.
13 Castillo C, Ceballos G, Rodriguez D, Villanueva C, Medina R, Lopez J, *et al*. Effects of estradiol on phenylephrine contractility associated with intracellular calcium release in rat aorta. Am J Physiol Cell Physiol 2006; 291: C1388–94.
14 Barton M, Cremer J, Mugge A. 17Beta-estradiol acutely improves endothelium-dependent relaxation to bradykinin in isolated human coronary arteries. Eur J Pharmacol 1998; 362: 73–6.
15 Salom JB, Burguete MC, Perez-Asensio FJ, Torregrosa G, Alborch E. Relaxant effects of 17-beta-estradiol in cerebral arteries through Ca^{2+} entry inhibition. J Cereb Blood Flow Metab 2001; 21: 422–9.
16 Belfort MA, Saade GR, Suresh M, Vedernikov YP. Effects of estradiol-17 beta and progesterone on isolated human omental artery from premenopausal nonpregnant women and from normotensive and preeclamptic pregnant women. Am J Obstet Gynecol 1996; 174: 246–53.
17 Kocic I, Szczepanska R, Wapniarska I. Estrogen-induced relaxation of the rat tail artery is attenuated in rats with pulmonary hypertension. Pharmacol Rep 2010; 62: 95–9.
18 Keung W, Man RY. Circulating sex hormones modulate vascular contractions and acute response to 17beta-estradiol in rat mesenteric arteries. Pharmacology 2011; 88: 55–64.
19 Keung W, Chan ML, Ho EY, Vanhoutte PM, Man RY. Non-genomic activation of adenylyl cyclase and protein kinase G by 17beta-estradiol in vascular smooth muscle of the rat superior mesenteric artery. Pharmacol Res 2011; 64: 509–16.
20 McFadzean I, Gibson A. The developing relationship between receptor-operated and store-operated calcium channels in smooth muscle. Br J Pharmacol 2002; 135: 1–13.
21 Nakajima T, Kitazawa T, Hamada E, Hazama H, Omata M, Kurachi Y. 17beta-Estradiol inhibits the voltage-dependent L-type Ca^{2+} currents in aortic smooth muscle cells. Eur J Pharmacol 1995; 294: 625–35.
22 Okabe K, Inoue Y, Soeda H. Estradiol inhibits Ca^{2+} and K^+ channels in smooth muscle cells from pregnant rat myometrium. Eur J Pharmacol 1999; 376: 101–8.
23 Hill BJ, Gebre S, Schlicker B, Jordan R, Necessary S. Nongenomic inhibition of coronary constriction by 17ss-estradiol, 2-hydroxyestradiol, and 2-methoxyestradiol. Can J Physiol Pharmacol 2010; 88: 147–52.
24 Li HF, Zheng TZ, Li W, Qu SY, Zhang CL. Effect of progesterone on the contractile response of isolated pulmonary artery in rabbits. Can J Physiol Pharmacol 2001; 79: 545–50.
25 Zhang M, Benishin CG, Pang PK. Rapid inhibition of the contraction of rat tail artery by progesterone is mediated by inhibition of calcium currents. J Pharm Pharmacol 2002; 54: 1667–74.
26 Zhang F, Ram JL, Standley PR, Sowers JR. 17beta-Estradiol attenuates voltage-dependent Ca^{2+} currents in A7r5 vascular smooth muscle cell line. Am J Physiol 1994; 266: C975–80.
27 Ruehlmann DO, Steinert JR, Valverde MA, Jacob R, Mann GE. Environmental estrogenic pollutants induce acute vascular relaxation by inhibiting L-type Ca^{2+} channels in smooth muscle cells. FASEB J 1998; 12: 613–9.
28 De Wet H, Allen M, Holmes C, Stobbart M, Lippiat JD, Callaghan R. Modulation of the BK channel by estrogens: examination at single channel level. Mol Membr Biol 2006; 23: 420–9.
29 Tsang SY, Yao X, Chan HY, Wong CM, Chen ZY, Au CL, *et al*. Contribution of K^+ channels to relaxation induced by 17beta-estradiol but not by progesterone in isolated rat mesenteric artery rings. J Cardiovasc Pharmacol 2003; 41: 4–13.
30 White RE, Han G, Maunz M, Dimitropoulou C, El-Mowafy AM, Barlow RS, *et al*. Endothelium-independent effect of estrogen on Ca^{2+}-activated K^+ channels in human coronary artery smooth muscle cells. Cardiovasc Res 2002; 53: 650–61.
31 Han G, Yu X, Lu L, Li S, Ma H, Zhu S, *et al*. Estrogen receptor alpha mediates acute potassium channel stimulation in human coronary artery smooth muscle cells. J Pharmacol Exp Ther 2006; 316: 1025–30.
32 Khalil RA. Sex hormones as potential modulators of vascular function in hypertension. Hypertension 2005; 46: 249–54.

33 Qiao X, McConnell KR, Khalil RA. Sex steroids and vascular responses in hypertension and aging. Gend Med 2008; 5 Suppl A: S46–S64.
34 Korovkina VP, Brainard AM, Ismail P, Schmidt TJ, England SK. Estradiol binding to maxi-K channels induces their down-regulation via proteasomal degradation. J Biol Chem 2004; 279: 1217–23.
35 Perusquia M, Hernandez R, Morales MA, Campos MG, Villalon CM. Role of endothelium in the vasodilating effect of progestins and androgens on the rat thoracic aorta. Gen Pharmacol 1996; 27: 181–5.
36 Rodriguez J, Garcia de Boto MJ, Hidalgo A. Mechanisms involved in the relaxant effect of estrogens on rat aorta strips. Life Sci 1996; 58 : 607–15.
37 Alvarez E, Cairrao E, Morgado M, Morais C, Verde I. Testosterone and cholesterol vasodilation of rat aorta involves L-type calcium channel inhibition. Adv Pharmacol Sci 2010; doi:10.1155/2010/534184.
38 Glusa E, Graser T, Wagner S, Oettel M. Mechanisms of relaxation of rat aorta in response to progesterone and synthetic progestins. Maturitas 1997; 28: 181–91.
39 Salom JB, Burguete MC, Perez-Asensio FJ, Centeno JM, Torregrosa G, Alborch E. Acute relaxant effects of 17-beta-estradiol through non-genomic mechanisms in rabbit carotid artery. Steroids 2002; 67: 339–46.
40 Geary GG, Krause DN, Duckles SP. Estrogen reduces myogenic tone through a nitric oxide-dependent mechanism in rat cerebral arteries. Am J Physiol 1998; 275: H292–300.
41 Omar HA, Ramirez R, Gibson M. Properties of a progesterone-induced relaxation in human placental arteries and veins. J Clin Endocrinol Metab 1995; 80: 370–3.
42 Iliescu R, Campos LA, Schlegel WP, Morano I, Baltatu O, Bader M. Androgen receptor independent cardiovascular action of the antiandrogen flutamide. J Mol Med 2003; 81: 420–7.
43 Ba ZF, Wang P, Kuebler JF, Rue LW, 3rd, Bland KI, Chaudry IH. Flutamide induces relaxation in large and small blood vessels. Arch Surg 2002; 137: 1180–6.
44 Truss M, Beato M. Steroid hormone receptors: interaction with deoxyribonucleic acid and transcription factors. Endocr Rev 1993; 14 : 459–79.
45 Simoncini T, Genazzani AR. Non-genomic actions of sex steroid hormones. Eur J Endocrinol 2003; 148: 281–92.
46 Simoncini T, Mannella P, Fornari L, Caruso A, Varone G, Genazzani AR. In vitro effects of progesterone and progestins on vascular cells. Steroids 2003; 68: 831-6.
47 Prossnitz ER, Arterburn JB, Smith HO, Oprea TI, Sklar LA, Hathaway HJ. Estrogen signaling through the transmembrane G protein-coupled receptor GPR30. Annu Rev Physiol 2008; 70: 165–90.
48 Filardo E, Quinn J, Pang Y, Graeber C, Shaw S, Dong J, *et al*. Activation of the novel estrogen receptor G protein-coupled receptor 30 (GPR30) at the plasma membrane. Endocrinology 2007; 148: 3236–45.
49 Haas E, Bhattacharya I, Brailoiu E, Damjanovic M, Brailoiu GC, Gao X, *et al*. Regulatory role of G protein-coupled estrogen receptor for vascular function and obesity. Circ Res 2009; 104: 288–91.

Acta Pharmacologica Sinica (2012) 33: 625–634
 1671-4083/12 $32.00
www.nature.com/aps

Original Article

Raisanberine protected pulmonary arterial rings and cardiac myocytes of rats against hypoxia injury by suppressing NADPH oxidase and calcium influx

Jie GAO#, Yi-qun TANG#, De-zai DAI*, Yu-si CHENG, Guo-lin ZHANG, Can ZHANG, Yin DAI

Research Division of Pharmacology, China Pharmaceutical University, Nanjing 210009, China

Aim: To investigate the protection of pulmonary arterial rings and cardiac myocytes of rats by raisanberine (RS), a derivative of berberine, against hypoxia injury and to elucidate the action mechanisms.
Methods: Adult SD rats were exposed to intermittent hypoxia for 17 d or 28 d. The pulmonary arterial rings were isolated and vascular activity was measured using a transducer and computer-aided system. The difference in the tension produced by phenylephrine in the presence and absence of *L*-nitroarginine (10 μmol/L) was referred to as the NO bioavailability; the maximum release of NO was assessed by the ratio of the maximal dilatation caused by ACh to those caused by sodium nitroprusside. After the lungs were fixed, the internal and the external diameters of the pulmonary arterioles were measured using a graphic analysis system. Cultured cardiac myocytes from neonatal rats were exposed to H_2O_2 (10 μmol/L) to mimic hypoxia injury. ROS generation and $[Ca^{2+}]_i$ level in the myocytes were measured using DHE and Fluo-3 fluorescence, respectively.
Results: Oral administration of RS (80 mg/kg), the NADPH oxidase inhibitor apocynin (APO, 80 mg/kg) or Ca^{2+} channel blocker nifedipine (Nif, 10 mg/kg,) significantly alleviated the abnormal increase in the vasoconstriction force and endothelium-related vasodilatation induced by the intermittent hypoxia. The intermittent hypoxia markedly decreased the NO bioavailability and maximal NO release from pulmonary arterial rings, which were reversed by APO or RS administration. However, RS administration did not affect the NO bioavailability and maximal NO release from pulmonary arterial rings of normal rats. RS, Nif or APO administration significantly attenuated the pulmonary arteriole remodeling. Treatment of cultured cardiac myocytes with RS (10 μmol/L) suppressed the ROS generation and $[Ca^{2+}]_i$ increase induced by H_2O_2, which were comparable to those caused by APO (10 μmol/L) or Nif (0.1 μmol/L).
Conclusion: Raisanberine relieved hypoxic/oxidant insults to the pulmonary artery and cardiac myocytes of rats by suppressing activated NADPH oxidase and increased calcium influx.

Keywords: raisanberin; apocynin; nifedipine; hypoxia; pulmonary artery; cardiac myocytes; NADPH oxidase; calcium influx

Acta Pharmacologica Sinica (2012) 33: 625–634; doi: 10.1038/aps.2012.7

Introduction

Pulmonary arterial hypertension (PAH) caused by hypoxia is characterized by a progressive elevation of the resistance of the pulmonary arterial system and insults to the heart; hypoxia causes oxidant lesions that adversely affect cardiac myocytes, contributing in part to right heart failure and increased mortality[1]. The pulmonary vascular endothelium is abnormal after exposure to hypoxia, elevating the pulmonary arterial pressure by enhancing constriction and reducing dilatative activity due to compromised NO availability. Extensive research demonstrates that an excess of ET-1 (endothelin-1) is actively involved in the pathogenesis of PAH and that PAH can be reversed by ET receptor-blocking agents[2, 3].

Endothelium-dependent relaxation depends on the biosynthesis and release of NO by endothelial nitric oxide synthase (eNOS) in the vascular endothelia. The activity of eNOS generates both NO and superoxide (O_2^-), which are key mediators of cellular signaling in regulating vascular activity[4]. Vascular relaxation by NO is counteracted by activated ET_A, resulting in compromised NO bioavailability and a decrease in the eNOS activity, which are related to an excess of reactive oxygen species (ROS), and is likely attributable to activated NADPH oxidase. ET-1 is an inducer of NADPH oxidase mainly through ET_A[5], and the biosynthesis and release of the vascular dilating substance, NO, in vascular endothelia are seriously affected by oxidative stress[6]. The pathogenesis of hypoxic PAH can be characterized by an activated ET pathway, which was relieved

# These authors contributed equally to this work.
* To whom correspondence should be addressed.
E-mail dezaidai@vip.sina.com
Received 2011-08-18 Accepted 2012-01-14

by the ET antagonists CPU0213[7] and CPU86017[8], and its isomers[9] by reducing ET_A expression in the pulmonary vasculature.

NADPH oxidase-derived ROS may play a major role in the pathology of hypoxia-induced PAH[10]. NADPH oxidase belongs to a family of proteins that consist of two groups of subunits, catalytic components, NOX1, $gp91^{phox}$ (NOX2), and NOX4, and modulating components, $p22^{phox}$, $p47^{phox}$, and $p67^{phox}$, which localize separately either at the membrane or in the cytosol[11]. Decreased vasorelaxation is mediated by an upregulated ET system, as found in hypoxic pulmonary arteries[12] and in aortic rings from diabetic rats[13], which are likely the consequence of activated NADPH oxidase enzymes. The insults due to hypoxia are mainly mediated by an increased generation of ROS, and the activation of ET_A is caused by either hypoxia[7, 8] or incubation with H_2O_2[14]. In fact, hypoxia activates NADPH oxidase, causing an increase in ROS production, which stimulates the ET system. The accumulated data suggest that the activity of ET_A is at least in part mediated by activated NADPH oxidase[6] and that an increase in calcium influx may be initiated by H_2O_2 (ROS) as a consequence of hypoxia: an involvement of NADPH oxidase may be critically implicated in the pathology of hypoxia-induced abnormalities of the pulmonary vasculature and cardiac myocytes.

Raisanberine (RS compound, an isomer of CPU86017: [+]-7*R*, 13αS-*p*-chloro-benzyl-tetra-hydro-berberine chloride) is active in reversing the abnormal expression of the ET system in pulmonary artery hypertension in rats[15, 16]. In our previous study, RS improved the remodeling of the pulmonary arterioles[9] and blocked calcium influx through L-type calcium channels[17]; however, it remained uncertain whether raisanberine was capable of reducing ROS generation through the suppression of NADPH oxidase in the pulmonary arterial vasculature and cardiac myocytes.

We hypothesized that an activated NADPH oxidase may be caused by hypoxia and induce abnormal pulmonary arterial activity and intracellular free calcium in cardiac myocytes. H_2O_2-induced abnormalities of intracellular calcium in cardiac myocytes mimic the insults due to hypoxia and are likely due to an activation of NADPH oxidase. The aim of our research was to verify this hypothesis by employing apocynin, an inhibitor of NADPH oxidase, the calcium channel blocker nifedipine, and RS to test their efficacy in alleviating the hypoxia-related abnormalities of pulmonary arteries and cardiac myocytes.

Materials and methods

Experimental animals

Male Sprague-Dawley rats, weighing 220–250 g, were purchased from the Experimental Animal Center of Zhejiang Province, Hangzhou. License No: SCXK (Zhe) 20080033. The procedures involving experimental animals were conducted by personnel trained according to the Experimental Animal Handling Act instituted by the Science-Technology Bureau of Jiangsu Province, China.

Drugs and reagents

Raisanberine (CPU86017-RS, RS) was synthesized and provided by the Department of Medicinal Chemistry, China Pharmaceutical University, Lot 20090301. Nifedipine (Nif) (10 mg/tablets) was obtained from Changzhou Kangpu Pharmaceutical Co, Ltd, Lot 0910004. Apocynin (APO) (white crystalline powder; Lot 122F20340) was obtained from Sigma-Aldrich Chemie GmbH, Steinheim, Germany. DHE and Fluo-3/AM were purchased from Sigma-Aldrich, St Louis, MO, USA.

Exposure to intermittent hypoxia

A total of 110 rats were randomly divided into two experiments: (1) in Exp 1, 4 groups (n=6) were exposed to intermittent hypoxia for 17 d, and in the last 12 d, APO 80 mg/kg and RS 80 mg/kg was administered (*po*); in Exp 2, hypoxic rats were untreated (Hyp) or treated (mg/kg, *po*) with Nif (10), APO (80), RS low dose (RSL, 20), RS medium dose (RSM, 40), or RS high dose (RSH, 80), and normal rats were either untreated (Nor) or received the RS high dose (N+RS, 80); these 8 groups (n=10) received the treatments in the last 14 d of the experiment. According to a previous report[8] we used a hypoxia chamber in which the oxygen fraction was maintained at 10%±0.5% by controlling the N_2 flow into the chamber. The water vapor and carbon dioxide were removed by placing anhydrous calcium chloride and sodium lime in the chamber. The rats were kept in the hypoxic chamber for 8 h per day for 17 and 28 d for Exp 1 and 2, respectively, except for the Nor and N+RS groups. The rats in the Nor, Hyp and N+RS groups were administered the same volume of 0.5% CMC-Na.

Vascular activity of isolated pulmonary arterial rings

The rats were anesthetized with urethane 1.5 g, ip, the chest was opened, and the pulmonary artery was rapidly harvested and placed in cold K-H solution, containing the following (in mmol/L): NaCl 119, $NaHCO_3$ 25, KCl 4.6, KH_2PO_4 1.2, $MgCl_2$1.2, $CaCl_2$ 2.5, and glucose 11, and saturated with 95% O_2+5% CO_2 (2 bubbles/s). The connective tissue surrounding the artery was removed, and the pulmonary artery was cut into rings of 2 mm in width. The rings were fixed by a triangular steel ring to the bottom of a 3 mL organ bath and connected to a transducer and a computer-aided system for real time recordings, as previous reported[8]. The resting tension baseline of the vascular ring was loaded to 0.6–0.7 g. After stabilization for 2 h with 3 tests of norepinephrine at 1 μmol/L, Phe (phenylephrine, 3, 30, and 300 nmol/L) was added in sequence for recordings of the developed tension of the vascular rings. After reaching the plateau, the isolated vascular rings were dilated by adding ACh (acetylcholine, 0.01, 0.1, 1, and 10 μmol/L), and the vascular rings were dilated further by adding SNP (sodium nitroprusside, 10 μmol/L) until reaching the maximum relaxation. After incubating the vascular rings for 15 min with *L*-NA (*L*-nitroarginine, an inhibitor of eNOS, 10 μmol/L), the testing of vascular contraction and relaxation was repeated. The difference in the tension produced by Phe in the presence and absence of *L*-NA was taken as the functional assessment of the NO released from the vascular

endothelium and referred to as the NO bioavailability; the maximum release of NO was assessed by using a functional approach. The relaxation caused by ACh is endothelium dependent and can be considered to represent the maximum release of NO. The ACh-induced relaxation was compared to those caused by SNP which was taken as 100%, therefore, the ability of the pulmonary artery to release NO could be calculated[13, 18].

Morphological analysis of pulmonary arterioles

The lungs were fixed with neutral formalin, embedded in paraffin, and sliced into 4-μm-thick sections (HE stain, ×400). The length of the internal (ID) and the external diameter (ED) of the pulmonary arterioles were measured using a graphic analysis system (IMAGE-PROPLUS [Media Cybernetics, Silver Spring, MD])[9]. The pulmonary arterioles with EDs less than 150 μm were selected, and 10 visual fields for each slide were randomly chosen.

The wall thickness (WT) percentage was calculated as follows:

$$WT(\%)=100\times0.5\times([ED-ID]/ED)$$[9].

ROS in cultured cardiac myocytes

The cardiac myocytes from neonatal rats (48 h) were employed for assessing the fluorescence intensity of ROS when stained with DHE (dihydroethidium), as based on a previous report[19]; the cell density was adjusted to 6×10^5/mL and diluted 3-fold. These cells were then divided into 7 groups: normal (Nor); hypoxic (Hyp, H_2O_2 10 μmol/L was used to mimic an increase in the ROS due to hypoxia exposure); nifedipine (Nif, 0.1 μmol/L); apocynin (APO, 10 μmol/L); RSL (RS, 1 μmol/L); RSM (RS, 3 μmol/L); and RSH (RS, 10 μmol/L). The cardiac myocytes were washed with fresh Tyrode's solution, incubated with DHE (10 μmol/L) under darkness, and then observed using a fluorescence microscope (×100, OLYMPUS, IX71). The fluorescence intensity was evaluated using Image-Pro Plus 6 and compared among the groups.

$[Ca^{2+}]_i$ in cultured cardiac myocytes

The primary cardiac cells isolated from adult rats were employed, and the measurements of $[Ca^{2+}]_i$ were obtained by incubation with fluorescent Fluo-3/AM at 10 μmol/L; the cardiac myocytes were stimulated using electric field stimulation, according to previous reports[20, 21]. The cardiac myocytes were divided into 7 groups: Nor (normal), Hyp (hypoxic injury was mimicked by incubation with H_2O_2 10 μmol/L), Nif (nifedipine, 0.1 μmol/L), APO (apocynin, 10 μmol/L), RSL (0.1 μmol/L), RSM (1 μmol/L) and RSH (10 μmol/L). The incubation with Fluo-3 was performed in the dark, and the fluorescent images of the cells were observed using a fluorescence microscope while the cells were beating due to stimulation with 0.5 Hz, 40 V electric-field stimulation. The fluorescence intensity was measured and recorded using Image-Pro Plus 6. After adding $CaCl_2$ (10 mmol/L) and A23187 (5 mmol/L) into Tyrode's solution, the fluorescence intensity was abruptly increased to reach the maximum and recorded as the F_{max} value. After $MnCl_2$ (5 mmol/L) and A23187 (5 mmol/L) were added, the fluorescence intensity gradually decreased to a certain level and remained unchanged; this was recorded and referred to as F_{min}. The levels of $[Ca^{2+}]_i$ were calculated according to the following formula: $[Ca^{2+}]_i=K_d\times(F-F_{min})/(F_{max}-F)$. The peak (systolic) and trough (diastolic) concentrations of $[Ca^{2+}]_i$ of the beating cardiac myocytes were obtained, and the difference between the two was considered a "change" in the intracellular calcium concentrations in the cardiac cycles. These data were compared among the groups.

Statistical analysis

All of the data were expressed as the mean±SD. Student's *t*-test was used to determine the significant differences between two groups, and a one-way ANOVA was used to evaluate three or more groups. Excel and the Graph Pad Prism 5 programs were used for the statistical analysis, and a value of $P<0.05$ was considered significant.

Results

An increase in constrictive force

Phe was added successively (3, 30, and 300 nmol/L) to induce constriction in the pulmonary arterial rings of the normal and hypoxic groups, and the increase in the developed force was significant ($P<0.01$) in the hypoxic group in Exp 1 and 2 compared with the normal group (Figure 1A–1D). Hypoxia exposure clearly enhanced the constrictive force of the pulmonary arterial rings, thereby increasing vascular resistance in the pulmonary arterial system. The increased vascular resistance caused hypoxia pulmonary artery hypertension. The abnormal increase in the vasocontractile force was reduced ($P<0.01$) by APO, Nif, and RS (Figure 1). RS did not affect the constrictive activity of the normal pulmonary arterial rings.

Impaired endothelium-dependent relaxation

After the vasoconstriction caused by Phe reached a plateau, ACh was added successively (0.01, 0.1, 1, and 10 μmol/L) to relax the pulmonary arterial rings. The endothelium-related vasodilatation was significantly compromised ($P<0.01$) in the hypoxic rats compared to the normal rats and was significantly alleviated by APO, Nif, and RS in Exp 1 and 2 (Figure 2). In contrast, following the addition of SNP 10 μmol/L, the vasorelaxation of vascular smooth muscle was dilated directly and was not impaired in the hypoxic group; therefore, no difference was found among the groups. RS did not cause an increase in the ACh-induced vasorelaxation in normal rats.

Reduced NO bioavailability and maximal NO release

The NO bioavailability was evaluated by vascular activity assessment of the pulmonary arterial rings using two procedures. First, the constrictive responses to three concentrations of Phe were monitored, and the AUC (area under the curve) of the vasoconstrictive force was calculated. Second, the AUC was estimated again after *L*-NA, an inhibitor for eNOS, was added in a separate experiment. The difference of the AUC in the presence and absence of *L*-NA represents the NO bio-

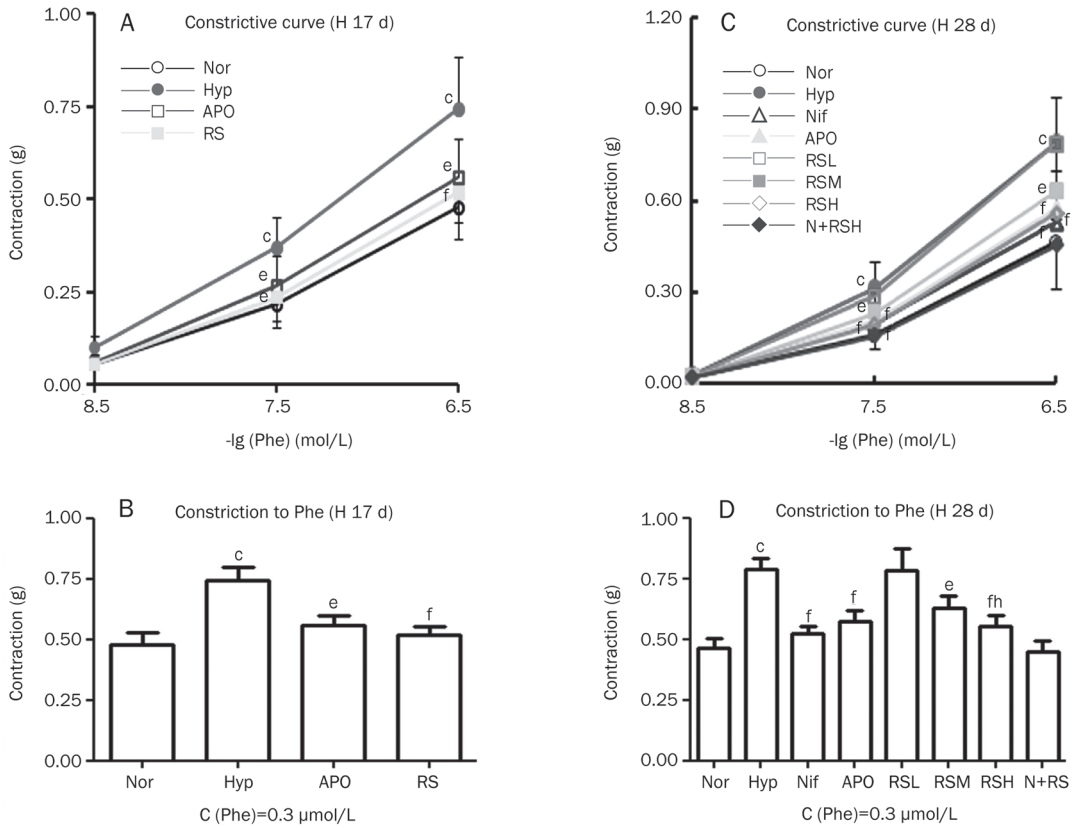

Figure 1. Vascular constrictive activity was increased in the hypoxic pulmonary artery and was alleviated by APO (apocynin), Nif (nifedipine), and RS (CPU86017-RS), respectively. (A, B) Hypoxia for 17 d (H 17 d), (n=6). Nor-normal (○), Hyp-hypoxia (●), APO (apocynin, 80 mg/kg, *po*) (□), RS (RS 80 mg/kg, *po*) (■). (C, D) Hypoxia for 28 d (H 28 d), (n=10). Nor-normal (○); Hyp-hypoxia (●); Nif (nifedipine 10 mg/kg, *po*) (△), APO (apocynin, 80 mg·kg^{-1}, *po*) (▲); RSL (RS 20 mg/kg, *po*) (□), RSM (RS 40 mg/kg, *po*) (■), RSH (RS 80 mg/kg, *po*) (◇); N+RS (normal rats medicated with RS 80 mg/kg, *po*) (◆). Mean±SD. n=6−10. ^{b}P<0.05, ^{c}P<0.01 *vs* Nor. ^{e}P<0.05, ^{f}P<0.01 *vs* Hyp. ^{h}P<0.05 *vs* RSL.

availability: the larger the difference between the two AUC values, the higher the NO availability in the tested artery. The increased constrictive force of the hypoxic pulmonary artery rings in the absence of *L*-NA was due to reduced NO availability in the pulmonary artery, and a smaller increase in the contractile force was observed while *L*-NA was added. NO bioavailability was decreased significantly in the Hyp group (P<0.01 *vs* Nor) in these two experiments and was remarkably increased (P<0.01 *vs* Hyp) after APO and RS interventions. RS did affect the NO bioavailability of the normal group (P>0.05) (Figure 3A, 3C).

Both in Exp 1 and 2, the maximal NO release was decreased significantly in the Hyp group (P<0.01) compared with Nor and a significant recovery in the NO release was found after APO and RS interventions (P<0.01 *vs* Hyp). RS had no effects on the maximum NO release of the normal group (P>0.05) (Figure 3B, 3D).

Remodeling of the pulmonary arterioles

Changes in vascular activity are always associated with a morphological remodeling of the pulmonary vasculature; therefore, the changes in the thickness of vascular smooth muscle in the pulmonary arteriole were examined. A wall thickness (WT) of the pulmonary arterioles less than 150 μm in diameter was evaluated in Exp 1 and 2, and a remodeling of the vasculature, characterized as increased vascular wall thickness, was significant (P<0.01) in the hypoxic rats when compared with the normal rats in Exp 2 (Figure 4A). Similar data from Exp 1 are not shown. Treatment with Nif, APO, and RS (20, 40, and 80 mg/kg) attenuated the pulmonary arteriole remodeling compared to the Hyp group. The reduction of the arteriolar vasculature thickness by RS occurred in a dose-dependent manner, and the RS 80 mg/kg alone did not affect the WT of the pulmonary arterioles in the normal rats (Figure 4A, 6).

Suppression of increased ROS in cultured cardiac cells

ROS generation was enhanced in the cardiac myocytes incubated with H_2O_2, which was suspected to activate NADPH oxidase in the myocytes. Accordingly, we added APO to the medium to determine whether APO could suppress the ROS generation, as labeled with DHE fluorescence in the cardiac cells; we also addressed whether direct evidence of ROS-suppressing activity for RS could be found. Hypoxia damages cells mainly by increasing ROS generation; therefore, isolated cardiac cells of neonate rats were cultured with H_2O_2 (10 μmol/L), which mimics the injury from hypoxia exposure.

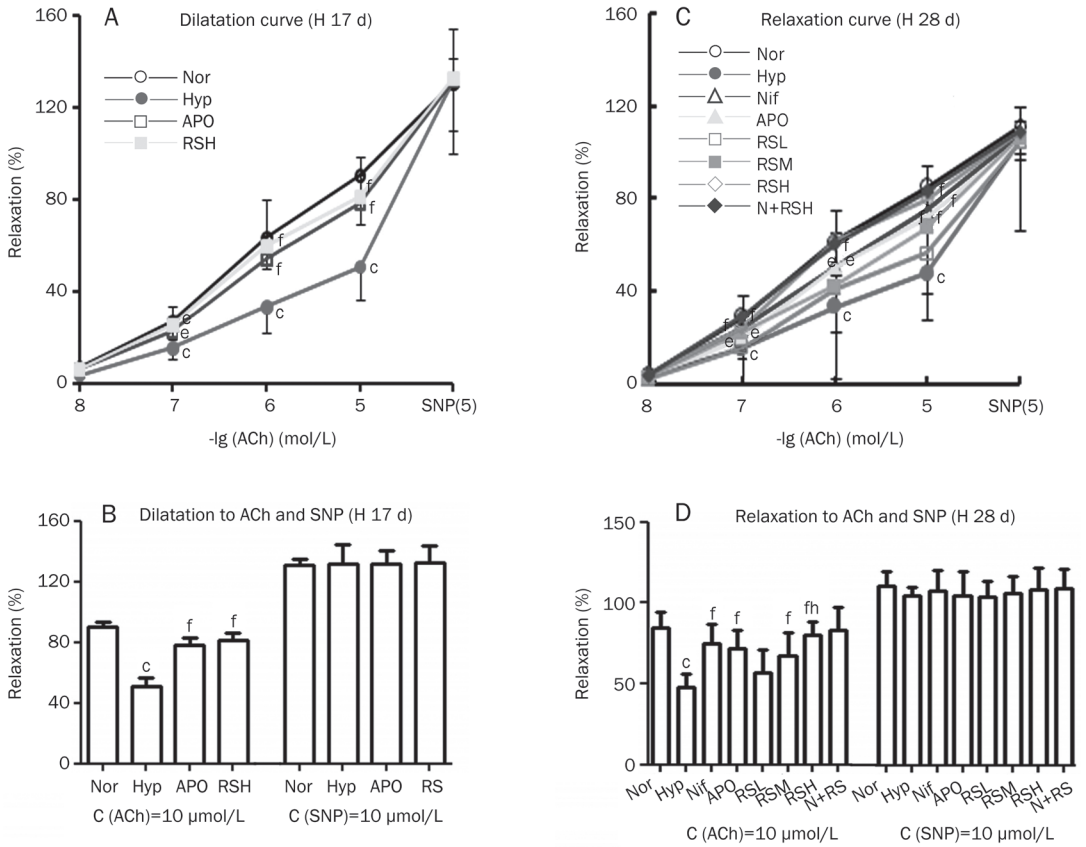

Figure 2. Vascular dilative activity was reduced in the hypoxic pulmonary artery and was alleviated by Nif, APO, and RS, respectively. (A, B) Hypoxia for 17 d (H 17 d) (n=6). Nor (○); Hyp (●); APO (apocynin, 80 mg/kg, *po*, □); RSH (RS 80 mg/kg, *po*, ■). (C, D) Hypoxia for 28 d (H 28 d): (n=10). Nor (○); Hyp (●); Nif (nifedipine 10 mg/kg, *po*, △); APO (apocynin, 80 mg/kg, *po*, ▲); RSL (RS 20 mg/kg, *po*, □); RSM (RS 40 mg/kg, *po*, ■); RSH (RS 80 mg/kg, *po*, ◇); N+RS (normal rats medicated with RS 80 mg/kg, *po*, ◆). Mean±SD. n= 6–10. ^{b}P<0.05, ^{c}P<0.01 *vs* Nor. ^{e}P<0.05, ^{f}P<0.01 *vs* Hyp. ^{h}P<0.05 *vs* RSL.

The fluorescence was significantly exaggerated in the H_2O_2 group (P<0.01), as compared with the normal group, and the exaggerated ROS generation was significantly suppressed (P<0.01) by APO, an inhibitor of NADPH oxidase. Interestingly, the beneficial effects of Nif were also significant. The suppressive effects of RS on ROS generation were positive and comparable to those of APO and Nif (Figure 4B, 6B).

Suppression of intracellular $[Ca^{2+}]_i$

To evaluate the suppression of $[Ca^{2+}]_i$ by APO and RS, the isolated primary cardiac myocytes were cultured with H_2O_2 to mimic hypoxia injury. An abnormal increase of $[Ca^{2+}]_i$ was found in the beating cardiac myocytes with Hyp (hypoxia that was mimicked by adding H_2O_2, P<0.01), as compared with the normal group). The systolic and diastolic values and their changes were significantly enhanced after exposure to H_2O_2, highlighting the likely involvement of an increase in the intracellular calcium in hypoxic pulmonary arteries. The abnormal increase of intracellular calcium was greatly reduced (P<0.01) by the intervention with Nif; however, the effects were reproduced by an NADPH oxidase blocker, APO. RS was found to reduce the enhanced $[Ca^{2+}]_i$ caused by hypoxia, which was comparable to that of Nif and APO (Figure 4C, 5, 6C).

Discussion

We reported previously that the pulmonary artery is more sensitive to hypoxia than the systemic circulation[22]. Chronic hypoxia exaggerates the production of ROS, which likely occurs in multiple steps. ROS are primarily produced from the abnormal electron transport in the mitochondria, and the produced ROS in turn stimulate NADPH oxidase to cause further and sustained ROS production (Figure 7). An excessive production of ET-1, a causal factor contributing to pulmonary hypertension, is stimulated by ROS; in fact, ET_A and ET_B receptors are actively implicated in the pulmonary hypertension caused by either hypoxia[7, 9] or the inflammatory substance, monocrotaline[8, 23]. Emerging data suggest that endothelin receptor antagonists, either selective ET_A blockers or dual ET_A and ET_B blockers, successfully alleviate pulmonary hypertension in both experimental animals and clinical settings[23, 24]. Therefore, ET-1 has been considered the most important factor affecting the pulmonary arterial system and critically impairs vascular activity. In addition, potent vasoconstrictive activity, *eg*, an activated ET_A, reduces the NO bioavailability and maxi-

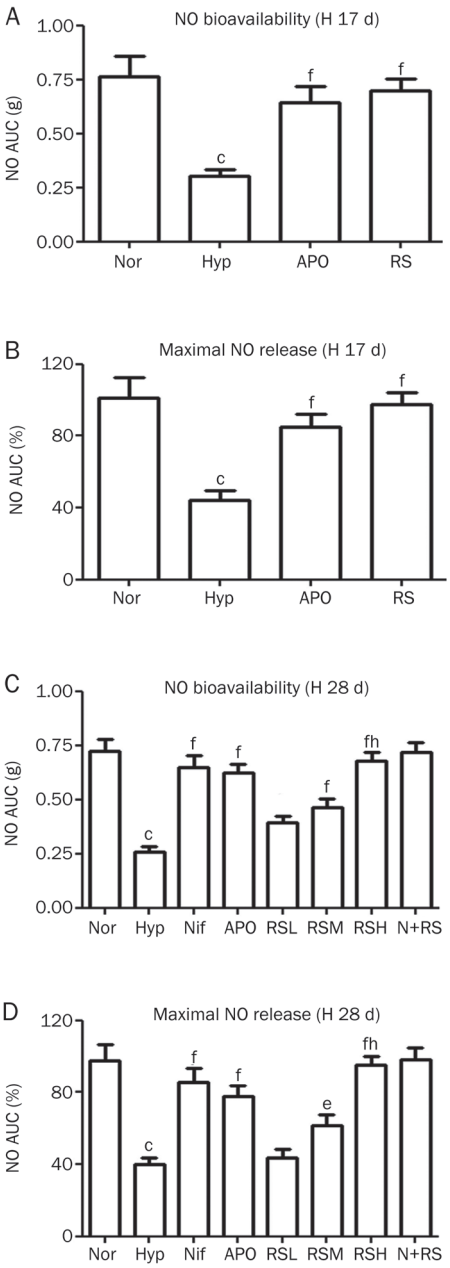

Figure 3. NO bioavailability and maximum NO release estimated functionally were reduced in hypoxic rats, in A, B (Exp 1) and C, D (Exp 2). Interventions with Nif, APO, and RS alleviated these changes significantly. Nor (Normal); Hyp (hypoxia); APO (apocynin, 80 mg/kg, *po*); RSH (RS 80 mg/kg, *po*). (C, D) Hypoxia for 28 d (H 28 d): (n=10). Nor (Normal); Hyp (Hypoxia); Nif (nifedipine 10 mg/kg, *po*); APO (apocynin, 80 mg/kg, *po*); RSL (RS 20 mg/kg, *po*); RSM (RS 40 mg/kg, *po*); RSH (RS 80 mg/kg, *po*); N+RS (normal rats medicated with RS 80 mg/kg, *po*). Mean±SD. n=6–10. ^{c}P<0.01 *vs* Nor. ^{e}P<0.05, ^{f}P<0.01 *vs* Hyp. ^{h}P<0.05 *vs* RSL.

mal NO release from the vascular endothelium, thus exacerbating vascular resistance and remodeling in pulmonary circulation.

The bioactivity of ET-1 is at least in part mediated by NADPH oxidase, these including positive inotropism in the heart and an elevated $[Ca^{2+}]_i$, which is due to an increased frequency of open individual L-type channels; therefore, increased calcium influx is a consequence of the activation of ET_A, and the activation of L-type channels by ET_A is mediated by the activation of NADPH oxidase[25, 26] (Figure 7).

Activated NADPH oxidase is the main source of ROS production, which is evidenced by the appearance of vascular abnormalities upon exposure to intermittent hypoxia and H_2O_2-induced ROS and an increase in the intracellular calcium in cardiomyocytes. NADPH oxidase as an important source of excessive ROS production, providing insight into many diseases, including diabetic nephropathy and cardiomyopathy and pulmonary hypertension[27-29]. In general, an activated NADPH oxidase produces ROS under hypoxic conditions; conversely, ROS serve as important inducers of ET-1, angiotensin, and tumor necrosis factor α, which stimulate NADPH oxidase. Our data are in agreement with our previous report that NADPH oxidase is an important source of ROS production in cardiac fibroblasts[5].

The calcium balance in the pulmonary vascular cells critically modulates the vasoactivity of the pulmonary artery, and an increase in $[Ca^{2+}]_i$ allows an increase in the vascular tone responding to vasoconstrictive agents. An intracellular release of calcium from RyRs (ryanodine receptors) in vascular smooth muscles[30] occurs in response to calcium influx through L-type channels, which is exacerbated by an enhanced influx of calcium, resulting in an increase in $[Ca^{2+}]_i$ in the systolic and diastolic cycles. However, it has been reported that the removal of extracellular Ca^{2+} may not affect the H_2O_2-induced increase in $[Ca^{2+}]_i$[18], indicating that a direct effect of stimulating intracellular Ca^{2+} release could be involved. In the present study, the application of nifedipine, which inhibits calcium influx, was expected to suppress the increased calcium levels by limiting the calcium ions transporting into the cells. L-type calcium channel activation by H_2O_2 (ROS) often follows hypoxemia after the exposure to intermittent hypoxia. In the present study, the increased calcium influx was suppressed by nifedipine and attenuated by the inhibition of NADPH oxidase. We provide direct evidence demonstrating that an activation of NADPH oxidase is also involved in exacerbated calcium influx; thus, by suppressing NADPH oxidase, apocynin treatment leads to a reduction in $[Ca^{2+}]_i$ in the cardiac myocytes. Therefore, as measured by an increase in ROS generation, we provide evidence that the activity of NADPH oxidase is linked to significant calcium influx, implying that a decline in $[Ca^{2+}]_i$ reduces ROS generation, thus preventing the activation of NADPH oxidase under hypoxia[31]. The NADPH oxidase blocker apocynin sufficiently normalizes the exaggerated intracellular calcium in cardiomyocytes. We emphasize that NADPH oxidase modulates the free calcium levels in cardiac myocytes and, thus, participates in the pathogenesis of the cardiomyopathy caused by hypoxemia and contributes to hypoxic pulmonary hypertension (Figure 7).

In conclusion, abnormal vascular activity and the remodeling of pulmonary arterioles are due to the activation of NADPH oxidase under hypoxia, which is linked to activated

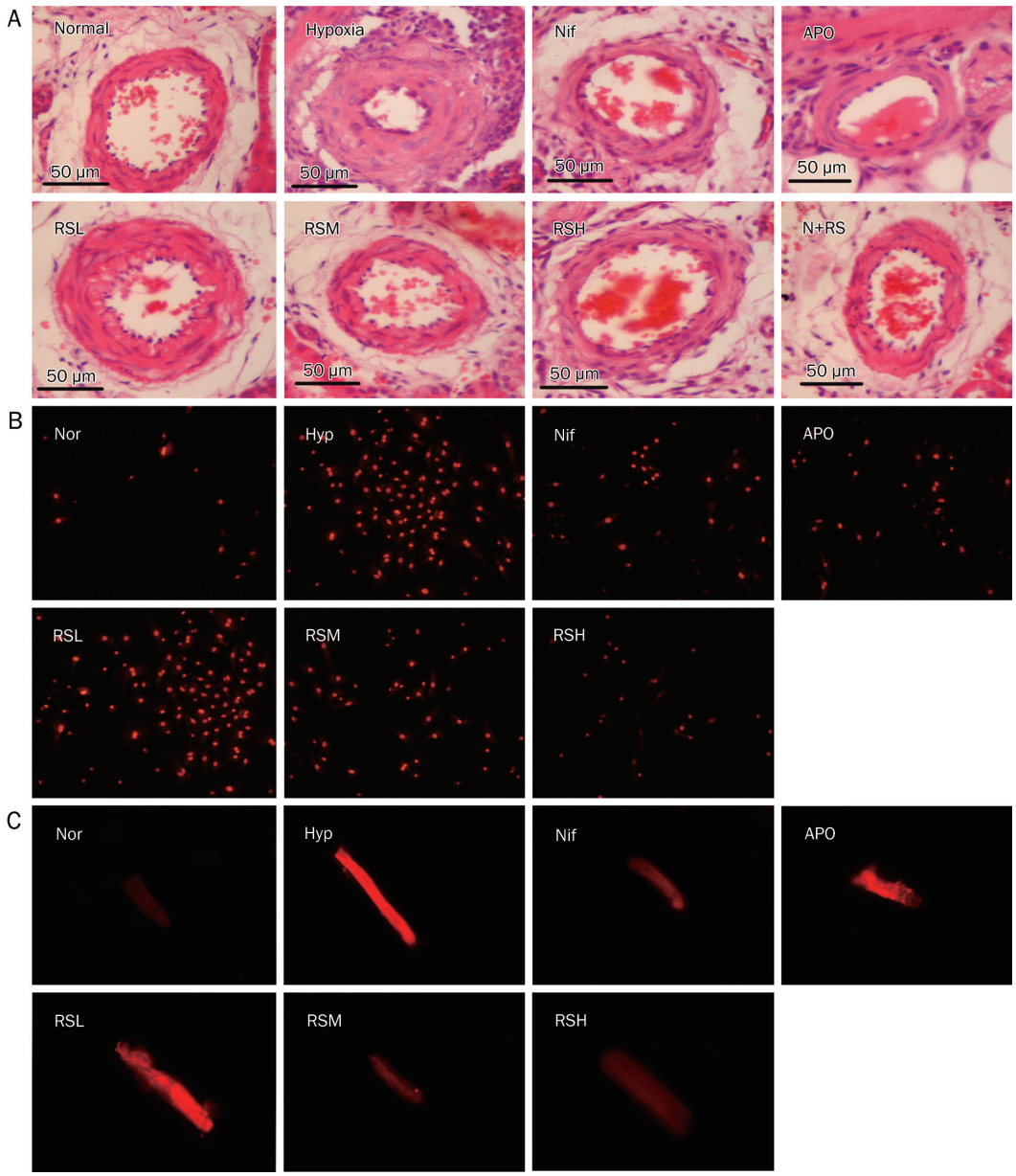

Figure 4. Histological changes of pulmonary arteriolar vascular wall (A), the fluorescent images of DHE for ROS in cardiac cells (B) , and the levels of $[Ca^{2+}]_i$ in cardiac cells (C) were compared. (A) Histological changes of the pulmonary arterioles with external diameter <150 μm (HE staining, ×400). Nor (Normal); Hyp (Hypoxia); Nif (nifedipine 10 mg/kg, *po*); APO (apocynin, 80 mg/kg, *po*); RSL (RS 20 mg/kg, *po*); RSM (RS 40 mg/kg, *po*); RSH (RS 80 mg/kg, *po*); N+RS (normal rats medicated with RS 80 mg/kg, *po*). (B) The fluorescence of dihydroethidium (DHE, 10 μmol/L) in neonate rat cardiac myocytes (×100). Normal (Nor), Hypoxia (Hyp, H_2O_2 10 μmol/L), nifedipine (Nif, 0.1 μmol/L), apocynin (APO, 10 μmol/L), RSL (RS, 1 μmol/L), RSM (RS, 3 μmol/L), RSH (RS, 10 μmol/L). (C) The fluorescent images of intracellular calcium. Normal (Nor), Hypoxia (Hyp, H_2O_2 10 μmol/L), nifedipine (Nif, 0.1 μmol/L), apocynin (APO, 10 μmol/L), RSL (RS 0.1 μmol/L), RSM (RS 1 μmol/L), RSH (RS, 10 μmol/L).

ET_A and a reduction in the bioavailability of NO. Exacerbation of the intracellular calcium levels by H_2O_2 to mimics injury due to hypoxia and can be blocked by apocynin, an inhibitor of NADPH oxidase. Therefore, the inhibition of NADPH oxidase attenuates both the abnormal pulmonary vascular activity and the increase in ROS generation in cardiac myocytes. These abnormalities are normalized by raisanberine, which presumably suppresses the calcium influx and inhibits NADPH oxidase in the pulmonary arteriole and cardiac cells, respectively.

Acknowledgements

This work was supported by National Key New Drug Innovation Program, the Ministry of Science and Technology of China, No: 2009ZXJ09004-070 and The National Natural Science Foundation of China No: 81070145.

Author contribution

Jie GAO conducted the project and prepared the manuscript. Yu-si CHENG assisted in performing the cellular experiments. Guo-lin ZHANG and Yi-qun TANG collected and processed data. Yin DAI supervised the experiments. Can ZHANG prepared and provided the tested compound. The project design, analyses of the results and revision of the manuscript were performed by De-zai DAI.

References

1 Hernandez-Rivera H, Martinez-Gonzalez H, Casal J, Rodriguez-Ospina L. Pulmonary arterial hypertension: from pathophysiology to management. Bol Asoc Med P R 2011; 103: 34–40.

2 Yuan SH, Dai DZ, Guan L, Dai Y, Ji M. CPU0507, an endothelin receptor antagonist, improves rat hypoxic pulmonary artery hypertension and constriction *in vivo* and *in vitro*. Clin Exp Pharmacol Physiol

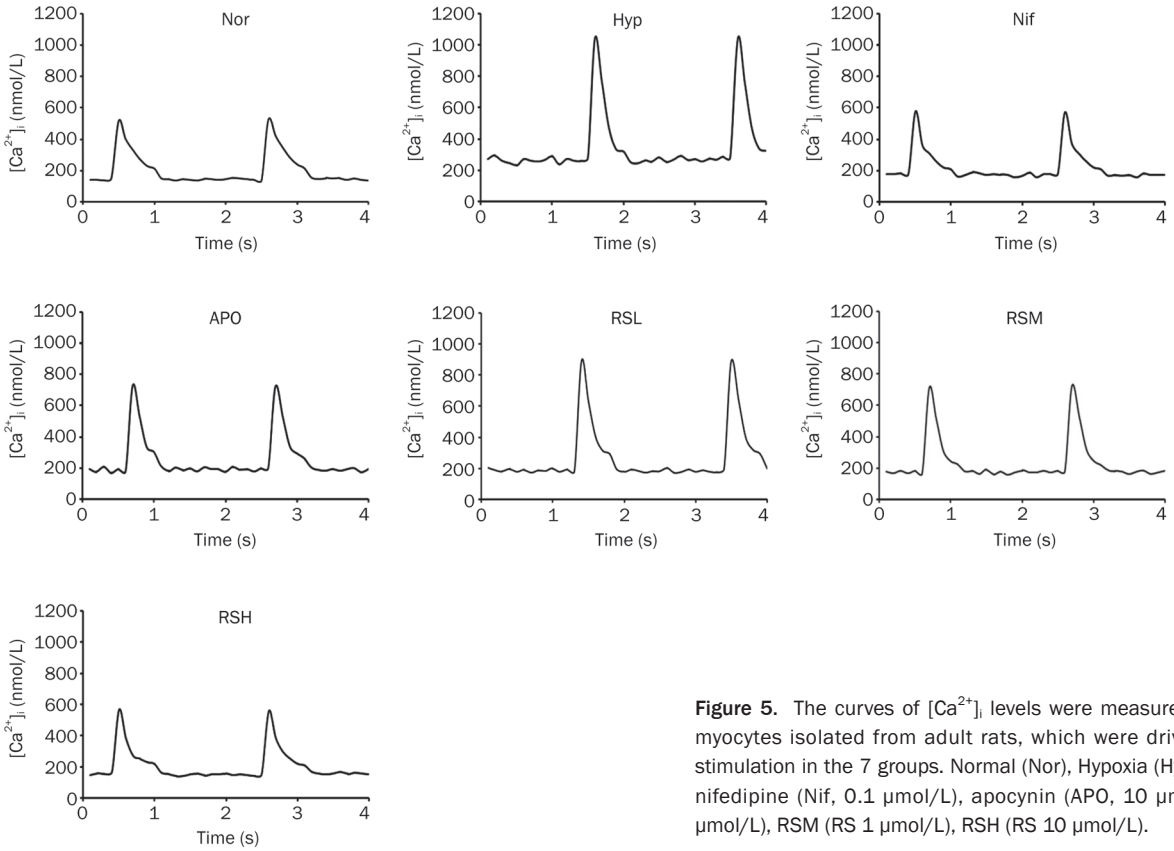

Figure 5. The curves of $[Ca^{2+}]_i$ levels were measured in beating cardiomyocytes isolated from adult rats, which were driven by electric field stimulation in the 7 groups. Normal (Nor), Hypoxia (Hyp, H_2O_2 10 μmol/L), nifedipine (Nif, 0.1 μmol/L), apocynin (APO, 10 μmol/L), RSL (RS 0.1 μmol/L), RSM (RS 1 μmol/L), RSH (RS 10 μmol/L).

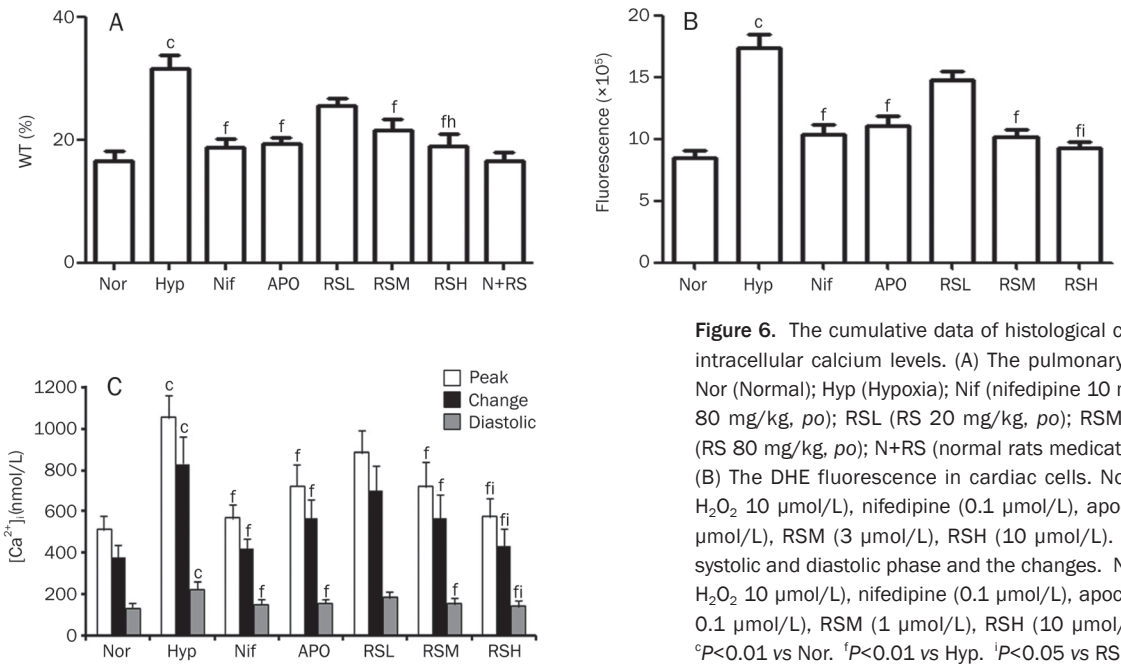

Figure 6. The cumulative data of histological changes, ROS genesis, and intracellular calcium levels. (A) The pulmonary arteriolar wall thickness. Nor (Normal); Hyp (Hypoxia); Nif (nifedipine 10 mg/kg, *po*); APO (apocynin, 80 mg/kg, *po*); RSL (RS 20 mg/kg, *po*); RSM (RS 40 mg/kg, *po*); RSH (RS 80 mg/kg, *po*); N+RS (normal rats medicated with RS 80 mg/kg, *po*). (B) The DHE fluorescence in cardiac cells. Normal (Nor), Hypoxia (Hyp, H_2O_2 10 μmol/L), nifedipine (0.1 μmol/L), apocynin (10 μmol/L), RSL (1 μmol/L), RSM (3 μmol/L), RSH (10 μmol/L). (C) the levels of $[Ca^{2+}]_i$ in systolic and diastolic phase and the changes. Normal (Nor), Hypoxia (Hyp, H_2O_2 10 μmol/L), nifedipine (0.1 μmol/L), apocynin (10 μmol/L), RSL (RS 0.1 μmol/L), RSM (1 μmol/L), RSH (10 μmol/L). Mean±SD. *n*=6–10. $^{c}P<0.01$ *vs* Nor. $^{f}P<0.01$ *vs* Hyp. $^{i}P<0.05$ *vs* RSL.

2006; 33: 1066–72.
3 Dupuis J, Hoeper MM. Endothelin receptor antagonists in pulmonary arterial hypertension. Eur Respir J 2008; 31: 407–15.
4 Chen CA, Wang TY, Varadharaj S, Reyes LA, Hemann C, Talukder MA, *et al*. *S*-glutathionylation uncouples eNOS and regulates its cellular and vascular function. Nature 2010; 468: 1115–8.
5 Peng HJ, Dai DZ, Ji H, Dai Y. The separate roles of endothelin receptors participate in remodeling of matrix metalloproteinase and connexin 43 of cardiac fibroblasts in maladaptive response to isoproterenol. Eur J Pharmacol 2010; 634: 101–6.
6 Dai DZ, Dai Y. Role of endothelin receptor A and NADPH oxidase in vascular abnormalities. Vasc Health Risk Manag 2010; 6: 787–94.

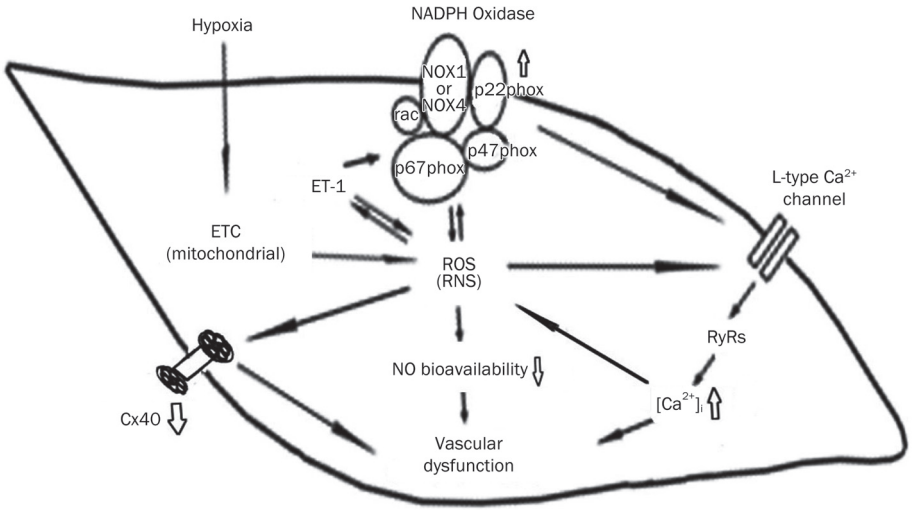

Figure 7. The mechanisms underlying the abnormal vascular activity in hypoxic pulmonary artery. Hypoxia promotes the genesis of ROS from the electron transport chain (ETC) at mitochondria, and thereafter, increases ET-1. ET-1 activates NADPH oxidase which contains catalytic (NOX1-4) and modulating subunits ($p22^{phox}$, $p47^{phox}$, and $p67^{phox}$). An increased ROS stimulates the L-type Ca^{2+} channels to increase calcium influx and subsequent intracellular Ca^{2+} release from RyRs. Increased $[Ca^{2+}]_i$ in turn stimulates the formation of ROS. ROS serves as an inducer for activating NADPH oxidase, therefore, blocking calcium influx is able to suppress NADPH oxidase. An increase in ET-1 and NADPH oxidase play key roles in the development of hypoxia pulmonary hypertension. A reduction in NO availability and release contributes to abnormal activity of hypoxic pulmonary artery. CPU86017-RS relieves hypoxic pulmonary arterial abnormality via blocking NADPH oxidase and calcium influx in the vasculature.

7 Cui B, Yu F, Dai DZ, Zhang TT, Tang XY, Dai Y. CPU0213, a novel endothelin receptor antagonist, relieves hypoxic pulmonary hypertension in rats by suppressing excessive ET-ROS pathway. Drug Dev Res 2007; 68: 42–52.

8 Zhang TT, Cui B, Dai DZ, Tang XY. Pharmacological efficacy of CPU 86017 on hypoxic pulmonary hypertension in rats: mediated by direct inhibition of calcium channels and antioxidant action, but indirect effects on the ET-1 pathway. J Cardiovasc Pharmacol 2005; 46: 727–34.

9 Li N, Dai D, Dai Y. CPU86017 and its isomers improve hypoxic pulmonary hypertension by attenuating increased ET_A receptor expression and extracellular matrix accumulation. Naunyn-Schmiedeberg's Arch Pharmacol 2008; 378: 541–52.

10 Nisbet RE, Graves AS, Kleinhenz DJ, Rupnow HL, Reed AL, Fan TH, *et al.* The role of NADPH oxidase in chronic intermittent hypoxia-induced pulmonary hypertension in mice. Am J Respir Cell Mol Biol 2009; 40: 601–9.

11 Selemidis S, Sobey CG, Wingler K, Schmidt HH, Drummond GR. NADPH oxidases in the vasculature: molecular features, roles in disease and pharmacological inhibition. Pharmacol Ther 2008; 120: 254–91.

12 Report. UAD, (Ed.) URDS. Research from the national institutes of Health, national Institute of diabetes and digestive kidney disease, and Charles R. Drew University of Medicine and Science High School Student Research Program — Summer 2005. *Ethn Dis* 2006; 16: 1–39.

13 Su W, Dai DZ, Liu HR, Na T, Dai Y. Upregulated endothelin system in diabetic vascular dysfunction and early retinopathy is reversed by CPU0213 and total triterpene acids from fructus corni. Clin Exp Pharmacol Physiol 2007; 34: 1228–33.

14 Li N, Jia N, Dai DZ, Dai Y. Endothelin receptor antagonist CPU0213 and vitamin E reverse downregulation of FKBP12.6 and SERCA2a: a role of hyperphosphorylation of PKCepsilon. Eur J Pharmacol 2008; 591: 211–8.

15 Qi MY, Feng Y, Dai DZ, Li N, Cheng YS, Dai Y. CPU86017, a berberine derivative, attenuates cardiac failure through normalizing calcium leakage and downregulated phospholamban and exerting antioxidant activity. Acta Pharmacol Sin 2010; 31: 165–74.

16 Zhang TT, Cui B, Dai DZ, Su W. CPU 86017, *p*-chlorobenzyltetrahyd roberberine chloride, attenuates monocrotaline-induced pulmonary hypertension by suppressing endothelin pathway. Acta Pharmacol Sin 2005; 26: 1309–16.

17 Li N, Yang L, Dai DZ, Wang QJ, Dai Y. Chiral separation of racemate CPU86017, an anti-arrhythmic agent, produces stereoisomers possessing favourable ion channel blockade and less alpha-adrenoceptor antagonism. Clin Exp Pharmacol Physiol 2008; 35: 643–50.

18 Luo L, Dai D, Cheng Y, Zhang Q, Yuan W, Dai Y. Sildenafil improves diabetic vascular activity through suppressing endothelin receptor A, iNOS and NADPH oxidase which is comparable with the endothelin receptor antagonist CPU0213 in STZ-injected rats. J Pharm Pharmacol 2011; 63: 943–51.

19 Hu C, Yu F, Dai DZ, Dai Y. Stress-up-regulated myocardial endothelin receptors are suppressed by chlorobenzyltetrahydroberberine CPU86017 and its RS chiral isomer. J China Pharm Univ 2009; 40: 374–9.

20 Huang ZJ, Dai DZ, Li N, Na T, Ji M, Dai Y. Calcium antagonist property of CPU228, a dofetilide derivative, contributes to its low incidence of torsades de pointes in rabbits. Clin Exp Pharmacol Physiol 2007; 34: 310–7.

21 Mirza MA, Zhang XQ, Ahlers BA, Qureshi A, Carl LL, Song J, *et al.* Effects of phospholemman downregulation on contractility and $[Ca^{2+}]_i$ transients in adult rat cardiac myocytes. Am J Physiol Heart Circ Physiol 2004; 286: H1322–30.

22 Yuan SH, Li N, Dai DZ. The different vasomotor of pulmonary and tail arteries from two pulmonary hypertension rat models and *in vitro* drug intervention. Prog Pharm Sci 2006; 30: 314–21.

23 Cui B, Cheng YS, Dai DZ, Li N, Zhang TT, Dai Y. CPU0213, a non-selective ETA/ETB receptor antagonist, improves pulmonary arteriolar remodeling of monocrotaline-induced pulmonary hypertension in rats. Clin Exp Pharmacol Physiol 2009; 36: 169–75.
24 Galiè N, Negro L, Simonneau G. The use of combination therapy in pulmonary arterial hypertension: new developments. Eur Respir Rev 2009; 18: 148–53.
25 De Giusti VC, Correa MV, Villa-Abrille MC, Beltrano C, Yeves AM, de Cingolani GE, *et al*. The positive inotropic effect of endothelin-1 is mediated by mitochondrial reactive oxygen species. Life Sci 2008; 83: 264–71.
26 Zeng Q, Zhou Q, Yao F, O'Rourke ST, Sun C. Endothelin-1 regulates cardiac L-type calcium channels via NAD(P)H oxidase-derived superoxide. J Pharmacol Exp Ther 2008; 326: 732–8.
27 Xu J, Yu F, Dai DZ, Dai Y. High glucose-induced vascular dysfunction and expression of vascular ET_AR and OB-Rb: intervention effects of ETR antagonist CPU0213. Prog Pharm Sci 2009; 3: 125–31.
28 Dennis KE, Aschner JL, Milatovic D, Schmidt JW, Aschner M, Kaplowitz MR, *et al*. NADPH oxidases and reactive oxygen species at different stages of chronic hypoxia-induced pulmonary hypertension in newborn piglets. Am J Physiol Lung Cell Mol Physiol 2009; 297: L596–607.
29 Sedeek M, Callera G, Montezano A, Gutsol A, Heitz F, Szyndralewiez C, *et al*. Critical role of Nox4-based NADPH oxidase in glucose-induced oxidative stress in the kidney: implications in type 2 diabetic nephropathy. Am J Physiol Renal Physiol 2010; 299: F1348–58.
30 Wang YX, Zheng YM. ROS-dependent signaling mechanisms for hypoxic Ca^{2+} responses in pulmonary artery myocytes. Antioxid Redox Signal 2010; 12: 611–23.
31 Amberg GC, Earley S, Glapa SA. Local regulation of arterial L-type calcium channels by reactive oxygen species. Circ Res 2010; 107: 1002–10.

Acta Pharmacologica Sinica (2012) 33: 635–643
 1671-4083/12 $32.00
www.nature.com/aps

Original Article

Inhibition of hypoxia inducible factor-1α ameliorates lung injury induced by trauma and hemorrhagic shock in rats

Hong JIANG#, Yan HUANG#, Hui XU, Rong HU, Qi-fang LI*

Department of Anesthesiology, Shanghai Ninth People's Hospital Affiliated to Shanghai Jiao Tong University School of Medicine, Shanghai 200011, China

Aim: Ischemia/reperfusion is an initial triggering event that leads to gut-induced acute lung injury (ALI). In this study, we investigated whether hypoxia inducible factor-1α (HIF-1α) played a role in the pathogenesis of lung injury induced by trauma and hemorrhagic shock (T/HS).

Methods: Male Wistar rats underwent laparotomy and hemorrhagic shock for 60 min. Sham-shock animals underwent laparotomy but without hemorrhagic shock. After resuscitation for 3 h, the rats were sacrificed. Morphologic changes of the lungs and intestines were examined. Bronchoalveolar lavage fluid (BALF) was collected. Lung water content, pulmonary myeloperoxidase (MPO) activity and the levels of malondialdehyde (MDA), nitrite/nitrate, TNF-α, IL-1β, and IL-6 in the lungs were measured. The gene expression of pulmonary HIF-1α and iNOS, and HIF-1α transcriptional activity in the lungs were also assessed. The apoptosis in the lungs was determined using TUNEL assay and cleaved caspase-3 expression.

Results: Lung and intestinal injuries induced by T/HS were characterized by histological damages and a significant increase in lung water content. Compared to the sham-shock group, the BALF cell counts, the pulmonary MPO activity and the MDA, nitrite/nitrate, TNF-α, IL-1β, and IL-6 levels in the T/HS group were significantly increased. Acute lung injury was associated with a higher degree of pulmonary HIF-1α and iNOS expression as well as apoptosis in the lungs. Intratracheal delivery of HIF-1α inhibitor YC-1 (1 mg/kg) significantly attenuated lung injury, and reduced pulmonary HIF-1α and iNOS expression and HIF-1α transcriptional activity in the T/HS group.

Conclusion: Local inhibition of HIF-1α by YC-1 alleviates the lung injury induced by T/HS. Our results provide novel insight into the pathogenesis of T/HS-induced ALI and a potential therapeutic application.

Keywords: trauma; hemorrhagic shock; acute lung injury; hypoxia inducible factor-1α; YC-1; inflammation

Acta Pharmacologica Sinica (2012) 33: 635–643; doi: 10.1038/aps.2012.5; published online 2 Apr 2012

Introduction

Trauma is the leading cause of death for those under 45 years of age in the United States[1]. Shock resulting from trauma and severe hemorrhage (trauma/hemorrhagic shock, T/HS) is a systemic inflammatory response that can result in multiple organ dysfunction syndrome (MODS). MODS is preceded by acute lung injury (ALI) in 83% of cases[2]. However, the cellular and molecular bases of ALI in the setting of T/HS are poorly defined. Many mechanistic studies have contributed to the development of several hypotheses, one of which is the gut hypothesis of MODS. A key element in the gut hypothesis of MODS is that a splanchnic ischemia-reperfusion (I/R) insult leading to gut inflammation and loss of barrier function is the initial triggering event that leads to MODS[3]. Currently, the majority of the molecular and cellular studies investigating T/HS-induced lung injury have focused primarily on the production of proinflammatory mediators. However, because the induction of many of these factors is secondary to or accentuated by hypoxia/ischemia, it seems likely that the molecular response triggered by the ischemic component of an I/R insult is a critical step in initiating the events that lead to the development of lung injury and MODS.

The cellular response to hypoxia or ischemia has been shown to be primarily regulated by hypoxia inducible factor (HIF)-1[4]. HIF-1 is composed of two subunits: HIF-1α and HIF-1β. HIF-1β is constitutively expressed and unaffected by hypoxia, whereas HIF-1α is continuously synthesized and

# These authors contributed equally to the paper.
* To whom correspondence should be addressed.
E-mail jiuyuanpaper@yahoo.cn
Received 2011-10-30 Accepted 2012-01-13

is destroyed under conditions of normoxia, as a result of its ubiquitination and subsequent degradation by the proteasomal system after hydroxylation[5]. HIF-1 activity is primarily regulated by the abundance of the HIF-1α subunit. Under hypoxic conditions, HIF-1α is stabilized and translocates into the nucleus where it dimerizes with HIF-1β and transactivates downstream target genes containing hypoxia-response elements (HRE) within their promoter or enhancer elements[6]. This master regulator of cellular and systemic oxygen homeostasis can directly regulate over 70 genes operating in all cells in response to hypoxia.

The accepted role of HIF-1α is that it acts as an adaptive and survival factor for cells exposed to hypoxia or cells undergoing stress, such as that caused by ischemic injury. However, under some circumstances, HIF-1α may be deleterious because of its ability to augment both apoptotic[7, 8] and inflammatory processes[9, 10]. In LPS-induced ALI, HIF-1α expression exacerbates acute lung epithelial cell injury and the expression of the BCL2/adenovirus E1B 19-kDa protein-interacting protein 3 (BNIP3) gene and many proinflammatory cytokines[11]. Moreover, it has been shown that partial HIF-1α deficiency (HIF-1α$^{+/-}$) could alleviate lung injury induced by T/HS or superior mesenteric artery occlusion (SMAO) in mice[12, 13]. In this study, we hypothesized that lung HIF-1α activation could be potentially maladaptive or injurious and could contribute to lung injury induced by T/HS. YC-1 [3-(5′-hydroxymethyl-2′-furyl)-1-benzyl indazole], an inhibitor of HIF-1α, has been widely used as a pharmacologic tool for investigating the physiologic and pathologic roles of HIF-1α[14]. Using YC-1, we tested the functional significance of HIF-1α in a T/HS-mediated lung injury model.

Materials and methods

Rats and the T/HS model

Adult male Wistar rats were purchased from the Animal Center of the Shanghai Jiao Tong University School of Medicine (Shanghai, China) and housed in air-filtered temperature-controlled units with access to food and water *ad libitum*. The experimental protocols were approved by the institutional animal care committee and complied with National Institutes of Health guidelines for animal experimentation. The rats were allowed to stabilize, and they were then randomized to one of four groups: (1) Sham; (2) T/HS; (3) T/HS+vehicle (dimethyl sulfoxide, DMSO); (4) T/HS+YC-1 (1 mg/kg diluted in DMSO, delivered intratracheally with a 22-gauge intubator 10 min before operation). Because DMSO has a sticky consistency, it was dissolved in phosphate-buffered saline (PBS) to prevent it from interfering with the respiration of the rats. The final concentration of DMSO was 1% for the intratracheal challenge, as described previously[15, 16]. The dosage of YC-1 administered in this study was based on previous I/R studies[17] and on our preliminary experiments showing that this dosage improved the outcome of T/HS in rats. For the T/HS model, the rats were anesthetized with pentobarbital (40–50 mg/kg, ip), and a 2.5-cm midline laparotomy was performed under strict asepsis. Anesthesia was maintained with pentobarbital sodium (12.5 mg·kg^{-1}·h^{-1}). Blood was withdrawn from the jugular vein until a mean arterial pressure (MAP) between 35 and 40 mmHg was obtained and maintained for 60 min. After 60 min, the rats were resuscitated with their shed blood for 3 h. Sham-shock animals underwent cannulation of the femoral artery and jugular vein followed by a laparotomy; however, no blood was withdrawn, and the MAP was kept within normal limits.

Water content determination and histologic examination

To evaluate the severity of the acute lung injury, the establishment of pulmonary edema was confirmed by the wet/dry weight ratios of the lungs. The lungs were removed, blotted dry and weighed. They were then incubated at 60 °C for 72 h and reweighed. The difference between the wet weight and the dry weight was considered to be the water weight and was calculated as the percentage of the wet tissue weight. The morphologic alterations in the lungs were examined in individual rats from each of the four groups. The lungs were fixed with 4% paraformaldehyde and embedded in paraffin. Paraffin sections that were 4 μm thick were stained with hematoxylin and eosin (H&E) for examination by light microscopy. A scoring system to grade the degree of lung injury was employed[18]. Simultaneously, gut injury was assessed according to the grading systems for villous injury as described previously[12]. The grading was performed by a blinded pathologist. Injury scores were calculated by adding the individual scores for each category.

Collection of bronchoalveolar lavage fluid

After resuscitation for 3 h, the rats were sacrificed by exsanguination. The trachea was exposed and lavaged 3 times with 1 mL of PBS with a 20-gauge catheter. The lavage fluids were pooled and then centrifuged at 300×*g* for 5 min at 4 °C. The resultant supernatants were stored at -80 °C for subsequent measurements. The pellets were resuspended in PBS to determine the total and differential cell counts of the bronchoalveolar lavage fluid (BALF). The total cell count was measured with a hemocytometer. The differential cell count was determined by manually counting 200 cells per mouse that were stained with Diff-Quick (Pusheng Biological Corporation, Shanghai, China) and fixed on glass slides.

Detection of malondialdehyde (MDA) levels and myeloperoxidase (MPO) activity in lung tissue

Lipid peroxidation as a result of I/R is one of the main causes of lung injury[19]. The MDA levels in the tissue samples were determined as an indicator of lipid peroxidation. The absorbance of the supernatant was measured by spectrophotometry at 515–553 nm. The concentration was expressed as nanomoles per milligram of protein in the tissue homogenate. Myeloperoxidase (MPO) activity was determined as an index of neutrophil accumulation in the lungs. As described previously[12], the MPO activity in the supernatants was determined by measuring the H_2O_2-mediated oxidation of *o*-dianisidine hydrochloride at 460 nm and normalizing relative to the num-

ber of milligrams of protein determined by bicinchoninic acid protein assay (Pierce, Rockford, IL, USA).

Determination of pulmonary nitrite/nitrate, tumor necrosis factor (TNF)-α, interleukin (IL)-1β and IL-6

At 3 h after resuscitation, the left lungs from mice in each group (n=6 for each group) were removed and snap frozen in liquid nitrogen and then stored at -80 °C for subsequent analysis. To determine the nitric oxide (NO) concentrations in collected samples, we chose to measure the sum of the stable NO metabolites, the nitrite concentration and the nitrate concentration using chemiluminescence as described previously[20]. The TNF-α, IL-1β, and IL-6 concentrations were measured using a commercially available enzyme-linked immunosorbent assay (ELISA) kit according to the manufacturers' instructions (R&D systems, Minneapolis, MN, USA).

Real-time quantitative polymerase chain reaction (PCR)

Real-time quantitative PCR estimation of the mRNA levels was performed as previously described[21]. Briefly, total RNA was prepared from the lung tissue using RNeasy (Qiagen, Shanghai, China), and cDNA was synthesized using the high-capacity cDNA reverse transcription kit (Applied Biosystems, Carlsbad, CA, USA) according to the manufacturer's protocols. The cDNA was then amplified by PCR using the TaqMan gene expression Master Mix and predesigned TaqMan probes for murine HIF-1α and inducible nitric oxide synthase (iNOS) as recommended by Applied Biosystems. Within each experimental group, the mRNA expression was normalized relative to the amplification of 18S rRNA. The value determined for the sham group was set as 100%, and the levels obtained for the other groups are represented as fold over sham.

Western blotting assay

As described previously, total p42/p44 was used as a loading control because the expression of commonly used loading controls, such as β-actin and tubulin, has been shown to be altered in the tissues of animals subjected to I/R injury[22]. Western blotting assays were performed as we have described previously[21]. The intensity of each band was quantified using Quantity One-4.2.3 software (Bio-Rad, Hercules, CA, USA) and normalized relative to the total level of p42/p44 by density analysis.

Electrophoretic mobility shift assay (EMSA)

Nuclear extracts were prepared from lung tissue using a nuclear extraction kit according to the manufacturer's instructions (Pierce, Rockford, IL USA), and aliquots were incubated with γ-^{32}P-ATP-labeled oligonucleotides encompassing the binding site for HIF-1α (5′-TCT GTA CGT GAC CAC ACT CAC CTC-3′) (TaKaRa, Dalian, China). The EMSA was performed as previously described[23].

Terminal deoxynucleotidyl transferase dUTP nick end labeling (TUNEL) assay

Apoptotic cells were detected and quantified by the TUNEL assay using the peroxidase (POD) *in situ* cell death detection kit (Roche Diagnostics, Indianapolis, IN, USA) according to the manufacturer's instructions.

Statistical analysis

The results were expressed as the mean±SEM. The differences among the groups for all variables except the pathological scores were evaluated with one-way analysis of variance (ANOVA) followed by the Student-Newman-Keuls test. For the pathological scores, the differences were evaluated using the Kruskal-Wallis rank test. The results were considered statistically significant when the P value was less than 0.05.

Results

Pathological changes to the lung and intestine

As a consequence of T/HS, severe lung injury was observed, as indicated by the presence of extensive interstitial edema, infiltration of leukocytes and red blood cell congestion in the lungs of the T/HS rats (Figure 1A). These changes were significantly ameliorated in the T/HS+YC-1 rats. No evidence of lung injury was seen in the sham group. Because the gut is a major source of factors that contribute to the development of a systemic inflammatory state during acute lung injury[3], we sought to assess the intestinal injuries induced by T/HS. As shown in Figure 1C, the intestinal tissues were obviously damaged by edema, hemorrhage, and cell infiltration in the T/HS group. There was a significant difference between the T/HS group and the controls with respect to the pathological scores of the intestines and lungs pathological scores (Figures 1B and 1D). In the T/HS+YC-1 group, the pathological scores for the intestine and lung tissues were significantly lower than those of the T/HS group, suggesting that YC-1 ameliorates intestinal and lung injury induced by T/HS.

YC-1 attenuates the infiltration of inflammatory cells

To determine whether inhibition of HIF-1α by YC-1 affected the T/HS-induced infiltration of inflammatory cells into the airways and parenchyma, we counted the inflammatory cells in the BALF after resuscitation. As shown in Figures 2A–2D, the total numbers of inflammatory cells (including macrophages and neutrophils) and lymphocytes in the BALF were significantly higher in rats in the T/HS group compared to those in the sham group. Moreover, the increase in these cell populations in the T/HS group was significantly attenuated in the T/HS+YC-1 group.

YC-1 attenuates pulmonary edema, MPO activity and the levels of MDA, nitrate and nitrite

As shown in Figure 3A, rats subjected to T/HS demonstrated a significantly higher lung water content than the sham-operated animals (P<0.05). YC-1 administration significantly decreased the T/HS-related pulmonary edema (P<0.05 *vs* T/HS group). The MPO activity and the MDA level in the T/HS group were significantly higher than those in the sham group (P<0.05). Compared with the T/HS group, the MPO activity and the MDA level in the T/HS+YC-1 group were

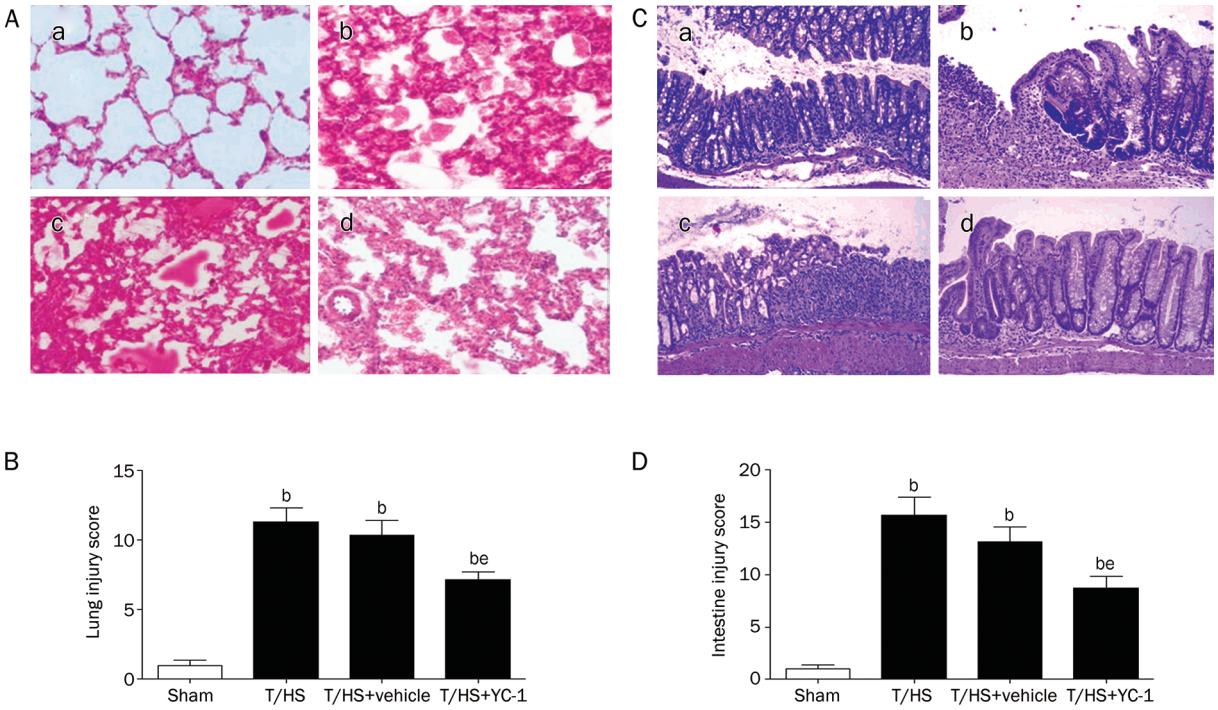

Figure 1. The effect of YC-1 on morphological changes in the lung and intestine after T/HS. Four hours after induction of T/HS, lung (A) and intestine (C) was removed for histopathologic examination using hematoxylin and eosin staining. Representative images from eight animals per group are shown. (a) sham; (b) T/HS; (c) T/HS+vehicle; (d) T/HS+YC-1. Original magnification×200. (B) and (D): pathological scores for lung injury and intestine injury. Data were expressed as mean±SEM (n=8). ^{b}P<0.05 *vs* sham group; ^{e}P<0.05 *vs* T/HS group.

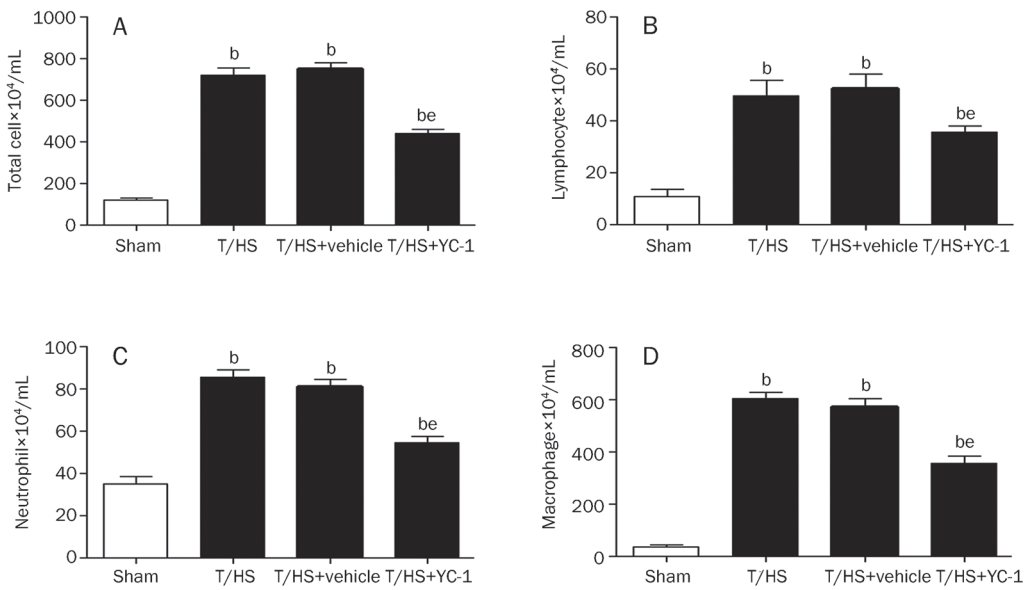

Figure 2. Effects of YC-1 on differential cell counts in bronchoalveolar fluid (BALF) of rats submitted to T/HS. Differential cell counts in BALF were determined after the resuscitation. (A) total cell; (B) lymphocyte; (C) neutrophil; and (D) macrophage. Data are expressed as mean±SEM (n=8). ^{b}P<0.05 *vs* sham group; ^{e}P<0.05 *vs* T/HS group.

markedly reduced (P<0.05) but were still higher than those in the sham group (P<0.05) (Figures 3B and 3C). As seen in Figire 3D, the mean nitrate and nitrite levels in the T/HS group were significantly higher than those in the sham group (P<0.05). T/HS resulted in an approximately 4-fold increase in the nitrate and nitrite levels in lung tissues. YC-1 admin-

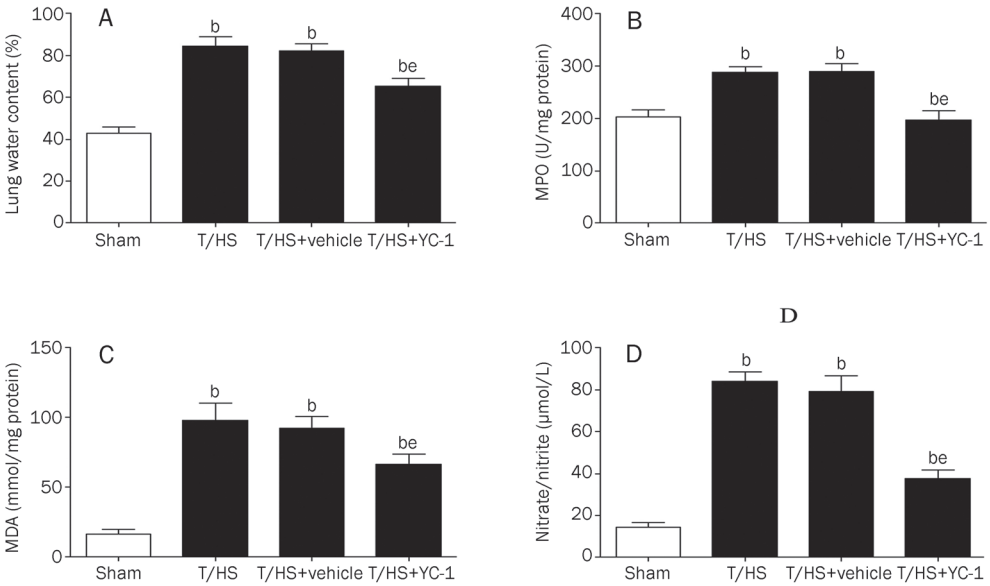

Figure 3. Effects of YC-1 on formation of lung edema measured by wet/dry lung weight ratios (A), neutrophil infiltration measured by MPO activity (B), lipid peroxidation measured by MDA (C) and NO levels measured by nitrite and nitrate (D) in lungs of rats submitted to T/HS. Data were expressed as mean±SEM (n=8). ^{b}P<0.05 *vs* sham group; ^{e}P<0.05 *vs* T/HS group.

istration significantly decreased the nitrate and nitrite levels compared with rats in the T/HS group (P<0.05).

YC-1 attenuates pulmonary TNF-α, IL-1β, and IL-6 levels

Compared with the sham group, T/HS induced a significant elevation of pulmonary TNF-α, IL-1 , and IL-6 levels. YC-1 ameliorated the accumulation of TNF-α, IL-1β, and IL-6 induced by T/HS. The values were significantly lower than those resulting from T/HS but still higher than the values in the sham group (Figures 4A–4C).

YC-1 attenuates pulmonary HIF-1α, iNOS expression, and HIF-1α transcriptional activity induced by T/HS

As shown in Figure 5A, real-time PCR analysis demonstrated a modest increase in HIF-1α expression in rats subjected to T/HS compared with their sham counterparts. T/HS was also capable of inducing the expression of iNOS (Figure 5B). We chose to characterize the iNOS response because iNOS has been identified as an HIF-1α target and is a key effector in the pathophysiology of acute lung injury during shocked states[24]. In agreement with earlier studies[25], the baseline levels of iNOS mRNA were significantly lower in the sham group relative to those in the T/HS group. Furthermore, negligible HIF-1α and iNOS protein levels were detected in the sham group, and both HIF-1α and iNOS protein levels were increased in the lungs of rats after T/HS compared with the sham-operated rats (Figures 5C–5F). YC-1 ameliorated the induction of HIF-1α and iNOS expression by T/HS as determined by real time PCR and Western blot analysis (Figures 5A–5F). Moreover, YC-1 reduced the transcriptional activity of HIF-1α induced by T/HS as demonstrated by EMSA (Figure 6A).

YC-1 attenuates lung epithelial cell apoptosis after T/HS

We next investigate whether YC-1 has an effect on lung apoptosis induced by T/HS. TUNEL staining indicated that T/HS resulted in significant apoptosis of alveolar epithelial cells, while YC-1-treated rats displayed a drastic reduction of

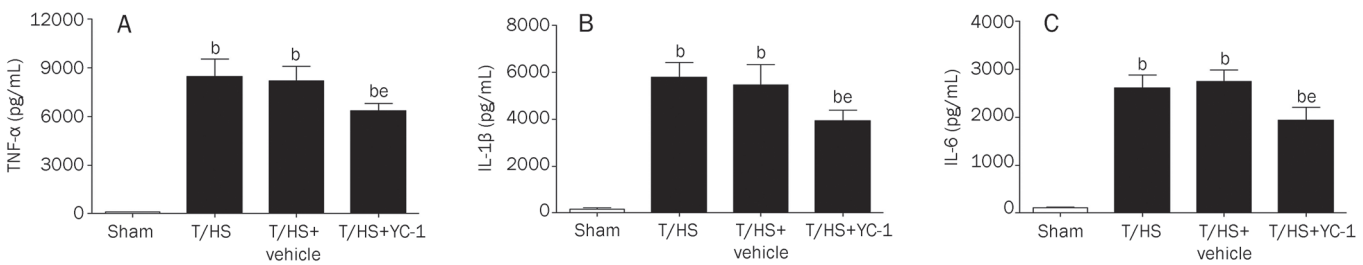

Figure 4. Effects of YC-1 on inflammatory cytokines in lungs of rats submitted to T/HS. Concentration of tumor necrosis factor (TNF)-α (A), interleukin (IL)-1β (B) and IL-6 (C) were measured by ELISA in lung homogenates. Data were expressed as mean±SEM (n=6). ^{b}P<0.05 *vs* sham group; ^{e}P<0.05 *vs* T/HS group.

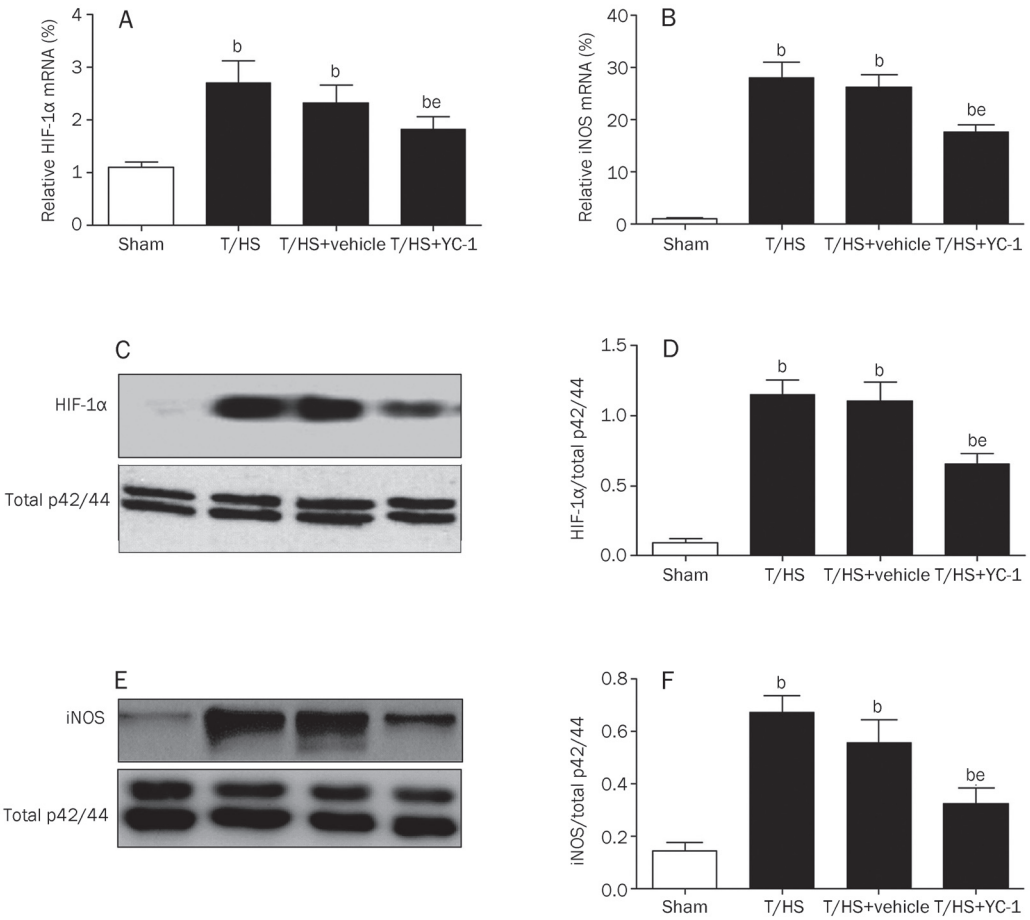

Figure 5. Effects of YC-1 on HIF-1α and iNOS gene expression. (A) and (B) HIF-1α and iNOS mRNA levels in indicated groups. (C) and (E) Representative Western blot analysis of HIF-1α and iNOS protein expression from 3 independent experiments. (D) and (F) The immunoblotting bands were quantitated by densitometry. Data were expressed as mean±SEM (n=3). $^{b}P<0.05$ *vs* sham group; $^{e}P<0.05$ *vs* T/HS group.

TUNEL-positive cells (Figure 6B). Apoptotic cells were not observed in the lungs of rats in the sham groups. In agreement with the increased number of apoptotic cells, the level of the cleaved form of caspase-3, an important member of the apoptotic pathway, was decreased in YC-1-treated rats compared with T/HS rats (Figure 6C).

Discussion

Recent data show that the HIF-1α$^{+/-}$ genotype could alleviate lung injury induced by T/HS or by superior mesenteric artery occlusion (SMAO) in mice[12, 13]. However, gene deletion studies have established that HIF-1α is indispensable during fetal development, as HIF-1α$^{-/-}$ mice die mid-gestation owing to defects in VEGF expression and vascularization[26]. In addition, HIF-1α$^{+/-}$ mice manifest impaired responses to hypoxia compared with their wild-type (WT) littermates[27]. Therefore, local application of a HIF-1α inhibitor may prevent interference with the global functions of HIF-1α. In the present study, we demonstrated that multiple indicators of lung injury, including histologic changes, apoptosis in the lung, pulmonary edema, cell counts in the BALF and pulmonary neutrophil accumulation, were substantially ameliorated by YC-1 in T/HS rats. YC-1 also abrogated the induction of pulmonary inflammatory cytokines and lung apoptosis in T/HS rats. Furthermore, we demonstrated that local application of YC-1 inhibited the activation of HIF-1α in the lungs, resulting in attenuation of the activation of the iNOS-NO pathway by T/HS. Therefore, our findings suggest a critical role for HIF-1α signaling in lung inflammatory injury triggered by T/HS.

The T/HS model (laparotomy plus 60 min of hemorrhagic shock at 35–40 mmHg) and 3 h of reperfusion represents a global I/R injury, and the gut is particularly susceptible to I/R injuries[28]. The mechanisms of lung injury after T/HS are complex and have been difficult to unravel. It has been shown that damage to the intestinal mucosal barrier following T/HS causes the dislocation of bacteria, resulting in systemic inflammatory reactions[29]. I/R involves the release of a large number of inflammatory mediators, including TNF-α, IL-1β, IL-6, and NO. The neutrophils and their enzymatic products are sequestered in the lung tissues, causing increased microvascular permeability and pulmonary edema[30, 31].

HIF-1α has emerged as a critical determinant in the pathophysiological response to I/R in conditions such as

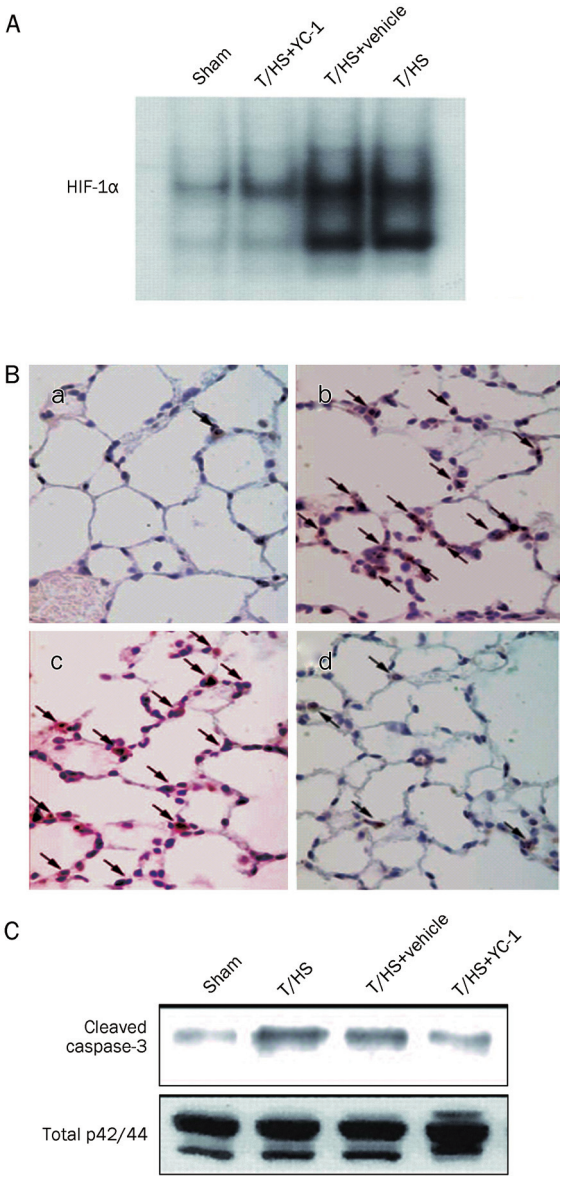

Figure 6. The effect of YC-1 on HIF-1α transcriptional activity and T/HS induced lung apoptosis. (A) HIF-1α transcriptional activity in the lung of rats subjected to T/HS as evaluated by EMSA. Autoradiograph is representative of three separate experiments. (B) A representative lung section stained with TUNEL from six animals of each group is shown. (a) sham, (b) T/HS, (c) T/HS+vehicle, (d) T/HS+YC-1, original magnification×400. (C) Protein extracts of whole lung were immunoblotted for cleaved caspase-3.

cerebral and myocardial ischemia, and its activation is an early component of the inflammatory response[32]. It has been documented that HIF-1 regulates iNOS expression[33, 34], and iNOS-derived NO is involved in the pathogenesis of lung injury[35, 36]. Recently, we found that LPS treatment induced the iNOS-NO pathway during the development of ALI[37]. In the present study, we examined the pulmonary levels of nitrate and nitrite, the oxidative metabolites of NO, to estimate NO production after T/HS injury. The pulmonary nitrate and nitrite levels were increased significantly in T/HS-treated animals. However, YC-1 significantly inhibited the T/HS-induced increases in pulmonary nitrate and nitrite levels. The results showed that YC-1 significantly reduced the generation of NO accompanied by the down-regulation of iNOS expression. Consistent with our findings, other studies have shown that HIF-1-induced iNOS mediates neuronal cell death in astrocytes[38]. Furthermore, recent studies have demonstrated increased caspase-3 protein levels and activity are regulated via iNOS[39, 40]. Accordingly, we found that YC-1 attenuated caspase-3 accumulation and lung epithelial cell apoptosis in T/HS rats. Therefore, HIF-1-induced increases in iNOS expression are, at least, partly responsible for the injurious effect of T/HS on the lungs. It has been suggested that the superoxide ions react with NO to produce peroxynitrite, which then causes accentuated lipid peroxidation, as well as protein and DNA modifications that result in cellular damage[41]. Thus, although HIF-1α appears to be involved in the regulation of lung homeostasis, it also appears to have dichotomous roles in lung inflammatory diseases in that it can be injurious or protective depending on the exact physiological conditions studied as well as the nature and duration of the insult.

Although YC-1 has been shown to be a HIF-1α inhibitor, our knowledge of the effects of YC-1 on HIF-1α gene expression is limited and to some extent controversial. For example, in contrast to the reduction in HIF-1α mRNA expression caused by YC-1 in T/HS rats in the current study, the level of HIF-1α mRNA was nearly unchanged in the presence of different concentrations of YC-1 in hypoxic PC-3 cells[42]. One explanation for this discrepancy may be that increased transcription of the HIF-1α gene was important for HIF-1α protein induction under nonhypoxic conditions[43], as shown in our T/HS model. However, hypoxia did not induce the expression of HIF-1α mRNA in PC-3 cells, as was also the case in other cell models[44]. It could be argued that our present data have demonstrated only the preventive effects of YC-1 in ALI, and thus the therapeutic role of YC-1 in ALI remains unknown. Although we did not apply YC-1 after the development of ALI in this study, previous studies have shown that when reduced levels of HIF-1α were evident at 30 min, similar reductions were also evident at 4 and 24 h after an insult[45, 46]. Based on those studies, it would appear that the effects of YC-1 on TH/S would be expected to persist after the insult.

It should be noted that although it is well accepted that YC-1 is an effective HIF-1α inhibitor, it was originally characterized as a cGMP inducer because it stimulates soluble guanylyl cyclase activation in response to nitric oxide or carbon monoxide in some cells[47]; only low concentrations of YC-1 (1–20 μmol/L) are required for anti-HIF-1α activity, whereas cGMP elevation requires higher concentrations (>50 μmol/L)[48, 49]. It has been reported that no serious toxicity is observed in nude mice treated with YC-1 over a 2-week period[46]. Nonetheless, whether and to what extent cGMP may play a role in the beneficial effects of YC-1 in ALI induced by T/HS, particularly in relation to the inhibitory effects on HIF-1α, remains to be

determined.

Although our findings suggest that HIF-1α inhibition attenuates the T/HS-induced gut-and lung-derived inflammatory response and lung apoptosis, a more extensive analysis of the HIF-1-driven lung inflammatory response is needed to resolve this issue. One limitation of this study was the fact that this was purely a pharmacologic study and that only one dose of the drug was used. Consequently, genetic-based studies should be carried out to complement the pharmacologic work reported here. For example, siRNA knockdown approaches and the use of HIF-1α conditional knockout mice could be used to validate as well as extend this work. This study shows that local inhibition of the HIF-1α signaling pathway attenuates T/HS-induced lung injury and inflammation, and it provides novel insights into the biology of this clinically important disease as well as potential therapeutic insights. These results are of potential clinical importance because T/HS has been associated with the development of MODS as well as worse clinical outcomes in severely injured and intensive care unit patient populations.

In our current study, local administration of YC-1 reduced lung and intestinal injury in the T/HS model. Two possibilities exist that may explain this apparent discrepancy with the "gut hypothesis". One possibility is that there is a feedback cycle between lung injury and intestinal injury during T/HS. Although injury to the gut is the initial triggering event in MODS, lung injury can also accelerate intestinal injury. It has been found that local acid aspiration can lead to systemic organ injury[50]. Another possibility is that the "gut hypothesis" has not been conclusively shown to play a role in the expression of cytokines or tissue injury in an animal model of T/HS. Many research groups have reported an absence of endotoxemia after T/HS[51, 52]. As a result, our observation that intratracheal administration of YC-1 can attenuate intestinal injury induced by T/HS highlights the concept that the lungs can be a target as well as a producer of organ injury. To our knowledge, the current work shows that the local inhibition of HIF-1α can specifically limit T/HS-induced lung and intestinal injury.

In conclusion, the present study indicates that the local inhibition of HIF-1α has a protective role in lung injury induced by T/HS, and this protection may be related to HIF-1α's regulation of the iNOS-NO pathway in lung tissue. The significant attenuation of T/HS-related lung injury when YC-1 was administered warrants further studies to improve our understanding of the specific roles of HIF-1α in T/HS-induced organ injury and to elucidate its potential therapeutic target in clinical settings.

Acknowledgements

This research was supported by funds from Shanghai Jiao Tong University (to Hong JIANG), the Shanghai Jiao Tong University School of Medicine (to Yan HUANG) and the National Natural Science Foundation of China (No 30801079) to Qi-fang LI.

Author contribution

Hong JIANG and Yan HUANG performed the research; Hui XU contributed new analytical reagents and tools; Rong HU analyzed data; Qi-fang LI designed the project and wrote the manuscript.

References

1 Minino AM, Anderson RN, Fingerhut LA, Boudreault MA, Warner M. Deaths: Injuries, 2002. Natl Vital Stat Rep 2006; 54: 1–124.
2 Ciesla DJ, Moore EE, Johnson JL, Burch JM, Cothren CC, Sauaia A. The role of the lung in postinjury multiple organ failure. Surgery 2005; 138: 749–57.
3 Clark JA, Coopersmith CM. Intestinal crosstalk: A new paradigm for understanding the gut as the "Motor" Of critical illness. Shock 2007; 28: 384–93.
4 Semenza GL. Hif-1: Mediator of physiological and pathophysiological responses to hypoxia. J Appl Physiol 2000; 88: 1474–80.
5 Huang LE, Gu J, Schau M, Bunn HF. Regulation of hypoxia–inducible factor 1alpha is mediated by an O_2-dependent degradation domain via the ubiquitin-proteasome pathway. Proc Natl Acad Sci U S A 1998; 95: 7987–92.
6 Kenneth NS, Rocha S. Regulation of gene expression by hypoxia. Biochem J 2008; 414: 19–29.
7 Bakker WJ, Harris IS, Mak TW. Foxo3a is activated in response to hypoxic stress and inhibits hif1-induced apoptosis via regulation of cited2. Mol Cell 2007; 28: 941–53.
8 Greijer AE, van der Wall E. The role of hypoxia inducible factor 1 (hif-1) in hypoxia induced apoptosis. J Clin Pathol 2004; 57: 1009–14.
9 Dehne N, Brune B. Hif-1 in the inflammatory microenvironment. Exp Cell Res 2009; 315: 1791–7.
10 Loor G, Schumacker PT. Role of hypoxia-inducible factor in cell survival during myocardial ischemia-reperfusion. Cell Death Differ 2008; 15: 686–90.
11 Yeh CH, Cho W, So EC, Chu CC, Lin MC, Wang JJ, *et al*. Propofol inhibits lipopolysaccharide-induced lung epithelial cell injury by reducing hypoxia-inducible factor-1alpha expression. Br J Anaesth 2011; 106: 590–9.
12 Feinman R, Deitch EA, Watkins AC, Abungu B, Colorado I, Kannan KB, *et al*. Hif-1 mediates pathogenic inflammatory responses to intestinal ischemia-reperfusion injury. Am J Physiol Gastrointest Liver Physiol 2010; 299: G833–43.
13 Kannan KB, Colorado I, Reino D, Palange D, Lu Q, Qin X, *et al*. Hypoxia-inducible factor plays a gut-injurious role in intestinal ischemia reperfusion injury. Am J Physiol Gastrointest Liver Physiol 2010; 300: G853–61.
14 Lee JJ, Li L, Jung HH, Zuo Z. Postconditioning with isoflurane reduced ischemia-induced brain injury in rats. Anesthesiology 2008; 108: 1055–62.
15 Rittirsch D, Flierl MA, Day DE, Nadeau BA, McGuire SR, Hoesel LM, *et al*. Acute lung injury induced by lipopolysaccharide is independent of complement activation. J Immunol 2008; 180: 7664–72.
16 Corteling R, Wyss D, Trifilieff A. *In vivo* models of lung neutrophil activation. Comparison of mice and hamsters. BMC Pharmacol 2002; 2: 1.
17 Yuan LB, Dong HL, Zhang HP, Zhao RN, Gong G, Chen XM, *et al*. Neuroprotective effect of orexin — a is mediated by an increase of hypoxia-inducible factor-1 activity in rat. Anesthesiology 2011; 114: 340–54.
18 Bachofen M, Weibel ER. Structural alterations of lung parenchyma in the adult respiratory distress syndrome. Clin Chest Med 1982; 3:

35–56.
19 Giakoustidis AE, Giakoustidis DE, Iliadis S, Papageorgiou G, Koliakou K, Kontos N, *et al*. Attenuation of intestinal ischemia/reperfusion induced liver and lung injury by intraperitoneal administration of (–)-epigallocatechin-3-gallate. Free Radic Res 2006; 40: 103–10.
20 Huang CL, Huang CJ, Tsai PS, Yan LP, Xu HZ. Acupuncture stimulation of st-36 (zusanli) significantly mitigates acute lung injury in lipopolysaccharide-stimulated rats. Acta Anaesthesiol Scand 2006; 50: 722–30.
21 Jiang H, Zhu YS, Xu H, Sun Y, Li QF. Inflammatory stimulation and hypoxia cooperatively activate hif-1{alpha} in bronchial epithelial cells: Involvement of pi3k and nf-{kappa}b. Am J Physiol Lung Cell Mol Physiol 2010; 298: L660–9.
22 Ono K, Condron MM, Ho L, Wang J, Zhao W, Pasinetti GM, *et al*. Effects of grape seed-derived polyphenols on amyloid beta-protein self-assembly and cytotoxicity. J Biol Chem 2008; 283: 32176–87.
23 Frede S, Freitag P, Otto T, Heilmaier C, Fandrey J. The proinflammatory cytokine interleukin 1beta and hypoxia cooperatively induce the expression of adrenomedullin in ovarian carcinoma cells through hypoxia inducible factor 1 activation. Cancer Res 2005; 65: 4690–7.
24 Farley KS, Wang LF, Razavi HM, Law C, Rohan M, McCormack DG, *et al*. Effects of macrophage inducible nitric oxide synthase in murine septic lung injury. Am J Physiol Lung Cell Mol Physiol 2006; 290: L1164–72.
25 Razavi HM, Wang le F, Weicker S, Rohan M, Law C, McCormack DG, *et al*. Pulmonary neutrophil infiltration in murine sepsis: Role of inducible nitric oxide synthase. Am J Respir Crit Care Med 2004; 170: 227–33.
26 Kotch LE, Iyer NV, Laughner E, Semenza GL. Defective vascularization of hif-1alpha-null embryos is not associated with vegf deficiency but with mesenchymal cell death. Dev Biol 1999; 209: 254–67.
27 Yu AY, Shimoda LA, Iyer NV, Huso DL, Sun X, McWilliams R, *et al*. Impaired physiological responses to chronic hypoxia in mice partially deficient for hypoxia-inducible factor 1alpha. J Clin Invest 1999; 103: 691–6.
28 Reilly PM, Wilkins KB, Fuh KC, Haglund U, Bulkley GB. The mesenteric hemodynamic response to circulatory shock: An overview. Shock 2001; 15: 329–43.
29 Olanders K, Sun Z, Borjesson A, Dib M, Andersson E, Lasson A, *et al*. The effect of intestinal ischemia and reperfusion injury on icam-1 expression, endothelial barrier function, neutrophil tissue influx, and protease inhibitor levels in rats. Shock 2002; 18: 86–92.
30 Ishii H, Ishibashi M, Takayama M, Nishida T, Yoshida M. The role of cytokine-induced neutrophil chemoattractant-1 in neutrophil-mediated remote lung injury after intestinal ischaemia/reperfusion in rats. Respirology 2000; 5: 325–31.
31 Ding R, Han J, Tian Y, Guo R, Ma X. Sphingosine-1-phosphate attenuates lung injury induced by intestinal ischemia/reperfusion in mice: Role of inducible nitric-oxide synthase. Inflammation 2012; 35: 158–66.
32 Hierholzer C, Harbrecht BG, Billiar TR, Tweardy DJ. Hypoxia-inducible factor-1 activation and cyclo-oxygenase-2 induction are early reperfusion-independent inflammatory events in hemorrhagic shock. Arch Orthop Trauma Surg 2001; 121: 219–22.
33 Matrone C, Pignataro G, Molinaro P, Irace C, Scorziello A, Di Renzo GF, *et al*. HIF-1alpha reveals a binding activity to the promoter of iNOS gene after permanent middle cerebral artery occlusion. J Neurochem 2004; 90: 368–78.
34 Melillo G, Taylor LS, Brooks A, Musso T, Cox GW, Varesio L. Functional requirement of the hypoxia-responsive element in the activation of the inducible nitric oxide synthase promoter by the iron chelator desferrioxamine. J Biol Chem 1997; 272: 12236–43.
35 Sedoris KC, Ovechkin AV, Gozal E, Roberts AM. Differential effects of nitric oxide synthesis on pulmonary vascular function during lung ischemia-reperfusion injury. Arch Physiol Biochem 2009; 115: 34–46.
36 Mehta S. The effects of nitric oxide in acute lung injury. Vascul Pharmacol 2005; 43: 390–403.
37 Li QF, Zhu YS, Jiang H, Xu H, Sun Y. Isoflurane preconditioning ameliorates endotoxin-induced acute lung injury and mortality in rats. Anesth Analg 2009; 109: 1591–7.
38 Vangeison G, Carr D, Federoff HJ, Rempe DA. The good, the bad, and the cell type-specific roles of hypoxia inducible factor-1 alpha in neurons and astrocytes. J Neurosci 2008; 28: 1988–93.
39 Kiang JG, Bowman PD, Lu X, Li Y, Wu BW, Loh HH, *et al*. Geldanamycin inhibits hemorrhage-induced increases in caspase-3 activity: Role of inducible nitric oxide synthase. J Appl Physiol 2007; 103: 1045–55.
40 Murao Y, Loomis W, Wolf P, Hoyt DB, Junger WG. Effect of dose of hypertonic saline on its potential to prevent lung tissue damage in a mouse model of hemorrhagic shock. Shock 2003; 20: 29–34.
41 Wang Y, Mathews WR, Guido DM, Farhood A, Jaeschke H. Inhibition of nitric oxide synthesis aggravates reperfusion injury after hepatic ischemia and endotoxemia. Shock 1995; 4: 282–8.
42 Zhao Q, Du J, Gu H, Teng X, Zhang Q, Qin H, *et al*. Effects of yc-1 on hypoxia-inducible factor 1-driven transcription activity, cell proliferative vitality, and apoptosis in hypoxic human pancreatic cancer cells. Pancreas 2007; 34: 242–7.
43 Blouin CC, Page EL, Soucy GM, Richard DE. Hypoxic gene activation by lipopolysaccharide in macrophages: Implication of hypoxia-inducible factor 1alpha. Blood 2004; 103: 1124–30.
44 Page EL, Robitaille GA, Pouyssegur J, Richard DE. Induction of hypoxia-inducible factor-1alpha by transcriptional and translational mechanisms. J Biol Chem 2002; 277: 48403–9.
45 Yeh WL, Lu DY, Lin CJ, Liou HC, Fu WM. Inhibition of hypoxia-induced increase of blood-brain barrier permeability by yc-1 through the antagonism of hif-1alpha accumulation and vegf expression. Mol Pharmacol 2007; 72: 440–9.
46 Yeo EJ, Chun YS, Cho YS, Kim J, Lee JC, Kim MS, *et al*. A potential anticancer drug targeting hypoxia-inducible factor 1. J Natl Cancer Inst 2003; 95: 516–25.
47 Teng CM, Wu CC, Ko FN, Lee FY, Kuo SC. Yc-1, a nitric oxide-independent activator of soluble guanylate cyclase, inhibits platelet-rich thrombosis in mice. Eur J Pharmacol 1997; 320: 161–6.
48 Slupski M, Szadujkis-Szadurski L, Grzesk G, Szadujkis-Szadurski R, Szadujkis-Szadurska K, Wlodarczyk Z, *et al*. Guanylate cyclase activators influence reactivity of human mesenteric superior arteries retrieved and preserved in the same conditions as transplanted kidneys. Transplant Proc 2007; 39: 1350–3.
49 Spirig R, Djafarzadeh S, Regueira T, Shaw SG, von Garnier C, Takala J, *et al*. Effects of tlr agonists on the hypoxia-regulated transcription factor hif-1alpha and dendritic cell maturation under normoxic conditions. PLoS One 2010; 5: e0010983.
50 St John RC, Mizer LA, Kindt GC, Weisbrode SE, Moore SA, Dorinsky PM. Acid aspiration-induced acute lung injury causes leukocyte-dependent systemic organ injury. J Appl Physiol 1993; 74: 1994–2003.
51 Shenkar R, Coulson WF, Abraham E. Hemorrhage and resuscitation induce alterations in cytokine expression and the development of acute lung injury. Am J Respir Cell Mol Biol 1994; 10: 290–7.
52 Grotz MR, Ding J, Guo W, Huang Q, Deitch EA. Comparison of plasma cytokine levels in rats subjected to superior mesenteric artery occlusion or hemorrhagic shock. Shock 1995; 3: 362–8.

Acta Pharmacologica Sinica (2012) 33: 644–651
 1671-4083/12 $32.00
www.nature.com/aps

Original Article

Treatment of 5/6 nephrectomy rats with sulodexide: a novel therapy for chronic renal failure

Ping LI[1, #], Lin-lin MA[1, 2, #], Ru-juan XIE[2], Yuan-sheng XIE[1], Ri-bao WEI[1], Min YIN[1], Jian-zhong WANG[1], Xiang-mei CHEN[1, *]

[1]*State Key Laboratory of Kidney Disease (Chinese PLA General Hospital, 2011DAV00088), Beijing 100853, China;* [2]*Harbin Medical University First Clinical Medical College, Department of Nephrology, Harbin 150001, China*

Aim: Sulodexide, a glycosaminoglycan, could reduce albuminuria in diabetic patients. The aim of this study was to determine whether sulodexide could be used to treat chronic kidney failure in rats.
Methods: Sixty Wistar rats undergone 5/6 nephrectomy, then were randomly divided into 4 groups: the model group, sulodexide group (sulodexide 5 mg/kg per day, im), irbesartan group irbesartan (20 mg/kg per day, ig) and sulodexide plus irbesartan group. Another 12 rats were enrolled into the sham operation group. After the treatments for 4, 8 and 12 weeks, urinary protein and serum creatinine levels were measured. After 12 weeks, serum cholesterin and triglycerides levels were measured, and the degrees of glomerular sclerosis and renal tubulointerstitial fibrosis were scored. The expression of aminopeptidase P (JG-12) in the renal tissue was examined using immunohistochemical staining. The renal expressions of endothelial nitric oxide synthase (eNOS) and tissue type plasminogen activator (tPA) were detected with RT-PCR and Western blot.
Results: Proteinuria was markedly attenuated in the sulodexide-treated groups. After 4 and 8 weeks only the sulodexide-treated groups showed significant reduction in serum creatinine; while after 12 weeks all the three treatment groups showed significant reduction in serum creatinine. Furthermore, all the three treatment groups showed significant reduction in the scores of glomerular sclerosis and tubulointerstitial fibrosis. The glomerular expression of JG-12 was increased in both the sulodexide group and the sulodexide plus irbesartan group, but not in the irbesartan group. The eNOS mRNA and protein expression was decreased and the tPA mRNA and protein expression was significantly increased in the model group compared with Sham group. Sulodexide, irbesartan, and their combination reversed the decrease of eNOS expression but increased the tPA expression much more compared with model group.
Conclusion: Sulodexide was similar to irbesartan that can decrease proteinuria and attenuate renal lesions in 5/6 nephrectomy rats. The renal protection by sulodexide might be achieved via its impact on renal vascular endothelial cells.

Keywords: chronic renal failure; 5/6 nephrectomy; sulodexide; irbesartan; endothelial nitric oxide synthase (eNOS); tissue type plasminogen activator (tPA); aminopeptidase P(JG-12); vascular endothelium

Acta Pharmacologica Sinica (2012) 33: 644–651; doi: 10.1038/aps.2012.2

Introduction

Chronic renal failure (CRF) is a disease that seriously endangers human health. Currently, significant progress has been made in delaying chronic renal failure (CRF) progression with therapy focusing on the blockade of the renin-angiotensin-aldosterone system (RAAS) and on blood pressure control. However, these measures are not sufficient to halt the progression of CRF[1]. It has remained a scientifically significant objective to find other agents to delay CRF progression. Renal vascular endothelium injury is one of the factors contributing to the progression of CRF pathological changes. Promoting the repair of injured endothelium can achieve the effects of stabilizing renal function and delaying the progression of CRF which is not related to the control of blood pressure and proteinuria[2].

Sulodexide is a compound created from the fractional precipitation of glycosaminoglycans extracted from the mucosa of swine intestines, and it consists mainly of fast-moving heparin (FMH) and dermatan sulfate (DS)[3]. Some research has shown that sulodexide can improve endothelial dysfunction in diabetic rats[4], and it has been proved that sulodexide can reduce cell proliferation and matrix accumulation in the kidneys[5]. Sulodexide has been shown to reduce proteinuria in patients with diabetic nephropathy[6]. Sulodexide also has anti-coagulant[7, 8], anti-inflammatory[9, 10], and anti-oxidative effects, as well as the effect of regulating blood fat[11–13]. These functions are related to the progression of CRF. Thus, we explored the

# These authors contributed equally to this work.
* To whom correspondence should be addressed.
E-mail xmchen301@126.com
Received 2011-10-22 Accepted 2012-01-05

efficacy of sulodexide in a CRF rat model using irbesartan, a commonly used ARB drug, as a control.

Materials and methods

Animals and model establishment

Seventy-two male Wistar rats, weighing 250 g to 330 g, were purchased from Beijing Vital River Company (License No: SCXK Jing 2001-0007) and were raised by the SPF Lab Animal Center of PLA General Hospital. All of the rats were housed in a constant-temperature room (maintained at 25±2 °C) with a consistent light cycle (from 7:00 am to 7:00 pm) and were fed a standard rat diet (0.5% Na, 22% protein). After one week of adaptability feeding, 12 rats were chosen randomly to receive a sham operation, and 5/6 nephrectomy was performed in the other 60 rats.

The rats that underwent 5/6 nephrectomy were randomly divided into a model control group, a sulodexide group, an irbesartan group, and a group combining sulodexide and irbesartan. Drug treatment commenced one week after the operations. Sulodexide injections, supplied by Alfa Issermann Pharmaceutical Inc, China (batch No 1884), were administered at a dosage of 5 mg/kg every other day by muscular injection. Irbesartan was supplied by Hangzhou Sanofi-Aventis Minsheng Pharmaceutical Co, Ltd (batch No 1564) and was administrated by gastric perfusion at a dose of 20 mg/kg each day. The combined group was treated with the same methods as the sulodexide group and the irbesartan group. Distilled water was given to the sham operation group and to the model control group. The rats were weighed each week, and the dosages of drugs and distilled water were adjusted accordingly for the entire course of 12 weeks. After 12 weeks, the numbers of rats remaining in the analysis were: 7 (control), 10 (sulodexide), 11 (irbesartan) and 11 (combined) (Figure 1).

General condition and urine/blood tests

The animals' energy level, activity, hair luster and food intake were observed. Upon completion of the 12-week experiment, the rats' blood pressure was measured with an LE5002 blood pressure instrument (Panlab SL Inc, Barcelona, Spain). 24-h urine was collected before the operations and at 4, 8, and 12 weeks after drug treatment. Urine protein was detected with a BS-400 Biochemical Analyzer purchased from Mindray Bio-Medical Electronics Co Ltd, Shenzhen, China.

Prior to the operation and 4 and 8 weeks after drug administration, 0.5 mL of blood from the endocanthion was drawn for serum creatinine testing with the 7600 Type Automatic Biochemistry Analyzer (HITACHI, Japan). Upon completion of the 12-week experiment, serum creatinine, triglycerides and cholesterin were measured.

Kidney pathologic examinations

A portion of the renal tissue was fixed in 10% formalin, and another portion was quickly frozen and stored in liquid nitrogen. After fixation with 10% formalin, the renal tissue was routinely treated and paraffin-embedded, and 2-μm sections were made. After staining with periodic acid-Schiff stain, the following semiquantitative scores were obtained using light microscopy[3].

Glomerular sclerosis score

The score was graded from 0 to 4 points (0 points: normal glomerulus; 1 point: area of mesangial expansion or sclerosis <25%; 2 points: area of sclerosis from up to 25% to 50%; 3 points: area of sclerosis from up to 50% to 75%; 4 points: area of sclerosis greater than 75%). Fifty glomeruli were observed from each specimen under a microscope with 400-fold magnification, and the mean value was referred to as the glomerular sclerosis index.

Renal tubule-interstitium score

The score was based on tubular atrophy, interstitial inflammation, and fibrosis area. The score was graded from 0 to 3 points (0 points: free of tubulointerstitial lesions; 1 point: changes affecting <25% of the section; 2 points, changes affecting 25% to 50% of the section; and 3 points, changes affecting an area greater than 50%). Ten fields of vision were observed for each specimen under a microscope with 100-fold magnification. The mean value was referred to as the tubulointerstitial lesion index.

Immunohistochemistry (IHC)

After fixation with 4% paraformaldehyde, the renal tissue was submitted to routine treatment and was then embedded with paraffin, and 2-μm-thick sections were made before incubation with monoclonal JG-12 mouse anti-rat antibody (Santa Cruz Company, Santa Cruz, CA, USA), by means of the streptavidin-peroxidase method (Zhongshan Goldenbridge Biotechnology Co, Ltd, Beijing, China). The number of capillaries was counted per 0.01 mm^2 of glomerular area under a microscope with 400-fold magnification.

Expression of eNOS and tPA mRNA in the kidneys

Upon the thawing of the renal tissues that had been stored in liquid nitrogen, Trizol was added, and homogenization was conducted for 2–3 min with a supersonic crusher. After extraction by chloroform, settling with isopropanol, and cleansing with 75% ethanol, the sample was dissolved in DEPC water,

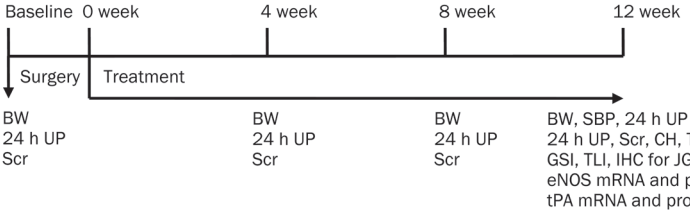

Figure 1. Animal experiments design.

and RNA was quantified with a UV spectrophotometer.

Five micrograms of RNA template was reverse transcribed (reverse transcription reagent box provided by GIBCO Company, MI, USA) into cDNA and was expanded by PCR. The primer sequences are shown in Table 1. The PCR reaction bulk was 25 μL, the sample cDNA product was 1 μL, the 10×PCR buffer was 2.5 μL; Tag DNA polymerase was 0.25 μL; and 2.5 mmol/L dNTP mix was 2.4 μL. We used 25 mmol/L Mg^{2+} 3.5 μL and 25 μmol/L primers (Beijing SBS Genetech Co, Ltd), 1 μL each; we also used 13.35 μL of deionized, distilled water.

Table 1. Primers sequences for PCR, annealing temperature, and predicted size.

Primers	Sequences	Annealing temperature (°C)	Predicted size (bp)
eNOS	5′-TAACACAGACAGTGCAGGGG-3′ 5′-CCTGGAACATCTTCCGTCTG-3′	62	380
tPA	5′-AGAGAGGTTTCCACCCCATC-3′ 5′-CTGTCCAGTCAGGGAGCTGT-3	58	248
GAPDH	5′-TGCACCACCAACTGCTTAGC-3′ 5′-GGCATGGACTGTGGTCATGAG-3′	58	191

The PCR products were subjected to electrophoresis on a 1.2% agarose gel before photographs were taken, and semi-quantitative analysis was carried out using Quantity One Software for gel quantitative analysis.

Evaluation of the expression of eNOS and tPA protein in the kidneys with Western blotting

The frozen renal tissue in liquid nitrogen was added to a suitable amount of buffer solution and was then homogenized. The protein concentration was measured by the Coomassie brilliant blue method. The proteins were denatured, electrophoresed, transferred to PVDF membrane, and blocked with 5% degreased milk. eNOS antibody, tPA antibody (rabbit anti-rat eNOS and tPA polyclonal antibody, Santa Cruz Biotechnology, Inc) and anti β-actin antibody (1:200 dilution) were added. Incubation took place overnight at 4 °C. After membrane washing, the secondary antibodies (dilution 1:1000) marked with horseradish peroxidase (HRP) were added. Quantitative analysis of eNOS and tPA was performed with Quantity One Software for gel quantitative analysis.

Statistical analysis

Statistical analysis was conducted with SPSS software, version 15.0. The data were expressed as the mean±standard deviation (mean±SD). ANOVA was adopted for the comparison between different groups at the same time points. The LSD method was adopted for comparisons between two groups. $P<0.05$ was considered statistically significant.

Results

General condition and blood pressure

In the beginning of the experiment, the rats in the sham operation group acted quickly, and their coats were lustrous and in good condition. Meanwhile, no abnormal conditions in their diets were observed. After the operations, the rats in all of the groups appeared listless, and they moved less. Their furs pricked up and did not show order or luster. As time went by, their entire skins gradually became white, especially the skin at the ears, nose, feet, back and tail. No hematomas or other adverse reactions at the injection sites were observed.

The mean blood pressure of the model control group (112±5 mmHg) was higher than that of the sham group (108±4 mmHg) at the 12th week of treatment ($P<0.05$). The blood pressure levels in the irbesartan-treated group (108±3 mmHg) and the group receiving combined sulodexide and irbesartan (105±4 mmHg) were lower than those of the model control group ($P<0.05$).

Body weight

There was no significant difference in body weight for the rats in any of the groups before the operations or after the 5/6 nephrectomy but prior to drug treatment (0 weeks). Body weight was lower in the experimental rats after the operations compared with the sham operation group ($P<0.05$). Body weight increased in all of the rats over time (Table 2).

Urinary protein and serum creatinine

Urinary protein and serum creatinine were not different among the 5 groups at baseline. Compared with the model

Table 2. Rats body weight condition at all groups. Mean±SD. $^bP<0.05$, $^cP<0.01$ *vs* Sham.

Group	Body weight (g)				
	Before operation	0 week	4 weeks	8 weeks	12 weeks
Sham (n=12)	282.84±18.51	364.89±25.17	447.36±32.08	491.46±53.68	532.01±56.84
Untreated (n=7)	282.45±20.28	312.26±20.47^b	381.68±28.53^c	431.46±37.02^b	454.44±56.65^b
IRB (n=11)	281.38±15.46	310.48±29.57^b	383.10±32.66^c	420.15±32.82^b	449.89±40.02^b
SLX (n=10)	275.50±12.57	317.47±20.04^b	384.48±28.11^c	431.54±32.41^b	445.40±53.52^b
SLX/IRB (n=11)	299.70±27.39	323.69±23.19^b	379.64±40.72^c	428.09±61.16^b	451.86±66.85^b

* Sham: sham group; Untreated: model control group; SLX: sulodexide treated group;
IRB: irbesartan treated group; SLX/IRB: combining group of sulodexide and irbesartan.

group, 24-h urine protein was clearly lower in the irbesartan group, the sulodexide group, and the combined sulodexide and irbesartan group than that in the control group after 8 and 12 weeks of treatment ($P<0.05$). Serum creatinine in the model control group increased gradually over time. From the 4th week after treatment, the levels of serum creatinine in the sulodexide group were lower than those of the model control group ($P<0.05$). After 12 weeks of treatment, the levels of serum creatinine in all of the treated groups were lower than those of the model control group (Table 3).

Serum cholesterin (CH) and triglycerides (TG)

In the 12th week after the operations, the level of serum cholesterin in the model control group was higher than in the sham group ($P<0.01$). The serum cholesterin level of the sulodexide-treated group was lower than that of the model control group ($P<0.05$). No differences were found in the levels of triglycerides among all of the groups (Table 4).

Pathology and immunohistochemistry

The model control group displayed glomerular hypertrophy, mesangial cell proliferation, mesangial matrix accumulation, telangiectasia or occlusions of the capillaries, thickening of the glomerular capsule wall, and focal or global sclerosis of some glomeruli. Furthermore, the renal tubules in this group showed dilation or atrophy, a large number of protein casts, interstitial widening, substantial infiltration of inflammatory cells, and focal distribution of renal interstitial microangiopathy, with narrowing and distortion of capillary cavities.

Compared with the model control group, the pathological changes in the sulodexide-treated group, the irbesartan-treated group, and the combination group were alleviated to different extents: lower glomerular sclerosis scores and tubulointerstitial scores were observed in these groups compared with the model control group (Figure 2, $P<0.05$).

JG-12 staining showed far fewer glomerular capillary loops per 0.01 mm^2 of cross-section area in the rats with 5/6 nephrectomy than in the sham group ($P<0.01$). There were more glomerular capillary loops per unit of area in the sulodexide-treated group and the combined sulodexide and irbesartan group than in the model control group ($P<0.05$) (Table 5).

Table 4. CH and TG changes after 12 weeks of treatment. Mean±SD. $^{b}P<0.05$, $^{c}P<0.01$ *vs* Sham. $^{e}P<0.05$ *vs* Model.

Group	Cholesterin (CH) (mmol/L)	Triglyceride (TG) (mmol/L)
Sham (*n*=12)	1.86±0.25	0.96±0.34
Model (*n*=7)	3.00±1.25^{c}	1.69±1.32
IRB (*n*=11)	2.70±0.37^{c}	1.39±0.63
SLX (*n*=10)	2.25±0.60^{e}	1.28±0.62
SLX/IRB (*n*=11)	2.50±0.50	0.96±0.49

The mRNA expression of eNOS and tPA

Compared with the sham group, the expressions of eNOS in the model control group was reduced ($P<0.01$); compared with the model control group, the expressions of eNOS mRNA

Table 5. Pathological scores and JG-12 immunohistochemistry staining after 12 weeks of treatment. Mean±SD. $^{b}P<0.05$, $^{c}P<0.01$ *vs* Sham. $^{e}P<0.05$, $^{f}P<0.01$ *vs* Model.

Groups	Glomerulus score	Tubulointerstitial score	Number of glomerular capillary loops (number/0.01 mm^2)
Sham (*n*=12)	0.05±0.02	0.05±0.05	12.99±4.02
Model (*n*=7)	1.83±0.32^{c}	2.10±0.12^{c}	4.72±2.91^{c}
IRB (*n*=11)	1.54±0.24^{cf}	1.71±0.30^{cf}	5.56±2.14^{c}
SLX (*n*=10)	1.58±0.21^{ce}	1.63±0.32^{cf}	7.28±3.01^{ce}
SLX/IRB (*n*=11)	1.50±0.27^{cf}	1.50±0.36^{cf}	7.12±4.45^{ce}

Table 3. Quantitative analysis of urine protein and serum creatinine. Mean±SD. $^{b}P<0.05$, $^{c}P<0.01$ *vs* Sham. $^{e}P<0.05$, $^{f}P<0.01$ *vs* Model.

Group	Urine protein quantity (mg/24 h)			
	Baseline	4 weeks	8 weeks	12 weeks
Sham (*n*=12)	9.86±4.57	11.34±3.57	19.21±5.94	17.83±4.22
Model (*n*=7)	9.57±5.35	34.79±15.11^{c}	119.91±23.60^{c}	159.19±66.51^{c}
IRB (*n*=11)	8.31±3.48	20.24±10.54	61.00±24.73^{cf}	65.70±20.98^{cf}
SLX (*n*=10)	9.33±4.41	31.00±21.10^{c}	65.16±24.50^{cf}	90.02±57.82^{ce}
SLX/IRB (*n*=11)	9.00±4.14	33.51±17.99^{c}	66.95±28.17^{cf}	59.13±32.30^{bf}
Group	Serum creatinine (μmol/L)			
	Baseline	4 weeks	8 weeks	12 weeks
Sham (*n*=12)	28.15±4.79	22.70±3.42	29.84±4.23	46.04±7.70
Model (*n*=7)	26.71±2.65	83.04±20.80^{c}	94.61±14.56^{c}	167.06±26.62^{c}
IRB (*n*=11)	25.74±1.16	76.74±19.67^{c}	86.94±20.96^{c}	130.09±29.84^{ce}
SLX (*n*=10)	25.62±1.49	60.31±14.33^{cf}	75.35±23.88^{ce}	125.84±60.58^{ce}
SLX/IRB (*n*=11)	26.11±3.40	71.47±24.75^{c}	85.47±28.58^{c}	121.39±33.55^{ce}

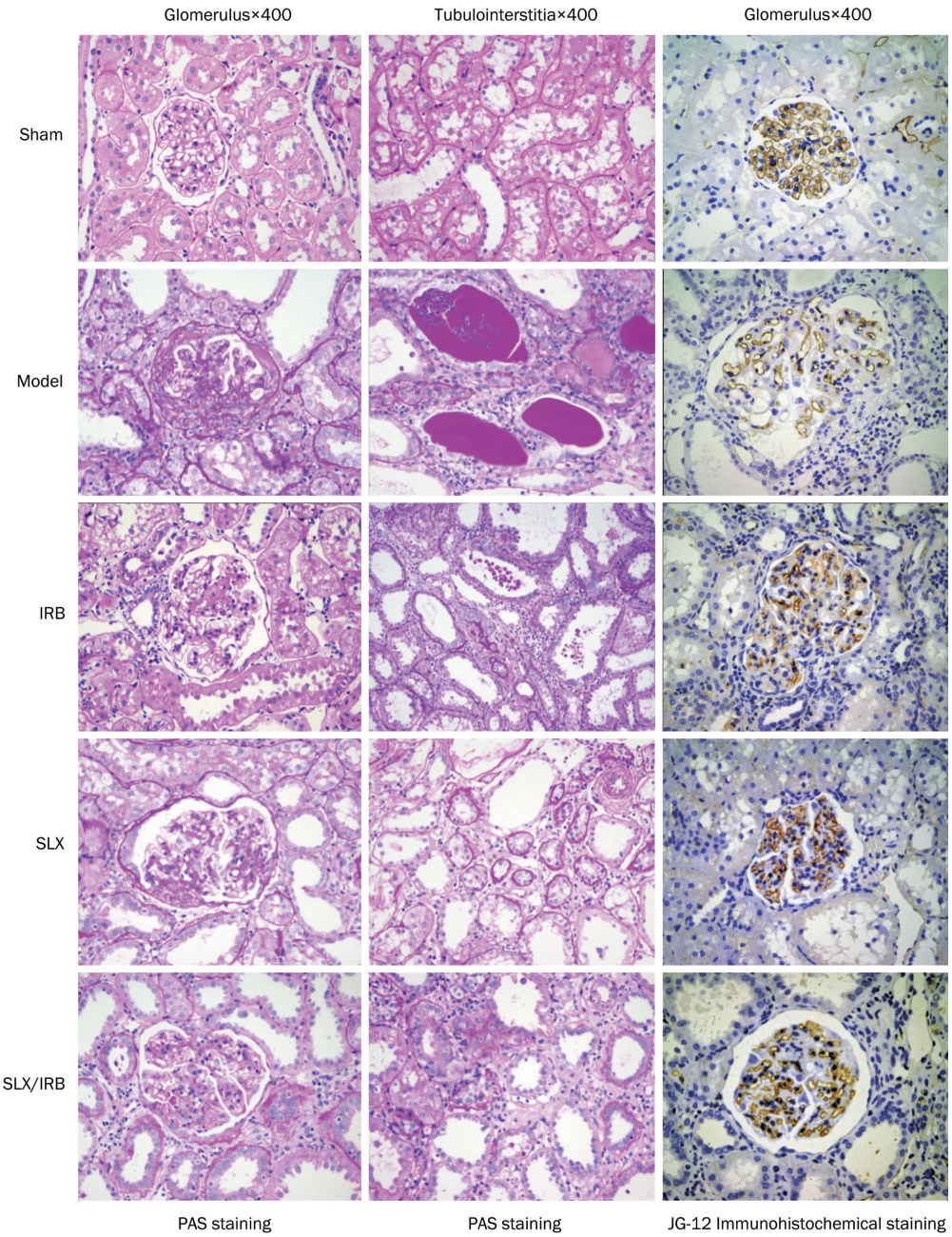

Figure 2. The glomerular and tubulointerstitial damage and loss of glomerular capillary loops were alleviated to different degrees in irbesartan (IRB), and sulodexide (SLX), and sulodexide combined with irbesartan (SLX/IRB) treated groups.

in the sulodexide-treated group, combined sulodexide and irbesartan therapy group, and irbesartan-treated group were increased (P<0.05, P<0.01, P<0.01, Figure 3A, 3B). The expression of tPA in the model control group was increased compared with Sham group, and the expression of tPA increased much more in the sulodexide-treated group, the combined sulodexide and irbesartan group, and irbesartan-treated group (all P<0.01, Figure 3A, 3C).

The protein expression of eNOS & tPA

Compared with the sham group, the protein expression of eNOS was reduced in the model control group (P<0.01). Compared with the model control group, the protein expression of eNOS was increased in the sulodexide-treated group, the combined sulodexide and irbesartan group, and the irbesartan-treated group (P<0.05) (Figure 4A, 4B).

The expression of tPA in the model control group was increased compared with Sham group (P<0.01), and it increased much more in the sulodexide-treated group, the combined sulodexide and irbesartan treated group, and irbesartan-treated group (P<0.01, P<0.01, P<0.05, Figure 4A, 4C).

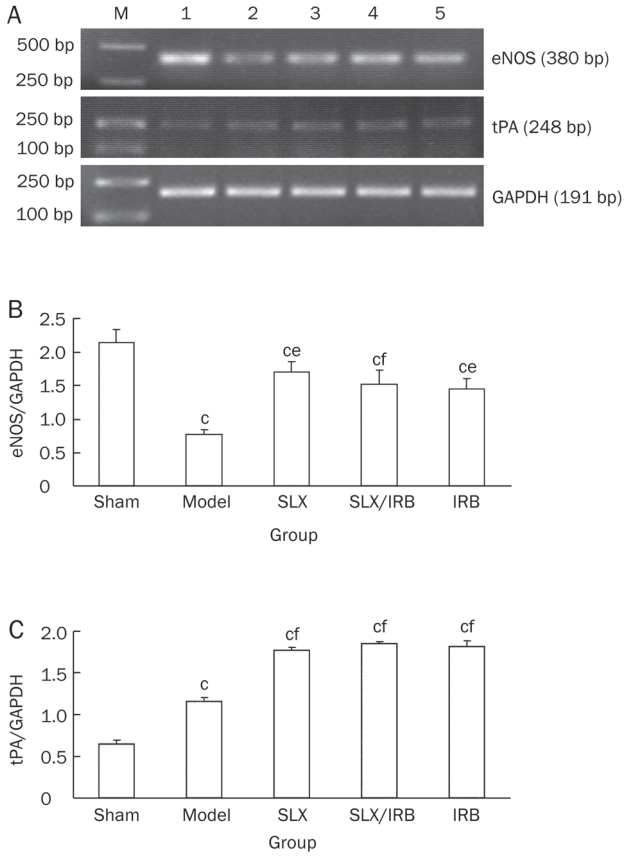

Figure 3. Semiquantitative analysis of renal mRNA eNOS (A, B) and tPA (A, C) expression after 12 weeks of treatment. $^{b}P<0.05$, $^{c}P<0.01$ *vs* sham group. Mean±SD. Sham: $n=12$; Model: $n=7$; SLX: $n=10$; SLX/IRB: $n=11$; IRB: $n=11$. $^{e}P<0.05$, $^{f}P<0.01$ *vs* model control group. M: marker; 1: Sham group; 2: model control group; 3: sulodexide treated group; 4: combined group of sulodexide and irbesartan; 5: irbesartan treated group.

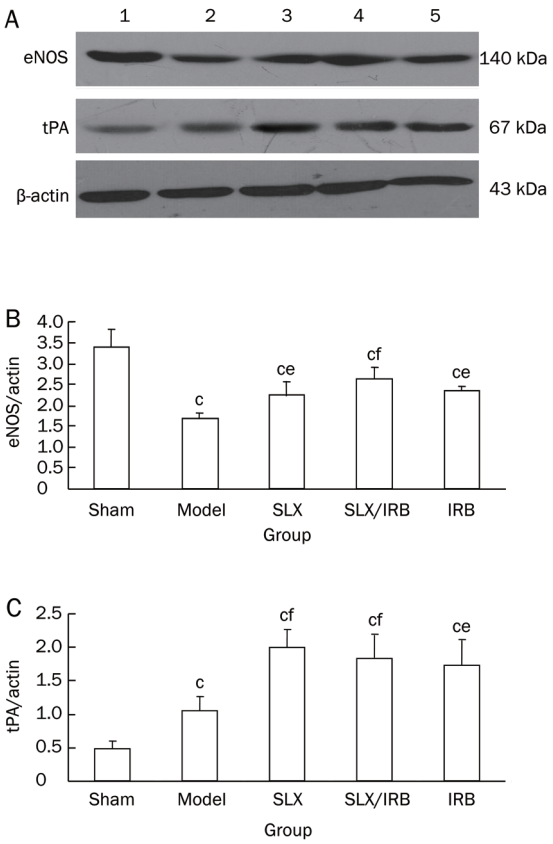

Figure 4. Analysis of renal eNOS (A, B) and tPA (A, C) protein expression after 12 weeks of treatment. 1: Sham group; 2: model control group; 3: sulodexide treated group; 4: combined therapy group of sulodexide and irbesartan; 5: irbesartan treated group. Mean±SD. Sham: $n=12$; Model: $n=7$; SLX: $n=10$; SLX/IRB: $n=11$; IRB: $n=11$. $^{b}P<0.05$, $^{c}P<0.01$ *vs* sham group; $^{e}P<0.05$, $^{f}P<0.01$ *vs* model control group.

Discussion

Sulodexide is a compound created from the fractional precipitation of glycosaminoglycans extracted from the mucosa of swine intestines, which mainly consists of fast-moving heparin (FMH) and dermatan sulfate (DS)[14]. Sulodexide has been used clinically in the treatment of patients with diabetic microvascular complications to reduce proteinuria in both type I and type II diabetes[15]. In a diabetic rat model induced by streptozotocin, sulodexide was reported to reduce the number of endothelial cells detached into the blood and to improve the diastolic function of the mesenteric artery[16]. However, whether sulodexide has a therapeutic function for the kidneys and for renal vascular endothelial cells in patients with CRF still needs to be demonstrated.

The 5/6 nephrectomy model is a common one for CRF[17, 18]. Sclerosis of the residual nephrons gradually occurs in response to the high perfusion, high pressure, and high filtration caused by 5/6 nephrectomy. The renal function will deteriorate, along with the retention of substances such as serum creatinine, which should be discharged via the kidney[19]. These changes are similar to the major mechanisms of renal function regression in CRF. In this study, after the establishment of the 5/6 nephrectomy model, it was observed that the serum creatinine and urine protein levels increased continually, together with changes in the development of glomerular sclerosis and interstitial fibrosis, which suggested that the model was successfully created.

Many animal experiments and clinical trials have demonstrated a sound curative effect of sulodexide for proteinuria in diabetic nephropathy[20–24]. As sulodexide consists of GAGs abundant in anion electrical charges, its effect in reducing proteinuria may be related to the recovery by the glomerular barrier of electric charges[22, 25]. Our results demonstrated that sulodexide was also able to reduce proteinuria in rats with 5/6 nephrectomy: 24-h urine protein was clearly lower in the sulodexide group and the combined sulodexide and irbesartan group than in the model control group after 8 or 12 weeks of treatment. In addition, the sulodexide group showed no difference in the degree of reduction of proteinuria compared with the irbesartan group, which resulted in the exciting finding that in rats with 5/6 nephrectomy, sulodexide was as effective as angiotensin receptor blocker (ARB)—the most approved agent in clinics for reducing proteinuria.

CRF is a disease that seriously endangers human health. Blocking renin-angiotensin-aldosterone system and controlling blood pressure are not sufficient to halt the progression of CRF[1]. It was in this study that sulodexide was first used in a 5/6 nephrectomy model. Over 4–12 weeks of treatment, sulodexide consistently decreased the levels of serum creatinine and steadily delayed the progression of renal failure. Furthermore, its effects were better than those of irbesartan in the early stages (fourth week). Unexpectedly, it was not observed that the combination of sulodexide and an ARB medicine had better effects. Currently, there is no proof that sulodexide and ARB medicines interact pharmacodynamically. The effect of sulodexide mainly focuses on the glomeruli, and sulodexide has an extremely high affinity for the vascular walls[26], whereas ARB drugs decrease the high filtration, high perfusion and the high pressure of the glomeruli. It is not clear whether the abovementioned functions interfere with sulodexide locating the capillary loop and recovering the basement membrane, which requires further research and confirmation.

Our results showed that sulodexide is as effective as irbesartan in mitigating glomerular sclerosis and tubulointerstitial fibrosis in rats with 5/6 nephrectomy. There is damage of the vascular endothelium in CRF patients, which can lead to the gradual loss of the renal capillary bed area; then, ischemia/hypoxia is involved in the continuous progression of renal pathological lesions. Mitigation of injury to renal vascular endothelial cells may delay the progression of CRF pathological lesions[20]. Promoting the repair of the injured endothelium can achieve the effect of stabilizing renal function and delaying the progression of pathological changes that are not related to the control of blood pressure and proteinuria[12]. It has been found in animal models that sulodexide protects vascular endothelial cells from detachment[26]. JG-12 is an aminopeptidase that anchors onto the cell membrane with glycosylphosphatidylinositol (GPI) and that serves as a specific marker for the vascular endothelium[27, 28]. Within the glomerular capsule, JG-12 is only expressed on the surface of the capillary endothelium[26, 29]. In our experiments, JG-12 immunohistochemical (IHC) staining showed that sulodexide was able to abrogate injury due to the loss of renal capillaries. However, irbesartan did not show the same effect.

In this study, we explored sulodexide's impact on two factors that are related to the function of the vascular endothelium: eNOS and tPA. In the kidney, eNOS remains mainly in the vascular endothelium[21, 22]. Previous studies have proved that nitric oxide, generated by eNOS, has a protective effect on the kidney[23]. NO is able to protect endothelial cells through its functions, including dilating blood vessels, inhibiting thrombocyte adhesion and aggregation, preventing white blood cells from attaching to the vascular wall, and inhibiting apoptosis of endothelial cells[24]. The expression of eNOS is reduced in damaged endothelial cells[25]. In this study, there was a decrease in both endothelial cells and eNOS expression in rats with 5/6 nephrectomy. After 12 weeks of treatment with sulodexide and irbesartan, renal eNOS expression clearly increased, suggesting a protective role for sulodexide in endothelial cells. Damaged endothelial cells also cause corresponding changes to their functions. One important physiological function of the endothelial cells is to regulate the proportion of blood-clotting substances and anti-clotting substances so the blood can flow smoothly in the vessels. Normal vascular endothelial cells manifest an "anti-clotting" phenotype. tPA and its specific inhibitor, type 1 plasminogen activator inhibitor (PAI-1), are mainly generated by vascular endothelial cells and are involved in the regulation of clotting and anti-clotting. The main function of tPA is to activate profibrinolysin in blood clots to produce fibrinolysin for the dissolution of thrombi. PAI-1 is a fast and specific physiological inhibitor of tPA. Both tPA and PAI-1 are markers for evaluating vascular endothelial function and injury. Under physiological conditions, tPA and PAI-1 are in states of dynamic equilibrium. Damaged endothelial cells transform from the anti-clotting type to the clotting type, with increased synthesis of PAI-1 and decreased synthesis of tPA[4, 30]. In our experiments, the increase in the expression of tPA in the model control group indicated an abnormal state of the clotting/anti-clotting system in this 5/6 nephrectomy model; that the expression of tPA increased much more in the sulodexide-treated group and the combined sulodexide and irbesartan group indicated a potential protective role for sulodexide in the endothelium.

Blood lipid disorders are among the complications of CRF that are related to the reduction of lipoprotein lipase activity, as well as the reduced intake of lipids in circulation by the organ and tissues[31]. Increased blood cholesterol can bind to receptors on the mesangial cells, leading to cellular proliferation, matrix accumulation, and the production of cytokines, which can boost the progression of pathological changes in renal sclerosis[32]. In animals fed a diet containing cholesterin, sulodexide was able to reduce the level of plasma cholesterin[12]. In the present study, the serum cholesterin levels of the sulodexide-treated group were significantly lower than those of the model control group. However, the irbesartan group did not show the same effect, which indicated that the efficacy of sulodexide treatment was related to the inhibition of CH production.

The progression of CRF involves a variety of mechanisms, including glomerular hemodynamic changes, proteinuria, angiotensin II, inflammation reactions, cellular proliferation, matrix accumulation, abnormal blood lipid metabolism, and the formation of microthrombi inside the capillaries. It has been shown that a single agent is unable to stop the progression of renal pathological changes in CRF[15]. In this study, we found that sulodexide has the effect of halting the deterioration of renal function in 5/6 nephrectomy rats, and it has the same efficacy at proteinuria reduction as irbesartan. Sulodexide has a renal protective role in mitigating glomerular sclerosis and tubulointerstitial fibrosis in rats that have undergone 5/6 nephrectomy. These effects might be achieved via protection of the vascular endothelium.

Acknowledgements

This work was supported by the following grants: Key science and technology Program of the Beijing Academy of Sciences(D09050104310000); "Significant Creation of New Drugs" of National Science and Major Project (2010ZX09102-204); National Natural Sciences Foundation of China (81072914)

Author contribution

Xiang-mei CHEN, Ru-juan XIE, Yuan-sheng XIE and Ri-bao WEI designed research; Lin-lin MA, Ping LI and Min YIN performed research; Ping LI and Lin-lin MA analyzed data; Ping LI, Lin-lin MA and Jian-zhong WANG wrote the paper.

References

1 Alborzi P, Patel NA, Peterson C, Bills JE, Bekele DM, Bunaye Z, *et al*. Paricalcitol reduces albuminuria and inflammation in chronic kidney disease: a randomized double-blind pilot trial. Hypertension 2008; 52: 249–55.
2 Kang DH, Kanellis J, Hugo C, Truong L, Anderson S, Kerjaschki D, *et al*. Role of the microvascular endothelium in progressive renal disease. J Am Soc Nephrol 2002; 13: 806–16.
3 Gadola L, Noboa O, Márquez MN, Rodriguez MJ, Nin N, Boggia J, *et al*. Calcium citrate ameliorates the progression of chronic renal injury. Kidney Int 2004; 65: 1224–30.
4 Vásquez J, Mathison Y, Romero-Vecchione E, Suárez C. Effect of sulodexide on aortic vasodilation capacity and associated morphological changes in rats with streptozotocin-induced diabetes. Invest Clin 2010; 51: 467–77.
5 Ceol M, Gambaro G, Sauer U, Baggio B, Anglani F, Forino M, *et al*. Glycosaminoglycan therapy prevents TGF-beta1 overexpression and pathologic changes in renal tissue of long-term diabetic rats. J Am Soc Nephrol 2000; 11: 2324–36.
6 Shah SV. Progress toward novel treatments for chronic kidney disease. J Ren Nutr 2010; 20: S122–6.
7 Cirujeda JL, Granado PC. A study on the safety, efficacy, and efficiency of sulodexide compared with acenocoumarol in secondary prophylaxis in patients with deep venous thrombosis. Angiology 2006; 57: 53–64.
8 Coccheri S, Scondotto G, Agnelli G, Aloisi D, Palazzini E, Zamboni V, *et al*. Randomised, double blind, multicentre, placebo controlled study of sulodexide in the treatment of venous leg ulcers. Thromb Haemost 2002; 87: 947–52.
9 Karoń J, Połubinska A, Antoniewicz AA, Sumińska-Jasińska K, Breborowicz A. Anti-inflammatory effect of sulodexide during acute peritonitis in rats. Blood Purif 2007; 25: 510–4.
10 Fracasso A, Baggio B, Masiero M, Bonfante L, Bazzato G, Feriani M, *et al*. Effect of oral treatment with the glycosaminoglycan sulodexide on peritoneal transport in CAPD patients. Perit Dial Int 2003; 23: 595–9.
11 Crepaldi G, Fellin R, Calabrò A, Baiocchi MR, Rossi A, Lenzi S, *et al*. Preliminary results of sulodexide treatment in patients with peripheral arteriosclerosis and hyperlipidemia. A multicentre trial. Monogr Atheroscler 1986; 14: 215–21.
12 Radhakrishnamurthy B, Sharma C, Bhandaru RR, Berenson GS, Stanzani L, Mastacchi R. Studies of chemical and biologic properties of a fraction of sulodexide, a heparin-like glycosaminoglycan. Atherosclerosis 1986; 60: 141–9.
13 Skrha J, Perusicová J, Kvasnicka J, Hilgertová J. The effect of glycosaminoglycan sulodexide on oxidative stress and fibrinolysis in diabetes mellitus. Sb Lek 1998; 99: 103–9.
14 Harenberg J. Review of pharmacodynamics, pharmacokinetics, and therapeutic properties of sulodexide. Med Res Rev 1998; 18: 1–20.
15 Perico N, Codreanu I, Schieppati A, Remuzzi G. Prevention of progression and remission/regression strategies for chronic renal diseases: can we do better now than five years ago? Kidney Int Suppl 2005; S21–4.
16 Hostetter TH, Olson JL, Rennke HG, Venkatachalam MA, Brenner BM. Hyperfiltration in remnant nephrons: a potentially adverse response to renal ablation. Am J Physiol 1981; 241: F85–93.
17 Matsumoto Y, Ueda S, Yamagishi S, Matsuguma K, Shibata R, Fukami K, *et al*. Dimethylarginine dimethylaminohydrolase prevents progression of renal dysfunction by inhibiting loss of peritubular capillaries and tubulointerstitial fibrosis in a rat model of chronic kidney disease. J Am Soc Nephrol 2007; 18: 1525–33.
18 Tsunenari I, *et al*. Renoprotective effects of telmisartan in the 5/6 nephrectomised rats. J Renin Angiotensin Aldosterone Syst 2007; 8: 93–100.
19 Hostetter TH, Olson JL, Rennke HG., Venkatachalam MA, Brenner BM. Hyperfiltration in remnant nephrons: a potentially adverse response to renal ablation. J Am Soc Nephrol 2001; 12: 1315–25.
20 Weiss R, Niecestro R, Raz I. The role of sulodexide in the treatment of diabetic nephropathy. Drugs 2007; 67: 2681–96.
21 Heerspink HL, Greene T, Lewis JB, Raz I, Rohde RD, Hunsicker LG, *et al*. Effects of sulodexide in patients with type 2 diabetes and persistent albuminuria. Nephrol Dial Transplant 2008; 23: 1946–54.
22 Gambaro G, Kinalska I, Oksa A, Pont'uch P, Hertlová M, Olsovsky J, *et al*. Oral sulodexide reduces albuminuria in microalbuminuric and macroalbuminuric type 1 and type 2 diabetic patients: the Di.N.A.S. randomized trial. J Am Soc Nephrol 2002; 13: 1615–25.
23 Achour A, Kacem M, Dibej K, Skhiri H, Bouraoui S, El May M, *et al*. One year course of oral sulodexide in the management of diabetic nephropathy. J Nephrol 2005; 18: 568–74.
24 Lambers Heerspink HJ, Fowler MJ, Volgi J, Reutens AT, Klein I, Herskovits TA, *et al*. Rationale for and study design of the sulodexide trials in type 2 diabetic, hypertensive patients with microalbuminuria or overt nephropathy. Diabet Med 2007; 24: 1290–5.
25 Dedov I, Shestakova M, Vorontzov A, Palazzini E. A randomized, controlled study of sulodexide therapy for the treatment of diabetic nephropathy. Nephrol Dial Transplant 1997; 12: 2295–300.
26 Kristova V, Liskova S, Sotnikova R, Vojtko R, Kurtansky A. Sulodexide improves endothelial dysfunction in streptozotocin-induced diabetes in rats. Physiol Res 2008; 57: 491–4.
27 Broekhuizen LN, Lemkes BA, Mooij HL, Meuwese MC, Verberne H, Holleman F, *et al*. Effect of sulodexide on endothelial glycocalyx and vascular permeability in patients with type 2 diabetes mellitus. Diabetologia 2010; 53: 2646–55.
28 Ciszewicz M, Polubinska A, Antoniewicz A, Suminska-Jasinska K, Breborowicz A. Sulodexide suppresses inflammation in human endothelial cells and prevents glucose cytotoxicity. Transl Res 2009; 153: 118–23.
29 Sulikowska B, Olejniczak H, Muszyńska M, Odrowaz-Sypniewska G, Gaddi A, Savini C, *et al*. Effect of sulodexide on albuminuria, NAG excretion and glomerular filtration response to dopamine in diabetic patients. Am J Nephrol 2006; 26: 621–8.
30 Messa G., La Placa G., Puccetti L, Di Perri T. Effectiveness and tolerability of heparan sulfate in the treatment of superficial thrombophlebitis. Controlled clinical study vs sulodexide. Minerva Cardioangiol 1997; 45: 147–53.
31 Kristová V, Kriska M, Babál P, Djibril MN, Slámová J, Kurtansky A. Evaluation of endothelium-protective effects of drugs in experimental models of endothelial damage. Physiol Res 2000; 49: 123–8.
32 Kristova V, Kriska M. Endothelial diseases and endothelium-protective agents. Bratisl Lek Listy 1998; 99: 511–7.

Acta Pharmacologica Sinica (2012) 33: 652–659
 1671-4083/12 $32.00
www.nature.com/aps

Original Article

Chronic ethanol consumption increases the levels of chemerin in the serum and adipose tissue of humans and rats

Rui-zhen REN[1, 2, 3, #], Xu ZHANG[1, 2, #], Jin XU[1, 2], Hai-qing ZHANG[1, 2], Chun-xiao YU[1, 2], Ming-feng CAO[1, 2], Ling GAO[4], Qing-bo GUAN[1, 2, *], Jia-jun ZHAO[1, 2, *]

[1]Department of Endocrinology, Provincial Hospital Affiliated to Shandong University, Ji'nan 250021, China; [2]Institute of Endocrinology, Shandong Academy of Clinical Medicine, Ji'nan 250021, China; [3]Department of Endocrinology, Yantai Yuhuangding Hospital Affiliated to Qingdao University, Yantai 264000, China; [4]Central Laboratory, Provincial Hospital Affiliated to Shandong University, Ji'nan 250021, China

Aim: Chemerin is a new adipokine involved in adipogenesis and insulin resistance. Since ethanol affects the insulin sensitivity that is closely associated with adipokines. The aim of this study was to investigate the effects of ethanol on chemerin in humans and rats.
Methods: In the human study, 148 men who consumed alcohol for more than 3 years and 55 men who abstained from alcohol were included. Based on ethanol consumption per day, the drinkers were classified into 3 groups: low-dose (<15 g/d), middle-dose (15–47.9 g/d) and high-dose (≥48 g/d). Anthropometric measurements and serum parameters were collected. In the rat study, 27 male Wistar rats were randomly divided into 4 groups administered water or ethanol (0.5, 2.5, or 5 $g{\cdot}kg^{-1}{\cdot}d^{-1}$) for 22 weeks. The chemerin levels in the sera, visceral adipose tissue (VAT) and liver were measured using ELISA.
Results: In the high-dose group of humans and middle- and high-dose groups of rats, chronic ethanol consumption significantly increased the serum chemerin level. Both the middle- and high-dose ethanol significantly increased the chemerin level in the VAT of rats. In humans, triglyceride, fasting glucose, insulin and HOMA-IR were independently associated with chemerin. In rats, the serum chemerin level was positively correlated with chemerin in the VAT after adjustments for the liver chemerin (r=+0.768). High-dose ethanol significantly increased the body fat in humans and the VAT in rats.
Conclusion: Chronic ethanol consumption dose-dependently increases the chemerin levels in the serum and VAT. The serum chemerin level is associated with metabolic parameters in humans. The increased serum chemerin level is mainly attributed to an elevation of chemerin in the VAT after the ethanol treatment.

Keywords: ethanol; adipokine; chemerin; insulin resistance; triglyceride; adipose tissue

Acta Pharmacologica Sinica (2012) 33: 652–659; doi: 10.1038/aps.2012.11; published online 26 Mar 2012

Introduction

Adipose tissue is classically considered a tissue that stores excess energy and provides insulation for the body; however, it is now considered to be an endocrine organ. The adipose tissue secretes multiple metabolic proteins known as adipokines, and some of these play important roles in glucose and lipid metabolism, insulin resistance, obesity and type 2 diabetes[1].

Chemerin, a newly found adipokine, is secreted as an 18-kDa inactive proprotein named prochemerin and is converted into the 16-kDa active chemerin by a serine protease cleavage of the C-terminal portion of the protein[2]. It is most highly expressed in the white adipose tissue and liver, which are followed by the lung, kidney, pituitary, placenta and ovary[3–5]. Chemerin is a novel chemoattractant protein that plays roles in adaptive and innate immunity[2, 5]. Recent research found that chemerin participated in the regulation of adipocyte differentiation[3, 4] and had effects on insulin sensitivity. Until now, the majority of studies have demonstrated that chemerin induces insulin resistance in the adipose tissue and skeletal muscle[6–8].

Ethanol consumption is a lifestyle factor and is relevant to type 2 diabetes. Moderate alcohol consumption and a high amount of alcohol intake produced different effects on lipid

# These authors contributed equally to this work.
* To whom correspondence should be addressed.
E-mail jjzhao@medmail.com.cn (Jia-jun ZHAO);
guanqingbo@medmail.com.cn (Qing-bo GUAN)
Received 2011-11-16 Accepted 2012-02-01

metabolism and insulin sensitivity[9, 10]. Until now, few studies have focused on the effects of ethanol on adipokines. Our previous study demonstrated that ethanol consumption elevated the leptin, resistin and visfatin levels and decreased the adiponectin concentrations in both the sera and visceral adipose tissues (VAT) of rats[11]. Unlike the other adipokines, chemerin was highly expressed in the adipose and liver tissues. Ethanol affects liver function, lipid metabolism and insulin sensitivity. Until now, there was no study on the correlations between chemerin and ethanol. Therefore, this study aimed to observe the effects of a long-term intake of different doses of ethanol on chemerin in humans and rats and to evaluate the relationship of chemerin with metabolic parameters in humans.

Materials and methods

Study 1: Human study

Subjects

Data were obtained from an epidemiological investigation of type 2 diabetes in the Shandong Provincial Hospital in China from September 2009 to June 2010. All of the participants were from two central communities (Shungen and Yangguang in Ji'nan, China), and were male who were 22–75 years of age and had been living here for more than 5 years. A total of 1502 men participated in the investigation. According to the study criteria, 148 men who consumed alcohol and 55 men who abstained from alcohol were included in the study.

The exclusion criteria were dependent on a self-reported history and the data from our measurements. The body mass indexes (BMI) of all of the subjects were less than 25 kg/m^2. Subjects were excluded for diabetes, any acute or chronic inflammatory diseases, hepatic diseases, liver function disorders, hypertension, cardiovascular or cerebrovascular diseases, renal diseases or thyroid diseases. None of the subjects were taking any medication that was known to influence glucose and lipid metabolism, blood pressure or weight. Each participant completed a self-administered questionnaire that included demographic characteristics, an ethanol and smoking history, a general health status and current medications. This study was approved by the Ethics Committee of the Shandong Provincial Hospital. The purposes and procedures of the study were explained to the participants prior to the questionnaire and fasting blood draw. Informed consents were obtained from all of the participants.

The ethanol intake was assessed by the frequency and amount of intake (a frequency of less than once per week was excluded). The average alcohol intake per day was calculated by the average quantity per occasion multiplied by the drinking frequency per week divided by seven. The drinkers were classified into three groups: a low-dose group (group L; ethanol consumption <15 g/d), a middle-dose group (group M; ethanol consumption 15–47.9 g/d), and a high-dose group (group H; ethanol consumption ≥48 g/d)[12, 13]. The length of time that each participant had been drinking was more than three years, and there was no difference among the three groups.

Anthropometric measurements

A complete physical examination was conducted on each individual under the condition of an empty bladder and stomach. The values of height and weight were taken with the subjects dressed in light clothing and without shoes. The height was determined to the nearest 1 cm, and the weight was determined to the nearest 0.5 kg. The BMI was calculated as the weight in kilograms divided by the height squared in meters. The waist circumference was measured at the midpoint between the lower costal margin and the iliac crest. The hip girth was measured as the horizontal circumference at the broadest part of the hip. The waist-to-hip ratio (WHR) was calculated as the waist circumference (cm) divided by hip circumference (cm). The percentage of body fat was assessed using the InBody720 body composition analyzer (Biospace, Seoul, Korea) and an established protocol.

Laboratory measurements

Blood samples were collected after an overnight fast. The serum samples were separated and immediately stored at -80 °C. The fasting plasma glucose (FPG) concentration was determined by the glucose oxidase method. The fasting serum insulin (FINS) was measured using a radioimmunoassay kit (Northern Bioengineering Institute, Beijing, China). The plasma concentrations of total cholesterol (TC), triglyceride (TG), low-density lipoprotein cholesterol (LDL-C), and high-density lipoprotein cholesterol (HDL-C) were measured using routine enzymatic methods with an Olympus 5400 Analyzer. The insulin sensitivity was estimated using the homeostasis model assessment for insulin resistance (HOMA-IR), which was calculated as fasting insulin (mU/L) multiplied by fasting glucose (mmol/L) divided by 22.5[14].

Study 2: Animal study

Animal protocols and housing

All animal protocols and procedures were approved by the Shandong University Institutional Animal Care and Use Committee (Ji'nan, China). Twenty-seven male Wistar rats (weights of 200–240 g; 8 weeks old) were purchased from the Experimental Animal Center, Shandong University, China. All rats were kept on a 12-h light and 12-h dark cycle in individual cages and had free access to water and normal chow. The rats were divided into four groups and given the following different treatments: control group (group C; distilled water at 5.0 $g{\cdot}kg^{-1}{\cdot}d^{-1}$), low-dose group (group L; ethanol at 0.5 $g{\cdot}kg^{-1}{\cdot}d^{-1}$), middle-dose group (group M; ethanol at 2.5 $g{\cdot}kg^{-1}{\cdot}d^{-1}$), and high-dose group (group H; ethanol at 5.0 $g{\cdot}kg^{-1}{\cdot}d^{-1}$). Distilled water or edible ethanol (50% *v/v*; Ji'nan Baotu Spring Distillery, Shandong, China) was given by a gastric tube every morning for 22 weeks. Using a body surface area conversion ratio between rats and humans, the ethanol dosages of 0.5, 2.5, and 5 $g{\cdot}kg^{-1}{\cdot}d^{-1}$ for the rats were equivalent to the dosages of 5.2, 27.3, and 53.95 g/d for a man weighing 65 kilograms, respectively. These three increasing ethanol treatments in rats were equal to the low-, middle-, and high-dose groups of humans.

Blood and tissue collection

Blood samples from all of the rats were obtained from the inferior vena cava after anesthetization by an intraperitoneal injection of sodium pentobarbital (0.1 mL/100 g body weight) after an overnight fast. The serum samples were separated after centrifugation and immediately stored at -80 °C for subsequent analyses. The epididymal and perirenal fat pads and livers were removed and rapidly frozen in liquid nitrogen for adipokine measurements.

Laboratory measurements

The FPG, FINS, and HOMA-IR were determined and calculated as described above. Samples of the liver and adipose tissues (200 mg) were excised from the frozen specimens while on ice. The excised tissues were added to 200 μL of phosphate-buffered saline (PBS) (pH 7.4) and homogenized using a VCX450 ultrasonic cell disruption system (Xinzhi Biotechnology Co, Ltd, Ningbo, China; homogenization parameters: time=30 s, temperature=4 °C, pulse on=3 s, pulse off=5 s and amplifier=28%–30%). The tissue homogenates were frozen overnight at -80 °C and thawed on ice the following day. After two freeze-thaw cycles, the homogenates were centrifuged with a high-speed refrigerated centrifuge (Beckman, Indianapolis, USA; Parameters: revolution=15 000 rounds per minute, time=30 min and temperature=4 °C). The middle layer of the adipose tissue homogenate and the supernatant of the liver homogenate were isolated and stored at -80 °C to determine the total protein level and chemerin concentration. The total protein concentrations of the liver and adipose tissues were measured with a protein assay kit (BCA; Bio-Rad, Hercules, CA, USA).

Enzyme-linked immunosorbent assay (ELISA)

The chemerin levels of humans and rats were determined by commercially available ELISA kits according to the manufacturer's instructions (Uscn Life Science & Technology Co, Ltd, Wuhan, China). The concentrations in the sera of humans and rats were directly determined without dilution. The isolated protein lysates were diluted to determine the chemerin levels because the isolated protein concentration of each liver and adipose tissue was different. Equal concentrations of isolated protein from the liver and VAT were taken to determine the chemerin content per 100 mg of protein.

Statistical analysis

Before proceeding with the statistical analysis, all of the parameters were tested for a normal distribution using the Kolmogorov-Smirnov test. Parameters that were not normally distributed were transformed to approximate a normal distribution. Comparisons between different groups of normally distributed parameters were made using an ANOVA, which was followed by a least-significant difference (LSD) *post hoc* test, and the parameters with skewed variables were tested by a Mann-Whitney U test. An analysis of covariance was carried out to compare the differences among the four groups of humans after adjustments for age. The descriptive data are presented as the mean±standard deviation (SD) and medians (interquartile range). Correlation analyses were performed using Pearson's test. A multiple linear regression analysis was performed to identify independent factors affecting the chemerin levels. Statistical analyses were performed using SPSS (Statistical Package for Social Sciences) 12.0 for Windows (SPSS, Chicago, IL, USA). Statistical significance was defined as $P<0.05$.

Results

Anthropometric and metabolic characteristics of the human participants

Anthropometric and metabolic characteristics of the subgroups studied are presented in Table 1. Lipid components, including the HDL-C, TC, and TG levels, increased with an elevated ethanol intake. Likewise, anthropometric parameters, including the WHR, body fat, waist-hip ratio of body fat, and percentage of body fat, were also elevated in group H. The FPG, FINS, and HOMA-IR in group H were also significantly elevated compared with group C. Because the average age of group H was significantly higher than the average ages of group C, group L, and group M, we further adjusted for age among the groups. Only the body fat, percentage of body fat, waist-hip ratio of body fat, TG, FPG, FINS, and HOMA-IR in group H were significantly elevated compared with group C after the adjustment for age (Table 2).

Chronic ethanol consumption increased serum chemerin in humans

Chronic ethanol consumption caused a dose-dependent increase of chemerin in human sera. The chemerin levels in group L, group M, and group H increased by 9.75% (P=0.265), 13.84% (P=0.094), and 40.83% (P<0.001), respectively, compared to group C (Table 1). Furthermore, even after the adjustment for age, chemerin remained significantly different among the groups (Table 2).

Serum chemerin levels are associated with TG and HOMA-IR in humans

A Pearson's correlation analysis was performed between the serum chemerin concentrations and the clinical characteristics (Table 3). The results showed that the chemerin levels positively correlated with the BMI, body fat, TG, FPG, FINS, and HOMA-IR and negatively correlated with the HDL-C. To study the factors that influenced the circulating chemerin, we performed a multivariate linear regression analysis using chemerin as the dependent variable (Table 4). The results revealed that the TG, FPG, FINS, and HOMA-IR were independently associated with the chemerin concentrations.

Characterization of the rats

The FINS levels and HOMA-IR of rats increased in the ethanol-treated groups compared with the controls. The rats in the four groups had similar body weights (BWs) at baseline. However, the BWs of group H decreased and the ratio of the epididymal adipose tissue weight to the BW of group H

Table 1. Clinical and laboratory characteristics of different groups in human. Log10 transformed FINS, FPG, HOMA-IR, and TG were used for statistical analysis. Normally distributed data are mean±SD and analyzed by ANOVA. Nonnormally distributed parameters are median (interquartile range) and analyzed by Mann-Whitney U test. Group C, control group; group L, low-dose group (ethanol <15 g/d); group M, middle-dose group (ethanol 15–47.9 g/d); group H, high-dose group (ethanol ≥48 g/d); BMI, body mass index; WHR, waist-hip ratio; WHR of body fat (BF), ratio of waist fat to hip fat; PBF, percentage of body fat; TC, total cholesterol; HDL-C, high-density lipoprotein cholesterol; LDL-C, low-density lipoprotein cholesterol; TG, triglycerides; FPG, fasting plasma glucose concentration; FINS, fasting insulin concentration; HOMA-IR, homeostatic model assessment of insulin resistance. [b]*P*<0.05, [c]*P*<0.01 *vs* group C. [e]*P*<0.05, [f]*P*<0.01 *vs* group L. [h]*P*<0.05, [i]*P*<0.01 *vs* group M.

Characteristics	Group C *n*=55	Group L *n*=54	Group M *n*=54	Group H *n*=40
Age (year)	42.96±15.16	42.61±14.25	43.89±15.27	51.08±12.30[cfh]
BMI (kg/m^2)	22.15 (20.79–24.10)	22.64 (21.13–24.23)	22.47 (21.59–23.65)	23.17 (20.99–23.84)
WHR	0.86 (0.84–0.89)	0.84 (0.82-0.88)	0.84 (0.82–0.88)	0.89 (0.85–0.91)[cfi]
WHR of BF	0.87 (0.84–0.90)	0.89 (0.86–0.92)	0.88 (0.85–0.91)	0.91 (0.90–0.94)[cfi]
Body fat (kg)	12.43±4.08	14.16±3.85	13.63±4.26	15.71±4.04[ch]
PBF (%)	19.31±5.77	21.13±2.50	20.70±5.94	22.59±5.07[c]
TC (mmol/L)	4.92±0.93	4.83±0.92	5.12±1.02	5.25±0.81[e]
HDL-C (mmol/L)	1.44±0.24	1.50±0.30	1.51±0.34	1.60±0.44[b]
LDL-C (mmol/L)	2.72±0.67	2.30±0.78	2.98±0.76	2.99±0.63
TG (mmol/L)	1.12±0.57	1.12±0.44	1.27±0.64	1.68±1.45[be]
FPG (mmol/L)	4.92±0.47	4.99±0.44	5.10±0.53	5.39±0.55[cfi]
FINS (mU/L)	5.05±1.85	5.89±3.03	5.53±2.73	6.68±3.40[b]
HOMA-IR	1.11±0.41	1.32±0.71	1.26±0.64	1.60±0.85[ceh]
Chemerin (ng/mL)	14.67±7.02	16.10±7.71	16.70±7.07	20.66±7.18[cfi]

Table 2. Comparison of characteristics between different groups in human adjusted for age. Analysis of covariance was carried out to compare the difference between the four groups in human adjusted for age. Log10 transformed FINS, FPG, HOMA-IR, and TG were used for statistical analysis. ARSIN transformed WHR of BF, COS transformed WHR and SQRT transformed BMI were used for statistical analysis. [b]*P*<0.05, [c]*P*<0.01 *vs* group C. [e]*P*<0.05, [f]*P*<0.01 *vs* group L. [h]*P*<0.05, [i]*P*<0.01 *vs* group M.

Characteristics	Group C *n*=55	Group L *n*=54	Group M *n*=54	Group H *n*=40
BMI (kg/m^2)	22.17±1.87	22.66±1.82	22.48±1.52	23.19±1.57
WHR	0.86±0.01	0.85±0.01	0.84±0.01	0.88±0.01
WHR of BF	0.87±0.17	0.90±0.18	0.86±0.18	0.91±0.21[ci]
Body fat (kg)	12.54±4.08	14.30±3.85[b]	13.68±4.26	15.31±4.04[c]
PBF (%)	19.53±5.77	21.42±2.50	20.80±5.94	21.79±5.07[b]
TC (mmol/L)	4.95±0.93	4.87±0.92	5.14±1.02	5.13±0.81
HDL-C (mmol/L)	1.44±0.24	1.50±0.30	1.52±0.34	1.58±0.44
LDL-C (mmol/L)	2.74±0.67	2.93±0.78	2.99±0.76	2.90±0.63
TG (mmol/L)	1.11±0.57	1.11±0.44	1.27±0.64	1.71±1.45[be]
FPG (mmol/L)	4.94±0.47	5.01±0.44	5.50±0.53	6.94±0.55[cfh]
FINS (mU/L)	4.98±1.85	5.81±3.03	5.50±2.73	6.68±3.40[ceh]
HOMA-IR	1.11±0.41	1.30±0.71	1.25±0.64	1.64±0.85[cei]
Chemerin (ng/mL)	14.56±7.02	15.96±7.71	16.65±7.07	21.06±7.18[cfi]

increased significantly compared to the control group after the 22-week treatment (Table 5).

Chronic ethanol treatment increased the chemerin levels in the sera and VAT of the rats

To observe changes in chemerin of rats after an ethanol treatment, we measured the chemerin levels in the sera, livers, and adipose tissues of rats with and without an ethanol treatment. The sera chemerin concentrations of rats in group M and group H were significantly higher than those in group C (18.26±3.07 and 22.00±5.96 *vs* 14.57±1.39 pg/mL, respectively; both $P<0.01$) (Figure 1A). Similarly, the chemerin levels in the adipose tissues from group M and group H were elevated compared to those from group C (3.87±0.69 and 4.31±1.08 *vs* 2.87±0.74 ng/100 mg protein, respectively; $P<0.05$ and $P<0.01$, respectively) (Figure 1B). The chemerin levels in the livers

Table 3. Correlation between serum chemerin concentration and metabolic variables.

Variables	*r*	*P*
Age (year)	-0.022	0.752
BMI (kg/m^2)	0.240	0.001
WHR	0.122	0.085
WHR of BF	0.029	0.686
Body fat (kg)	0.171	0.015
PBF (%)	0.097	0.171
TC (mmol/L)	0.014	0.846
HDL-C (mmol/L)	-0.156	0.026
LDL-C (mmol/L)	0.011	0.877
TG (mmol/L)	0.339	<0.001
FPG (mmol/L)	0.261	<0.001
FINS (mU/L)	0.499	<0.001
HOMA-IR	0.529	<0.001

Table 4. Linear regression analysis of variables associated with serum chemerin levels in human. In multiple linear regression analysis using sera chemerin as dependent varable, values included were TG, FPG, FINS, and HOMA-IR.

Independent	β	*P*
Age (year)	0.001	0.263
BMI (kg/m^2)	0.009	0.328
WHR	0.063	0.646
WHR of BF	0.001	0.957
Body fat (kg)	-0.004	0.667
PBF (%)	-0.001	0.821
TC (mmol/L)	-0.041	0.230
HDL-C (mmol/L)	0.013	0.768
LDL-C (mmol/L)	0.035	0.376
TG (mmol/L)	0.056	0.001
FPG (mmol/L)	0.154	<0.001
FINS (mU/L)	0.117	0.001
HOMA-IR	0.387	0.011

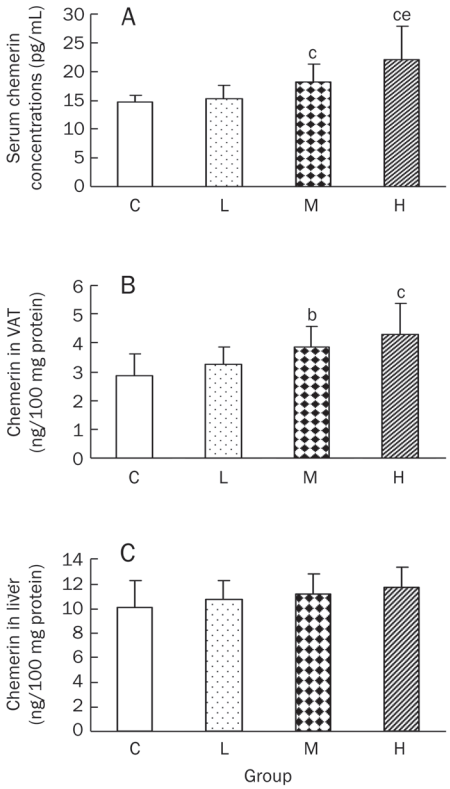

Figure 1. The effects of chronic ethanol treatment on the chemerin levels in serum (A), VAT (B), and liver (C) of rats. Wistar rats in group C, group L, group M, and group H were fed with edible ethanol doses of 0, 0.5, 2.5, and 5.0 g·kg^{-1}·d^{-1}, respectively, for 22 weeks. The chemerin levels in the sera, VATs and livers were measured by ELISAs. The values are given as the mean±SD (*n*=9 in group C; *n*=6 in group L, group M and group H). VAT, visceral adipose tissue. ^{b}P<0.05, ^{c}P<0.01 *vs* group C. ^{e}P<0.05 *vs* group L.

also had a tendency to rise, but the increase was not statistically significant (Figure 1C).

Positive correlation of chemerin levels between the serum and VAT

To clarify the source of the elevated chemerin levels, we con-

Table 5. Characterization of rats treated with different dosages of ethanol. Wistar rats in group C, group L, group M and group H were fed with edible ethanol at doses of 0, 0.5, 2.5, and 5.0 g·kg^{-1}·d^{-1} for 22 weeks, respectively. Data are mean±SD and analyzed by ANOVA. BW, body weight; EAT, ratio of epididymal adipose tissue weight to body weight; PAT, ratio of perinephric adipose tissue weight to body weight; FPG, fasting plasma glucose concentration; FINS, fasting insulin concentration; HOMA-IR, homeostatic model assessment of insulin. ^{b}P<0.05, ^{c}P<0.01 *vs* group C; ^{e}P<0.05, ^{f}P<0.01 *vs* group L; ^{h}P<0.05 *vs* group M.

Characteristics	Group C *n*=9	Group L *n*=6	Group M *n*=6	Group H *n*=6
Initia BW (g)	221.56±9.13	223.83±11.57	219.33±13.03	225.00±11.44
Final BW (g)	436.00±16.65	433.67±14.36	413.00±14.18^{ce}	408.83±15.11^{ce}
EAT (% of BW)	0.93±0.07	0.92±0.07	0.98±0.08	1.10±0.11^{cfh}
PAT (% of BW)	1.11±0.10	1.04±0.08	1.09±0.09	1.13±0.10
FPG (mmol/L)	3.72±0.54	3.45±0.34	3.52±0.56	3.55±0.48
FINS (mIU/L)	22.03±4.96	24.33±10.34	26.31±12.12	32.68±10.36^{b}
HOMA-IR	3.61±0.83	3.83±2.08	4.05±1.71	5.20±1.91^{b}

ducted a correlation analysis between the serum and VAT or liver chemerin (Figure 2). The results showed that the serum chemerin concentrations were positively associated with the chemerin in the VAT after adjusting for the liver chemerin. The relationship between the serum and liver chemerin was not statistically significant after adjusting for the chemerin in the VAT.

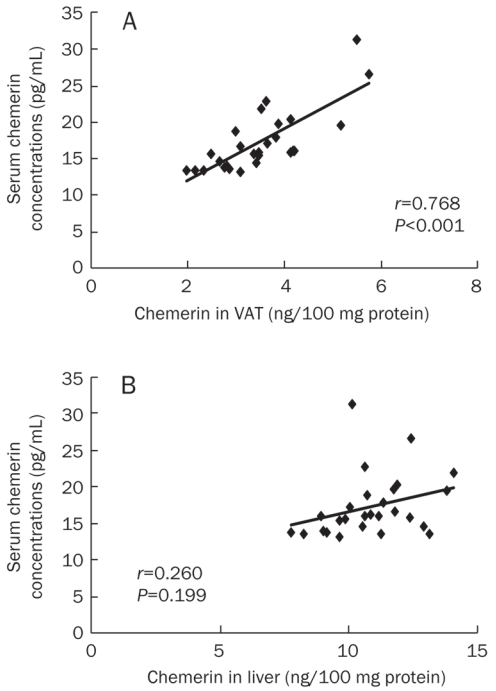

Figure 2. Correlation of the chemerin levels between the sera and tissues of the rats. Wistar rats in group C, group L, group M, and group H were fed with edible ethanol doses of 0, 0.5, 2.5, and 5.0 g·kg^{-1}·d^{-1}, respectively, for 22 weeks. The chemerin levels in the sera, VATs and livers were measured by ELISAs. (A) The correlation between the serum and VAT chemerin levels after adjusting for the liver chemerin. (B) The correlation between the serum and liver chemerin levels after adjusting for the VAT chemerin. VAT, visceral adipose tissue.

Discussion

In this study, we found that the serum chemerin concentrations in both humans and rats were elevated with increasing doses of ethanol. Furthermore, the serum chemerin was associated with TG and the HOMA-IR in humans. The increase in serum chemerin was mainly attributed to the elevation of chemerin in the VAT of rats.

We observed that ethanol increased the serum chemerin, which was associated with TG in humans. Ethanol may increase chemerin via the mechanisms discussed below. Studies have demonstrated that ethanol increased the circulating free fatty acid (FFA) levels[15, 16], which induced chemerin significantly in differentiated 3T3-L1 cells and elevated the soluble chemerin in the supernatant[17]. Chronic ethanol ingestion increased the circulating levels of lipopolysaccharide (LPS), and the differentiation of 3T3-L1 cells in the presence of LPS significantly induced cellular and soluble chemerin[17, 18]. Moreover, our previous study observed that chronic ethanol consumption caused a dose-dependent increase of TNF-α in the sera of rats[11]. An *in vitro* chronic ethanol treatment also increased TNF-α in peripheral blood monocytes[19]. TNF-α induced the chemerin mRNA expression in 3T3-L1 adipocytes in a dose- and time-dependent manner and increased the bioactive chemerin levels in the mouse serum and primary adipocyte media[8, 20]. Similarly, chronic alcohol consumption increased interleukin-1-beta (IL-1β) *in vivo* and *in vitro*. In 3T3-L1 adipocytes and brown fat cells, IL-1β stimulated the chemerin gene expression and induced the chemerin protein secretion in a dose-dependent fashion[7, 21–24]. In addition, we also observed that ethanol increased insulin and the HOMA-IR, which were independently associated with chemerin, in the human study. Tan *et al* reported that insulin elevated the chemerin level in human adipose tissue explants *in vitro* and in healthy individuals[25]. Conversely, the ethanol-induced increase of chemerin may be involved in ethanol-induced insulin resistance. Previous research demonstrated that chemerin played roles in insulin resistance by decreasing glucose transport and interfering with insulin signaling transduction[6–8]. The elevated insulin level that is induced by ethanol led to an increase of chemerin, and the increased chemerin may participate in insulin resistance, thereby forming a vicious cycle.

Although the chemerin levels increased with higher doses of ethanol in the sera of humans and rats, the elevations in the middle-dose group of rats were more significant than those in the humans. Species differences and the ethanol consumption pattern may partly contribute to this phenomenon. The rats were given a fixed dose of ethanol once a day at the same time by a gastric tube over a short period of time, and most of the ethanol was absorbed. In contrast, the human subjects usually drank slowly during meals, and the absorption of ethanol was diminished. Therefore, the peak ethanol concentration in rats was higher than that in humans at the same dose of ethanol, which resulted in a more severe insulin resistance in the rats. Accordingly, the chemerin levels that were induced by the elevated insulin in the rats were higher than those in the humans.

The source of the circulating chemerin is presently unclear. Both the liver and white adipose tissue highly expressed chemerin[3, 4]. To determine the source of the elevated serum chemerin after the ethanol treatment, we tested the chemerin concentrations in the VAT and liver. The results showed that the chemerin levels in the liver were higher than those in the VAT, but the chemerin levels in the VAT positively correlated with the serum chemerin after adjusting for the liver chemerin. Therefore, we inferred that the increased serum chemerin was mainly attributed to the elevated VAT chemerin after the ethanol treatment. Ethanol significantly increased the VAT in both humans and rats, and the increased adipose tissue may directly secrete more chemerin. Alternatively, ethanol may induce the VAT chemerin via the various mechanisms that were discussed prior. Nevertheless, the consistency of the elevated chemerin in the serum and adipose tissues cannot be

completely explained. Further research should be conducted to determine the mechanism.

Our study showed that after adjusting for age, the elevation of TG in group H remained significant. This may be because ethanol increased the FFAs, and more FFAs participated in the anabolism of TG, which led to the increased TG. Whether the ethanol-induced increase of chemerin plays a role in lipid metabolism is unknown, and further research is required for elucidation. Our study also found that the WHR and waist-hip ratio of body fat in the high-dose group were significantly higher than those in the control group. Similarly, the relative weights of the epididymal adipose tissue increased in the high-dose group of rats even though their body weight decreased. In this study, we observed that the high-dose ethanol increased insulin and the HOMA-IR in both humans and rats. Many studies have demonstrated that insulin was responsible for primary preadipocyte differentiation and confirmed its adipogenic effect[26–28]. Elevated insulin, which was induced by ethanol, may increase the fat mass by its adipogenic effect. Alternatively, an ethanol treatment also upregulated sterol regulatory element-binding protein-1 (SREBP-1), and SREBP-1 activated a cascade of genes that are required for endogenous lipogenesis and pre-adipocyte differentiation[29, 30]. In addition, the ethanol-induced increase of chemerin may also participate in adipocyte differentiation, thereby leading to the elevation of fat mass[3, 4]. Meanwhile, the increased fat might synthesize and secrete more chemerin, which is involved in adipocyte differentiation, and thereby generate a vicious cycle of elevated adipogenesis.

This study had some limitations. First, because there are fewer female drinkers than male drinkers and to eliminate the effects of endogenous sex hormones, we chose to study only male drinkers. Accordingly, we selected male Wistar rats for the animal experiment. Second, samples of adipose tissue and livers from humans were difficult to acquire, and therefore, we selected rats for the study of chemerin levels in tissues. In addition, although the current study was capable of identifying correlations between ethanol and chemerin, further experimental studies are required to unravel the molecular mechanism for the observed associations between ethanol and chemerin.

In conclusion, our study demonstrates that ethanol treatment increases serum chemerin and that chemerin levels are associated with several key parameters of metabolic syndrome. Moreover, the ethanol-induced elevation of serum chemerin was mainly derived from adipose tissue. Chemerin may participate in chronic, ethanol-induced insulin resistance and lipid metabolism disorder. Lower TG and reduced body fat may decrease the chemerin level and consequently decrease the insulin resistance that is induced by ethanol.

Acknowledgements

We thank the staff of the central laboratory at the Provincial Hospital that is affiliated with Shandong University for their pertinent advice and excellent technical assistance.

This work was supported by the National Natural Science Foundation of China (No 30940038) and the Natural Science Foundation of Shandong Province, China (No ZR2009CM008).

Author contribution

Jia-jun ZHAO and Qing-bo GUAN designed the research; Rui-zhen REN was responsible for the practical parts of the study, including participating in the epidemiological investigation, conducting experiments, analyzing the data and writing the article; Xu ZHANG participated in the epidemiological investigation and the experiments; Jin XU, Hai-qing ZHANG, and Ming-feng CAO participated in the epidemiological investigation and human sera collection; Chun-xiao YU and Ling GAO supervised the experiments; and Ling GAO was also responsible for revising the manuscript.

References

1 Rosen ED, Spiegelman BM. Adipocytes as regulators of energy balance and glucose homeostasis. Nature 2006; 444: 847–53.
2 Nagpal S, Patel S, Jacobe H, DiSepio D, Ghosn C, Malhotra M, *et al*. Tazarotene-induced gene 2 (TIG2), a novel retinoid-responsive gene in skin. J Invest Dermatol 1997; 109: 91–5.
3 Goralski KB, McCarthy TC, Hanniman EA, Zabel BA, Butcher EC, Parlee SD, *et al*. Chemerin, a novel adipokine that regulates adipogenesis and adipocyte metabolism. J Biol Chem 2007; 282: 28175–88.
4 Roh SG, Song SH, Choi KC, Katoh K, Wittamer V, Parmentier M, *et al*. Chemerin — a new adipokine that modulates adipogenesis via its own receptor. Biochem Biophys Res Commun 2007; 362: 1013–8.
5 Wittamer V, Franssen JD, Vulcano M, Mirjolet JF, Le Poul E, Migeotte I, *et al*. Specific recruitment of antigen-presenting cell by chemerin, a novel processed ligand from human inflammatory fluids. J Exp Med 2003; 198: 977–85.
6 Becker M, Rabe K, Lebherz C, Zugwurst J, Göke B, Parhofer KG, *et al*. Expression of human chemerin induces insulin resistance in the skeletal muscle but does not affect weight, lipid levels and atherosclerosis in LDL receptor knockout mice on high fat diet. Diabetes 2010; 59: 2898–903.
7 Kralisch S, Weise S, Sommer G, Lipfert J, Lossner U, Bluher M, *et al*. Interleukin-1 beta induces the novel adipokine chemerin in adipocytes *in vitro*. Regul Pept 2009; 154: 102–6.
8 Sell H, Laurencikiene J, Taube A, Eckardt K, Cramer A, Horrighs A, *et al*. Chemerin is a novel adipocyte-derived factor inducing insulin resistance in primary human skeletal muscle cells. Diabetes 2009; 58: 2731–40.
9 Greenfield JR, Samaras K, Jenkins AB, Kelly PJ, Spector TD, Campbell LV. Moderate alcohol consumption, estrogen replacement therapy and physical activity are associated with increased insulin sensitivity: is abdominal adiposity the mediator? Diabetes Care 2003; 26: 2734–40.
10 Kang L, Sebastian BM, Pritchard MT, Pratt BT, Previs SF, Nagy LE. Chronic ethanol-induced insulin resistance is associated with macrophage infiltration into adipose tissue and altered expression of adipocytokines. Alcohol Clin Exp Res 2007; 31: 1581–8.
11 Yu HC, Li SY, Cao MF, Jiang XY, Feng L, Zhao JJ, *et al*. Effects of chronic ethanol consumption on levels of adipokines in visceral adipose tissues and sera of rats. Acta Pharmacol Sin 2010; 31: 461–9.
12 Koppes LL, Dekker JM, Hendriks HF, Bouter LM, Heine RJ. Moderate alcohol consumption lowers the risk of type 2 diabetes: a meta-analysis of prospective observational studies. Diabetes Care 2005; 28: 719–25.

13 Yoon YS, Oh SW, Baik HW, Park HS, Kim WY. Alcohol consumption and the metabolic syndrome in Korean adults: the 1998 Korean National Health and Nutrition Examination Survey. Am J Clin Nutr 2004; 80: 217–24.
14 Matthews DR, Hosker JP, Rudenski AS, Naylor BA, Treacher DF, Turner RC. Homeostasis model assessment: insulin resistance and beta-cell function from fasting plasma glucose and insulin concentrations in man. Diabetologia 1985; 28: 412–9.
15 Nanji AA, Dannenberg AJ, Jokelainen K, Bass NM. Alcoholic liver injury in the rat is associated with reduced expression of peroxisome proliferator-alpha (PPARalpha)-regulated genes and is ameliorated by PPARalpha activation. J Pharmacol Exp Ther 2004; 310: 417–24.
16 You M, Fischer M, Deeg MA, Crabb DW. Ethanol induces fatty acid synthesis pathways by activation of sterol regulatory element-binding protein (SREBP). J Biol Chem 2002; 277: 29342–7.
17 Bauer S, Wanninger J, Schmidhofer S, Weigert J, Neumeier M, Dorn C, *et al*. Sterol regulatory element-binding protein 2 (SREBP2) activation after excess triglyceride storage induces chemerin in hypertrophic adipocytes. Endocrinology 2011; 152: 26–35.
18 Fukui H, Brauner B, Bode J, Bode C. Plasma endotoxin concentrations in patients with alcoholic and non-alcoholic liver disease: reevaluation with an improved chromogenic assay. J Hepatol 1991; 12: 162–9.
19 Kishore R, Hill JR, McMullen MR, Frenkel J, Nagy LE. ERK1/2 and Egr-1 contribute to increased TNF-alpha production in rat Kupffer cells after chronic ethanol feeding. Am J Physiol Gastrointest Liver Physiol 2002; 282: G6–15.
20 Parlee SD, Ernst MC, Muruganandan S, Sinal CJ, Goralski KB. Serum chemerin levels vary with time of day and are modified by obesity and tumor necrosis factor-{alpha}. Endocrinology 2010; 151: 2590–602.
21 Laso FJ, Vaquero JM, Almeida J, Marcos M, Orfao A. Production of inflammatory cytokines by peripheral blood monocytes in chronic alcoholism: relationship with ethanol intake and liver disease. Cytometry B Clin Cytom 2007; 72: 408–15.
22 Ahluwalia B, Wesley B, Adeyiga O, Smith DM, Da-Silva A, Rajguru S. Alcohol modulates cytokine secretion and synthesis in human fetus: an *in vivo* and *in vitro* study. Alcohol 2000; 21: 207–13.
23 Valles SL, Blanco AM, Azorin I, Guasch R, Pascual M, Gomez-Lechon MJ, *et al*. Chronic ethanol consumption enhances interleukin-1-mediated signal transduction in rat liver and in cultured hepatocytes. Alcohol Clin Exp Res 2003; 27: 1979–86.
24 Hsiang CY, Wu SL, Cheng SE, Ho TY. Acetaldehyde-induced interleukin-1 beta and tumor necrosis factor-alpha production is inhibited by berberine through nuclear factor-kappaB signaling pathway in HepG2 cells. J Biomed Sci 2005; 12: 791–801.
25 Tan BK, Chen J, Farhatullah S, Adya R, Kaur J, Heutling D, *et al*. Insulin and metformin regulate circulating and adipose tissue chemerin. Diabetes 2009; 58: 1971–7.
26 Geloen A, Collet AJ, Guay G, Bukowiecki LJ. Insulin stimulates *in vivo* cell proliferation in white adipose tissue. Am J Physiol 1989; 256: C190–6.
27 Suryawan A, Swanson LV, Hu CY. Insulin and hydrocortisone, but not triiodothyronine, are required for the differentiation of pig preadipocytes in primary culture. J Anim Sci 1997; 75: 105–11.
28 Deslex S, Negrel R, Ailhaud G. Development of a chemically defined serum-free medium for differentiation of rat adipose precursor cells. Exp Cell Res 1987; 168: 15–30.
29 You M, Fischer M, Deeg MA, Crabb DW. Ethanol induces fatty acid synthesis pathways by activation of sterol regulatory element-binding protein (SREBP). J Biol Chem 2002; 277: 29342–7.
30 Kim JB, Spiegelman BM. ADD1/SREBP1 promotes adipocyte differentiation and gene expression linked to fatty acid metabolism. Genes Dev 1996; 10: 1096–107.

Acta Pharmacologica Sinica (2012) 33: 660–667
 1671-4083/12 $32.00
www.nature.com/aps

Original Article

Contribution of *Myostatin* gene polymorphisms to normal variation in lean mass, fat mass and peak BMD in Chinese male offspring

Hua YUE[1], Jin-wei HE[1], Hao ZHANG[1], Chun WANG[1], Wei-wei HU[1], Jie-mei GU[1], Yao-hua KE[1], Wen-zhen FU[1], Yun-qiu HU[1], Miao LI[1], Yu-juan LIU[1], Song-hua WU[2, *], Zhen-lin ZHANG[1, *]

[1]Metabolic Bone Disease and Genetic Research Unit, Department of Osteoporosis and Bone Disease and [2]Department of Endocrinology and Metabolism, Shanghai Jiao Tong University Affiliated the Sixth People's Hospital, Shanghai 200233, China

Aim: *Myostatin* gene is a member of the transforming growth factor-β (TGF-β) family that negatively regulates skeletal muscle growth. Genetic polymorphisms in *Myostatin* were found to be associated with the peak bone mineral density (BMD) in Chinese women. The purpose of this study was to investigate whether *Myostatin* played a role in the normal variation in peak BMD, lean mass (LM), and fat mass (FM) of Chinese men.

Methods: Four hundred male-offspring nuclear families of Chinese Han ethnic group were recruited. Anthropometric measurements, including the peak BMD, body LM and FM were measured using dual-energy X-ray absorptiometry (DXA). The single nucleotide polymorphisms (SNPs) studied were tag-SNPs selected by sequencing. Both rs2293284 and +2278G>A were genotyped using TaqMan assay, and rs3791783 was genotyped with PCR-restriction fragment length polymorphism (RFLP) analysis. The associations of the SNPs with anthropometric variations were analyzed using the quantitative transmission disequilibrium test (QTDT).

Results: Using QTDT to detect within-family associations, neither single SNP nor haplotype was found to be associated with peak BMD at any bone site. However, rs3791783 was found to be significantly associated with fat mass of the trunk ($P<0.001$). Moreover, for within-family associations, haplotypes AGG, AAA, and TGG were found to be significantly associated with the trunk fat mass (all $P<0.001$).

Conclusion: Our results suggest that genetic variation within *Myostatin* may play a role in regulating the variation in fat mass in Chinese males. Additionally, the *Myostatin* gene may be a candidate that determines body fat mass in Chinese men.

Keywords: *Myostatin*; single nucleotide polymorphism (SNPs); bone mineral density; lean mass; fat mass; within-family association; quantitative transmission disequilibrium test (QTDT); Chinese male

Acta Pharmacologica Sinica (2012) 33: 660–667; doi: 10.1038/aps.2012.12; published online 19 Mar 2012

Introduction

Myostatin is a member of the transforming growth factor-beta (TGF-β) family, and it acts as a negative regulator of skeletal muscle growth. Currently, there is only one study, reported by our institute, on variation in the *Myostatin* gene and its role in the bone mineral density (BMD) and body mass index (BMI) of Chinese females[1]. However, the multiple regulatory mechanisms of the *Myostatin* gene in BMD and body composition have not yet been elucidated.

The TGF-β super-family encompasses a large number of growth and differentiation factors that play important roles in regulating embryonic development and in maintaining tissue homeostasis in adult animals. The TGF-β signaling pathway interacts with the PPAR-γ and Wnt signaling pathway, which has complex effects on marrow stromal cell differentiation[2]. High expression of *TGF-β* in bone suppresses adipocyte differentiation and promotes the proliferation and differentiation of osteoblasts[3]. *TGF-β* can repress the expression of *PPAR-γ* in marrow stromal cells and down-regulate the target genes of *PPAR-γ*[4]. In addition, *TGF-β* has an effect on the Wnt signaling pathway, which is responsible for the regulated expression of *Wnt* and *LRP5* and the stabilization of *β-Catenin*. *TGF-β* stimulates the differentiation of chondrocytes and restrains the differentiation of marrow stromal cells to adipocytes[2, 5].

Myostatin, or *GDF-8*, which is situated on chromosome

* To whom correspondence should be addressed.
E-mail ZZL2002@medmail.com.cn (Zhen-lin ZHANG);
drwush@msn.com (Song-hua WU)
Received 2011-12-29 Accepted 2012-02-01

2q32.2, is a member of the TGF-β super-family and is important for the control and maintenance of skeletal muscle mass[6]. *Myostatin* is a negative regulator of skeletal muscle growth in mammals, and loss-of-function mutations are associated with increased skeletal muscle mass in mice, cattle, and humans[6]. Most of *Myostatin*-null mice ($Mstn^{-/-}$) are 40%–100% larger than their wild-type littermates. This phenomenon is mainly caused by the hyperplasia and hypertrophy of myocytes[7]. Schuelke *et al*[8] described a boy with protruding muscles at birth who had a mutation in the *Myostatin* gene. Further study indicated that the femoral bone density of *Myostatin*-null mice ($Mstn^{-/-}$) was significantly higher than that of wild-type mice[5–11]. A recent study showed that *Myostatin*-null mice that performed physical exercise had a greater increase in bone strength relative to the wild-type mice with physical exercise and the *Myostatin*-null mice without exercise. This finding illustrated that physical exercise combined with increased muscle mass has a greater influence on bone strength than either increased muscle mass or strengthening physical exercise alone[12]. In 2008, Zhang *et al*[1] developed studies using QTDT of 401 nuclear families with female offspring consisting of 1260 subjects. Zhang *et al*[1] detected that rs2293284 was significantly associated with total hip, neck, and trochanter BMD. Total hip and trochanter BMD was significantly associated with rs7570532, and +2278G>A was significantly associated with BMI. Therefore, these findings indicate that the *Myostatin* gene plays a role in regulating bone mass and muscle mass. A correlation between genetic variation in *Myostatin* and peak BMD or body composition has not been reported in males. Thus, the aim of this study was to investigate the associations between genetic variants in *Myostatin* with peak BMD, fat mass, lean mass, and BMI variation among 400 male-offspring nuclear families. Furthermore, we sought to observe the expression of the *Myostatin* gene in muscular tissues and adipose tissues and quantitate discrepancies in *Myostatin* expression. These data will help to establish a foundation upon which further study may elucidate the roles of *Myostatin* in bone, muscle, and fat tissues.

Materials and methods

Subjects

The 400 male-offspring nuclear families were recruited from 2004 to 2007. The group of subjects consisted of 1215 individuals with at least one healthy male child aged 18–44 years old (mean age 30.4±6.1 years). The average family size was 3.03. 385 families had 1 child, and 15 families had 2 children. All of the study subjects belonged to the Chinese Han ethnic group. For each study subject, we recorded age and sex and collected information about medical history, family history, marital status, physical activity, alcohol use, diet habits, and smoking history. We also collected information on menses, obstetrical history, and history of hormonal contraceptive use in the female subjects. The following exclusion criteria were used: (1) serious sequelae of cerebrovascular disease; (2) diabetes mellitus; (3) chronic kidney disease; (4) serious chronic liver disease or alcoholism; (5) significant chronic lung disease; (6) corticosteroid therapy at pharmacologic levels for >6 months duration; (7) anticonvulsant therapy for >6 months duration; (8) evidence of other metabolic or inherited bone disorders, such as hyper- or hypo-parathyroidism, Paget's disease of the bone, osteomalacia, or osteogenesis imperfecta; (9) rheumatoid arthritis or collagen disease; (10) recent (within the past year) major gastrointestinal disease, such as peptic ulcer, malabsorption syndromes, chronic ulcerative colitis, regional enteritis, or any significant chronic diarrhea state; (11) significant disease of any endocrine organ that would affect bone mass; (12) hyperthyroidism; and (13) any neurological or musculoskeletal condition that would be a non-genetic cause of low bone mass.

The study was approved by the Ethics Committee of the Shanghai Jiao Tong University Affiliated Sixth People's Hospital. All of the subjects involved in this study signed written informed consent before entering this study and were recruited by the osteoporosis center from a local population in Shanghai City, which is located in the middle of the east coast of China.

Anthropometric measurements

BMD (g/cm^2) of the anteroposterior lumbar vertebrae 1–4 and the left proximal femur (including total hip, femoral neck, and trochanter) were measured by dual-energy X-ray absorptiometry (DXA). Fat mass (kg) and lean mass (kg) (including arms, legs, trunk, and total body) were also measured by DXA, using the same method. The DXA measurements were made using a Lunar Prodigy scanner (GE Lunar Corp, Madison, WI, USA), and the scanner was used on the fan-beam mode. The machine was calibrated daily. The coefficient of variability (*CV*) values were obtained from 15 volunteers with 3 measurements each. The respective *CV* values for the BMD of the lumbar spine 1–4, total hip, femoral neck, and trochanter were 1.39%, 0.70%, 2.22%, and 1.41%[1, 13-15]. The respective *CV* values for the fat mass measurements at the upper limbs, lower limbs, trunk, and total body were 7.58%, 3.28%, 2.52%, and 3.72%; the *CV* values for the lean mass at these sites were 1.18%, 1.59%, 1.12%, and 1.18%, respectively[15]. The long-term precision (expressed as the *CV* of our DXA instrument, as was determined by daily measurements of a phantom) was 0.45% during the study period [1, 14, 15].

The data were analyzed with Prodigy Encore software (version 6.70, standard-array mode). Height was measured to the nearest centimeter on a wall-mounted stadiometer, and body weight was measured to the nearest 0.1 kg on a standard balance beam scale, with subjects wearing light indoor clothing and no shoes. Both the stadiometer and the scale were regularly calibrated during the study. BMI was calculated by dividing the weight in kilograms by the square of the height in meters, and the percentage fat mass (PFM) was calculated as the ratio of the fat mass to body weight (*ie*, the sum of fat mass, lean mass, and bone mass). The percentage of lean mass (PLM) was calculated as the ratio of lean mass to body weight.

SNP selection and genotyping

The studied SNPs were selected by direct sequencing, which was performed in our previous study of Chinese women[1]. The SNPs from our previous work were selected for further study in our male-offspring nuclear families. These three tag-SNPs included rs2293284, +2278G>A, and rs7570532. Unfortunately, the primer and probe sequences of rs7570532 could not be synthesized by Applied Biosystems, and the polymorphism rs3791783 was selected as an alternative because of the strong LD (D′=1) between the two SNPs.

Genomic DNA was extracted from the peripheral blood samples by routine methods. The TaqMan allelic discrimination assay (Applied Biosystems, Foster City, CA, USA) was used for the genotyping of rs2293284 and +2278G>A. The primer and probe sequences were optimized using the SNP assay-by-design service of Applied Biosystems. The SNPs, rs2293284 and +2278G>A, were submitted for custom Taqman SNP genotyping assay design (Applied Biosystems) and typed on a thermal cycler (Mx3000P Real-Time PCR System, STRATAGENE, CA, USA). The final SNP, rs3791783, was genotyped by PCR-restriction fragment length polymorphism (RFLP) analysis and was identified by electrophoresis through 2% agarose gels. The oligonucleotides used to amplify rs3791783 were as follows: 5′-TTTTTTTTTTATTTTTTTTATTTTTTTTAG-GATGTTGATGCACTGATGTG-3′ (forward); and 5′-GAA-TGCTAAGGCAGCTCAGAAA-3′ (reverse). The PCR was performed using Taq DNA polymerase (Applied Biosystems) with the supplied buffer and a 55 °C annealing temperature. The utilized restriction endonuclease was *NIa* III (Takara, Japan), and the RFLP sizes were 147, 99, and 48 bp. Random duplicate genotyping was routinely undertaken during the study: a mean genotyping error rate of less than 1% was found for all of the SNPs.

Tissue RNA extraction and mRNA expression analysis

Subcutaneous fat and muscle of the patients with fractures caused by traffic accident were collected for RNA extraction, altogether 2 fat and 6 muscle samples were acquired. Total RNA was extracted by conventional methods. After purity quotient, concentration detection and production assessment, reverse transcription was performed from RNA to cDNA. RT-PCR was performed in a 7300 Real-Time PCR System (Applied Biosystems, USA). The following primers were used: 5′-ACCTGTTTATGCTGATTGTTGCT-3′ (forward) and 5′-GAGCTGTTTCCAGACGAAGTTTA-3′ (reverse). The *Myostatin* gene mRNA size is 177 bp. Human GAPDH was used as control. The following GAPDH-specific primers were used: 5′-GGTGGTCTCCTCTGACTTCAACA-3′ (forward) and 5′-GTTGCTGTAGCCAAATTCGTTGT-3′ (reverse).

LD and haplotype analyses

Haplotypes were constructed from the population genotype data using the Stephens algorithm and the Phase program version 2.0.2[16]. The significance level of the LD between the markers for this gene was assessed based on the observed haplotypes and allele frequencies using the Haploview software (vision 3.2)[17]. We examined Lewontin's D′ and LD coefficient (r^2) between all pairs of biallelic loci. The frequencies of the genotypes and haplotypes were calculated using a group of 800 unrelated subjects (the parents from the 400 male-offspring nuclear families).

Statistical analysis

The allele frequencies were estimated by gene counting. The Hardy-Weinberg equilibrium was tested by a χ^2 goodness-of-fit statistic. The QTDT program and the orthogonal model were used to test for population stratification, linkage, and within-family association between the SNPs and haplotypes of BMD and obesity-related phenotypes. The QTDT software package is available on the internet at the following address: http://www.sph.umich.edu/csg/abecasis/QTDT/. This method, as implemented in the QTDT software, extends the trios-based TDT to quantitative trait data and uses the genotype data from the available siblings and parents. In our male-offspring nuclear families, all of the children were sons, and the effects of the parent's phenotypes were excluded in the QTDT. Thus, sex was not used as a covariate by which to adjust the son's phenotype variations. Therefore, the BMD values were adjusted by age, height, and weight as covariates, and the obesity phenotypes were adjusted by age. Owing to the possibility of false-positives in multiple tests, 1000 permutations of the data set were performed to obtain the empirical *P* values and assess the reliability of the results. The QTDT program generates *P* values for various tests using a distribution that is asymptotically χ^2. A *P* value threshold of 0.05 was considered significant for all of the analyses.

In addition, one son from each of the 400 families was randomly selected to form a new group for testing the population-based association hypothesis. A general linear model-ANOVA (GLM-ANOVA) was used to compare the mean values of the phenotypic variables across the genotype combinations while adjusting for covariates (age, height, and weight). The statistical analyses were performed using the SPSS software package, version 11.0 (SPSS, Chicago, IL, USA). Significance was defined as $P<0.05$.

Results

Characteristics of the study population

Overall, 1215 individuals from the 400 male-offspring nuclear families were recruited for this study. The study population was composed of 400 pairs of parents and 415 sons. The basic characteristics of the study subjects are shown in Table 1.

SNP genotyping and linkage disequilibrium

A total of 1215 subjects from the 400 families were successfully genotyped. All of the 3 polymorphisms met the expectations of the Hardy-Weinberg equilibrium (HWE). Detailed information on the *Myostatin* SNPs and on the MAFs in dbSNP is listed in Table 2.

Based on the D′ values, we found that the 3 SNPs were in strong LD and had D′ values=1 in each pairwise comparison in the male-offspring nuclear families (Figure 1). Based on the

Table 1. The basic characteristics of the male-offspring nuclear families.

	Father (*n*=400)	Mother (*n*=400)	Son (*n*=415)
Age (years)	61.1±7.1	58.4±6.4	30.4±6.1
Height (cm)	166.7±6.0	155.8±5.5	173.0±5.9
Weight (kg)	69.6±9.5	58.3±8.2	70.6±10.7
Spine BMD (g/cm^2)	1.139±0.172	0.993±0.171	1.139±0.138
Femoral neck BMD (g/cm^2)	0.891±0.132	0.796±0.144	0.997±0.143
Total BMD (g/cm^2)	0.966±0.130	0.869±0.149	1.013±0.137
BMI (kg/m^2)	25.2±2.7	24.0±3.1	24.2±3.2
Trunk fat mass (kg)			9.341±4.37
Fat mass (kg)	–	–	16.31±7.56
Lean mass (kg)	–	–	51.43±5.76
PFM (%)	–	–	21.9±7.3

All data are presented as the mean±SD for the raw phenotype values without adjustment.

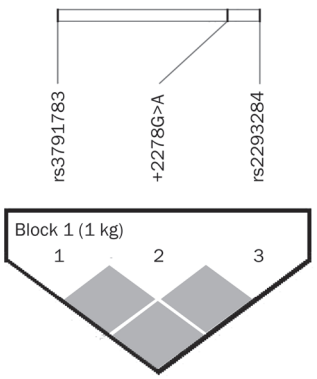

Figure 1. The linkage disequilibrium (LD) pattern in the *Myostatin* gene is depicted as an LD matrix. The classic D′ measurement for all pairs of SNP markers was calculated to construct the LD matrix. The D′ value of each panel is substituted with different colors. Squares in red indicate a strong LD.

strong LD among the polymorphisms, 5 haplotypes that had frequencies of >3% were inferred in the block, using the likelihood method from the PHASE software. The respective frequencies of the haplotypes AGA, AGG, AAA, TGA, and TGG were 68.5%, 7.46%, 3.15%, 3.18%, and 17.6%. Together, the 5 haplotypes accounted for 99.38% of the total population.

Association between peak BMD and SNPs and haplotypes in the male-offspring nuclear families

There were 238, 53, and 264 informative nuclear families for the TDT analysis at rs2293284, +2278G>A, and rs3791783, respectively. At the haplotypes AGA, AGG, AAA, TGA, and TGG, there were 286, 106, 52, 44, and 217 informative nuclear families, respectively. Population stratification was detected for +2278G>A and lumbar spine BMD (P=0.0271). We failed to find a relationship between any polymorphism or haplotype and peak BMD in the male-offspring nuclear families (Table 3).

Association between obesity-related phenotypes and SNPs and haplotypes in the male-offspring nuclear families

There were 226, 50, and 249 informative nuclear families for the TDT analysis at rs2293284, +2278G>A, and rs3791783, respectively. At the haplotypes AGA, AGG, AAA, TGA, and TGG, there were 269, 99, 49, 42, and 206 informative nuclear families, respectively. Population stratification was detected for the haplotype AGG and fat mass in the arms (P=0.0380) and total fat mass (P=0.0366). A significant within-family association was found between rs3791783 and fat mass variation at the trunk (P<0.001). One thousand permutation tests were performed to improve the fidelity and further conform the above finding (P<0.001). The other two SNPs had no significant within-family association with any obesity-related phenotype. However, significant within-family associations were found between haplotypes AGG, AAA, and TGG and the fat mass of the trunk (all P<0.001) (Table 4).

No significant linkages between SNPs or haplotypes and peak BMD or obesity-related phenotypes were observed in the male-offspring nuclear families using linkage tests and linkage tests with modeling association (data not shown).

Gene expression of *Myostatin* in skeletal muscle and fat tissues

The mRNA transcribed from the *Myostatin* gene was examined with reverse transcription polymerase chain reaction (RT-PCR) in 8 samples of skeletal muscle and fat tissues. We found that *Myostatin* gene mRNA expressed in all eight samples, but no statistical significance was detected in different tissues (data not shown).

Discussion

In our previous study involving the sequencing of the full

Table 2. Information on the *Myostatin* polymorphisms used in this study.

SNP	Allele	Function	Position	Amino acid change	MAF in dbSNP (CHB)	MAF in dbSNP (CEU)	Typing method	MAF in this study
rs2293284	A/T	Intron1	41134662	–	–	T: 2%	FAM/VIC	T: 14.2%
+2278G>A	G/A	Exon2	41134494	Glu153 (GAG)>Lys (AAG)	0	G: 1.7%	FAM/VIC	A: 2.9%
rs3791783	C/T	Intron2	41133580	–	C: 21.1%	C: 28.3%	FAM/VIC	C: 24 %

MAF, minor-allele frequency; FAS, fluorescent allele-specific PCR (FAM/VIC); the chromosome position of the base pairs are obtained from dbSNP build 129.

Table 3. Associations between the *Myostatin* polymorphisms and haplotypes and BMD in the male-offspring nuclear families (using QTDT).

	rs2293284	+2278G>A	rs3791783	Haplotype AGG	Haplotype AAA	Haplotype TGG
Tests of population stratification						
Lumbar spine BMD	0.0873	**0.0271**	0.7146	0.2085	0.0691	0.4929
Femoral neck BMD	0.9257	0.4524	0.5155	0.7640	0.2639	0.4894
Total hip BMD	0.4261	0.1967	0.9103	0.9678	0.1292	0.4697
Tests of total association						
Lumbar spine BMD	0.6352	0.1253	0.3089	0.2216	0.2117	0.6743
Femoral neck BMD	0.7324	0.5295	0.5475	0.3459	0.6428	0.9498
Total hip BMD	0.9155	0.9887	0.2569	0.1338	0.9090	0.5512
Tests of within-family association						
Lumbar spine BMD	0.0879	0.2405	0.8404	0.5675	0.0880	0.4214
Femoral neck BMD	0.9245	0.7192	0.7859	0.8882	0.4567	0.5262
Total hip BMD	0.4643	0.2641	0.5012	0.4663	0.1710	0.3547

BMD values are adjusted for age, height and weight as covariates. Boldface type indicates significant *P* values ($P<0.05$).

length of *Myostatin* gene, 17 SNPs were identified. Of these 17 SNPs, 6 SNPs were novel. Each of these SNPs was in strong LD (D′=1), and the entire gene was in one block of LD in the Chinese Han population[1]. The 3 selected SNPs, rs2293284, rs7570532, and +2278G>A, were found to have associations with BMD or BMI in female-offspring nuclear families. However, because the body composition in female-offspring nuclear families was not measured, the correlation between these SNPs and body composition could not be further analyzed. Although the molecular mechanism by which these SNPs influence *Myostatin* function has not been determined, our previous study hinted that genetic variants of *Myostatin* could play a role in achieving and maintaining peak bone mass in females. In addition, the correlation between +2278G>A and BMI in females requires further validation in a larger sample size and in male populations. It was known that mutations in the *Myostatin* gene could result in changes to the lean mass of the body and bone strength. Additionally, the femoral bone density of *Myostatin*-null mice ($Mstn^{-/-}$) was significantly higher than that of wild-type mice[5–11]. However, whether the variation in BMD is independent of the lean mass change is not clear. Therefore, the correlation between *Myostatin* gene polymorphisms and bone mass, lean mass, and fat mass is worthy of further study.

Our present study utilized the complete BMD and body composition database, and we analyzed the relationship between the SNPs and haplotypes of the *Myostatin* gene and peak BMD, lean mass, and fat mass using the QTDT statistical method in 400 male-offspring nuclear families. The genotype frequencies of rs2293284, +2278G>A, and rs3791783 were in accordance with our previous study in female-offspring nuclear families[1]. In the current study, we failed to find an association between any polymorphism or haplotype and peak BMD, which was quite different from the results observed in females. To further examine this discrepancy, we should first analyze whether the study sample size has sufficient power to detect positive results. Our sample size in this study is in line with the sample size of the female-offspring nuclear families in our previous study. The latter has more than 80% power to test a candidate gene as a quantitative trait loci (QTL) and can explain about 10% of the bone phenotype variation[1, 13, 18, 19]. Using the female-offspring nuclear families, we not only detected an association between *Myostatin* polymorphisms and BMD variation, but we also successfully observed that genetic polymorphisms in estrogen receptor α and collagen1α2 likely influenced the attainment of peak BMD in Chinese females[1, 18, 20]. In addition, our latest study of genetic variants in the vitamin D receptor in relation to peak BMD in our male-offspring nuclear families detected an association[15]. In summary, the sample size of our male-offspring nuclear families had sufficient power to detect a candidate gene as a QTL. Taaffe *et al*[21] indicated that bone geometry and density of the femoral diaphysis differed by sex more than by race. Sex- and compartment-specific regulatory QTLs have been found in mice in some studies[22, 23]. Studies in humans have also revealed a gender difference in the degree of heritability of BMD at specific skeletal sites[24–26]. Ralston *et al*[27] provided evidence for gender-specific, site-specific and age-specific QTLs that regulate BMD in humans. However, exactly which gene is responsible for the differences observed between the males and females is still unclear. Therefore, our conclusion should be cautiously interpreted.

In recent years, multiple studies have focused on the role of brown adipocytes in regulating obesity. One recent study demonstrated that *Myostatin* is a potent negative regulator of brown adipogenic differentiation by the modulation of Smad3-induced β-catenin stabilization[28]. A recent animal study showed that *Myostatin* plays an important role in myogenic and adipogenic cells, and that the gene had different roles in the adipogenesis of pig adipose-derived stem cells (ADSCs) and muscle satellite cells (MSCs)[29]. Another animal study showed that the resistance of *Myostatin*-null mice to

Table 4. Associations between the *Myostatin* polymorphisms and haplotypes and obesity-related phenotypes in the male-offspring nuclear families (using QTDT).

	rs2293284	+2278G>A	rs3791783	Haplotype AGG	Haplotype AAA	Haplotype TGG
Tests of population stratification						
Arms FM	0.8369	0.8863	0.5231	**0.0380**	0.2941	0.8020
Legs FM	0.8770	0.6429	0.2073	0.1628	0.3308	0.9252
Trunk FM	0.8360	0.9887	0.4130	0.2095	0.9978	0.6234
Total FM	0.6361	0.7558	0.3065	**0.0366**	0.1704	0.6735
Arms LM	0.8434	0.3007	0.6973	0.2123	0.9965	0.9340
Legs LM	0.8565	0.8388	0.3404	0.1911	0.3654	0.6376
Trunk LM	0.9700	0.3212	0.5018	0.5890	0.6590	0.1432
Total LM	0.8543	0.4315	0.6170	0.3543	0.4873	0.3508
PFM	0.5920	0.7613	0.1565	0.0748	0.3228	0.5666
BMI	0.4997	0.8251	0.8770	0.3337	0.6569	0.7534
Tests of total association						
Arms FM	0.3257	0.9983	0.7203	0.2177	0.8140	0.4036
Legs FM	0.4830	0.7070	0.4520	0.1241	0.9067	0.6460
Trunk FM	0.7110	0.9008	**9e-011**	**1e-010**	**1e-010**	**1e-010**
Total FM	0.5192	0.7586	0.4999	0.1939	0.7371	0.5938
Arms LM	0.3248	0.4647	0.8148	0.5211	0.4268	0.2989
Legs LM	0.9976	0.6983	0.6973	0.9987	0.9875	0.9943
Trunk LM	0.9669	0.8866	0.2653	0.1344	0.8042	0.9428
Total LM	0.8674	0.7421	0.4502	0.3334	0.7260	0.8909
PFM	0.6581	0.7086	0.3939	0.1882	0.9170	0.7340
BMI	0.7354	0.5902	0.2277	0.0992	0.9181	0.8823
Tests of within-family association						
Arms FM	0.3723	0.8014	0.5204	0.4385	0.3696	0.4379
Legs FM	0.5077	0.7687	0.9215	0.8879	0.4126	0.8352
Trunk FM	0.9999	0.7539	**9e-011**	**1e-010**	**8e-011**	**1e-010**
Total FM	0.3393	0.8366	0.6002	0.4447	0.2328	0.4987
Arms LM	0.5708	0.7574	0.5859	0.1714	0.5647	0.4864
Legs LM	0.9889	0.6936	0.5266	0.6683	0.9856	0.9932
Trunk LM	0.6566	0.6374	0.8479	0.1633	0.9004	0.2888
Total LM	0.8131	0.6397	0.6402	0.1784	0.8205	0.4546
PFM	0.4922	0.9674	0.7037	0.6164	0.4471	0.5206
BMI	0.4514	0.9527	0.4671	0.1114	0.7364	0.8398
1000 permutations of within-family association						
Trunk FM	0.9463	0.7889	**9e-011**	**1e-010**	**8e-011**	**1e-010**

Obesity-related phenotype values are adjusted for age as a covariate. Bold values indicate significant *P* values ($P<0.01$).

diet-induced obesity, fat mass accumulation and metabolic dysfunction is not only a result of their large skeletal muscle mass, but it may also be a result of significant changes in the phenotype of white adipose tissue (WAT)[30]. Based on this research, we focused our study on the relationship between *Myostatin* and obesity-related phenotype in humans and we found that rs3791783 is significantly correlated with the trunk fat mss in the Chinese young males, which indicated that apart from the polymorphism itself is the functionally relevant locus or the polymorphism is in linkage disequilibrium with other functional variants in closely situated genes of *Myostatin* gene.

The SNP, rs3791783 is located in intron2 of the *Myostatin* gene, and further functional studies on rs3791783 are needed to determine whether this locus is functionally relevant. In this study, we also collected skeletal muscle and fat tissue from the patients with non-osteoporotic fractures to detect expression of the *Myostatin* gene using RT-PCR. The mRNA of *Myostati*n, which is primarily expressed in muscle, was found in both skeletal muscle and fat tissues. Further study in a larger sample of skeletal muscle and fat tissues is needed to measure the mRNA expression of the rs3791783 genotype in the above two tissues. This work may elucidate the molecular mechanisms of the *Myostatin* gene and its impact on lean mass and fat mass variation.

The DXA is generally accepted as a precise instrument to detect body composition. The fat mass of the trunk that we

detected is mainly observed as fat accumulated in the abdomen. It is well known that fat accumulated in the abdomen is an important risk factor for type 2 diabetes and metabolic syndrome. Our finding of an association between rs3791783 and the fat mass of the trunk has great clinical significance, and we will screen for this SNP in patients with type 2 diabetes and metabolic syndrome in future experiments, to verify whether this polymorphism is a genetic risk factor of such diseases.

In conclusion, our study investigated the relationship between the *Myostatin* gene and obesity-related phenotype variation. The SNP rs3791783 and haplotypes AGG, AAA, and TGG had significant associations with the fat mass of the trunk in healthy young Chinese males aged 20–40 years. This result suggested that the *Myostatin* gene plays a role in regulating the variation in fat mass in males and that *Myostatin* may be a candidate gene for predicting body composition in males of the Chinese Han ethnic group. Further studies are required to elucidate the molecular mechanisms by which rs3791783 affects variations in fat mass and to verify whether this polymorphism is a genetic risk factor for type 2 diabetes and metabolic syndrome. In addition, our study did not detect a correlation between variants of the *Myostatin* gene and peak bone density variation, which indicates that the effect of *Myostatin* on peak bone mass variation may be gender specific.

Acknowledgements

The study was supported by grants from the project of the National Natural Science Foundation of China (81170803, 81070692, 81000360, and 30800387), Shanghai Rising-star Program (11QA1404900), Shanghai Natural Science Foundation (11ZR1427300), STCSM10DZ1950100, and Academic Leaders in Health Sciences in Shanghai (XBR2011014).

Author contribution

Hua YUE genotyped SNPs, extracted tissue RNA, carried out statistical analyses and drafted the manuscript. Zhen-lin ZHANG conceived and designed the study and revised the manuscript. Song-hua WU designed the study and provided part of the research funds. Jin-wei HE guided the work of the genetic laboratory, guaranteed and confirmed the quality of the genetic data. Hao ZHANG, Chun WANG, Wei-wei HU, Jie-mei GU, and Yao-hua KE were involved in the collection of the nuclear families. Wen-zhen FU and Yu-juan LIU contributed to collect blood specimen and DNA database management. Yun-qiu HU and Miao LI were responsible for measuring bone mineral density and body composition.

References

1 Zhang ZL, He JW, Qin YJ, Hu YQ, Li M, Zhang H, *et al*. Association between *Myostatin* gene polymorphisms and peak BMD variation in Chinese nuclear families. Osteoporos Int 2008; 19: 39–47.
2 Zhao LJ, Jiang H, Papasian CJ, Maulik D, Drees B, Hamilton J, *et al*. Correlation of obesity and osteoporosis: effect of fat mass on the determination of osteoporosis. J Bone Miner Res 2008; 23: 17–29.
3 Zhou S, Eid K, Glowacki J. Cooperation between TGF-beta and Wnt pathways during chondrocyte and adipocyte differentiation of human marrow stromall cells. J Bone Miner Res 2004; 19: 463–70.
4 Zhou S, Lechpammer S, Greenberger JS, Glowacki J. Hypoxia inhibition of adipocytogenesis in human bone marrow stromall cells requires transforming growth factor-beta/Smad3 signaling. J Biol Chem 2005; 280: 22688–96.
5 Wrighton KH, Lin X, Yu PB, Feng XH. TGFbeta can stimulate Smad1 phosphorylation idependently of BMP receptors. J Biol Chem 2009; 284: 9755–63.
6 McPherron AC, Lawler AM, Lee SJ. Regulation of skeletal muscle mass in mice by a new TGF-beta superfamily member. Nature 1997; 387: 83–90.
7 McPherron AC, Lee SJ. Double muscling in cattle due to mutations in the myostatin gene. Proc Natl Acad Sci U S A 1997; 94: 12457–61.
8 Schuelke M, Wagner KR, Stolz LE, Hübner C, Riebel T, Kömen W, *et al*. Myostatin mutation associated with gross muscle hypertrophy in a child. N Engl J Med 2004; 350: 2682–8.
9 Hamrick MW. Increased bone mineral density in the femoral of GDF8 gene knockout mice. Anat Rec A Discov Mol Cell Evol Biol 2003; 272: 388–91.
10 Hamrick MW, McPherron AC, Lovejoy CO, Hudson J. Femoral morphology and cross-sectional geometry of adult myostatin-deficient mice. Bone 2000; 27: 343–9.
11 Hamrick MW, McPherron AC, Lovejoy CO. Bone mineral concent and density in the humerous of adult myostatin-deficient mice. Calcif Tissue Int 2005; 71: 63–8.
12 Hamrick MW, Samaddar T, Pennington C, McCormick J. Increased muscle mass with *myostatin* deficiency improves gains in bone strength with exrcise. J Bone Miner Res 2006; 21: 477–83.
13 Zhang ZL, He JW, Qin YJ, Hu YQ, Li M, Liu YJ, *et al*. Association between the SNPs and haplotypes in the PPARGC1 and adiponectin genes and bone mineral density in Chinese women and men. Acta Pharmocal Sin 2007; 28: 287–95.
14 Gao G, Zhang ZL, Zhang H, Hu WW, Huang QR, Lu JH, *et al*. Hip axis length changes in 10,554 males and females and the association with femoral neck fracture. J Clin Densitom 2008; 11: 360–6.
15 Gu JM, Xiao WJ, He JW, Zhang H, Hu WW, Hu YQ, *et al*. Association between VDR and ESR1 gene polymorphisms with bone and obesity phenotypes in Chinese male nuclear families. Acta Pharmacol Sin 2009; 30: 1634–42.
16 Stephens M, Smith NJ, Donnelly P. A new statistical method for haplotype reconstruction from population data. Am J Hum Genet 2001; 68: 978–89.
17 Barrett JC, Fry B, Maller J, Daly MJ. Haploview: analysis and visualization of LD and haplotype maps. Bioinformatics 2005; 21: 263–5.
18 Qin YJ, Shen H, Huang QR, Zhao LJ, Zhou Q, Li MX, *et al*. Estrogen receptor alpha gene polymorphisms and peak bone density in Chinese nuclear families. J Bone Miner Res 2003; 18: 1028–35.
19 Liu XH, Liu YJ, Jiang DK, Li YM, Li MX, Qin YJ, *et al*. No evidence for linkage and/or association of human Alpha2-HS glycoprotein gene with bone mineral density variation in Chinese nuclear families. Calcif Tissue Int 2003; 73: 244–50.
20 Deng FY, Liu MY, Li MX, Lei SF, Qin YJ, Zhou Q, *et al*. Tests of linkage and association of the COL1A2 gene with bone phenotypes variation in Chinese nuclear families. Bone 2003; 33: 614–9.
21 Taaffe DR, Lang TF, Fuerst T, Cauley JA, Nevitt MC, Harris TB. Sex- and race-related differences in cross-sectional geometry and bone density of the femoral mid-shaft in older adults. Ann Hum Biol 2003; 30: 329–46.
22 Beamer WG, Shultz KL, Ackert-Bicknell CL, Horton LG, Delahunty KM, Coombs HF 3rd, *et al*. Genetic dissection of mouse distal chromosome 1 reveals three linked BMD QTLs with sex-dependent regulation of bone phenotypes. J Bone Miner Res 2007; 22: 1187–96.

23 Edderkaoui B, Baylink DJ, Beamer WG, Shultz KL, Wergedal JE, Mohan S. Genetic regulation of femoral bone mineral density: complexity of sex effect in chromosome 1 revealed by congenic sublines of mice. Bone 2007; 41: 340–5.
24 Peacock M, Koller DL, Fishburn T, Krishnan S, Lai D, Hui S, *et al*. Sex-specific and non-sex-specific quantitative trait loci contribute to normal variation in bone mineral density in men. J Clin Endocrinol Metab 2005; 90: 3060–6.
25 Long JR, Liu PY, Liu YJ, Lu Y, Shen H, Zhao LJ, *et al*. APOE haplotypes influence bone mineral density in Caucasian males but not females. Calcif Tissue Int 2004; 75: 299–304.
26 Duncan EL, Cardon LR, Sinsheimer JS, Wass JA, Brown MA. Site and gender specificity of inheritance of bone mineral density. J Bone Miner Res 2003; 18: 1531–8.
27 Ralston SH, Galwey N, MacKay I, Albagha OM, Cardon L, Comnston JE, *et al*. Loci for regulation of bone mineral density in men and women identified by genome wide linkage scan: The FAMOS study. Hum Mol Genet 2005; 14: 943–51.
28 Kim WK, Choi HR, Park SG, Ko Y, Bae KH, Lee SC. Myostatin inhibits brown adipocyte differentiation via regulation of Smad3-mediated β-catenin stabilization. Int J Biochem Cell Biol 2012; 44: 327–34.
29 Deng B, Wen J, Ding Y, Peng J, Jiang S. Different regulation role of myostatin in differentiating pig ADSCs and MSCs into adipocytes. Cell Biochem Funct 2012; 30: 145–50.
30 Lebrasseur NK. Building muscle, browning fat and preventing obesity by inhibiting myostatin. Diabetologia 2012; 55: 13–7.

Acta Pharmacologica Sinica (2012) 33: 668–674
 1671-4083/12 $32.00
www.nature.com/aps

Original Article

Sirt1 overexpression protects murine osteoblasts against TNF-α-induced injury *in vitro* by suppressing the NF-κB signaling pathway

Wei HUANG*, Wei-lin SHANG, Hua-dong WANG, Wen-wen WU, Shu-xun HOU

Department of Orthopaedic Surgery, the First Affiliated Hospital of the General Hospital of PLA, Beijing 100048, China

Aim: Sirtuin 1 (Sirt1) is the class III histone/protein deacetylase that interferes with the NF-κB signaling pathway, thereby has anti-inflammatory function. This study was undertaken to investigate whether Sirt1 could protect osteoblasts against TNF-α-induced injury *in vitro*.

Methods: Murine osteoblastic cell line, MC3T3-E1, was used. Overexpress of Sirt1 protein in MC3T3-E1 cells was made by transfection the cells with Sirt1-overexpressing adenovirus. The levels of mRNAs and proteins were determined with qRT-PCR and Western blotting, respectively. The activity of NF-κB was examined using NF-κB luciferase assay. The NO concentration was measured using the Griess method.

Results: Treatment of MC3T3-E1 cells with TNF-α (2.5–10 ng/mL) suppressed Sirt1 protein expression in a concentration-dependent manner. TNF-α (5 ng/mL) resulted in an increase in apoptosis and a reduction in ALP activity in the cells. Overexpression of Sirt1 in the cells significantly attenuated TNF-α-induced injury through suppressing apoptosis, increasing ALP activity, and increasing the expression of Runx2 and osteocalcin mRNAs. Furthermore, overexpression of Sirt1 in the cells significantly suppressed TNF-α-induced NF-κB activation, followed by reducing the expression of iNOS and NO formation. Sirt1 activator resveratrol (10 μmol/L) mimicked the protection of the cells by Sirt1 overexpression against TNF-α-induced injury, which was reversed by the Sirt1 inhibitor EX-527 (5 μmol/L).

Conclusion: Overexpression of Sirt1 protects MC3T3-E1 osteoblasts aganst TNF-α-induced cell injury *in vitro*, at least in part, via suppressing NF-κB signaling. Sirt1 may be a novel therapeutic target for treating rheumatoid arthritis-related bone loss.

Keywords: Sirt1; osteoblast; TNF-α; NO; NF-κB; alkaline phosphatase; runt-related transcription factor 2 (Runx2); osteocalcin; resveratrol; EX-527

Acta Pharmacologica Sinica (2012) 33: 668–674; doi: 10.1038/aps.2011.189; published online 26 Mar 2012

Introduction

Rheumatoid arthritis is characterized by chronic inflammation that results in excessive production of pro-inflammatory cytokines within bone tissue[1–4]. One such cytokine, tumor necrosis factor-α (TNF-α), is overproduced within the synovium of rheumatoid arthritis lesions, contributing to both systemic and local bone loss[5, 6]. The pathogenic significance of TNF-α has been established by the clinical effectiveness of blocking TNF-α in the treatment of active rheumatoid arthritis[7, 8]. It has been demonstrated that TNF-α decreases osteoblastic bone formation through the suppression of osteoblast proliferation, the induction of osteoblast apoptosis, the inhibition of osteoblast differentiation and the suppression of matrix proteins, such as osteocalcin, which is produced by mature osteoblasts[9–11]. Therefore, further *in vitro* studies are needed to identify potential therapeutic targets that protect osteoblasts from TNF-α-induced injury and to elucidate the underlying mechanisms mediating this protection.

Sirtuin 1 (Sirt1), a member of the silent information regulator 2 family in mammals, has recently been found to be involved in age-related diseases, such as cancer, metabolic diseases, cardiovascular disease, neurodegenerative diseases, and osteoporosis. This involvement is primarily mediated through the deacetylation of substrates, which include p53, forkhead box class O, peroxisome proliferator activated receptor γ (PPARγ) co-activator 1α, and nuclear factor-κB (NF-κB)[12, 13]. Activation of Sirt1 in mesenchymal stem cells can decrease adipocyte differentiation and increase osteoblast differentiation by regulating p53 and PPARγ[12]. In addition, the Sirt1 activator, resveratrol, can inhibit the receptor activator of NF-κB ligand

* To whom correspondence should be addressed.
E-mail huang2011341@hotmail.com
Received 2011-08-18 Accepted 2011-12-06

(RANKL)-induced osteoclastogenesis in bone-derived cells[14]. Recently, the inhibition of osteoblast differentiation and bone formation by cytokines, including TNF-α, was demonstrated and correlated with activation of the NF-κB signaling pathway[15]. Because NF-κB is a direct target of Sirt1[13], we hypothesize that Sirt1 will protect osteoblasts against TNF-α-induced cytotoxicity by suppressing NF-κB activity. To test this hypothesis, we characterized the *in vitro* protective effects of Sirt1 overexpression in TNF-α-treated osteoblasts.

In addition, iNOS, a downstream target of NF-κB, plays an important role in the cell injury induced by TNF-α in osteoblasts[16, 17]. Therefore, we also tested the relationship between Sirt1 and iNOS expression in osteoblasts treated with TNF-α.

In this study, we used a murine calvarial osteoblastic cell line (MC3T3-E1) as a model to test the molecular mechanisms of Sirt1 in the protection of osteoblasts against TNF-α-induced cell injury.

Materials and methods

Cell culture

The murine osteoblastic cell line, MC3T3-E1, was cultured at 37 °C in 5% CO_2 and 90% humidity in α-MEM medium (Invitrogen, Paisley, UK) supplemented with 10% fetal bovine serum and 100 μg/mL gentamicin (Invitrogen, Life Technologies, Paisley, Scotland). Chemicals, drugs, and reagents were obtained from Sigma Chemical (St Louis, MO, USA) unless otherwise stated.

Experiment 1

MC3T3-E1 cells were seeded in culture dishes and treated with TNF-α (0, 2.5, 5.0, and 10.0 ng/mL) for 24 h. Sirt1 expression was then assessed by Western blot analysis.

Experiment 2

MC3T3-E1 cells were transfected with Ad-Sirt1 or Ad-lacZ for 12 h. After transfection, the cells were washed with PBS and then placed in fresh medium. After culture for 36 h, Sirt1 expression was the assessed by Western blot analysis, and deacetylase activity of Sirt1 was measured using a fluorogenic substrate. NF-κB activity was measured by a luciferase reporter assay, and IκB-α expression was assessed by Western blot analysis.

Both groups of cells (transfected with either Ad-Sirt1 or Ad-lacZ) were treated with TNF-α (50 ng/mL) for 4 h, after which the rate of apoptosis was determined.

Both groups of cells were treated with TNF-α (5.0 ng/mL) for 24 h, and the NOx (NO_3^-+NO_2^-) content in the supernatant was then determined using the Griess method. Cellular iNOS expression was determined by Western blot analysis.

Both groups of cells were treated with TNF-α (5.0 ng/mL) for 5 d, after which ALP activity and levels of Runx2 and osteocalcin mRNA were determined.

Experiment 3

MC3T3-E1 cells stimulated with TNF-α (5.0 ng/mL) were treated with BAY-11-7082 (10 μmol/L, an NF-κB inhibitor) or SP600125 (10 μmol/L, a JNK inhibitor) for 24 h. The expression of iNOS was then assayed by Western blot analysis.

Experiment 4

MC3T3-E1 cells were treated with α-MEM alone (control), TNF-α (5.0 ng/mL), TNF-α with resveratrol (10 μmol/L, a Sirt1 activator), or TNF-α with resveratrol and EX-527 (5 μmol/L, a Sirt1 inhibitor) for 1 h. NF-κB activity was then analyzed by luciferase reporter assay.

Cells were treated as described above for 24 h, and the NOx (NO_3^-+NO_2^-) content of the supernatant was determined by the Griess method.

Cells were treated as described above for 5 d, after which ALP activity and levels of Runx2 and osteocalcin mRNA were determined.

MC3T3-E1 cells were treated with α-MEM alone (control), TNF-α (50 ng/mL), TNF-α with resveratrol (10 μmol/L, a Sirt1 activator), or TNF-α with resveratrol and EX-527 (5 μmol/L, a Sirt1 inhibitor) for 4 h, after which the rate of cell apoptosis was measured.

Construction of recombinant adenoviruses

A Sirt1-overexpressing adenovirus was constructed according to the method described by Lee *et al*[18]. Briefly, mouse Sirt1 cDNA was cloned into *Kpn*I and *Xho*I sites of the pENTR 2B vector (Invitrogen), and the Sirt1 cDNA insert was then transferred to the pAd/CMV/V5-DEST vector (Invitrogen). The plasmids were linearized with *Pac*I (Promega, Madison, WI) and were transfected into 293A cells using Lipofectamine 2000. As a control, the pAd/CMV/V5-GW/lacZ vector (Invitrogen) was used to produce a lacZ-bearing adenovirus.

Sirt1 deacetylase activity assay

Cells were homogenized in 100 μL of CytoBuster Protein Extraction Buffer (Invitrogen). Enzyme activity was then measured using a fluorescence-based deacetylase activity kit (Millipore, Bedford, MA, USA).

Apoptosis assay

Cells were seeded into a 6-well plate and treated with the indicated reagents for 4 h. After treatment, the cells were washed with PBS and lysed for 30 min at 4 °C with lysis buffer. The expression levels of cleaved and total caspase-3 were determined by Western blot analysis. The ratio of cleaved caspase-3 to total caspase-3 was used as the marker of apoptosis.

Measurement of ALP activity

The induction of ALP is an unequivocal marker of bone cell differentiation. To measure the ALP activity, the cells were seeded into a 12-well plate and treated with the indicated reagents for 5 d. After treatment, cultured osteoblasts were washed with PBS and then lysed with buffer containing 0.9% NaCl, 0.6% Tris, 1 mmol/L EGTA, 1% NP-40, and 0.25% deoxycholate dissolved in RIPA buffer at 4 °C for 30 min. Cell lysates were then sonicated in an ice bath, centrifuged at 1500×*g* for 5 min, and mixed with buffer containing 0.1

mol/L 2-amino-2-methyl-1-propanol, 1 mmol/L $MgCl_2$, and 8 mmol/L *p*-nitrophenyl phosphate disodium. After incubation at 37 °C for 20 min, the reaction was halted with 0.1 mol/L NaOH, and the absorbance was read at 405 nm. A standard curve was prepared using *p*-nitrophenol. Data were normalized to the concentration of total protein.

RNA purification and quantitative RT-PCR analysis

MC3T3-E1 cells were plated at 100 000 cells per well in 6-well plates and treated with the indicated reagents for 5 d. After treatment, total RNA was isolated with the Rneasy RNA purification kit (Qiagen, Solna, Stockholm, Sweden). A total of 1 mg RNA was reverse transcribed to cDNA using Superscript II (Invitrogen, Stockholm, Sweden) according to the manufacturer's protocol. Gene transcription levels of Runx2 (5′-GCCGGGAATGATGAGAACTA-3′; 5′-GGTGAAACTCTTGCCTCGTC-3′) and osteocalcin (5′-GCCATCACCCTGTCTCCTAA-3′; 5′-GCTGTGGAGAAGACACACGA-3′) were analyzed by quantitative PCR using gene-specific primers and a SYBR Green Supermix (Bio-Rad, Hercules, CA). PCR reactions were performed under the following conditions: initial denaturation of one cycle at 95 °C for 10 min, followed by amplification at 95 °C for 30 s, 55 °C for 30 s, and 72 °C for 30 s, for a total of 35 cycles. The housekeeping gene, β-tubulin (5′-CTGCTCATCAGCAAGATCAGAG-3′; 5′-GCATTATAGGGCTCCACCACAG-3′), was used as an endogenous control. Data analysis was performed using Ct values normalized to β-tubulin expression.

Western blot analysis

Osteoblasts were seeded onto 6-well plates at a density of 1×10^5 cells/well. After incubation with a test reagent, the cells were washed with PBS and lysed for 30 min at 4 °C with lysis buffer. Protein suspensions were loaded and resolved on a 10% SDS-PAGE and were then transferred to a polyvinylidene difluoride (PVDF) membrane (Perkin-Elmer, Norwalk, CT, USA). Sirt1, iNOS, eNOS, IκB-α, total caspase-3, and cleaved caspase-3 were detected using specific antibodies from Santa Cruz Biotechnology (Santa Cruz, CA; sc-74465, sc-650, sc-654, sc-1643, sc-7148, and sc-22171, respectively). Detection of GAPDH using an HRP-conjugated monoclonal antibody (1:8000 , Sigma) served as a loading control. Reactivity was visualized using Super Signal West Pico Chemiluminescent Substrate (Pierce, Rockford, IL, USA).

Determination of nitrite and nitrate (NOx) concentrations

Cells were seeded onto a 12-well plate and treated with the indicated reagents for 24 h. After treatment, the supernatants were collected, and the levels of NOx, which are the stable end products of NO, were measured using a Total Nitrite/Nitrate Assay kit (Dojindo, Kumamoto, Japan), which employs the Griess method.

NF-κB luciferase assay

NF-κB activity was measured using an NF-κB luciferase assay. Cells were seeded onto 24-well culture plates at 2×10^4 cells/well. Cells were incubated for 1 h with plasmids (85 ng of NF-κB-dependent luciferase reporter and 85 ng of pcDNA3-β-gal), 1 μL of Tfx-50 reagent (Promega), and 200 μL of serum-free RPMI-1640. After 1 h, 800 μL of RPMI-1640 containing FBS was added, and the cells were incubated for 24 h. Cells were then treated with the indicated reagents for 1 h. Luciferase activity was measured using a luciferase assay system and normalized against β-galactosidase activity.

MC3T3-E1 cells were transfected with Ad-Sirt1 or Ad-lacZ for 12 h. Cells were then treated as described above to assay for NF-κB activity after treatment with TNF-α (5.0 ng/mL).

Statistical analysis

The *in vitro* experiments were performed at least three times, and each experiment was performed with replicates. Data are expressed as the mean±SD. The significance level was determined by the Student's *t*-test. A difference was considered to be statistically significant at $P<0.05$.

Results

Effect of TNF-α on Sirt1 expression in MC3T3-E1 cells

To investigate the involvement of Sirt1 protein in TNF-α-induced cytotoxicity in osteoblasts, we examined Sirt1 expression levels in response to TNF-α. Western blot analysis showed that incubation with TNF-α (0, 2.5, 5.0, and 10.0 ng/mL) resulted in a reduction of Sirt1 protein expression in osteoblasts (Figure 1).

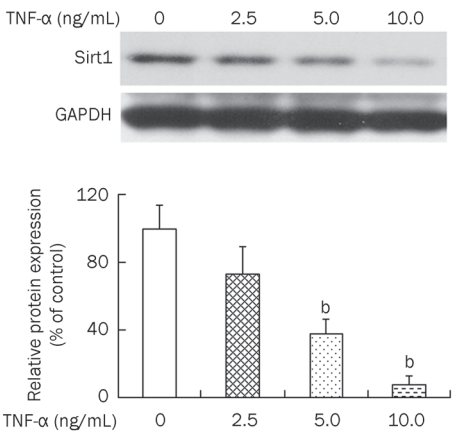

Figure 1. The effect of TNF-α on Sirt1 expression in MC3T3-E1 cells. MC3T3-E1 cells were cultured with an increasing concentration of TNF-α (2.5, 5.0, and 10 ng/mL) for 24 h. Western blot results and responding quantification of Sirt1 were displayed. GAPDH, glyceraldehyde phosphate dehydrogenase. The group without stimulation of TNF-α served as control. The ratio of Sirt1 to GAPDH of other groups was normalized to the control. $^bP<0.05$ *vs* control.

Overexpression of Sirt1 protein in MC3T3-E1 cells

To gain insights into the function of Sirt1 in osteoblasts, Sirt1 was overexpressed using a recombinant adenovirus. Transfection of osteoblasts with Ad-Sirt1 markedly increased Sirt1 protein levels (Figure 2A). Sirt1 deacetylase activity was also

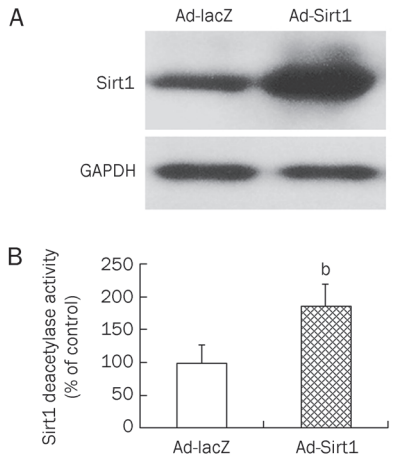

Figure 2. Sirt1 protein was overexpressed by transfecting MC3T3-E1 cells with Ad-Sirt1 adenovirus. MC3T3-E1 cells were transfected with Ad-Sirt1 or Ad-lacZ for 12 h. The expression of Sirt1 (A) was assayed by Western blotting analysis, and deacetylase activity (B) of overexpressed Sirt1 was measured using fluorogenic substrate. GAPDH, glyceraldehyde phosphate dehydrogenase. $^{b}P<0.05$ *vs* Ad-lacZ cells.

enhanced in Ad-Sirt1-transfected osteoblasts (Figure 2B).

Overexpression of Sirt1 attenuated TNF-α-induced cell injury in MC3T3-E1 cells

Treatment with TNF-α resulted in an increase in apoptosis and a reduction in ALP activity in osteoblasts. However, overexpression of Sirt1 significantly attenuated TNF-α-induced cell injury through suppressing apoptosis (Figure 3A), increasing ALP activity (Figure 3B), and increasing the expression of Runx2 (Figure 3C) and osteocalcin (Figure 3D) mRNA.

Effect of Sirt1 overexpression on TNF-α-induced NF-κB activation

We investigated the effects of Sirt1 overexpression on NF-κB signaling in MC3T3-E1 cells. Degradation of IκBα induced by TNF-α (5.0 ng/mL) was partially blocked by Sirt1 overexpression (Figure 4A). As demonstrated by the luciferase reporter assay, TNF-α (5.0 ng/mL) increased the activity of NF-κB in MC3T3-E1 cells. This increase was also partially blocked by Sirt1 overexpression (Figure 4B). Without TNF-α treatment, Sirt1 overexpression had no significant effect on NF-κB activity.

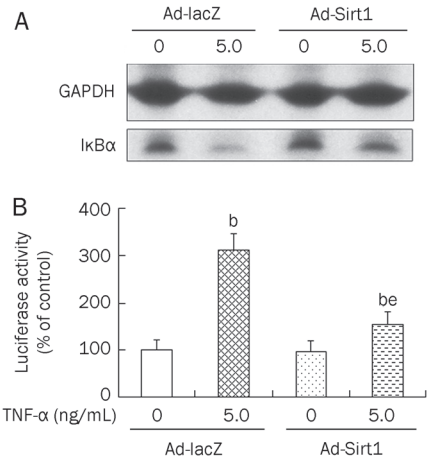

Figure 4. The effect of Sirt1 overexpression on TNF-α-induced IκBα degradation (A) and NF-κB activation (B). Control or Sirt1-overexpressing osteoblastic cells were treated with TNF-α (5.0 ng/mL) for 1 h. Activity of NF-κB was analyzed by luciferase reporter assay. $^{b}P<0.05$ *vs* Ad-lacZ cells. $^{e}P<0.05$ vs TNF-α-treated Ad-lacZ cells.

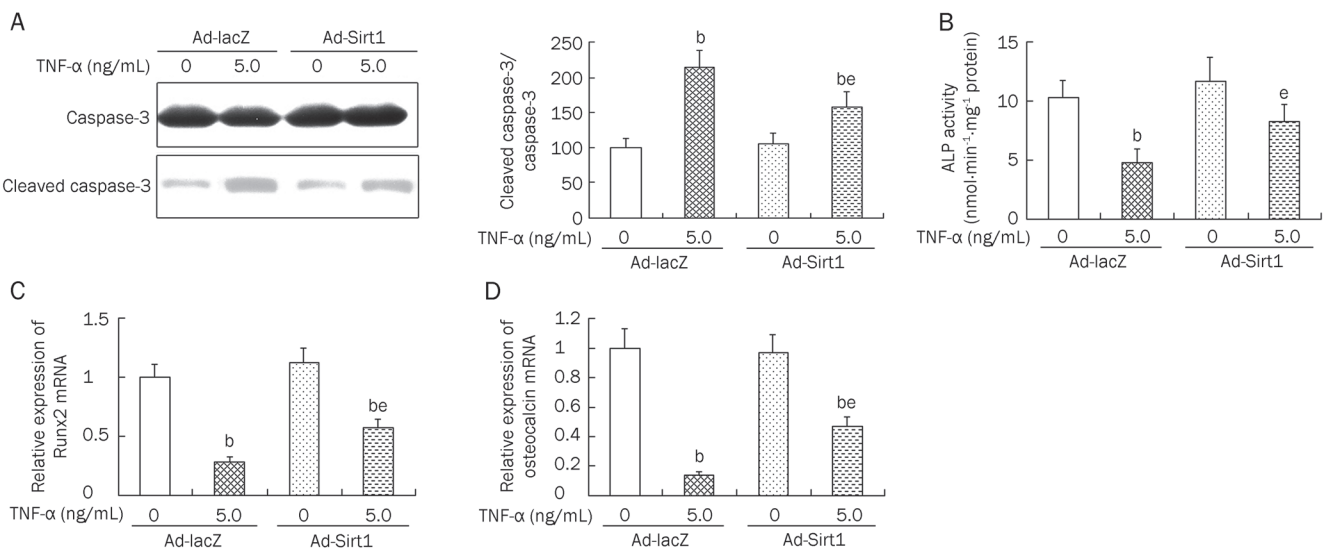

Figure 3. The effect of Sirt1 overexpression on TNF-α-induced cell injury in MC3T3-E1 cells. After successfully transfected with Ad-Sirt1 or Ad-lacZ, two groups of cells were stimulated with TNF-α, the apoptosis (Western blot results and responding quantification of cleaved caspase-3 and caspase-3, A), ALP activity (B), and mRNA levels of Runx2 (C) and osteocalcin (D) were assessed. ALP, alkaline phosphatase; Runx2, runt-related transcription factor 2. $^{b}P<0.05$ *vs* Ad-lacZ cells. $^{e}P<0.05$ *vs* TNF-α-treated Ad-lacZ cells.

Effect of Sirt1 overexpression on TNF-α-induced NO production and iNOS protein expression

In this study, incubation of osteoblasts with TNF-α (5.0 ng/mL) led to an increase in iNOS expression. To define the link between TNF-α and iNOS expression, we investigated downstream signaling pathways of TNF-α, which primarily activates the JNK and NF-κB pathways[19, 20]. BAY-11-7082, an NF-κB inhibitor, and SP600125, a JNK inhibitor, were used to block activation of NF-κB and JNK, respectively. Data showed that TNF-α-induced iNOS expression was inhibited by BAY-11-7082 (10 μmol/L) and not by SP600125 (10 μmol/L) (Figure 5A), indicating that the TNF-α-induced increase in iNOS expression was mediated by the NF-κB pathway and not the JNK pathway. Because NF-κB activation induced by TNF-α was inhibited by Sirt1 overexpression, we examined the effect of Sirt1 overexpression on TNF-α-induced iNOS expression. We found that Sirt1 overexpression suppressed the iNOS induction by TNF-α (5.0 ng/mL) (Figure 5B). Furthermore, NO production induced by TNF-α (5.0 ng/mL) was also reduced by Sirt1 overexpression (Figure 5C). In untreated osteoblasts, Sirt1 overexpression increased the formation of NO. Because iNOS is expressed at low levels in a steady state[20], we examined the effect of Sirt1 overexpression on the expression of eNOS in basal conditions and found it to also be enhanced by Sirt1 overexpression (Figure 5D).

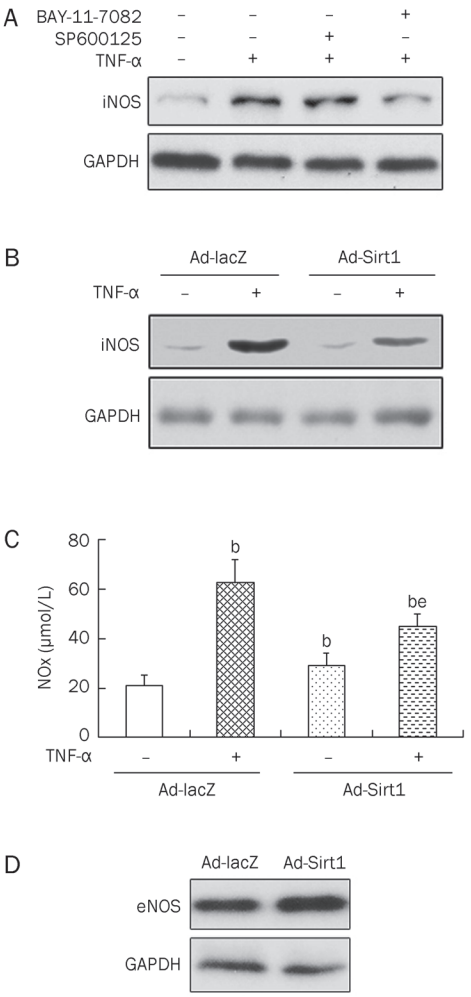

Figure 5. Effect of Sirt1 overexpression on TNF-α-induced NO production and iNOS protein expression. Cells were treated with BAY-11-7082 (10 μmol/L, an NF-κB inhibitor) or SP600125 (10 μmol/L, a JNK inhibitor) in the absence or presence of TNF-α (5.0 ng/mL) for 24 h. The iNOS expression was assayed by Western blotting analysis (A). Control or Sirt1-overexpressing osteoblastic cells were cultured in the absence or presence of TNF-α (5.0 ng/mL) for 24 h. Then, the iNOS expression was assayed by Western blotting analysis (B) and NO formation was detected by the Griess method (C). Control or Sirt1-overexpressing osteoblastic cells were cultured and eNOS expression was assayed by Western blotting analysis (D). NOx, nitrite and nitrate; iNOS, inducible nitric oxide synthase; eNOS, endothelial nitric oxide synthase; GAPDH, glyceraldehyde phosphate dehydrogenase. $^{b}P<0.05$ *vs* Ad-lacZ cells. $^{e}P<0.05$ *vs* TNF-α-treated Ad-lacZ cells.

Activation of Sirt1 by resveratrol attenuated TNF-α-induced cell injury in MC3T3-E1 cells

Resveratrol (10 μmol/L), a Sirt1 activator, reversed the TNF-α-induced inhibition of Sirt1 deacetylase activity (Figure 6A) and activation of NF-κB activity (Figure 6B). We further assessed the protective effects of resveratrol (10 μmol/L) against cell injury induced by TNF-α in osteoblasts to complement the results obtained by using the overexpression approach. Treatment with resveratrol (10 μmol/L) decreased NO formation (Figure 6C), restored ALP activity (Figure 6D), increased the expression of both Runx2 (Figure 6E) and osteocalcin mRNA (Figure 6F), and suppressed apoptosis (Figure 6G) after treatment with TNF-α. Incubation of osteoblasts with EX-527 (5 μmol/L), a Sirt1 inhibitor, reversed the effect of resveratrol on TNF-α-induced cell injury, affirming the role of Sirt1 in TNF-α-induced cell injury.

Discussion

Sirt1, a class III histone/protein deacetylase, interferes with the NF-κB signaling pathway and thereby has an anti-inflammatory function[21]. Because of the central role of NF-κB in cytokine-mediated injury in osteoblasts, we hypothesized that Sirt1 might play a role in osteoblast models of cytokine-induced cell damage. Our data provide multiple lines of evidence that Sirt1 has a protective effect against TNF-α-induced cell injury in osteoblast cells. First, treatment of osteoblast cells with TNF-α decreased Sirt1 protein levels. Second, Sirt1 overexpression attenuated TNF-α-induced cell injury in osteoblasts. Third, Sirt1 overexpression suppressed the TNF-α-induced NF-κB activation, reduced iNOS expression, and reduced NO formation in the osteoblast cells. Fourth, the Sirt1 activator, resveratrol, mimicked the protective effects of Sirt1 overexpression against TNF-α-induced cell injury in osteoblasts. These data suggest that Sirt1 plays a cytoprotective role against TNF-α in osteoblast cells, at least in part, by suppressing NF-κB activity.

We first showed that Sirt1 protein levels were decreased in osteoblast cells by treatment with TNF-α. A recent report by Takayama *et al*[22] showed that Sirt1 protein levels were down-

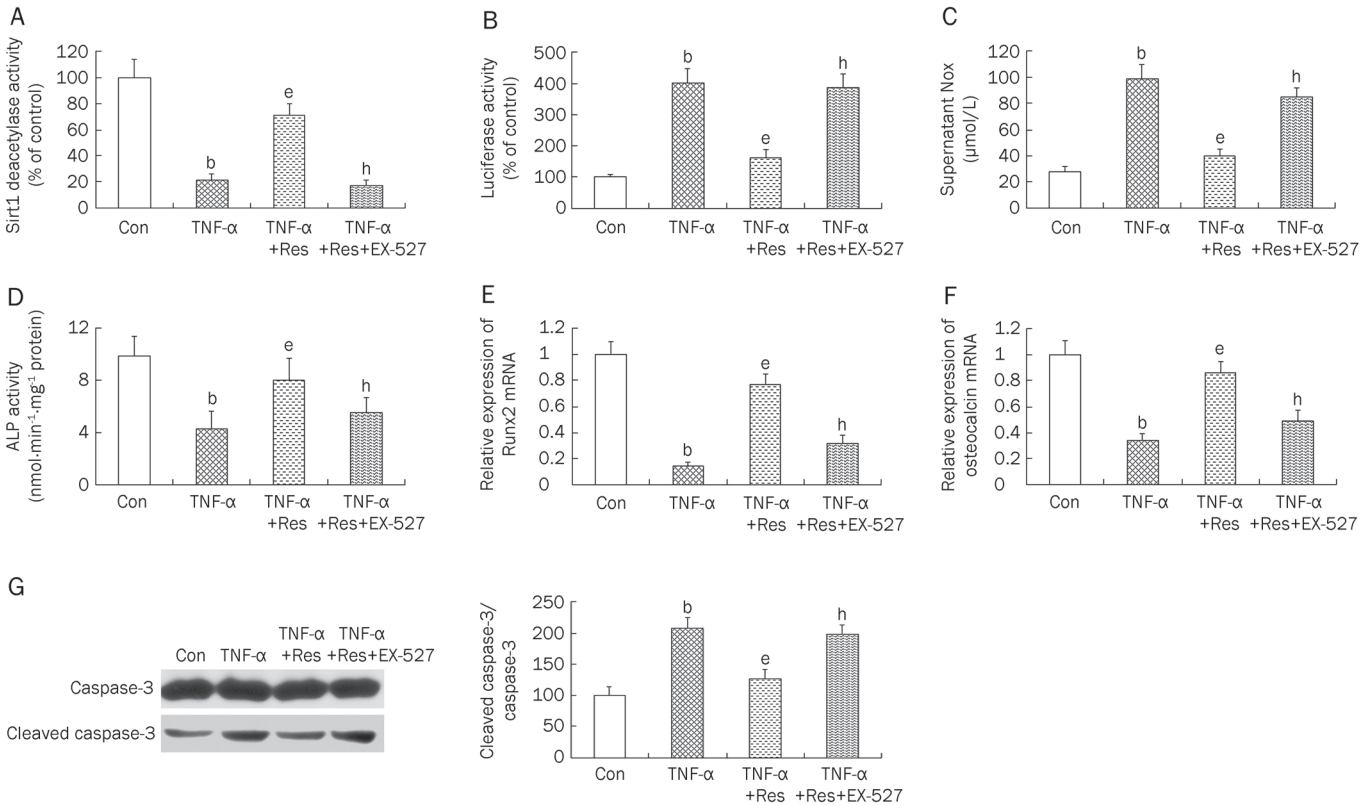

Figure 6. The effect of resveratrol on TNF-α-induced cell injury in MC3T3-E1 cells. Cells were treated with α-MEM (control), TNF-α (5 ng/mL), TNF-α+Resveratrol (10 μmol/L, a Sirt1 activator), TNF-α+Resveratrol+EX-527 (5 μmol/L, a Sirt1 inhibitor). Sirt1 deacetylase activity (A), Luciferase activity (B), supernatant NOx content (C), ALP activity (D), and expressions of Runx2 (E) and osteocalcin (F), apoptosis (Western blot results and responding quantification of cleaved caspase-3 and caspase-3, G), were assessed. NOx, nitrite and nitrate; ALP, alkaline phosphatase; TNF-α, tumor necrosis factor alpha; Res, Resveratrol. $^{b}P<0.05$ *vs* control. $^{e}P<0.05$ *vs* only TNF-α-treated cells. $^{h}P<0.05$ *vs* TNF-α+Resveratrol-treated cells.

regulated by various stresses, including nutritional stress, catabolic stress, and mechanical shear stress in human chondrocytes. Together with our findings, these data suggest that Sirt1 might be involved in the modulation of osteoporosis induced by inflammation or other factors. However, TNF-α induced elevated expression of Sirt1 in vascular smooth muscle cells[23]. Thus, the underlying mechanisms of these contradictory observations in different cell types require further investigation.

Several cytokines can regulate inflammatory responses in osteoblast cells by modulating the NF-κB signaling pathway. TNF-α, a pro-inflammatory cytokine, has been implicated in the early events related to osteoblast cell destruction. Suppression of TNF-α production or blockade of its interaction with its cellular receptors significantly inhibits deleterious effects in related osteoporotic diseases[24–27]. TNF-α activates several intracellular signaling pathways, including the AP-1 pathway, the MAPK pathway, and the JNK pathway in osteoblastic cells[28–30]. However, to our knowledge, TNF-α exerts deleterious effects primarily through the NF-κB signaling pathway in osteoblastic cells[31–33]. Because NF-κB is a molecular target of Sirt1[34, 35], we investigated the influence of the overexpression of Sirt1 on NF-κB signaling pathways in TNF-α-treated osteoblasts. As expected, Sirt1 overexpression suppressed the NF-κB activity induced by TNF-α. In addition, treatment with resveratrol, a Sirt1 activator, also attenuated TNF-α-induced cell injury, which was, at least in part, due to activation of Sirt1 deacetylase and subsequent inhibition of NF-κB activity.

Sirt1 overexpression also blocked the TNF-α-induced expression of iNOS and formation of NO. Activation of the iNOS system has been shown to partly mediate inflammation-induced osteoporosis[16]. High concentrations of NO, such as those observed after stimulation with pro-inflammatory cytokines, not only mediate cytokine-induced apoptosis[17] but also have potent inhibitory effects on osteoblast growth and differentiation[20, 36, 37]. Therefore, Sirt1 exerted its protective role against TNF-α, at least in part, through suppressing iNOS protein expression downstream of NF-κB.

In conclusion, overexpression of Sirt1 protects osteoblasts against TNF-α-induced cell injury, at least in part, by repressing NF-κB activity and genes downstream of NF-κB, including iNOS. Our results suggest that Sirt1 is a novel therapeutic target for treating inflammation-related bone loss.

Author contribution

This research was designed by Wei HUANG. The experiments were performed by Wei HUANG, Wei-lin SHANG, Hua-dong WANG, Wen-wen WU, and Shu-xun HOU. The manuscript

was written by Wei HUANG, Wei-lin SHANG, and Hua-dong WANG.

References

1 Pacifici R. Estrogen, cytokines, and pathogenesis of postmenopausal osteoporosis. J Bone Miner Res 1996; 11: 1043–51.
2 Romas E, Martin TJ. Cytokines in the pathogenesis of osteoporosis. Osteoporos Int 1997; 7: S47–53.
3 Angeli A, Dovio A, Sartori ML, Masera RG, Ceoloni B, Prolo P, *et al*. Interactions between glucocorticoids and cytokines in the bone microenvironment. Ann NY Acad Sci 2002; 996: 97–107.
4 Nowell MA, Richards PJ, Fielding CA, Ognjanovic S, Topley N, Williams AS, *et al*. Regulation of pre-B cell colony-enhancing factor by STAT-3-dependent interleukin-6 trans-signaling: implications in the pathogenesis of rheumatoid arthritis. Arthritis Rheum 2006; 54: 2084–95.
5 Feldmann M, Brennan FM, Maini RN. Role of cytokines in rheumatoid arthritis. Annu Rev Immunol 1996; 14: 397–440.
6 Pfeilschifter J, Köditz R, Pfohl M, Schatz H. Changes in proinflammatory cytokine activity after menopause. Endocr Rev 2002; 23: 90–119.
7 Scott DL, Kingsley GH. Tumor necrosis factor inhibitors for rheumatoid arthritis. New Engl J Med 2006; 355: 704–12.
8 Feldmann M, Maini RN. Anti-TNF alpha therapy of rheumatoid arthritis: what have we learned? Annu Rev Immunol 2001; 19: 163–96.
9 Kuno H, Kurian SM, Hendy GN, White J, deLuca HF, Evans CO, *et al*. Inhibition of 1,25-dihydroxyvitamin D3 stimulated osteocalcin gene transcription by tumor necrosis factor-alpha: structural determinants within the vitamin D response element. Endocrinology 1994; 134: 2524–31.
10 Kitajima I, Soejima Y, Takasaki I, Beppu H, Tokioka T, Maruyama I. Ceramide-induced nuclear translocation of NF-kappa B is a potential mediator of the apoptotic response to TNF-alpha in murine clonal osteoblasts. Bone 1996; 19: 263–70.
11 Gilbert L, He X, Farmer P, Boden S, Kozlowski M, Rubin J, *et al*. Inhibition of osteoblast differentiation by tumor necrosis factor-alpha. Endocrinology 2000; 141: 3956–64.
12 Bäckesjö CM, Li Y, Lindgren U, Haldosén LA. Activation of Sirt1 decreases adipocyte formation during osteoblast differentiation of mesenchymal stem cells. J Bone Miner Res 2006; 21: 993–1002.
13 Haigis MC, Sinclair DA. Mammalian sirtuins: Biological insights and disease relevance. Annu Rev Pathol 2010; 5: 253–95.
14 Shakibaei M, Buhrmann C, Mobasheri A. Resveratrol-mediated SIRT-1 interactions with p300 modulate receptor activator of NF-κB ligand (RANKL) activation of NF-κB signaling and inhibit osteoclastogenesis in bone-derived cells. J Biol Chem 2011; 286: 11492–505.
15 Chang J, Wang Z, Tang E, Fan Z, McCauley L, Franceschi R, *et al*. Inhibition of osteoblastic bone formation by nuclear factor-κB. Nat Med 2009; 15: 682–9.
16 Armour KE, van't Hof RJ, Grabowski PS, Reid DM, Ralston SH. Evidence for a pathogenic role of nitric oxide in inflammation-induced osteoporosis. J Bone Miner Res 1999; 14: 2137–42.
17 Chen RM, Chen TL, Chiu WT, Chang CC. Molecular mechanism of nitric oxide-induced osteoblast apoptosis. J Orthop Res 2005; 23: 462–8.
18 Lee JH, Song MY, Song EY, Kim EK, Moon WS, Han MK, *et al*. Overexpression of sirt1 protects pancreatic β-cells against cytokine toxicity by suppressing the nuclear factor-κB signaling pathway. Diabetes 2009; 58: 344–51.
19 Moncada S, Higgs A. The L-arginine nitric oxide pathway. N Engl J Med 1993; 329: 2002–12.
20 MacPherson H, Noble BS, Ralston SH. Expression and functional role of nitric oxide synthase isoforms in human osteoblast-like cells. Bone 1999; 24: 179–85.
21 Yang SR, Wright J, Bauter M, Seweryniak K, Kode A, Rahman I. Sirtuin regulates cigarette smoke-induced proinflammatory mediator release via RelA/p65 NF-κB in macrophages *in vitro* and in rat lungs *in vivo*: implications for chronic inflammation and aging. Am J Physiol Lung Cell Mol Physiol 2007; 292: L567–76.
22 Takayama K, Ishida K, Matsushita T, Fujita N, Hayashi S, Sasaki K, *et al*. Sirt1 regulation of apoptosis of human chondrocytes. Arthritis Rheum 2009; 60: 2731–40.
23 Zhang HN, Li L, Gao P, Chen HZ, Zhang R, Wei YS, *et al*. Involvement of the p65/RelA subunit of NF-kappaB in TNF-alpha-induced Sirt1 expression in vascular smooth muscle cells. Biochem Biophys Res Commun 2010; 397: 569–75.
24 Ammann P, Rizzoli R, Bonjour JP, Bourrin S, Meyer JM, Vassalli P, *et al*. Transgenic mice expressing soluble tumor necrosis factor-receptor are protected against bone loss caused by estrogen deficiency. J Clin Invest 1997; 99: 1699–703.
25 Kimble RB, Bain S, Pacifici R. The functional block of TNF but not of IL-6 prevents bone loss in ovariectomized mice. J Bone Miner Res 1997; 12: 935–41.
26 Brennan FM, Chantry D, Jackson A, Maini R, Feldmann M. Inhibitory effect of TNF alpha antibodies on synovial cell interleukin-1 production in rheumatoid arthritis. Lancet 1989; 2: 244–7.
27 Redlich K, Hayer S, Maier A, Dunstan CR, Tohidast-Akrad M, Lang S, *et al*. Tumor necrosis factor alpha-mediated joint destruction is inhibited by targeting osteoclasts with osteoprotegerin. Arthritis Rheum 2002; 46: 785–92.
28 Aggarwal BB. Tumor necrosis factors receptor associated signaling molecules and their role in activation of apoptosis, JNK and NF-kappaB. Ann Rheum Dis 2000; 59: 6–16.
29 Chen G, Goeddel DV. TNF-R1 signaling: a beautiful pathway. Science 2002; 296: 1634–5
30 Mukai T, Otsuka F, Otani H, Yamashita M, Takasugi K, Inagaki K, *et al*. TNF-alpha inhibits BMP-induced osteoblast differentiation through activating SAPK/JNK signaling. Biochem Biophys Res Commun 2007; 356: 1004–10.
31 Wajant H, Pfizenmaier K, Scheurich P. Tumor necrosis factor signaling. Cell Death Differ 2003; 10: 45–65.
32 Kurokouchi K, Kambe F, Yasukawa K, Izumi R, Ishiguro N, Iwata H, *et al*. TNF-α increases expression of IL-6 and ICAM-1 genes through activation of NF-κB in osteoblast-like ROS17/2.8 cells. J Bone Miner Res 1998; 13: 1290–9.
33 Lee HL, Yi T, Woo KM, Ryoo HM, Kim GS, Baek JH. Msx2 mediates the inhibitory action of TNF-α on osteoblast differentiation. Exp Mol Med 2010; 42: 437–45.
34 Yeung F, Hoberg JE, Ramsey CS, Keller MD, Jones DR, Frye RA, *et al*. Modulation of NF-kappaB-dependent transcription and cell survival by the SIRT1 deacetylase. EMBO J 2004; 23: 2369–80.
35 Salminen A, Kauppinen A, Suuronen T, Kaarniranta K. SIRT1 longevity factor suppresses NF-kappaB-driven immune responses: regulation of aging via NF-kappaB acetylation? Bioessays 2008; 30: 939–42.
36 Damoulis PD, Hauschka PV. Cytokines induce nitric oxide production in mouse osteoblasts. Biochem Biophys Res Commun 1994; 201: 924–31.
37 Saura M, Tarin C, Zaragoza C. Recent insights into the implication of nitric oxide in osteoblast differentiation and proliferation during bone development. Sci World J 2010; 10: 624–32.

Acta Pharmacologica Sinica (2012) 33: 675–681
 1671-4083/12 $32.00
www.nature.com/aps

Original Article

FoxM1 mediated resistance to gefitinib in non-small-cell lung cancer cells

Nuo XU[1, #], Xin ZHANG[1, #], Xun WANG[1], Hai-yan GE[1], Xiao-ying WANG[1], David GARFIELD[2], Ping YANG[3], Yuan-lin SONG[1], Chun-xue BAI[1, *]

[1]*Department of Pulmonary Medicine, Zhongshan Hospital, Fudan University, Shanghai 200032, China;* [2]*ProMed Cancer Centers – Shanghai, Shanghai 200020, China;* [3]*Department of Health Sciences Research, Mayo Clinic, Rochester, MN 55905, USA*

Aim: Gefitinib is effective in only approximately 20% of patients with non-small-cell lung cancer (NSCLC), and the underlying mechanism remains unclear. FoxM1 is upregulated in NSCLC and associated with a poor prognosis in NSCLC patients. In this study, we examined the possible role of FoxM1 in gefitinib resistance and the related mechanisms.
Methods: Gefitinib resistant human lung adenocarcinoma cell line SPC-A-1 and gefitinib-sensitive human lung mucoepidermoid carcinoma cell line NCI-H292 were used. mRNA and protein expression of FoxM1 and other factors were tested with quantitative RT PCR and Western blot analysis. RNA interference was performed to suppress FoxM1 expression in SPC-A-1 cells, and lentiviral infection was used to overexpress FoxM1 in H292 cells. MTT assay and flow cytometry were used to examine the proliferation and apoptosis of the cells.
Results: Treatment of SPC-A-1 cells with gefitinib (1 and 10 μmol/L) upregulated the expression of FoxM1 in time- and concentration-dependent manners, while gefitinib (1 μmol/L) downregulated in H292 cells. In SPC-A-1 cells treated with gefitinib (1 μmol/L), the expression of several downstream targets of FoxM1, including survivin, cyclin B1, SKP2, PLK1, Aurora B kinase and CDC25B, were significantly upregulated. Overexpression of FoxM1 increased the resistance in H292 cells, while attenuated FoxM1 expression restored the sensitivity to gefitinib in SPC-A-1 cells by inhibiting proliferation and inducing apoptosis.
Conclusion: The results suggest that FoxM1 plays an important role in the resistance of NSCLC cells to gefitinib *in vitro*. FoxM1 could be used as a therapeutic target to overcome the resistance to gefitinib.

Keywords: FoxM1; non-small-cell lung cancer; gefitinib; drug resistance; RNA interference; human lung adenocarcinoma cell; human lung mucoepidermoid carcinoma cell

Acta Pharmacologica Sinica (2012) 33: 675–681; doi: 10.1038/aps.2011.188; published online 26 Mar 2012

Introduction

Forkhead box M1 (FoxM1), a member of the Fox family of transcriptional factors, has been shown to be essential for cell cycle progression and plays an important role in cell-cycle regulation by controlling the transition from G_1 to S phase, as well as the entry into and completion of mitosis[1–4]. FoxM1 mainly functions through the regulation of several cell cycle effectors, including p27/Kip1, cyclin B1, CDC25B, survivin, Cks1, polo-like kinase-1 (PLK1) and Aurora B kinase[5–8]. Downregulation of FoxM1 expression could thus cause cell cycle arrest, chromosome misaggregation and spindle defects. Moreover, FoxM1 was also found to be overexpressed in a wide range of solid tumors, including lung, liver and breast cancers[7, 9–11]. In addition, the function of FoxM1 was reported to be mediated by phosphoinositide-3-kinase (PI3K)/AKT signaling, one of the epidermal growth factor receptor (EGFR) downstream signaling pathways[12]. Gefitinib, an EGFR inhibitor, can block downstream signaling pathways, such as PI3K/AKT and Ras/Raf/MAPK, by competitively binding to the EGFR receptor tyrosine kinase domain[13–16]. However, the dysregulation of PI3K/AKT signaling has been reported to contribute to the resistance of non-small-cell lung cancer (NSCLC) to epidermal growth factor receptor tyrosine kinase inhibitors (EGFR-TKIs)[17, 18]. This suggests that FoxM1 plays a role in the resistance of NSCLC to gefitinib.

In this study, we investigated whether FoxM1 overexpression in the EGFR-positive SPC-A-1 NSCLC cell line could confer resistance to gefitinib, and whether downregulation of FoxM1 expression could sensitize such cells to therapy. We found that FoxM1 not only mediates the inherent resistance of NSCLC cells to the EGFR-TKI, gefitinib, but may also be used

# These authors contributed equally to this paper.
* To whom correspondence should be addressed.
E-mail bai.chunxue@zs-hospital.sh.cn
Received 2011-07-09 Accepted 2011-12-06

as a biomarker to predict the response of NSCLC patients to this agent.

Materials and methods

Cell lines, cell culture and chemotherapeutic reagents

The human lung adenocarcinoma cell line SPC-A-1 was obtained from the Cellular Institute of the Chinese Academy of Science (Shanghai, China). The cell line was established in 1980 from a surgical specimen of a Chinese male patient with advanced lung adenocarcinoma by the Shanghai Chest Hospital and Cellular Institute of Chinese Academy of Science[19]. The human lung mucoepidermoid carcinoma cell line NCI-H292 was purchased from the Cellular Institute of Chinese Academy of Science. These cells were cultured at 37 °C under a 5% CO_2 atmosphere in Dulbecco's modified Eagle's medium (DMEM), and supplemented with 10% fetal bovine serum (FBS, Hyclone, UT, USA), 100 U/mL penicillin, and 100 μg/mL streptomycin. Cells were regularly certified as free of mycoplasma contamination. Gefitinib (AstraZeneca) was dissolved in DMSO at various concentrations and quantities, per the experimental design. The cells were counted 3 times using a hemocytometer, seeded to an appropriate confluence and incubated for certain durations depending on the intended application.

MTT assays

Cell growth was evaluated by 3-(4,5-dimethylthiazol-2-yl)-2, 5-diphenyltetrazolium bromide (MTT) assays according to previous reports[20]. After shaking for 10 min at room temperature, the optical density (OD) of each well was examined by a plate reader at a 490 nm test wavelength.

FCM analysis

Cells were harvested 72 h after administration of gefitinib, trypsinized and washed twice with complete media. Aliquots of cells (1×10^6) were resuspended and stained with fluorescein isothiocyanate (FITC)-labeled annexin-V according to the manufacturer's instructions. Propidium iodide (PI) was subsequently added to the samples, followed by a 30 min-incubation with annexin-V stain in the dark. Flow cytometry (BD, FACSCalibur, USA) was performed immediately after staining.

siRNA analyses

Small interfering RNA (siRNA) for FoxM1 (5′-GCCGGAACAUGACCAUCAATT-3′) and negative control siRNA (5′-UUCUCCGAACGUGUCACGUTT-3′) were purchased from Genepharma (Shanghai, China). According to the manufacturer's protocol, cells were transfected using the Lipofectamine 2000 reagent (Invitrogen, USA). The cells were harvested after 48 h of transfection. The depletion of FoxM1 was determined by real-time PCR.

Transduction of tumor cells

The plasmid (EX-Z5438-LV135) and the Lenti-Pac™ HIV Expression Packaging Kit were purchased from GeneCopoeia Inc (Guangzhou, China). Transductions of H292 cells were performed according to instructions supplied by the manufacturers. Stable transfectants were further confirmed by both RT-PCR and immunoblotting based on their FoxM1 expression.

Quantitative real-time PCR

Total RNA was extracted using TRIzol reagent (Invitrogen, USA), and cDNA was synthesized using reverse transcriptase (TaKaRa, Japan). GAPDH was used as the internal control to quantitate initial cellular transcripts. Primer sequences included the following:

FoxM1 sense 5′-AAGAACTCCATCCGCCACAAC-3′, FoxM1 anti-sense 5′-GCTTAAACACCTGGTCCAATGTC-3′.

GAPDH sense 5′-ATACTCCTGCTTGCTGATCC-3′, GADPH anti-sense 5′-CCTGTACGCCAACACAGTGC-3′.

Survivin sense 5′-AACCAGACCCTCATGGCTAC-3′, Survivin anti-sense 5′-TTCCCAGACTCCACTCCAAC-3′.

PLK1 sense 5′-CCCCTCACAGTCCTCAATA-3′, PLK1 anti-sense 5′-TGTCCGAATAGTCCACCC-3′.

Cyclin B1 sense 5′-GTTGGTTTCTGCTGGGTG-3′, Cyclin B1 anti-sense 5′-ATGTTGATCTTCGCCTTA-3′.

Aurora B kinase sense 5′-CTCTGGGCAAAGGCAAGT-3′, Aurora B kinase anti-sense 5′-ACGCAGGATGTTGGGATG-3′.

CDC25B sense 5′-TCAAATATCAGTTACCCACTCG-3′, CDC25B anti-sense 5′-TCCATCCGCAACAAGACA-3′.

Skp2 sense 5′-GAAAGAGGAGCCCGACAG-3′, Skp2 anti-sense 5′-CTCAGGGAGGCACAGACA-3′.

The amplification data, measured by fluorescence, were collected in real-time and analyzed by the Rotor-Gene 3000 software.

Western blot

A Western blot was performed with whole cell extracts by the protocols described previously[21]. The antibodies used were anti-β-actin antibody (1:5000, Abcam), rabbit polyclonal anti-FoxM1 antibody (1:2000, Santa Cruz Biotechnology), rabbit monoclonal anti-survivin antibody (1:1000, CST) or rabbit polyclonal anti-cyclin B1 antibody (1:1000, CST), rabbit monoclonal anti-Skp2 antibody (1:1000, CST), rabbit monoclonal anti-Aurora B kinase antibody (1:1000, CST), rabbit monoclonal anti-PLK1 antibody (1:1000, CST), and rabbit monoclonal anti-CDC25B antibody (1:1000, CST). β-Actin was used as the loading control. Protein was visualized using enhanced chemiluminescence (ECL). Quantification was performed using the Image J software.

Statistical analysis

Data are presented as the mean±standard deviation (SD) and were evaluated with the paired, two-tailed Student's *t*-test. $P<0.05$ was accepted as statistically significant.

Results

Expression levels of FoxM1 increased after gefitinib treatment in the resistant cell line but decreased in the sensitive cell line

To investigate whether the expression of FoxM1 was changed

by treatment with gefitinib, we applied different gefitinib concentrations to the resistant cell line, SPC-A-1 (1 μmol/L and 10 μmol/L), and to the sensitive cell line, H292 (1 μmol/L), for 0, 24, 48, and 72 h, respectively. Expression levels of FoxM1 were measured by qRT-PCR and Western blot analysis. As shown in Figure 1A and 1B, mRNA expression levels of FoxM1 in gefitinib-treated SPC-A-1 cells increased at 24, 48, and 72 h, compared with the untreated control group. Moreover, the protein levels of FoxM1 in the treated group were also upregulated, with a 2 to 10 fold increase compared with the control group (Figure 1C). In contrast, the mRNA and protein levels of FoxM1 were significantly reduced in the H292 cells (Figure 1D and 1E). Together, these results indicated that FoxM1 showed a different expression pattern between resistant and sensitive NSCLC cell lines treated with gefitinib, implying that FoxM1 has an important role in the resistance of such cells to gefitinib.

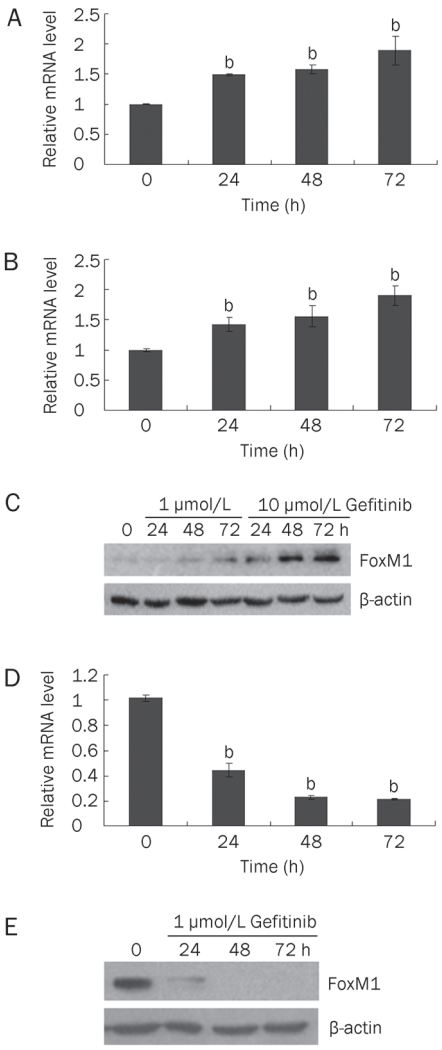

Figure 1. Expression level of FoxM1 in the resistant and sensitive lung cancer cells with gefitinib treatment. (A and B) mRNA expression of FoxM1 in gefitinib-resistant SPC-A-1 lung cancer cell line upon the treatment of 1 μmol/L (A) and 10 μmol/L (B) concentration of gefitinib for 24, 48, and 72 h. (C) Protein expression level of FoxM1 in SPC-A-1 lung cancer cell line upon treatment of 1 μmol/L and 10 μmol/L concentration of gefitinib for 24, 48, and 72 h. β-actin was used as a loading control. mRNA (D) and protein (E) levels of FoxM1 in gefitinib-sensitive NCI-H292 cells upon treatment of 1 μmol/L concentration of gefitinib for 24, 48, and 72 h. Mean±SD. $^{b}P<0.05$ *vs* control.

Increased expression of FoxM1 contributed to the resistance of NSCLC cells to gefitinib

To determine whether an increase of FoxM1 expression plays a role in the resistance of NSCLC cells to gefitinib, FoxM1 expression was first knocked down by RNA interference in SPC-A-1 cells, which was confirmed by qRT-PCR (Figure 2A). Cells undergoing transfection of siRNAs were also incubated with gefitinib for 72 h, respectively. As shown in Figure 2B, survival rates of SPC-A-1 cells significantly decreased ($P<0.05$) in the group that was transfected with siRNAs against FoxM1 (siRNA-FoxM1) compared with the siRNA-targeting negative control (siRNA-NC), with all cells being exposed to different concentrations of gefitinib treatment (0, 0.1, 1, 5, 10, and 20 μmol/L). In addition, the apoptosis rate of SPC-A-1 cells significantly increased from 7.55% to 14.11% and from 8.88% to 18.69% in the siRNA-FoxM1 groups compared with the siRNA-NC groups, with 1 μmol/L and 10 μmol/L gefitinib concentrations, respectively (Figure 2C). These data strongly suggest that FoxM1 plays an important role in the resistance of SPC-A-1 cells to gefitinib, implying that targeting FoxM1 could sensitize SPC-A-1 cells to the drug.

To further demonstrate the role of FoxM1 in the resistance to gefitinib, we employed lentiviral transfection in order to establish FoxM1 overexpressing cells (H292-FoxM1), which was confirmed at the mRNA (Figure 3A) and protein levels (Figure 3B). Consistently, when treated with 0, 0.25, 0.5, 1, 2, and 4 μmol/L concentrations of gefitinib for 72 h, the survival rate of H292-FoxM1 increased (Figure 3C), while the apoptosis rate was abrogated with the treatment of 1 μmol/L and 2 μmol/L concentrations of gefitinib (Figure 3D). These data suggest that the introduction of FoxM1 can protect lung cancer cells against gefitinib.

FoxM1 mediated the resistance of lung cancer cells to gefitinib by the upregulation of downstream targeted genes

To further explore the mechanisms of how FoxM1 may mediate the resistance of SPC-A-1 cells to gefitinib, the expression levels of several cell cycle-related genes were examined, including Aurora B kinase, Skp2, PLK1, CDC25B, survivin, and cyclin B1, all known targets of FoxM1. These targets participate in multiple cellular functions, including cytoprotection, cell death, and cell cycle regulation. As shown in Figure 4A, mRNA expression levels of these downstream targets were significantly upregulated in gefitinib-treated SPC-A-1 cells (1 μmol/L and 10 μmol/L) for 48 h. When treated with a 1 μmol/L concentration of gefitinib, the mRNA expression levels of survivin, cyclin B1, SKP2, PLK1, Aurora B kinase and CDC25B increased. Additionally, when treated with 10 μmol/L gefitinib, the expression levels of the downstream targets survivin, cyclin B1, SKP2, PLK1, Aurora B kinase and

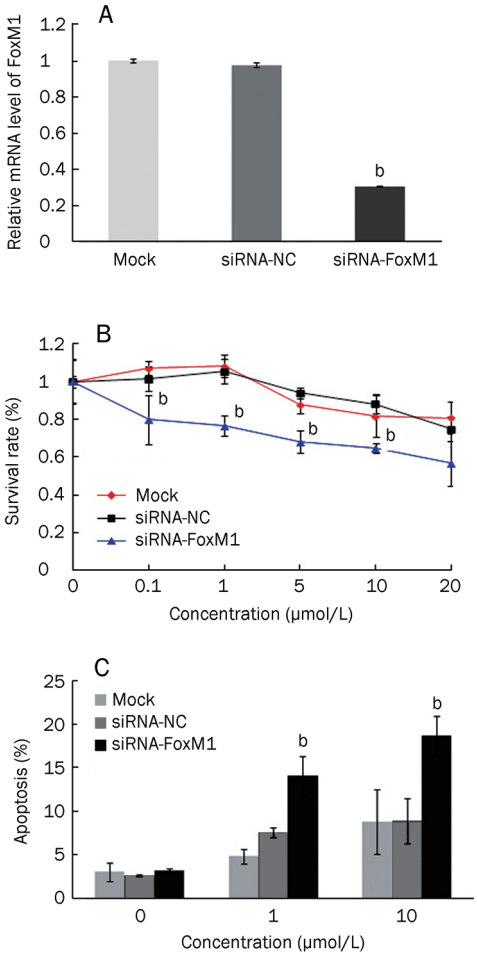

Figure 2. Survival rate and apoptosis rate of SPC-A-1 cells in siRNA-FoxM1, siRNA-NC, and mock groups. (A) qRT-PCR assays of FoxM1 expression level in SPC-A-1 cells transfected with indicated siRNAs. (B) Survival rate of SPC-A-1 cells in siRNA-FoxM1 (blue line), siRNA-NC (black line), and mock (red line) groups with the treatment of 0, 0.1, 1, 5, 10, and 20 μmol/L concentrations of gefitinib for 72 h. Apoptosis rate of SPC-A-1 cells in the siRNA-FoxM1, siRNA-NC, and mock groups with the treatment of 1 μmol/L and 10 μmol/L concentration of gefitinib for 72 h. Mean±SD. $^{b}P<0.05$ *vs* the mock and siRNA-NC groups.

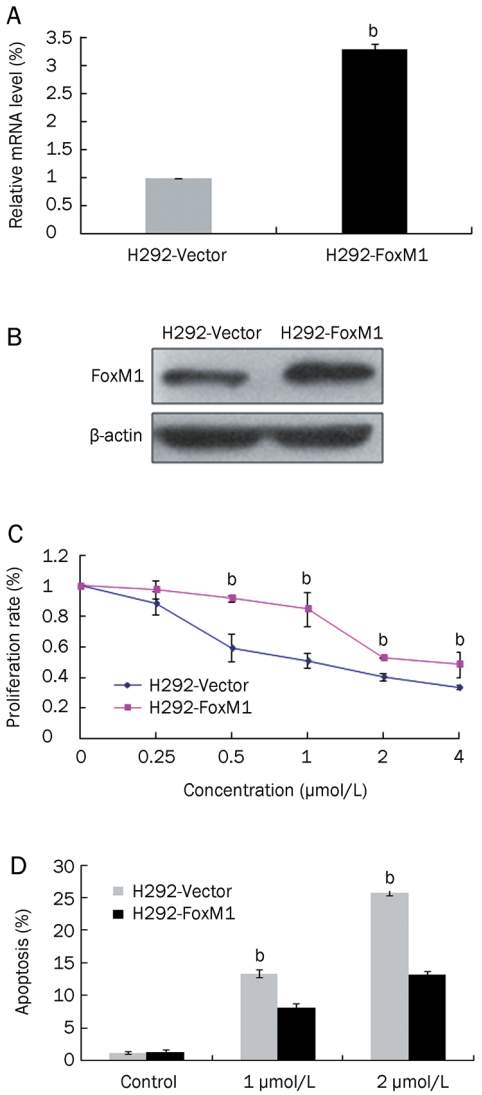

Figure 3. Survival rate and apoptosis rate of H292 cells overexpressiong FoxM1. (A) qRT-PCR assays of FoxM1 expression level in H292 cells with lenti-virus infection. (B) Western blot analysis of FoxM1 expression level in H292 cells with lenti-virus infection. β-actin was used as a loading control. (C) Survival rate of H292 cells in H292-FoxM1 (red line) and vector (blue line) groups with the treatment of 0, 0.25, 0.5, 1, 2, and 4 μmol/L concentrations of gefitinib for 72 h. (D) Apoptosis rate of H292 cells in the H292-FoxM1 and vector groups with the treatment of 1 μmol/L and 2 μmol/L concentration of gefitinib for 72 h. Mean±SD. $^{b}P<0.05$ *vs* the vector group.

CDC 25B increased in the resistant cell line compared with the control (Figure 4A).

Among these factors, there was a significant increase in survivin and cyclin B1 expression as compared to the other factors. Thus, they were chosen for further examination of their protein levels in the resistant cell line. As shown in Figure 4B, the expression levels of both genes were significantly upregulated in cells treated with gefitinib (1 μmol/L and 10 μmol/L) for 0, 24, 48, and 72 h, respectively.

Furthermore, we examined the expression levels of these factors in SPC-A-1 siRNA-FoxM1 and H292-FoxM1 cell lines. A decrease in Aurora B kinase, cyclin B1, survivin and Skp2 (Figure 5A, 5C) expression was observed in SPC-A-1 cells transfected with siRNA against FoxM1. An increase of Aurora B kinase, cyclin B1, survivin and Skp2 (Figure 5B, 5D) was observed in H292-FoxM1 cells, which revealed that an overexpression of FoxM1 conferred the resistance of NSCLC cells to gefitinib. Taken together, these data suggest that FoxM1 mediated the resistance of lung cancer cells to gefitinib, probably by upregulating the expression of several downstream targets of FoxM1, including Aurora B kinase, Skp2, PLK1, CDC25B, survivin and cyclin B1, which are all important factors in the regulation of cell cycle progression and proliferation.

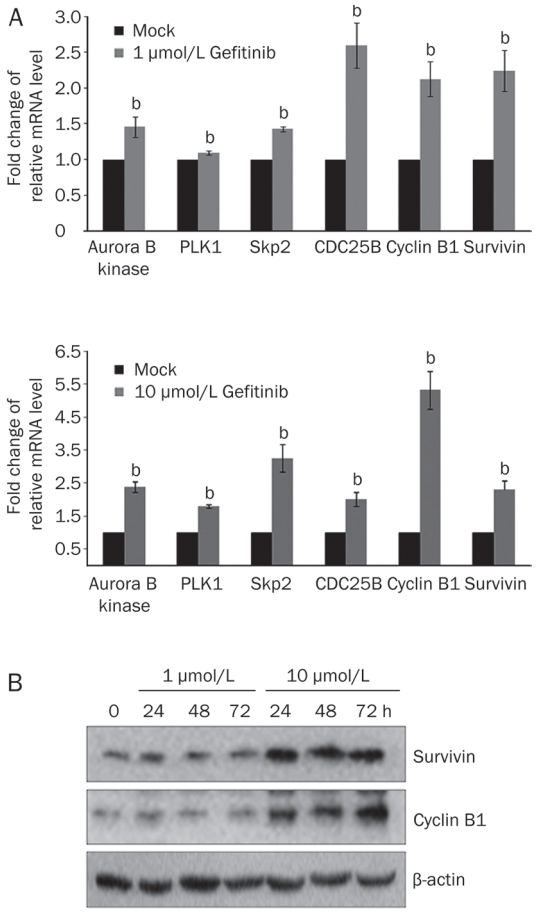

Figure 4. Expression levels of downstream targets of FoxM1 in the SPC-A-1 cells with gefitinib treatment. (A) mRNA expression levels of downstream targets of FoxM1 with treatment of 1 μmol/L and 10 μmol/L concentration of gefitinib for 48 h. (B) Protein level of cyclinB1 and survivin in the SPC-A-1 cells with the treatment of 1 μmol/L and 10 μmol/L concentration of gefitinib for 24, 48, and 72 h. β-actin was used as a loading control. Mean±SD. $^bP<0.05$ *vs* the mock group.

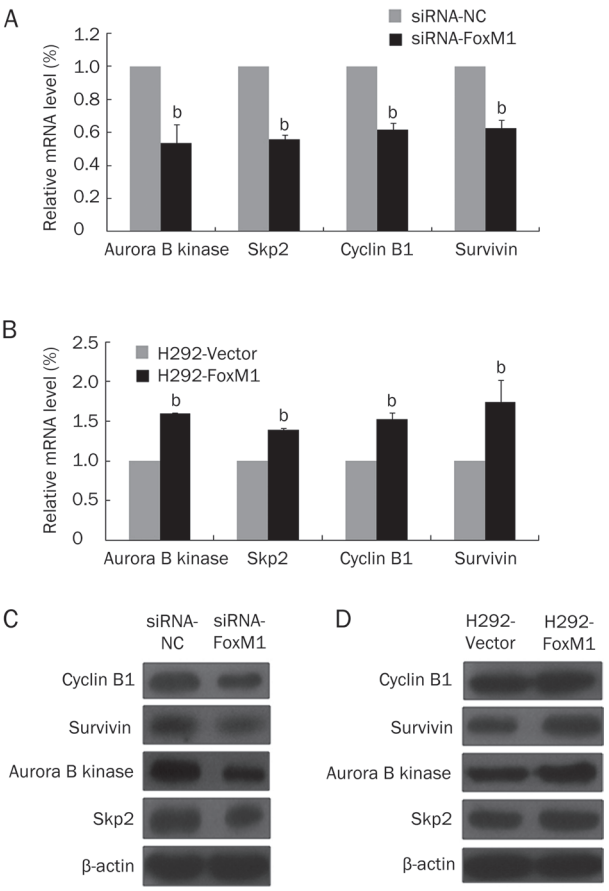

Figure 5. Expression levels of downstream targets when FoxM1 was knockdown in SPC-A-1 and overexpressed in H292 cells. (A) mRNA expression levels of downstream targets of FoxM1 in SPC-A-1 siRNA-FoxM1 (black bar) and siRNA-NC (grey bar) groups. (B) mRNA expression levels of downstream targets of FoxM1 in H292-FoxM1 (black bar) and vector (grey bar) groups. Quantification values normalized to GAPDH are shown as mean±SD. (C) Protein levels of downstream targets of FoxM1 in siRNA-FoxM1 and siRNA-NC groups. β-actin was used as a loading control. (D) Protein levels of downstream targets of FoxM1 in H292-FoxM1 and vector groups. β-actin was used as a loading control. Mean±SD. $^bP<0.05$ *vs* the siRNA-NC or vector group.

Discussion

According to the World Health Organization, lung cancer is responsible for more than 1.3 million deaths every year. Although there have been advances in cancer treatment, drug resistance is the most common cause of therapy failure in lung cancer patients[22]. FoxM1, a member of the Forkhead box family of transcription factors, is known to play an important role in cell cycle progression[23, 24] and is overexpressed in a panel of solid tumors, including liver, lung, cervical, colorectal and breast cancers[7, 9–11]. FoxM1 also participates in the drug resistance of various cancer cells by protecting cancer cell proliferation and abrogating apoptosis[25, 26]. For example, enhanced expression of FoxM1 was reported to inhibit cell death induced by gefitinib in some breast cancer cell lines[15]. However, gefitinib can also inhibit the expression of FoxM1 in sensitive breast cancer cells[27]. These findings suggest that FoxM1 has an important role in gefitinib-induced proliferative arrest. Thus, its expression might be used to determine the sensitivity of breast cancer cells to gefitinib. It is important to note that attenuating the activity of FoxM1 in traztuzumab-resistant breast cancer cells has also been shown to increase their sensitivity to traztuzumab, a tyrosine kinase receptor antibody inhibitor that targets the HER2 oncogene product. Traztuzumab, in fact, shares similar signaling pathway inhibition with gefitinib, including PI3K/Akt[26]. Moreover, the knockdown of FoxM1 expression can induce apoptosis in breast cancer cells that are otherwise resistant to cisplatin[25]. However, the role of FoxM1 in the EGFR-TKI resistance of NSCLC is largely unknown.

In this study, we show that treatment with gefitinib not only decreases FoxM1 expression in sensitive H292 lung cancer cells, which is consistent with previous studies demonstrat-

ing that gefitinib repressed expression of FoxM1 in sensitive breast cancer cell lines[27], but also that gefitinib paradoxically increases FoxM1 expression in resistant SPC-A-1 lung cancer cells. Additionally, to determine if FoxM1 has the ability to confer resistance to NSCLC cells exposed to gefitinib, we knocked down FoxM1 expression in the resistant SPC-A-1 cells, and overexpressed it in the sensitive H292 cells. The results showed that when FoxM1 was suppressed, the proliferation of SPC-A-1 cells was inhibited and apoptosis was increased, while the overexpression of FoxM1 enhanced the resistance of H292 cells to gefitinib. Taken together, these findings strongly suggest that FoxM1 plays an important role in gefitinib-resistant cells through promoting cell proliferation and inhibiting apoptosis. Importantly, the inhibition of FoxM1 expression partially restores sensitivity to gefitinib in the otherwise resistant cells.

To further determine the molecular mechanism by which FoxM1 contributes to gefitinib resistance in the resistant cells, the expression levels of several FoxM1-targeted genes implicated in drug resistance, including Aurora B kinase, Skp2, PLK1, CDC25B, survivin and cyclin B1, were analyzed[28, 29]. Through gene amplification of Aurora B kinase, Skp2, PLK1, CDC25B, survivin and cyclin B1, FoxM1 promotes G_1-S and G_2-M transition and mitosis. We also found that the mRNA expression levels of these genes significantly increased with gefitinib exposure, possibly contributing to gefitinib resistance. In addition, among these factors, survivin and cyclin B1 increased more significantly with exposure to gefitinib than the other factors. Survivin, a member of the inhibitor of apoptosis (IAP) family, has been reported to function in chemotherapy and radiation therapy resistance[30]. Thus, survivin has been a target for therapy in several cancers, including rectal, ovarian and esophageal cancers[30–32]. These findings suggest that an increase of survivin in cancer cells would decrease chemotherapy sensitivity. Cyclin B1, a G_2/mitotic-specific cyclin, is essential for the transition from G_2 to mitosis, and it has been implicated in the drug-resistance of several cancers[33, 34]. For example, targeting cyclin B1 inhibits proliferation in several breast and cervical cancer cell lines, and sensitized breast cancer cells to paclitaxel[29]. In addition, in head and neck squamous cell carcinomas, the overexpression of cyclin B1 correlates with radiotherapy resistance[34], and nuclear cyclin B1-positive breast carcinomas are resistant to hormonal, radio- and chemotherapy adjuvant treatment[33].

We have demonstrated that FoxM1 can upregulate the expression levels of survivin, cyclin B1 and other downstream cell cycle regulators in SPC-A-1 cells treated with gefitinib. The expression of the downstream targets could be decreased with low FoxM1 expression and thus lead to the reduced proliferation and enhanced apoptosis of tumor cells. Moreover, these downstream targets could be upregulated with high FoxM1 expression and may increase proliferation and decrease apoptosis in tumor cells. This implies that these molecules participate in the FoxM1-mediated resistance of NSCLC cells to gefitinib, thereby reducing drug sensitivity. Thus, the deregulation of FoxM1 and its downstream targets may play a pivotal clinical role in NSCLC resistance to gefitinib. Our results could help explain the results of the phase III clinical study ISEL (Iressa Survival Evaluation in Lung Cancer). In this study, it was demonstrated that gefitinib, employed as a second-line treatment alone, failed to show clinical benefit compared with the placebo group[35]. This could be due to gefitinib's induction of survivin and cyclin B1 expression in resistant cases, thus suppressing its efficacy.

In summary, we have found that FoxM1 can mediate and even increase the resistance of NSCLC cells to gefitinib, perhaps by increasing the expression of its downstream targets, survivin and cyclin B1 in particular, indicating that targeting FoxM1 for inhibition could sensitize otherwise resistant NSCLC cells to gefitinib. To the best of our knowledge, this report demonstrated that FoxM1 overexpression in the clinical setting might provide protection for NSCLC tumors from gefitinib, suggesting that FoxM1 targeting might be an attractive strategy for use in combination with conventionally used cytotoxic agents and/or target therapy.

Acknowledgements

This work was supported by the Shanghai Leading Academic Discipline Project(No B115) and China National "985" Project (phase III).

Author contribution

Nuo XU and Xin ZHANG performed the research and wrote the paper; Xun WANG, Hai-yan GE, Xiao-ying WANG, and Yuan-lin SONG analyzed data and helped with the reagents. David GARFIELD and Ping YANG helped revise the paper. Chun-xue BAI designed and supervised the research.

References

1 Elzagallaai AA, Garcia-Bournissen F, Finkelstein Y, Bend JR, Rieder MJ, Koren G. Severe bullous hypersensitivity reactions after exposure to carbamazepine in a HAN-Chinese child with a positive HLA-B*1502 and negative *in vitro* toxicity assays: evidence for different pathophysiological mechanisms. J Popul Ther Clin Pharmacol 2011; 18: e1–9.

2 Raychaudhuri P. FoxM1: a master regulator of tumor metastasis. Cancer Res 2011; 71: 4329–33.

3 Sun H, Teng M, Liu J, Jin D, Wu J, Yan D, *et al*. FOXM1 expression predicts the prognosis in hepatocellular carcinoma patients after orthotopic liver transplantation combined with the Milan criteria. Cancer Lett 2011; 306: 214–22.

4 Yu J, Deshmukh H, Payton JE, Dunham C, Scheithauer BW, Tihan T, *et al*. Array-based comparative genomic hybridization identifies CDK4 and FOXM1 alterations as independent predictors of survival in malignant peripheral nerve sheath tumor. Clin Cancer Res 2011; 17: 1924–34.

5 Balli D, Zhang Y, Snyder J, Kalinichenko VV, Kalin TV. Endothelial cell-specific deletion of transcription factor FoxM1 increases urethane-induced lung carcinogenesis. Cancer Res 2011; 71: 40–50.

6 Wang X, Kiyokawa H, Dennewitz MB, Costa RH. The forkhead box m1b transcription factor is essential for hepatocyte DNA replication and mitosis during mouse liver regeneration. Proc Natl Acad Sci U S A 2002; 99: 16881–6.

7 Wang IC, Chen YJ, Hughes D, Petrovic V, Major ML, Park HJ, *et al*.

Forkhead box M1 regulates the transcriptional network of genes essential for mitotic progression and genes encoding the SCF (SKP2-1) ubiquitin ligase. Mol Cell Biol 2005; 25: 10875–94.
8 aoukili J, Kooistra MR, Brás A, Kauw J, Kerkhoven RM, Morrison A, *et al*. FoxM1 is required for execution of the mitotic rogramme and chromosome stability. Nat Cell Biol 2005; 7: 126–36.
9 Wonsey DR, Follettie MT. Loss of the forkhead transcription factor FoxM1 causes centrosome amplification and mitotic catastrophe. Cancer Res 2005; 65: 5181–9.
10 Iin TV, Wang IC, Ackerson TJ, Major ML, Detrisac CJ, Kalinichenko VV, *et al*. Increased levels of the FoxM1 transcription factor accelerate development and progression of prostate carcinamas in both TRAMP and LADY transgenic mice. Cancer Res 2006; 66: 1712–20.
11 Kim IM, Ackerson T, Ramakrishna S, Tretiakova M, Wang IC, Kalin TV, *et al*. The Forkhead Box m1 transcription factor stimulates the proliferation of tumor cells during development of lung cancer. Cancer Res 2006; 66: 2153–61.
12 Le XF, Pruefer F, Bast RC Jr. HER2-targeting antibodies modulate the cyclin-dependent kinase inhibitor p27Kip1 via multiple signaling pathways. Cell Cycle 2005; 4: 87–95.
13 Wakeling AE. Epidermal growth factor receptor tyrosine kinase inhibitors. Curr Opin Pharmacol 2002; 2: 382–7.
14 F Ciardiello. Epidermal growth factor receptor inhibitors in cancer treatment. Future Onclo 2005; 1: 221–34.
15 Nelson MH, Dolder CR. Lapatinib: a novel dual tyrosine kinase inhibitor with activity in solid tumors. Ann Pharmacother 2006; 40: 261–9.
16 Wakeling AE, Guy SP, Woodburn JR, Ashton SE, Curry BJ, Barker AJ, *et al*. ZD1839 (Iressa): an orally active inhibitor of epidermal growth factor signaling with potential for cancer therapy. Cancer Res 2002; 62: 5749–54.
17 Hay N. The Akt-mTOR tango and its relevance to cancer. Cancer Cell 2005; 8: 179–83.
18 Morgillo F, Lee HY. Resistance to epidermal growth factor receptor-targeted therapy. Drug Resist Update 2005; 8: 298–310.
19 Jia D, Yan M, Wang X, Hao X, Liang L, Liu L, *et al*. Development of a highly metastatic model that reveals a crucial role of fibronectin in lung cancer cell migration and invasion. BMC Cancer 2010; 10: 364–75.
20 Macha MA, Matta A, Chauhan S, Siu KM, Ralhan R. 14-3-3 zeta is a molecular target in guggulsterone induced apoptosis in head and neck cancer cells. BMC Cancer 2010; 10: 655–66.
21 Zheng Y, Ritzenthaler JD, Roman J, Han S. Nicotine stimulates human lung cancer cell growth by inducing fibronectin expression. Am J Respir Cell Mol Biol 2007; 37: 681–90.
22 Uchida A, Hirano S, Kitao H, Ogino A, Rai K, Toyooka S, *et al*. Activation of downstream epidermal growth factor receptor (EGFR) signaling provides efitinibresistance in cells carrying EGFR mutation. Cancer Sci 2007; 98: 357–63.
23 Laoukili J, Stahl M, Medema RH. FoxM1: at the crossroads of ageing and cancer. Biochim Biophys Acta 2007; 1775: 92–102.
24 Myatt SS, Lam EW. The emerging roles of forkhead box (Fox) proteins in cancer. Nat Rev Cancer 2007; 7: 847–59.
25 Kwok JM, Peck B, Monteiro LJ, Schwenen HD, Millour J, Coombes RC, *et al*. FOXM1 confers acquired cisplatin resistance in breast cancer cells. Mol Cancer Res 2010; 8: 24–34.
26 Carr JR, Park HJ, Wang Z, Kiefer MM, Raychaudhuri P. FoxM1 mediates resistance to Herceptin and Paclitaxel. Cancer Res 2010; 70: 5054–63.
27 McGovern UB, Francis RE, Peck B, Guest SK, Wang J, Myatt SS, *et al*. Gefitinib (Iressa) represses FOXM1 expression via FOXO3a in breast cancer. Mol Cancer Ther 2009; 8: 582–91.
28 Estève PO, Chin HG, Pradhan S. Molecular mechanisms of transactivation and doxorubicin-mediated repression of survivin gene in cancer cells. J Biol Chem 2007; 282: 2615–25.
29 Androic I, Krämer A, Yan R, Rödel F, Gätje R, Kaufmann M, *et al*. Targeting cyclin B1 inhibits proliferation and sensitizes breast cancer cells to taxol. BMC Cancer 2008; 8: 391.
30 Rödel F, Hoffmann J, Distel L, Herrmann M, Noisternig T, Papadopoulos T, *et al*. Survivin as a radioresistance factor, and prognostic and therapeutic target for radiotherapy in rectal cancer. Cancer Res 2005; 65: 4881–7.
31 Kato J, Kuwabara Y, Mitani M, Shinoda N, Sato A, Toyama T, *et al*. Expression of survivin in esophageal cancer: correlation with the prognosis and response to chemotherapy. Int J Cancer 2001; 95: 92–5.
32 Zaffaroni N, Pennati M, Colella G, Perego P, Supino R, Gatti L, *et al*. Expression of the anti-apoptotic gene survivin correlates with taxol resistance in human ovarian cancer. Cell Mol Life Sci 2002; 59: 1406–12.
33 Suzuki T, Urano T, Miki Y, Moriya T, Akahira J, Ishida T, *et al*. Nuclear cyclin B1 in human breast carcinoma as a potent prognostic factor. Cancer Sci 2007; 98: 644–51.
34 Hassan KA, Ang KK, El-Naggar AK, Story MD, Lee JI, Liu D, *et al*. Cyclin B1 overexpression and resistance to radiotherapy in head and neck squamous cell carcinama. Cancer Res 2002; 62: 6414–17.
35 Thatcher N, Chang A, Parikh P, Rodrigues Pereira J, Ciuleanu T, von Pawel J, *et al*. Gefitinib plus best supportive care in previously treated patients with refractory advanced non-small-cell lung cancer: results from a randomised, placebo-controlled, multicentre study (Iressa Survival Evaluation in Lung Cancer). Lancet 2005; 366: 1527–37.

Acta Pharmacologica Sinica (2012) 33: 682–690
 1671-4083/12 $32.00
www.nature.com/aps

Original Article

Celecoxib induces apoptosis and cell-cycle arrest in nasopharyngeal carcinoma cell lines via inhibition of STAT3 phosphorylation

Dong-bo LIU, Guang-yuan HU, Guo-xian LONG, Hong QIU, Qi MEI, Guo-qing HU*

Cancer Center, Tongji Hospital, Tongji Medical College, Huazhong University of Science and Technology, Wuhan 430030, China

Aim: To investigate the mechanisms underlying the anticancer effect of celecoxib on nasopharyngeal carcinoma (NPC).
Methods: NPC cell lines, HNE1 and CNE1-LMP1, were treated with various concentrations of celecoxib for 48 h. The antiproliferative effect of celecoxib was assessed using MTT assay. Both cell cycle profiles and apoptosis were analyzed using flow cytometry. Western blot was used to measure the levels of signal transducer and activator of transcription 3 (STAT3), phosphorylated STAT3^{Y705} (pSTAT3^{Y705}), COX-2, Survivin, Mcl-1, Bcl-2 and Cyclin D1.
Results: Celecoxib (10–75 μmol/L) inhibited the proliferation of the NPC cell lines in a dose-dependent manner. Celecoxib (25 and 50 μmol/L) induced apoptosis and cell-cycle arrest at the G_0/G_1 checkpoint in the NPC cell lines, which was associated with significantly reduced STAT3 phosphorylation. The genes downstream of STAT3 (*ie*, Survivin, Mcl-1, Bcl-2 and Cyclin D1) were significantly down-regulated after exposure to celecoxib (25 and 50 μmol/L).
Conclusion: The anticancer effects of celecoxib on NPC cell lines results from inducing apoptosis and cell cycle arrest, which may be partly mediated through the STAT3 pathway.

Keywords: celecoxib; nasopharyngeal carcinoma; apoptosis; cell cycle; STAT3

Acta Pharmacologica Sinica (2012) 33: 682–690; doi: 10.1038/aps.2012.18; published online 16 Apr 2012

Introduction

Nasopharyngeal carcinoma (NPC) is the most common head and neck cancer in Southeast Asia and South China. The annual incidence rate of NPC in endemic areas is approximately 20 to 50 per 100 000 individuals[1]. NPC is characterized by its highly invasive and metastatic tendencies. Approximately 70% of NPC patients are initially diagnosed with locally advanced disease. Although aggressive concurrent chemo-radiotherapy is the standard treatment modality for NPC at the locally advanced stage, approximately 30% to 40% of NPC patients fail with local recurrence and/or distant metastasis[2]. The reported median survival time for an NPC patient with metastatic or advanced disease is only 5 to 11 months[3]. Due to the poor survival rate, more effective strategies and drugs to prevent and treat NPC are needed. The selective cyclooxygenase-2 (COX-2) inhibitor celecoxib shows great promise in this respect.

Celecoxib was the first COX-2-selective nonsteroidal anti-inflammatory drug (NSAID) approved for the clinical treatment of adult arthritis. Celecoxib exerts potent anticancer activities against various human cancers, including brain, lung, colon and liver cancers[4–7]. One mechanism through which celecoxib acts to reduce cancer development is by the inhibition of COX-2 activity. Furthermore, celecoxib can also act through COX-2-independent mechanisms involving the arrest of cell cycle progression, angiogenesis and the induction of apoptosis[8]. COX-2 is overexpressed in 43% to 75% of NPCs, contributes to nodal metastases and is associated with poorer prognosis[9, 10]. Although some studies have demonstrated certain antitumor effects of celecoxib on NPC *in vitro*, the molecular mechanisms underlying its inhibitory effects are still unclear[11–13].

Signal transducer and activator of transcription 3 (STAT3) is constitutively activated or overexpressed in a variety of human cancers. This pivotal transcription factor plays a significant role in regulating cell growth, apoptosis, angiogenesis, immune escape, invasion and metastasis. Accumulating evidence has demonstrated that STAT3 is a promising molecule target for anticancer treatment and cancer prevention[14, 15]. More recently, STAT3 has also been found to be activated in

* To whom correspondence should be addressed.
E-mail gqhu@tjh.tjmu.edu.cn
Received 2011-12-13 Accepted 2012-02-07

more than 75% of NPC cases, and this molecule plays a significant role in driving NPC progression and metastasis[16–18]. A recent study identified celecoxib as a novel inhibitor of STAT3[6]. Celecoxib was demonstrated and verified to have specificity to STAT3, and this drug has been shown to exert anticancer effects in colon cancer cells, hepatocellular carcinoma cells and rhabdomyosarcoma cells through the inhibition of STAT3 phosphorylation[6, 7, 19].

In contrast to other head and neck cancers, NPC possesses the unique feature of being strongly associated with the Epstein-Barr virus (EBV). In EBV-endemic regions, most NPC patients are EBV-infected[20]. Latent membrane protein 1 (LMP1), LMP2A, Epstein-Barr nuclear antigen 1 (EBNA1), *Bam*H I-A rightward transcripts (BARTs) and Epstein-Barr virus-encoded RNAs (EBERs) are expressed in EBV. LMP1 is the principal oncoprotein expressed by EBV, and LMP1 protein expression is detected in more than 70% of NPC patients. LMP1 plays an important role in the tumorigenesis and development of NPC and contributes to the promotion of invasion and metastasis[21]. Moreover, a recent study demonstrated that LMP1 could induce STAT3 phosphorylation through the mitogen-activated protein kinase (MAPK)/extracellular signal-regulated kinase (ERK) and Janus kinase (JAK)/STAT pathways[22].

Given the importance of STAT3 in NPC progression and the potent anticancer effect of celecoxib, we chose to investigate the potential molecular mechanisms of this drug with an emphasis on determining whether celecoxib inhibits STAT3 phosphorylation in NPC cells. We also explored whether the anticancer effects of celecoxib may be due to the induction of apoptosis and cell cycle arrest.

Materials and methods

Chemicals and antibodies

Lyophilized celecoxib was purchased from Sigma Chemical Co, MO, USA. Stock celecoxib solutions were prepared by dissolving the powder in DMSO and then storing at -20 °C. The drugs were freshly diluted into culture medium before the commencement of each experiment, and the final DMSO concentration in the culture medium never exceeded 0.1%. Primary antibodies including rabbit anti-human phsopho-STAT3-Tyr705, Survivin, Mcl-1 and Cyclin D1 monoclonal antibodies were purchased from Epitomics Inc, Burlingame, CA, USA. Rabbit anti-human Bcl-2 and STAT3 monoclonal antibodies were obtained from Cell Signaling Technology, Danvers, USA. Goat anti-human COX-2 and rabbit anti-human β-actin polyclonal antibodies were obtained from Santa Cruz Biotechnology, USA. The horseradish peroxidase (HRP)-conjugated goat anti-rabbit and HRP-conjugated rabbit anti-goat secondary antibodies were obtained from Santa Cruz Biotechnology. The 3-(4, 5-dimethylthiazol-2-yl)-2, 5-diphenyltetrazolium bromide (MTT) was obtained from Sigma.

Cell culture

HNE1 was derived from a poorly differentiated NPC that has lost the EB virus due to long-term *in vitro* passaging (over 100 passages)[23]. CNE1 is a poorly differentiated NPC cell line that is also EBV negative. CNE1-LMP1 is a stably transfected cell line established by introducing LMP1 cDNA into CNE1 cells[24]. The HNE1 and CNE1-LMP1 cell lines were provided by the Cancer Research Institute of Central South University (Changsha, China). All lines were maintained in Roswell Park Memorial Institute (RPMI)-1640 medium (Gibco, Grand Island, USA) supplemented with 10% newborn calf serum (Gibco, Grand Island, USA) and incubated in a 5% CO_2 atmosphere.

Growth inhibition assay

The antiproliferative effect of celecoxib on NPC cells was assessed using an MTT assay. Cells were seeded into 96-well plates and allowed to attach for 24 h. The cells were then treated with increasing concentrations of celecoxib (0, 5, 10, 25, 50 or 75 μmol/L) dissolved in DMSO (final concentration ≤0.1%) and incubated for up to 48 h. After the incubation, 20 μL of MTT dye (5 mg/mL) were added to each well and cells were incubated at 37 °C for 4 h. After removing the supernatants, the crystals were dissolved in DMSO and the absorbance was measured at 490 nm. The percentage growth inhibition was calculated as $(OD_{control} - OD_{drug})/OD_{control} \times 100\%$. The half-maximal inhibitory concentration (IC_{50}) values and the 95% confidence intervals were calculated using probit regression using SPSS 15.0 software (SPSS Inc, Chicago, IL, USA). The experiment was performed in triplicate and repeated at least three times.

Apoptosis assay

Cells were treated with increasing doses of celecoxib (0, 10, 25, 50 or 75 μmol/L) for 48 h and then harvested and washed with phosphate buffered saline (PBS). After washing, the cells were stained with Annexin V-fluorescein isothiocyanate (FITC) and propidium iodide (PI) for 15 min at 4 °C in the dark, in accordance with the manufacturer's instructions (Nanjing KeyGen Biotech Co, Nanjing, China). After incubation, the cells were immediately analyzed using flow cytometry (EPICS XL, Beckman Coulter Inc, Fullerton, CA, USA). Early apoptotic cells stained positive for Annexin V-FITC and negative for PI. Late apoptotic cells were positive for both Annexin V-FITC and PI. The experiment was performed in triplicate and repeated at least three times.

Cell cycle analysis

Cells were treated with increasing concentrations of celecoxib (0, 10, 25, 50 or 75 μmol/L) for 48 h. The adherent and the nonadherent cell fractions were then collected and fixed in 70% ice-cold ethanol overnight. Cells were washed with cold PBS, treated with RNase for 30 min at 37 °C, and then stained with PI for 30 min at 4 °C in the dark. DNA content was analyzed using flow cytometry (EPICS XL, Beckman Coulter Inc, Fullerton, CA, USA). The data were analyzed using the ModFit™ for Mac version 3.0 software (Verity Software House, Topsham, ME, USA). The experiment was performed in triplicate and repeated at least three times.

Western blot analysis

Cells were treated with DMSO (control) or increasing concentrations of celecoxib (10, 25, 50 or 75 μmol/L) for 48 h. The cells were then washed with PBS and lysed in Radio-Immunoprecipitation Assay (RIPA) buffer with phosphatase and protease inhibitors (Roche Diagnostics, Mannheim, Germany). The protein concentrations were determined using the Bradford protein assay kit (Bio-Rad Laboratories Inc, Hercules, CA, USA) according to the manufacturer's instructions. Protein samples were separated by sodium dodecylsulfate-polyacrylamide gel electrophoresis (SDS-PAGE) and transferred to polyvinylidene difluoride (PVDF) membranes (Millipore, Billerica, MA, USA). After blocking the membrane's non-specific binding sites using non-fat milk, the membranes were separately incubated with primary antibodies overnight and then probed with HRP-conjugated goat anti-rabbit or HRP-conjugated rabbit anti-goat secondary antibodies. The specific proteins of interest were visualized using the enhanced chemiluminescence (ECL) detection system. Densitometric quantification of the bands was performed using the AlphaEaseFC software tool (Alpha Innotech, San Leandro, CA, USA). The experiment was performed in triplicate and repeated at least three times.

Statistical analysis

All data were expressed as the mean±standard deviations (SD). Statistical analysis was performed using Student's *t* test. $P<0.05$ was considered statistically significant.

Results

COX-2 protein expression in NPC cell lines

To investigate the COX-2 protein expression patterns in HNE1 and CNE1-LMP1 cells, Western blots were performed after 48 h incubations with different doses of celecoxib (0, 10, 25, 50 or 75 μmol/L). Western blot analysis revealed that both cell lines expressed COX-2. The HNE1 cells exhibited higher protein expression levels of COX-2 than the CNE1-LMP1 cells ($P<0.01$). In the HNE1 cell line, COX-2 expression was significantly down-regulated upon celecoxib treatment at concentrations of 10, 25 and 50 μmol/L ($P<0.01$, $P<0.01$ and $P<0.01$, respectively). However, at the 50 and 75 μmol/L concentrations of celecoxib in CNE1-LMP1 cells, COX-2 expression was significantly up-regulated ($P<0.01$ and $P<0.01$, respectively) (Figure 1A and 1B).

Anti-proliferative effect of celecoxib on NPC cell lines

To investigate whether celecoxib was capable of inhibiting NPC cell growth, HNE1 and CNE1-LMP1 cells were treated with increasing concentrations of celecoxib (0, 5, 10, 25, 50 or 75 μmol/L) for 48 h, followed by an MTT assay. As shown in Figure 1C and 1D, we observed that the inhibitory effect of celecoxib occurred in a dose-dependent manner. The average IC_{50} values of celecoxib in HNE1 and CNE1-LMP1 were 32.86±1.13 μmol/L and 61.31±4.30 μmol/L, respectively.

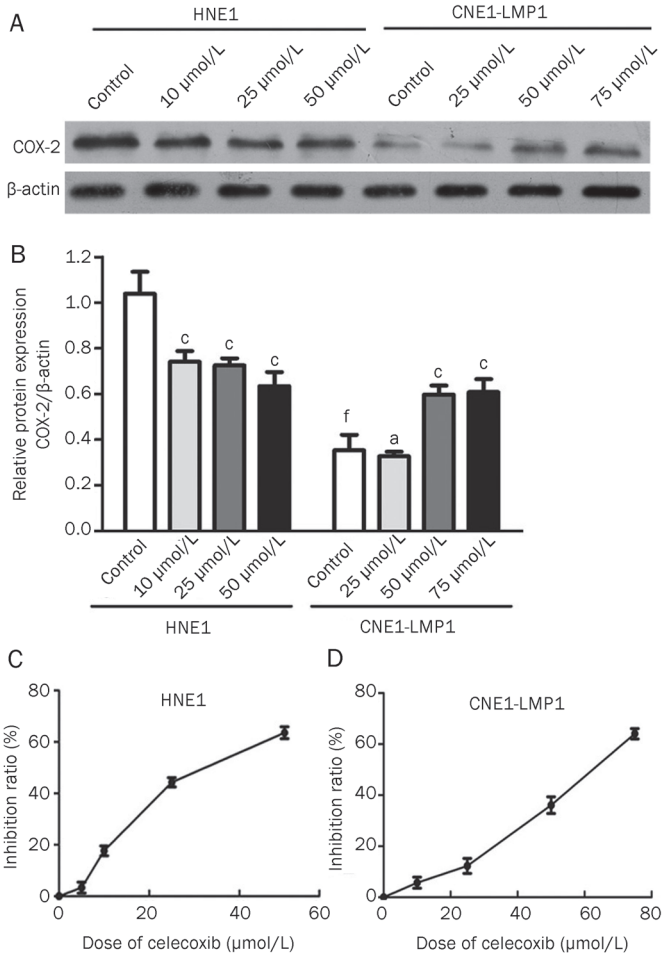

Figure 1. Celecoxib regulated COX-2 expression levels and inhibited cell proliferation in human nasopharyngeal carcinoma cells. (A and B) COX-2 was consistently expressed in both HNE1 and CNE1-LMP1 cell lines. Western blot analysis of the control cells and cells treated with various concentrations celecoxib (0, 10, 25, 50 or 75 μmol/L). HNE1 cells expressed higher levels of COX-2 than CNE1-LMP1 cells. COX-2 expression levels were significantly reduced in HNE1 cells but were significantly increased in the CNE1-LMP1 cells after drug treatment. (C and D) Celecoxib induced dose-dependent growth inhibition in both HNE1 and CNE1-LMP1 cells. Values displayed are the mean±SD ($n=3$). $^{a}P>0.05$, $^{c}P<0.01$ *vs* control; $^{f}P<0.01$ CNE1-LMP1 control *vs* HNE1 control.

Celecoxib induces apoptosis in NPC cell lines

Because celecoxib has been reported to exert an anticancer effect by mediating apoptosis in a COX-2-independent manner in many tumors[25], we examined whether the inhibitory effect of celecoxib was associated with the induction of apoptosis. Flow cytometric analysis using Annexin V/PI double staining in both celecoxib-treated and control cells was used to detect apoptosis. After treatment with increasing doses of celecoxib (0, 10, 25, 50 or 75 μmol/L) for 48 h, induction of apoptosis was observed in both HNE1 and CNE1-LMP1 cells in a concentration-dependent manner. Celecoxib induced significant increases in the percentage apoptotic cells in HNE1 cells

at concentrations of 25 and 50 μmol/L (P<0.01 and P<0.01, respectively) and in CNE1-LMP1 cells at concentrations of 50 and 75 μmol/L (P<0.05 and P<0.01, respectively) (Figure 2).

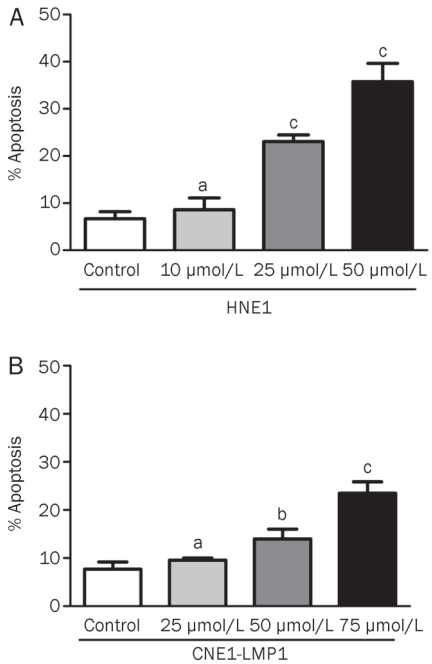

Figure 2. Celecoxib induced apoptosis in HNE1 and CNE1-LMP1 cells. After 48 h of incubation with drugs, flow cytometry analysis using Annexin V and propidium iodide (PI) double staining was performed on both control and celecoxib-treated cells. The population in the figure is the total number of apoptotic cells, which includes both early and late apoptotic populations. Early apoptotic cells were positive for Annexin V-FITC and negative for PI. Late apoptotic cells were positive for both Annexin V-FITC and PI. Significant apoptosis was observed in HNE1 cells (A) with 25 and 50 μmol/L of celecoxib, and in CNE1-LMP1 cells (B) with 50 and 75 μmol/L of celecoxib. The data are presented as the mean±SD (n=3). [a]P>0.05, [b]P<0.05, [c]P<0.01 *vs* control.

Celecoxib induces cell-cycle arrest in NPC cell lines

To investigate whether cell-cycle arrest contributed to cell growth inhibition by celecoxib, cell-cycle progression was assayed. Flow cytometric analysis was performed on NPC cells treated with increasing concentrations of celecoxib (0, 10, 25, 50 or 75 μmol/L) for 48 h. As displayed in Figure 3, celecoxib induced a marked G_0/G_1 cell-cycle arrest in NPC cell lines in a concentration-dependent manner. Compared with the DMSO control treatment group, a significant increase in the G_0/G_1 population was observed in both NPC cell lines. At 25 and 50 μmol/L concentrations of celecoxib, significant increases (P<0.01 and P<0.01, respectively) in the proportion of cells arrested in the G_0/G_1 cell-cycle phase were observed in HNE1 cells. Subsequently, significant inhibition of S phase transition (P<0.01 and P<0.01 at 25 and 50 μmol/L, respectively) and G_2/M phase (P<0.05 and P<0.01 at 25 and 50 μmol/L, respectively) were observed. In CNE1-LMP1 cells there were significant increases in the proportion of cells that were arrested in the G_0/G_1 phase of the cell cycle after celecoxib treatment at concentrations of 25, 50 and 75 μmol/L (P<0.01, P<0.01 and P<0.01, respectively). Subsequently, significant inhibition of S phase transition (P<0.05 and P<0.01 at 50 and 75 μmol/L, respectively) and G_2/M phase (P<0.01 and P<0.01 at 50 and 75 μmol/L, respectively) were observed (Figure 3B and 3C).

Celecoxib inhibits STAT3 phosphorylation

To investigate whether celecoxib could inhibit STAT3 phosphorylation, Western blotting was used to analyze the levels of phosphorylated STAT3 after celecoxib treatment. The HNE1 and CNE1-LMP1 cell lines were treated with increasing concentrations of celecoxib (0, 10, 25, 50 or 75 μmol/L). As displayed in Figure 4, we observed that the amount of phosphorylated $STAT3^{Y705}$ (pSTAT3) was significantly reduced after the treatment of celecoxib at concentrations of 10, 25 or 50 μmol/L (P<0.01, P<0.01 and P<0.01, respectively) in HNE1 cells. Additionally, phosphorylated $STAT3^{Y705}$ was significantly down-regulated in CNE1-LMP1 cells after celecoxib treatment at concentrations of 25, 50 and 75 μmol/L (P<0.01, P<0.01 and P<0.01, respectively). The pSTAT3 expression levels in the CNE1-LMP1 cell line were higher than those in the HNE1 cell line (P<0.01) (Figures 4A and 4B), and the amount of total STAT3 expressed was consistent after treatment with increasing celecoxib doses.

To provide further evidence of the inhibition of STAT3 phosphorylation, we analyzed the important downstream proteins of STAT3 by Western blot. Survivin, Mcl-1, Bcl-2 and Cyclin D1 proteins displayed reduced expression levels after treatment with escalating doses of celecoxib (0, 10, 25, 50 and 75 μmol/L) in HNE1 and CNE1-LMP1 cells (Figure 4A). In HNE1 cells, celecoxib significantly down-regulated Survivin (P<0.01 and P<0.01 at 25 and 50 μmol/L, respectively), Mcl-1 (P<0.01 and P<0.01 at 25 and 50 μmol/L, respectively), Bcl-2 (P<0.01, P<0.01 and P<0.05 at 10, 25 and 50 μmol/L, respectively) and Cyclin D1 (P<0.01, P<0.01 and P<0.01 at 10, 25 and 50 μmol/L, respectively). In CNE1-LMP1 cells, Survivin (P<0.01, P<0.01 and P<0.01 at 25, 50 and 75 μmol/L, respectively), Mcl-1 (P<0.01, P<0.01 and P<0.01 at 25, 50 and 75 μmol/L, respectively), Bcl-2 (P<0.01 and P<0.01 at 50 and 75 μmol/L, respectively) and Cyclin D1 (P<0.01, P<0.01 and P<0.01 at 25, 50 and 75 μmol/L, respectively) were significantly down-regulated after celecoxib treatment (Figure 4C and 4D). This provides additional evidence that celecoxib inhibits STAT3 phosphorylation.

Celecoxib inhibits interleukin-6 (IL-6)-induced STAT3 phosphorylation

To investigate whether celecoxib may inhibit interleukin-6 (IL-6)-induced STAT3 phosphorylation, Western blotting was performed. We chose the HNE1 cell line due to its low levels of endogenous $pSTAT3^{Y705}$. Cells were cultured in serum-free medium for 24 h and then pretreated with 25 μmol/L or 50 μmol/L of celecoxib for 2 h. The cells were then treated with 25 ng/mL of human IL-6 (Peprotech Inc, Rocky Hill, NJ,

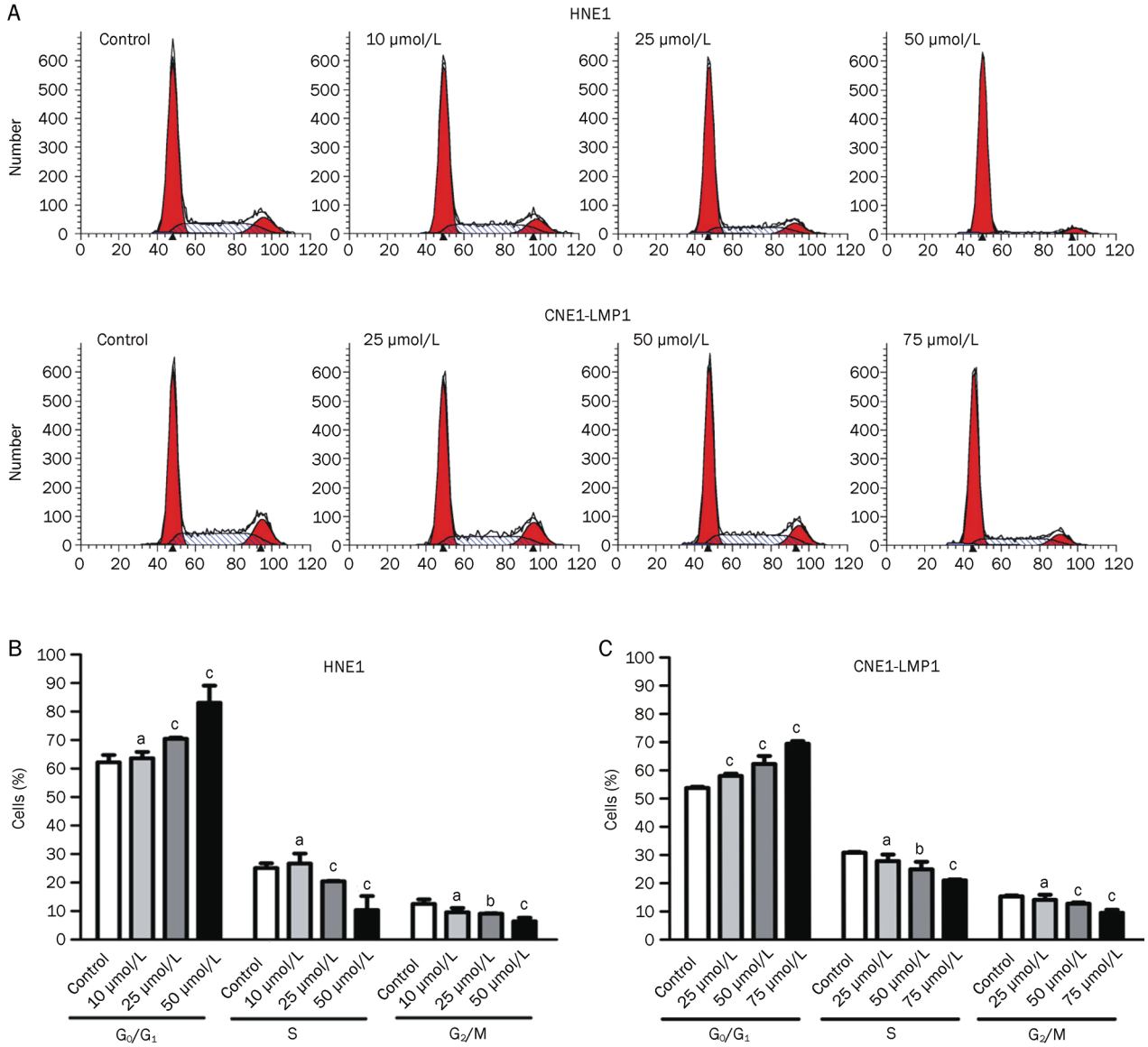

Figure 3. Celecoxib caused cell-cycle arrest in HNE1 and CNE1-LMP1 cells. Flow cytometry analysis of cells treated with DMSO (control) or celecoxib (10, 25, 50 or 75 μmol/L) for 48 h. Cells were fixed with 70% ethanol, stained with PI, and analyzed by flow cytometry. (A) Representative DNA histogram of cells after treatment with control or various concentrations of celecoxib for 48 h. Significant G_0/G_1 checkpoint arrest was observed in HNE1 (B) treated with 25 and 50 μmol/L of celecoxib, and this arrest was also observed in CNE1-LMP1 cells (C) treated with 25, 50 or 75 μmol/L of celecoxib. The data shown are the mean± SD from triplicate replicates and three independent experiments. $^aP>0.05$, $^bP<0.05$, $^cP<0.01$ *vs* control.

USA) for 30 min. After IL-6 treatment, $pSTAT3^{Y705}$ and STAT3 protein levels were analyzed by Western blot. We observed that IL-6 significantly promoted STAT3 phosphorylation ($P<0.01$) and that celecoxib significantly inhibited IL-6-induced STAT3 phosphorylation at concentrations of 25 and 50 μmol/L ($P<0.01$ and $P<0.01$, respectively) (Figure 5A and 5B).

Discussion

STAT3 is a novel anticancer drug target. Constitutive STAT3 activation has a critical role in tumor development and tumorigenesis in multiple tumors and cell lines. Critical gene expression changes induced by aberrant activation of STAT3 may promote cancer cell growth and survival via the upregulation of Cyclin D1, c-Myc, Pim-1[26, 27]. Additionally, STAT3 may inhibit apoptosis via the upregulation of Bcl-2, Survivin and Mcl-1[28–30]. STAT3 may also promote cancer cell invasion and metastasis through the induction of matrix metalloprateinase-2 (MMP-2)[31] and increase angiogenesis via the induction of vascular endothelial growth factor (VEGF) and hypoxia-inducible factor 1-alpha (HIF-1α)[32]. Increasing evidence has shown that the inhibition of constitutively activated STAT3 could lead to cancer cell death and tumor regression[33–35].

The activation or overexpression of STAT3 is very common in NPC. Indeed, it is detected in more than 75% of NPC cases.

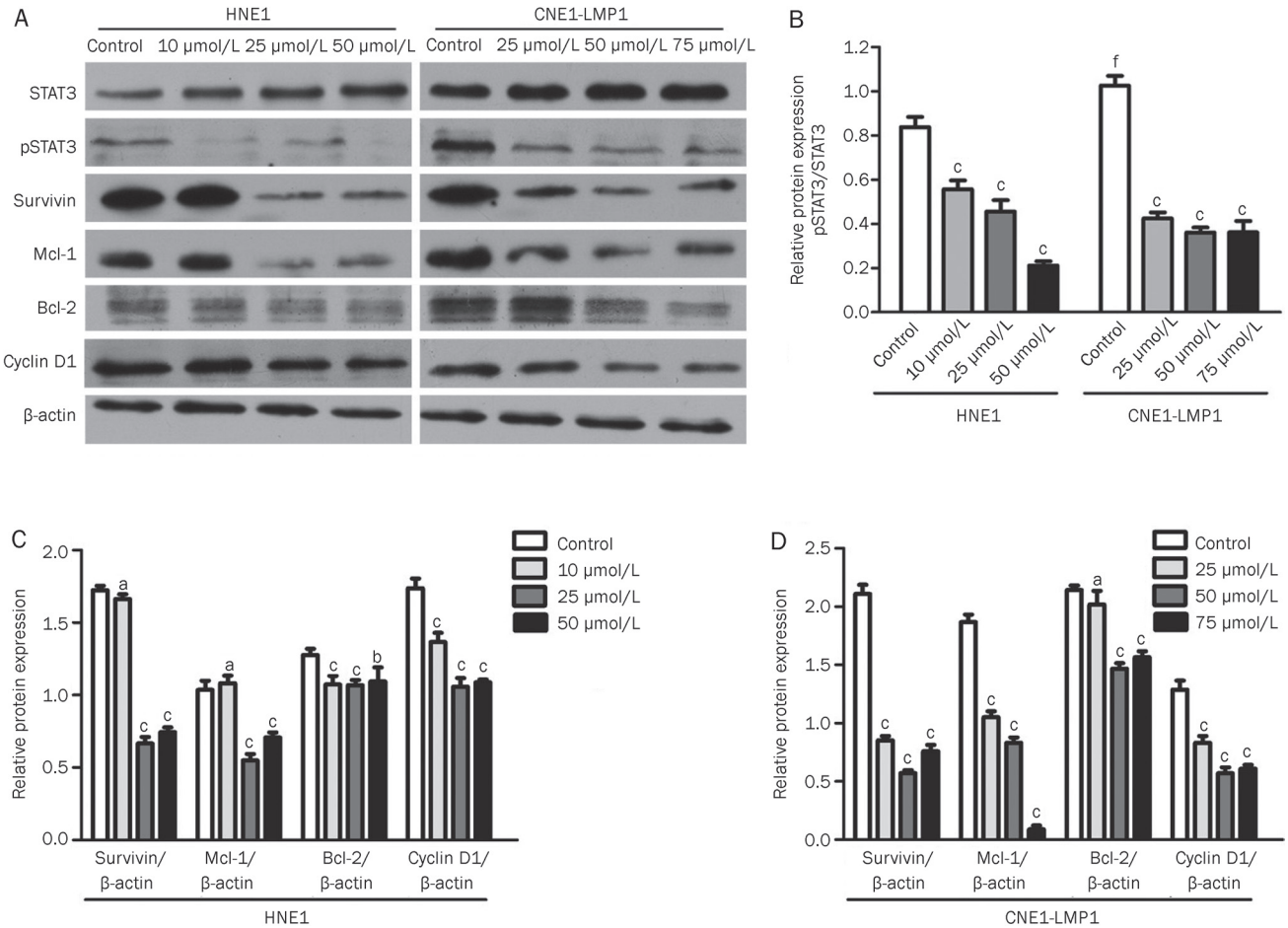

Figure 4. Celecoxib inhibited STAT3 phosphorylation and down-regulated the levels of STAT3 downstream targets. HNE1 and CNE1-LMP1 cells were treated with DMSO (control) or celecoxib (10, 25, 50 or 75 μmol/L) for 48 h. Celecoxib significantly inhibited STAT3 phosphorylation in both cell lines. The pSTAT3 expression level was higher in the CNE1-LMP1 cell line than that in the HNE1 cell line (A and B). Celecoxib also down-regulated the downstream proteins of STAT3 (Survivin, Mcl-1, Bcl-2 and Cyclin D1) (C and D). The blots displayed are from a representative experiment repeated three times with similar results. $^{a}P>0.05$, $^{b}P<0.05$, $^{c}P<0.01$ *vs* control; $^{f}P<0.01$ CNE1-LMP1 control *vs* HNE1 control.

Growing evidence indicates that STAT3 activation contributes to the progression and invasiveness of NPC[16–18]. Therefore, the activation of STAT3 provides a promising and valid target for NPC therapeutic modalities.

Even though a great number of studies have demonstrated that celecoxib could exert its anticancer effect in a wide variety of tumor types through COX-2-dependent and/or COX-2-independent pathways, studies on the anticancer effect and molecular mechanisms of celecoxib in NPC are scarce[11–13]. The majority of NPC patients are EBV infected, and LMP1 is the main EBV oncoprotein expressed in these tumors. Therefore, the HNE1 (EBV-negative) and CNE1-LMP1 cell lines were chosen for this study. The results presented in our study clearly illustrate that celecoxib significantly inhibits cell proliferation in both of the NPC cell lines in a dose-dependent manner. However, the mechanism of the anticancer effect of celecoxib is not fully dependent on COX-2 expression. COX-2 protein expression levels in HNE1 cells are higher than in CNE1-LMP1 cells. Additionally, the COX-2 expression pattern was different between the two cell lines after treatment with celecoxib, with down-regulated COX-2 expression observed in HNE1 cells, but up-regulated COX-2 expression in CNE1-LMP1 cells. The mechanism for increased COX-2 expression in CNE1-LMP1 cells is still unclear.

The observation that celecoxib can increase COX-2 expression was reported in breast cancer MDA-MB-231 cells, 184 hTERT breast cancer cells and human osteosarcoma MG-63 cells[36–38]. One or more products produced by COX may be capable of inhibiting COX expression via a negative feedback loop. Celecoxib treatment could remove the negative feedback and lead to COX-2 induction. In addition, Murono *et al* determined that LMP1 could induce COX-2 expression in NPC cell lines, increase prostaglandin E2 production through COX-2 induction and that celecoxib could inhibit prostaglandin E2 production[39]. Therefore, LMP1 may induce COX-2 expression to up-regulate prostaglandin E2 expression after the inhibition of prostaglandin E2 expression by celecoxib. Furthermore, celecoxib is known to inhibit the phosphatidylinositol 3-kinase

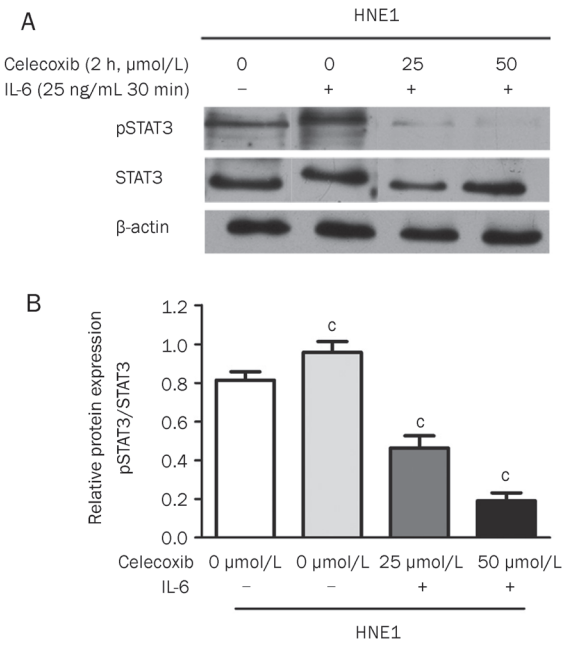

Figure 5. Celecoxib inhibited STAT3 phosphorylation induced by IL-6. HNE1 cells were pretreated with celecoxib for 2 h followed by 25 ng/mL of IL-6 for 30 min. Western blot analysis was performed for STAT3 phosphorylation. IL-6 promoted pSTAT3 expression, which was significantly suppressed by celecoxib at concentrations of 25 and 50 μmol/L (A and B). The blots displayed are from a representative experiment repeated three times with similar results. $^{c}P<0.01$ *vs* control.

(PI3K)/Protein Kinase B (Akt) pathway[40]. Monick *et al* reported that P13K inhibition resulted in an increase in COX-2 protein[41]. PI3K negatively regulates the activation of the p38 pathway, and active p38 is necessary for COX-2 production. Therefore, celecoxib could up-regulate COX-2 expression via the downregulation of PI3K.

Regardless of the COX-2 expression patterns in HNE1 and CNE1-LMP1 cells, at the molecular level, in accordance with the recent similarly reported findings in colon cancer cells, hepatocellular carcinoma cells and rhabdomyosarcoma cells[6, 7, 19], celecoxib strongly inhibited STAT3 phosphorylation in both NPC cell lines, which is a critical step in the activation of downstream signaling. pSTAT3 expression levels in CNE1-LMP1 cells were higher than in the HNE1 cells. One potential mechanism for this discrepancy may be that LMP1 could activate STAT3 phosphorylation through the MAPK/ERK and JAK/STAT pathways[22]. Subsequently, the critical downstream proteins Survivin, Mcl-1, Bcl-2 and Cyclin D1, were down-regulated, ultimately leading to cell growth inhibition, cell cycle arrest and apoptosis. To the best of our knowledge, the anticancer effect of celecoxib on the STAT3 signaling cascade in NPC cells has not yet been investigated. Our results revealed that the STAT3 pathway may be a COX-2-independent anticancer mechanism for celecoxib.

IL-6 induces STAT3 phosphorylation in various human cancers[42–44]. We hypothesized that celecoxib could exert anticancer effect by blocking inflammatory pathways, such as the IL-6/STAT3 pathway. In agreement with previously published studies[6, 7, 19], our results indicated that celecoxib could inhibit IL-6-induced STAT3 phosphorylation in HNE1 cells, demonstrating that celecoxib has great promise as a molecular targeting therapy for human cancers with aberrant IL-6 expression.

Studies in various cancers have indicated that celecoxib possesses a unique capacity to induce apoptosis independent of COX-2 inhibition, making celecoxib a potent anticancer drug[8, 25]. At the cellular level, our results showed that celecoxib induced apoptosis in both the HNE1 and CNE1-LMP1 cell lines and that apoptosis was associated with the down-regulation of the anti-apoptotic proteins Survivin, Mcl-1 and Bcl-2. Survivin, Mcl-1 and Bcl-2 are important downstream apoptotic genes in the IL-6/STAT3 pathway. Constitutively active STAT3 up-regulates Survivin, Mcl-1 and Bcl-2, leading to the dysregulation of apoptosis and thereby promoting cancer cell survival and proliferation. The apoptosis induction and the down-regulation of critical downstream anti-apoptotic proteins (Survivin, Mcl-1 and Bcl-2) further indicated that celecoxib could work via the inhibition of STAT3 phosphorylation. Several studies demonstrated that inhibition of 3-phosphoinositide-dependent kinase 1 (PDK-1) and its downstream substrate, PKB/AKT, plays a central role in the induction of apoptosis and cell cycle arrest[8]. However, whether this is the case in NPC still requires further investigation.

It is well described in the literature that celecoxib inhibits cell growth and survival in several different tumor types through the induction of G_0/G_1 cell cycle arrest. However, no consensus exists concerning the underlying molecular mechanisms of these effects. Consistent with previous studies[36, 45, 46], our results demonstrated that celecoxib induced G_0/G_1 cell cycle arrest in HNE1 and CNE1-LMP1 cell lines and that this arrest was accompanied by the down-regulation of Cyclin D1[12, 45–47], which is one of the major cyclins known to be up-regulated in cancers. Cyclin D1 activates Cyclin Dependent Kinase 2 (CDK2) and CDK4, leading to the phosphorylation of the retinoblastoma protein (pRb), which forces its release from the E2F transcription factor. Consequently, the cell cycle progresses from G_1 to S phase[48]. In our studies, the celecoxib-induced cell-cycle arrest in G_0/G_1 phase occurred, at least partially, via the downregulation of Cyclin D1 expression. It has been reported in other cancer types that celecoxib induces G_0/G_1 cell-cycle arrest by down-regulating c-Myc, Cyclins A and B, up-regulating cell-cycle inhibitors $p21^{wafl}$ and $p27^{kipl}$ and losing CDK activity[8]. It is unclear whether these mechanisms are involved in NPC cells after celecoxib treatment.

In addition to the above work, preclinical findings and a Phase I clinical trial suggest celecoxib could synergistically enhance radiation therapy treatment in prostate, lung and recurrent head and neck cancers[49–51]. Radiotherapy (RT) is the primary treatment modality for non-metastatic NPC. A recent Phase I clinical trial in NPC determined that celecoxib can be safely administered concurrently with radiotherapy at doses of up to 800 mg/d with good rates of local control and overall

survival[52]. However, whether celecoxib improved treatment efficacy is still unclear due to the lack of a control arm. Therefore, further studies are required to investigate whether synergistic effects exist with combination of celecoxib and radiation therapy in NPC *in vitro* and *in vivo* and to elucidate the underlying molecular mechanisms of this treatment.

There are certain limitations in the present study. First, different cell lines may respond differently to celecoxib; therefore, additional cell lines must be investigated to fully elucidate the underlying mechanism of the proliferation inhibitory effect with celecoxib treatment. Additionally, further studies are needed to differentiate the anticancer effect of celecoxib in NPC on different pathways. Celecoxib could act through COX-2-dependent and/or COX-2-independent mechanisms, including the COX-2 pathway, the PI3K/AKT pathway, the ERK pathway, the IL-6/STAT3 pathway, and other pathways. Elucidating the precise molecular mechanism would provide a precise molecular target for future NPC therapy. *In vivo* studies also need to be evaluated.

In summary, at the cellular level, the present study demonstrated that celecoxib inhibited growth and induced apoptosis and cell-cycle arrest at the G_0/G_1 phase in NPC cells. At the molecular level, pSTAT3 was inactivated in parallel with reduced activation of the downstream anti-apoptotic proteins Survivin, Mcl-1, Bcl-2 and the cell-cycle regulatory protein Cyclin D1. Taken together, the anticancer effects of celecoxib in NPC may be partly achieved through the STAT3 pathway.

Acknowledgements

We thank Prof Ya CAO at the Cancer Research Institute of Central South University for his gift of the HNE1 and CNE1-LMP1 cell lines. This project was supported by a grant from the National Natural Science Foundation of China (No 30470525).

Author contribution

Dong-bo LIU and Guang-yuan HU performed the research and wrote the manuscript; Guo-xian LONG, Hong QIU and Qi MEI performed some of the experiments and analyzed the data; and Guo-qing HU designed the experiments.

References

1 Yu MC, Yuan JM. Epidemiology of nasopharyngeal carcinoma. Semin Cancer Biol 2002; 12: 421–9.
2 Agulnik M, Epstein JB. Nasopharyngeal carcinoma: current management, future directions and dental implications. Oral Oncol 2008; 44: 617–27.
3 Teo PM, Kwan WH, Lee WY, Leung SF, Johnson PJ. Prognosticators determining survival subsequent to distant metastasis from nasopharyngeal carcinoma. Cancer 1996; 77: 2423–31.
4 Kim TH, Jeong YI, Jin SG, Pei J, Jung TY, Moon KS, *et al*. Preparation of polylactide-co-glycolide nanoparticles incorporating celecoxib and their antitumor activity against brain tumor cells. Int J Nanomed 2011; 6: 2621–31.
5 Zhang M, Xu ZG, Shi Z, Shao D, Li O, Li W, *et al*. Inhibitory effect of celecoxib in lung carcinoma by regulation of cyclooxygenase-2/cytosolic phospholipase A2 and peroxisome proliferator-activated receptor gamma. Mol Cell Biochem 2011; 355: 233–40.
6 Li H, Liu A, Zhao Z, Xu Y, Lin J, Jou D, *et al*. Fragment-based drug design and drug repositioning using multiple ligand simultaneous docking (MLSD): identifying celecoxib and template compounds as novel inhibitors of signal transducer and activator of transcription 3 (STAT3). J Med Chem 2011; 54: 5592–6.
7 Liu Y, Liu A, Li H, Li C, Lin J. Celecoxib inhibits interleukin-6/interleukin-6 receptor-induced JAK2/STAT3 phosphorylation in human hepatocellular carcinoma cells. Cancer Prev Res (Phila Pa) 2011; 4: 1296–305.
8 Grösch S, Maier TJ, Schiffmann S, Geisslinger G. Cyclooxygenase-2 (COX-2)-independent anticarcinogenic effects of selective COX-2 inhibitors. J Natl Cancer Inst 2006; 98: 736–47.
9 Chen WC, McBride WH, Chen SM, Lee KF, Hwang TZ, Jung SM, *et al*. Prediction of poor survival by cyclooxygenase-2 in patients with T4 nasopharyngeal cancer treated by radiation therapy: clinical and *in vitro* studies. Head Neck 2005; 27: 503–12.
10 Peng JP, Chang HC, Hwang CF, Hung WC. Overexpression of cyclooxygenase-2 in nasopharyngeal carcinoma and association with lymph node metastasis. Oral Oncol 2005; 41: 903–8.
11 Chen PY, Long QC. Effects of cyclooxygenase 2 inhibitors on biological traits of nasopharyngeal carcinoma cells. Acta Pharmacol Sin 2004; 25: 943–9.
12 Chan CM, Ma BB, Wong SC, Chan AT. Celecoxib induces dose dependent growth inhibition in nasopharyngeal carcinoma cell lines independent of cyclooxygenase-2 expression. Biomed Pharmacother 2005; 59: S268–71.
13 Chen J, Ran Y, Hong C, Chen Z, You Y. Anti-cancer effects of celecoxib on nasopharyngeal carcinoma HNE-1 cells expressing COX-2 oncoprotein. Cytotechnology 2010; 62: 431–8.
14 Yang J, Chatterjee-Kishore M, Staugaitis SM, Nguyen H, Schlessinger K, Levy DE, *et al*. Novel roles of unphosphorylated STAT3 in oncogenesis and transcriptional regulation. Cancer Res 2005; 65: 939–47.
15 Yu H, Jove R. The STATs of cancer — new molecular targets come of age. Nat Rev Cancer 2004; 4: 97–105.
16 Ma N, Kawanishi M, Hiraku Y, Murata M, Huang GW, Huang Y, *et al*. Reactive nitrogen species-dependent DNA damage in EBV-associated nasopharyngeal carcinoma: the relation to STAT3 activation and EGFR expression. Int J Cancer 2008; 122: 2517–25.
17 Liu YP, Tan YN, Wang ZL, Zeng L, Lu ZX, Li LL, *et al*. Phosphorylation and nuclear translocation of STAT3 regulated by the Epstein-Barr virus latent membrane protein 1 in nasopharyngeal carcinoma. Int J Mol Med 2008; 21: 153–62.
18 Lui VW, Wong EY, Ho Y, Hong B, Wong SC, Tao Q, *et al*. STAT3 activation contributes directly to Epstein-Barr virus–mediated invasiveness of nasopharyngeal cancer cells *in vitro*. Int J Cancer 2009; 125: 1884–93.
19 Reed S, Li H, Li C, Lin J. Celecoxib inhibits STAT3 phosphorylation and suppresses cell migration and colony forming ability in rhabdomyosarcoma cells. Biochem Biophys Res Commun 2011; 407: 450–5.
20 Raab-Traub N. Epstein-Barr virus in the pathogenesis of NPC. Semin Cancer Biol 2002; 12: 431–41.
21 Tsao SW, Tramoutanis G, Dawson CW, Lo AK, Huang DP. The significance of LMP1 expression in nasopharyngeal carcinoma. Semin Cancer Biol 2002; 12: 473–87.
22 Wang Z, Luo F, Li L, Yang L, Hu D, Ma X, *et al*. STAT3 activation induced by Epstein-Barr virus latent membrane protein1 causes vascular endothelial growth factor expression and cellular invasiveness via JAK3 and ERK signaling. Eur J Cancer 2010; 46: 2996–3006.

23 Du CW, Wen BG, Li DR, Lin YC, Zheng YW, Chen L, *et al*. Latent membrane protein-1 of Epstein-Barr virus increases sensitivity to arsenic trioxide-induced apoptosis in nasopharyngeal carcinoma cell. Exp Oncol 2005; 27: 267–72.
24 Lin X, Liu S, Luo X, Ma X, Guo L, Li L, *et al*. EBV-encoded LMP1 regulates Op18/stathmin signaling pathway by cdc2 mediation in nasopharyngeal carcinoma cells. Int J Cancer 2009; 124: 1020–7.
25 Jendrossek V. Targeting apoptosis pathways of celecoxib in cancer. Cancer Lett 2011; doi:10.1016/j.canlet.2011.01.012.
26 Masuda M, Suzui M, Yasumatu R, Nakashima T, Kuratomi Y, Azuma K, *et al*. Constitutive activation of signal transducers and activators of transcription 3 correlates with cyclin D1 overexpression and may provide a novel prognostic marker in head and neck squamous cell carcinoma. Cancer Res 2002; 62: 3351–5.
27 Shirogane T, Fukada T, Muller JM, Shima DT, Hibi M, Hirano T. Synergistic roles for Pim-1 and c-Myc in STAT3-mediated cell cycle progression and antiapoptosis. Immunity 1999; 11: 709–19.
28 Epling-Burnette PK, Liu JH, Catlett-Falcone R, Turkson J, Oshiro M, Kothapalli R, *et al*. Inhibition of STAT3 signaling leads to apoptosis of leukemic large granular lymphocytes and decreased Mcl-1 expression. J Clin Invest 2001; 107: 351–62.
29 Alas S, Bonavida B. Rituximab inactivates signal transducer and activation of transcription 3 (STAT3) activity in B-non-Hodgkin's lymphoma through inhibition of the interleukin 10 autocrine/paracrine loop and results in down-regulation of Bcl-2 and sensitization to cytotoxic drugs. Cancer Res 2001; 61: 5137–44.
30 Kim KW, Mutter RW, Cao C, Albert JM, Shinohara ET, Sekhar KR, *et al*. Inhibition of signal transducer and activator of transcription 3 activity results in down-regulation of Survivin following irradiation. Mol Cancer Ther 2006; 5: 2659–65.
31 Xie TX, Wei D, Liu M, Gao AC, Ali-Osman F, Sawaya R, *et al*. Stat3 activation regulates the expression of matrix metalloproteinase-2 and tumor invasion and metastasis. Oncogene 2004; 23: 3550–60.
32 Xu Q, Briggs J, Park S, Niu G, Kortylewski M, Zhang S, *et al*. Targeting Stat3 blocks both HIF-1 and VEGF expression induced by multiple oncogenic growth signaling pathways. Oncogene 2005; 24: 5552–60.
33 Gao LF, Wen LJ, Yu H, Zhang L, Meng Y, Shao YT, *et al*. Knockdown of Stat3 expression using RNAi inhibits growth of laryngeal tumors *in vivo*. Acta Pharmacol Sin 2006; 27: 347–52.
34 Lui VW, Yau DM, Wong EY, Ng YK, Lau CP, Ho Y, *et al*. Cucurbitacin I elicits anoikis sensitization, inhibits cellular invasion and *in vivo* tumor formation ability of nasopharyngeal carcinoma cells. Carcinogenesis 2009; 30: 2085–94.
35 Kortylewski M, Kujawski M, Wang T, Wei S, Zhang S, Pilon-Thomas S, *et al*. Inhibiting Stat3 signaling in the hematopoietic system elicits multicomponent antitumor immunity. Nat Med 2005; 11: 1314–21.
36 Basu GD, Pathangey LB, Tinder TL, Gendler SJ, Mukherjee P. Mechanisms underlying the growth inhibitory effects of the cyclooxygenase-2 inhibitor celecoxib in human breast cancer cells. Breast Cancer Res 2005; 7: R422–35.
37 Levitt RJ, Buckley J, Blouin MJ, Schaub B, Triche TJ, Pollak M. Growth inhibition of breast epithelial cells by celecoxib is associated with upregulation of insulin-like growth factor binding protein-3 expression. Biochem Biophys Res Commun 2004; 316: 421–8.
38 Liu B, Shi ZL, Feng J, Tao HM. Celecoxib, a cyclooxygenase-2 inhibitor, induces apoptosis in human osteosarcoma cell line MG-63 via down-regulation of PI3K/Akt. Cell Biol Int 2008; 32: 494–501.
39 Murono S, Inoue H, Tanabe T, Joab I, Yoshizaki T, Furukawa M, *et al*. Induction of cyclooxygenase-2 by Epstein-Barr virus latent membrane protein 1 is involved in vascular endothelial growth factor production in nasopharyngeal carcinoma cells. Proc Natl Acad Sci U S A 2001; 98: 6905–10.
40 Arico S, Pattingre S, Bauvy C, Gane P, Barbat A, Codogno P, *et al*. Celecoxib induces apoptosis by inhibiting 3-phosphoinositide-dependent protein kinase-1 activity in the human colon cancer HT-29 cell line. J Biol Chem 2002; 277: 27613–21.
41 Monick MM, Robeff PK, Butler NS, Flaherty DM, Carter AB, Peterson MW, *et al*. Phosphatidylinositol 3-kinase activity negatively regulates stability of cyclooxygenase 2 mRNA. J Biol Chem 2002; 277: 32992–3000.
42 Bollrath J, Phesse TJ, von Burstin VA, Putoczki T, Bennecke M, Bateman T, *et al*. gp130-mediated Stat3 activation in enterocytes regulates cell survival and cell-cycle progression during colitis-associated tumorigenesis. Cancer Cell 2009; 15: 91–102.
43 Grivennikov S, Karin E, Terzic J, Mucida D, Yu GY, Vallabhapurapu S, *et al*. IL-6 and Stat3 are required for survival of intestinal epithelial cells and development of colitis-associated cancer. Cancer Cell 2009; 15: 103–13.
44 Berishaj M, Gao SP, Ahmed S, Leslie K, Al-Ahmadie H, Gerald WL, *et al*. Stat3 is tyrosine-phosphorylated through the interleukin-6/glycoprotein 130/Janus kinase pathway in breast cancer. Breast Cancer Res 2007; 9: R32.
45 Patel MI, Subbaramaiah K, Du B, Chang M, Yang P, Newman RA, *et al*. Celecoxib inhibits prostate cancer growth: evidence of a cyclooxygenase-2-independent mechanism. Clin Cancer Res 2005; 11: 1999–2007.
46 Bock JM, Menon SG, Sinclair LL, Bedford NS, Goswami PC, Domann FE, *et al*. Celecoxib toxicity is cell cycle phase specific. Cancer Res 2007; 67: 3801–8.
47 Sobolewski C, Cerella C, Dicato M, Diederich M. Cox-2 inhibitors induce early c-Myc downregulation and lead to expression of differentiation markers in leukemia cells. Cell Cycle 2011; 10: 2978–93.
48 Kato J, Matsushime H, Hiebert SW, Ewen ME, Sherr CJ. Direct binding of cyclin D to the retinoblastoma gene product (pRb) and pRb phosphorylation by the cyclin D-dependent kinase CDK4. Genes Dev 1993; 7: 331–42.
49 Handrick R, Ganswindt U, Faltin H, Goecke B, Daniel PT, Budach W, *et al*. Combined action of celecoxib and ionizing radiation in prostate cancer cells is independent of pro-apoptotic Bax. Radiother Oncol 2009; 90: 413–21.
50 Klenke FM, Abdollahi A, Bischof M, Gebhard MM, Ewerbeck V, Huber PE, *et al*. Celecoxib enhances radiation response of secondary bone tumors of a human non-small cell lung cancer via antiangiogenesis *in vivo*. Strahlenther Onkol 2011; 187: 45–51.
51 Kao J, Genden EM, Chen CT, Rivera M, Tong CC, Misiukiewicz K, *et al*. Phase 1 trial of concurrent erlotinib, celecoxib, and reirradiation for recurrent head and neck cancer. Cancer 2011; 117: 3173–81.
52 Xue WP, Bai SM, Luo M, Bi ZF, Liu YM, Wu SK. Phase I clinical trial of nasopharyngeal radiotherapy and concurrent celecoxib for patients with locoregionally advanced nasopharyngeal carcinoma. Oral Oncol 2011; 47: 753–7.

Acta Pharmacologica Sinica (2012) 33: 691–700
 1671-4083/12 $32.00
www.nature.com/aps

Original Article

Hedgehog signaling pathway mediates invasion and metastasis of hepatocellular carcinoma via ERK pathway

Jing-tao LU#, Wen-di ZHAO#, Wei HE, Wei WEI*

Institute of Clinical Pharmacology, Anhui Medical University, Key Laboratory of Anti-inflammatory and Immunopharmacology of Education Ministry, Anhui Engineering Technology Research Center of Anti-inflammatory and Immunodrugs, Hefei 230032, China

Aim: To investigate the role of Hedgehog (Hh) signaling pathway in the invasion and metastasis of human hepatocellular carcinoma (HCC).
Methods: Eighty six HCC tissues samples and HCC cell line Bel-7402 were examined. The protein expression of sonic hedgehog (Shh), nuclear glioma-associated oncogene-1 (Gli1), MMP-9 and p-ERK1/2 in HCC was analyzed using immunohistochemistry and Western blot analysis. Boyden chamber assay and wound-healing assay were used to quantify the invasion and metastasis of Bel-7402 cells.
Results: In 86 HCC tissue samples, the positive ratio of Shh and nucleus Gli1 was 67.44% (58/86) and 60.47% (52/86), respectively; the expression of nucleus Gli1 was correlated with the tumor pathological grade (P=0.034), and with the ability of the tumor to invade and metastasize (P=0.001); the expression of nucleus Gli1 was also correlated with p-ERK1/2 (P=0.031) and with MMP-9 (P=0.034). Neither Shh, nor nucleus Gli1 was observed in normal liver tissue. KAAD-cyclopamine (KAAD-cyc), a specific inhibitor of the Hh pathway, at the concentrations of 1 and 4 μmol/L inhibited the invasion and migration of Bel-7402 cells and decreased the expression of Gli1 in nucleus and MMP-9, p-ERK1/2 proteins in Bel-7402 cells. On the other hand, Shh, a ligand of the Hh pathway, at the concentration of 0.5 μg/mL produced opposite effects. The MAPK pathway inhibitors U0126 and PD98059 at the concentrations of 5 and 10 μmol/L inhibited invasion and metastasis of Bel-7402 cells induced by Shh, and decreased the expression of p-ERK1/2 and MMP-9. However, U0126 and PD98059 had no effect on the expression of Gli1.
Conclusion: Hh signaling pathway mediates invasion and metastasis of human HCC by up-regulating the protein expression of MMP-9 via ERK pathway.

Keywords: human hepatocellular carcinoma; invasion and metastasis; hedgehog signaling pathway; nuclear glioma-associated oncogene-1 (Gli1); ERK pathway; MMP-9

Acta Pharmacologica Sinica (2012) 33: 691–700; doi: 10.1038/aps.2012.24; published online 30 Apr 2012

Introduction

Hepatocellular carcinoma (HCC) is the common primary cancer with a multifaceted molecular pathogenesis. HCC has become the fifth most prevalent malignancy worldwide and the third leading cause of cancer-related death, most importantly, the incidence of HCC is increasing[1, 2], and 82% of cases are in developing countries, with 55% in China alone[3]. Invasion and metastasis are two fundamental properties, which determine the prognosis of the HCC patients[4, 5]. Many signaling pathways are thought to be involved in the development and invasion of HCC, including the MAPK pathway[6, 7], phosphatidylinositol-3 kinase (PI3K)/AKT/mammalian target of rapamycin (mTOR) pathway[8–10], the wnt/beta-catenin pathway[9, 11], hepatocyte growth factor/c-MET pathway[12, 13], hedgehog (Hh) signaling pathway, and so on.

Hh signaling pathway is a highly conserved system, which plays a crucial role in tissue patterning, cell differentiation and proliferation[14]. Hedgehog, including sonic hedgehog (Shh), Indian hedgehog (Ihh), and desert hedgehog (Dhh), appear to bind to a transmembrane receptor protein, known as Patched (Ptc), which in the absence of Shh exerts an inhibitory effect on the seven transmembrane receptor smoothened (Smo). Binding of Shh to Ptc alleviates the inhibitory effect of Ptc on Smo. Once activated, Smo induces a complex series of intracellular reactions that targets the glioma-associated oncogenes (Gli) transcription factor families, the zincfinger transcription effectors[15, 16]. At least three members (Gli1, Gli2, and Gli3)

# These authors contributed equally to this work.
* To whom correspondence should be addressed.
E-mail wwei@anhu.edu.cn
Received 2011-12-08 Accepted 2012-02-29

of nuclear proteins Gli families have been identified in mammalian tissues[14, 17]. Gli1 is a transcriptional activator[18], which induces the expression of numerous target genes that regulates proliferation, differentiation, and extracellular matrix interactions[19, 20].

Increasing evidence has demonstrated that the Hh signaling pathway plays an important role in multiple tumor types, for example, basal cell carcinoma[21, 22], pancreatic cancer[23], colon carcinoma[24], gastric cancer[25], small cell lung cancer[26], prostate cancer[27–29], breast cancer[30, 31], early childhood hepatoblastoma[32], and esophageal cancers[33].

Recent studies have revealed that the Hh signaling pathway is abnormally activated in human HCC[34-36], and this pathway is thought to participate in the development of HCC[37–39]. Moreover, activation of the Hh pathway is correlated closely to invasion and metastasis of HCC[36, 40]. Activated markers of the Hh signaling pathway such as Gli1 is significantly up-regulated in the HCC tumor tissues[41], and Gli inhibition can also suppress HCC tumor growth and metastases *in vivo* and *in vitro*[42]. However, the mechanism by which Hh signaling pathway is involved in HCC development is still unclear.

Hh signaling pathway can affect MAPK/ERK phosphorylation[43] and lead to carcinogenesis[44]. For example, it also can activate ERK1/2 in the breast epithelial cell[45]. However, other studies have revealed that in cancer the MAPK signaling pathway regulates Hh signaling, specifically Gli activity and expression[46]. Therefore, what cellular mediators are involved in the crosstalk between the Hh signaling pathway and the MAPK signaling pathway in HCC? Now, there is no report about it.

Matrix metalloproteinase-9 (MMP-9 or gelatinase-B) is mostly associated with tumor migration, invasion and metastasis for various human cancers[10, 47, 48]. The Hh signaling pathway up-regulates cell migration and invasion in human gliomas and in pancreatic cancer by increasing the expressions of MMP-9[49, 50]. In addition, Smo and MMP-9 were overexpressed and associated with invasion and metastasis in HCC tissues[51]. Does the Hh signaling pathway mediate the migration and invasion of HCC by increasing the expressions of MMP-9? What is the correlation between MMP-9 and ERK pathway? However, they are incompletely understood in HCC.

In the present study, we investigated the mechanisms of the Hh signaling pathway in invasion and metastasis of HCC, specifically focused on the correlation between the Hh signaling pathway and the MAPK signaling pathway. Further we determined whether Hh signaling pathway involved in human HCC invasion and metastasis by up-regulating the expression of MMP-9 through ERK pathway.

Materials and methods

Patients and specimens

A total of 86 HCC patients, who had undergone liver resection without preoperative treatment at the First Affiliated Hospital of Anhui Medical University between June 2008 and December 2010, were examined. All tumor specimens were pathologically diagnosed as HCC. Prior written informed consent was obtained from all patients according to the World Medical Association Declaration of Helsinki, and the study received ethics board approval from the Affiliated Hospital of Anhui Medical University. The age of patients ranged from 33 to 75 years, with an average age of 48.1 years. There were 68 males and 18 females, 50 I–II type- and 36 III–IV type-differentiated HCC, 37 patients with invasion and/or metastasis (Table 1).

Reagents

Dulbecco's modified Eagle's medium (DMEM) was obtained from Gbico Chemical Company (Gbico, USA). Shh and Gli1 antibodies were purchased from Santa Cruz Biotechnology Inc (Santa Cruz, CA, USA). p-ERK1/2 and MMP-9 antibodies were purchased from Abcam Biotechnology Inc (Abcam, UK). KAAD-cyclopamine(KAAD-cyc), Shh, U0126, and PD98059 were purchased from Toronto Research Chemicals (North York, Ontario, Canada) and Santa Cruz Biotechnology Inc (Santa Cruz, CA, USA). All chemicals were purchased in the purest form available.

Cell line and culture conditions

Human HCC cell line Bel-7402, obtained from the Shanghai Institute of Cell Biology, Chinese Academy of Sciences, was grown in DMEM supplemented with 10% heat-inactivated fetal bovine serum (FBS, Gbico, USA), 100 μg/mL streptomycin and 100 U/mL penicillin in a humidified atmosphere containing 5% CO_2 at 37°C. Cells during exponential growth phase were used in the experiments. Cells were treated with KAAD-cyc, the special antagonist of Smo, Shh, U0126, or PD98059, control medium contained DMSO alone. In the invasion and metastasis experiments, cells were cultured in a serum-free medium.

Immunohistochemistry staining

Briefly, immunohistochemical stains were performed on formalin-fixed and paraffin-embedded tissue sections (4 μm). The sections were prepared according to classical methods and treated with blocking solution before being sequentially incubated with primary antibodies against Shh (1:100), Gli1 (1:200), MMP-9 (1:100), and p-ERK1/2 (1:200) overnight at 4°C. The primary antibodies were visualized by incubating in a biotinylated antibody and HRP-conjugated streptavidin. Antigen staining was performed using diaminobenzidine then counterstained with hematoxylin. Negative controls were treated with the same species normal IgG in place of primary antibody. Images of each sample were taken and the percentage of positive cancer cells was quantified as the number of positive cells over the total number of cancer cells in that image. Expression was evaluated independently by two pathologists. Staining of sections was assessed in 10 consecutive fields (200× magnification) using a validated semi-quantitative scale, which was indicated by both the percentage of positively stained tumor cells and the staining intensity. The percent positivity was scored as "0" (<5%, negative), "1" (5%–25%, sporadic), "2" (25%–50%, focal), or "3" (>50%,

diffuse). The staining intensity was scored as "0" (no staining), "1" (weakly stained), "2" (moderately stained), or "3" (strongly stained). The immunostaining score was calculated as the percentage positive score × the staining intensity score. The expression levels were defined as follows: '–' (score 0–1), '+' (score 2–3), '++' (score 4–6), and '+++' (score >6). The HCC patients were divided into the low expression group (– or +) and the high expression group (++ or +++).

Boyden chamber invasion assay

The effect of KAAD-cyc, Shh, U0126, and PD98059 on HCC Bel-7402 was determined using Boyden chamber assay. Briefly, 24-well transwell units with polycarbonate membrane filters (8 μm pore size, Costar, USA) were coated with 100 μL matrigel (25 μg in 100 μL PBS, Becton Dickinson), dried in a laminar hood overnight, and reconstituted in 100 μL, washed with phosphate-buffered saline (PBS) at 37 °C for 2 h, then PBS was discharged. Bel-7402 cells were resuspended in DMEM with 0.5% BSA (5×10^4 cells/200 μL) in the presence or absence of KAAD-cyc, Shh, U0126, or PD98059, which was added to the upper side of the invasion chamber. DMEM (500 μL) with 2.5% FBS as chemoattractant was added to the lower chamber. After 24 h, filter inserts were removed from the wells, the cells on the upper surface of the filter were wiped off using cotton swabs. The cells that penetrated to the lower surface were fixed with 4% paraformaldehyde, stained with 0.1% crystal violet in 20% ethanol, and counted in five randomly selected fields under phase contrast microscope. The invasion cells were monitored by photographing at 400× magnification with Olympus Microscope. The assay was performed in triplicate.

Wound-healing assay

Cell migration was examined using the wound-healing assay. Briefly, Bel-7402 cells were cultured to about 80%–90% confluence in a 6-well plate at 37 °C and 5% CO_2. A wound about 1 mm width was created by scratching cells with a sterile 100 μL micropipette tip. Cells were washed with PBS (pH 6.8) three times to remove floating cells, then 1 mL serum-free DMEM was added. A computer-based microscopy imaging system was used to determine wound healing at 0 h with a microscope at 200× magnification. Then 1 mL serum-free DMEM was added with different concentrations of KAAD-cyc, Shh, U0126, or PD98059. After 24 h, photoes of the wound were taken under 200× magnification. The values of wound-healing were assessed by measuring the pixel of wound area by Photoshop 7.01 software. The experiments were performed in triplicate.

Western blots analysis

Cells were plated onto culture flask at a density of 2×10^5 cells/mL, cultured at 37 °C and 5% CO_2. The next day, different concentrations of KAAD-cyc, Shh, U0126, or PD98059 were added. After 24 h, the levels of Shh, Gli1, MMP-9, p-ERK1/2 proteins were quantified through Western blots. The proteins were extracted through the addition of 200 μL of lysis buffer (1 mmol/L EDTA, 1.5 mmol/L $MgCl_2$, 150 mmol/L NaCl, 50 mmol/L Hepes, 50 μmol/L DTT, 1 mmol/L phenylmethylsulfonyl fluoride and 10 mg/mL leupeptin, pH 7.4) to each well. The cell lysates were incubated on ice for 30 min vortexing every 10 min, followed by centrifugation at 12000×*g* for 30 min at 4 °C, 50 μg/μL protein of cell lysate was mixed equally with 2×electrophoresis buffer [50% glycerol, 25% mercaptoethanol, 10% SDS, 0.3 mol/L Tris (pH 6.8), 0.025% bromophenol blue] and boiled for 10 min. The samples (50 μg of protein) of total cell lysates were separated by sodium dodecyl sulfate–polyacrylamide gel electrophoresis and electrophoretically transferred onto a polyvinylidene difluoride membrane (Millipore) in transfer buffer containing 25 mmol/L Tris, 150 mmol/L glycine and 20% methanol. The membranes were blocked using 5% BSA (pH 7.4, 0.5% Tween 20). The membranes were incubated with primary antibodies, anti-MMP-9 (1:1000), anti-p-ERK1/2 (1:500) and anti-Gli1 (1:500) for 16–18 h at 4 °C. The membranes were subsequently probed with anti-mouse or anti-rabbit IgG antibodies (1:5000) with the HRP for 1 h. Control blots were performed using anti-actin antibody (1:500, Santa Cruz, CA, USA). The membranes were washed in PBS for 30 min at room temperature, and detection was achieved by measuring the chemiluminescence of the blotting agent after exposure of the filters on films. At last, the densities of the bands were quantified with a computerized densitometer (Image J Launcher, Broken Symmetry Software).

Statistical analysis

Statistical analyses were performed using the SPSS 11.0 software program (SPSS Software Products, Chicago, IL, USA). All data were presented as number or mean±standard deviation (SD). Associations between protein expression and clinicopathologic variables were analyzed by ChiSquare Test. Statistical analysis among more groups was performed by one-way analysis of variance (ANOVA). The Spearman coefficient of correlation was used to examine the correlation. Statistical significance of differences were accepted at $P<0.05$.

Results

Overexpression of Shh, Gli1, p-ERK1/2, and MMP-9 in HCC liver tissues with invasion and metastasis compared with non-metastasis HCC liver tissue

We detected Shh, Gli1 MMP-9, and p-ERK1/2 expressions in 86 cases of HCC liver tissues with or without invasion and metastasis by IHC staining. We further evaluated the relationships between Gli1 and p-ERK1/2, Gli1 and MMP-9 on invasion and metastasis of HCC. The results indicated Shh, Gli1, p-ERK1/2, and MMP-9 expressions had no notable relationship with age and tumor diameter. However, Gli1, p-ERK1/2, and MMP-9 expressions had a significant correlation with the pathological grade and metastasis of the tumor sample (Table 1). Positive expressions of Shh, p-ERK1/2, and MMP-9 were remarkably stronger in HCC liver tissues with metastasis than in non-metastasis HCC liver tissues. A significant difference was observed in expression of Gli1 in the nucleus between HCC tissues with metastasis and non-metastatic HCC liver tissue (91.89% *vs* 36.74%, $P<0.01$, Figure 1). Interestingly,

Table 1. Relationship between expression of Shh, Gli1, p-ERK1/2, and MMP-9 and clinical features of HCC (*n*=86).

Clinical parameter	Cases (*n*)	Shh (exp-h/exp-l)	Gli1 (nuclei) (exp-h/exp-l)	p-ERK1/2 (exp-h/exp-l)	MMP-9 (exp-h/exp-l)	*P* value (Shh, Gli1, p-ERK1/2, MMP-9)
Age (year)						
>50	40	31/9	25/15	23/17	24/16	0.1041, 0.8902, 0.3493, 0.6264
≤50	46	27/19	27/19	32/14	31/15	
Tumor diameter (cm)						
>3	67	42/25	36/31	45/22	42/25	0.1361, 0.0332, 0.3713, 0.9614
≤3	19	16/3	16/3	10/9	13/6	
Pathological grade						
I–II	50	27/23	25/25	27/23	29/21	0.0041, 0.0342, 0.0423, 0.2604
III–IV	36	31/5	27/9	28/8	26/10	
Invasion or metastasis						
Positive	37	30/7	30/7	32/5	30/7	0.0351, 0.0012, 0.0013, 0.0084
Negative	49	28/21	22/27	23/26	25/24	

Abbreviations: exp-h, high expression; exp-l, low expression.

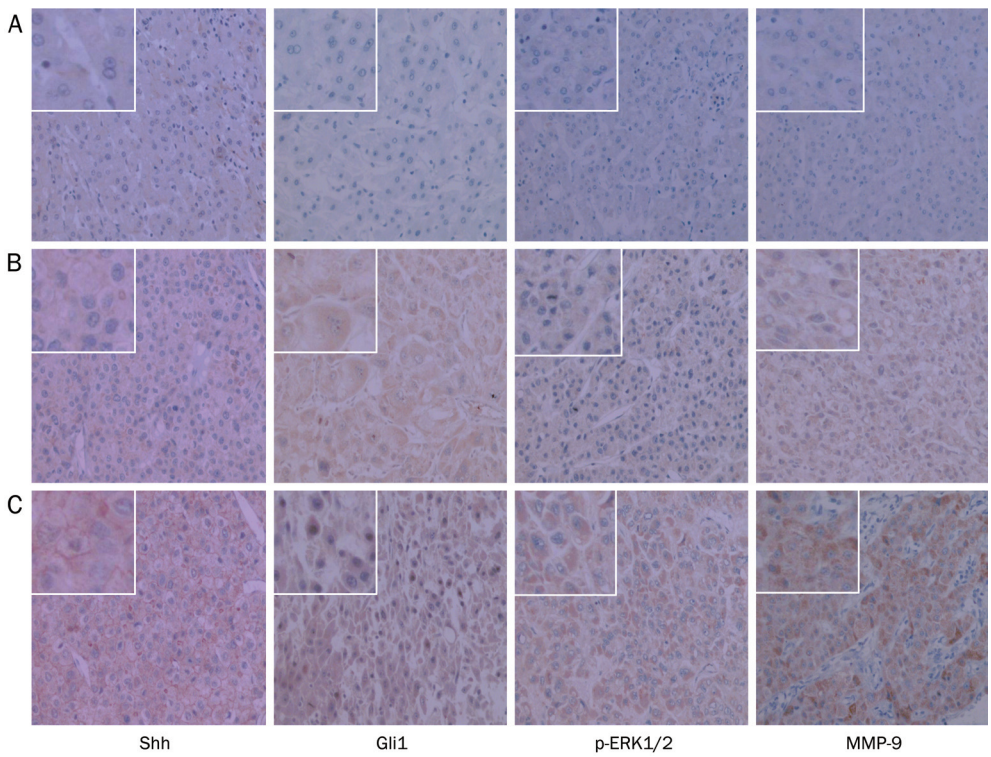

Figure 1. Results of IHC staining for Shh, Gli1, p-ERK1/2, and MMP-9 from 86 HCC liver tissues including 37 cases with metastasis at 200× magnification. Representative images are displayed. Expression of Shh was defined as the cytoplasmic and plasmalemmal staining. Expression of MMP-9 was defined as cytoplasmic staining. Gli1, and p-ERK1/2 were located in cytoplasm and/or nucleus. (A) Normal liver tissues; (B) Non-metastatic HCC liver tissues; (C) Metastatic HCC liver tissues.

expression of Gli1 was also notably correlated to expressions of MMP-9 and p-ERK1/2 (P<0.01, Table 1). Those results suggested that Hh signal pathway mediated invasion and metastasis of human HCC by up-regulating the protein expression MMP-9 and p-ERK1/2.

KAAD-cyc inhibited the invasion and migration of Bel-7402 cells

Bel-7402 cell invasion and motility were investigated using a Boyden chamber invasion assay and wound-healing assay, respectively. KAAD-cyc is a specific inhibitor of the Hh signaling pathway and was utilized to determine the effect of this pathway on invasion and metastasis in Bel-7402 cells. The results indicated KAAD-cyc notably inhibited migration of Bel-7402 cells on the surface of the tissue culture plate, significantly decreased area of wound-healing by 45.87% at most compared with controls in the wound-healing assay.

Meanwhile, KAAD-cyc significantly decreased the numbers of cells to the lower chamber when the cells were treated with 1 μmol/L and 4 μmol/L of KAAD-cyc for 24 h in Boyden chamber invasion assay, inhibitory rates were 43.50%±15.41% and 56.36%±15.17%, respectively. Collectively, these data demonstrated that KAAD-cyc could suppress the invasion and metastasis of Bel-7402 cells (Figure 2).

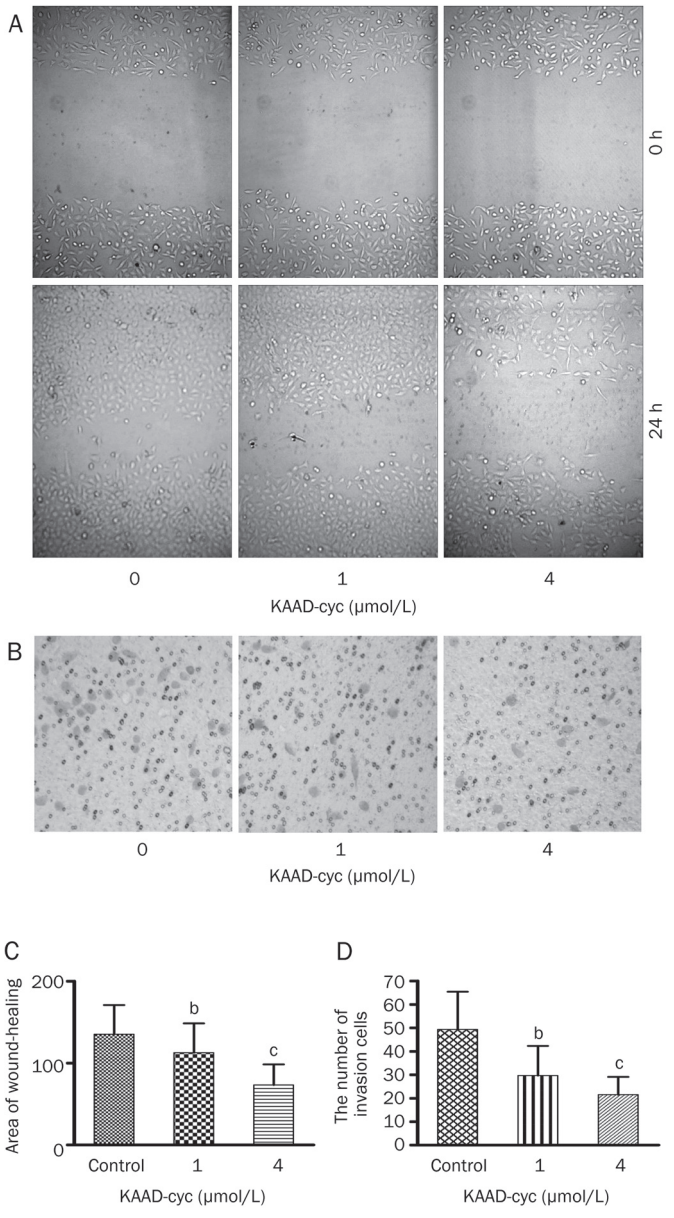

Figure 2. KAAD-cyc inhibits the invasion and migration of Bel-7402 cells. (A) Representative photographs (200×magnification) of cells treated with and without KAAD-cyc for 24 h after wounding from a representative experiment. (B) Representative photographs (400×magnification) of Bel-7402 cells treated with and without KAAD-cyc for 24 h in the invasion assay from 1 of 3 independent experiments. (C) Values of wound-healing assessed by measuring the pixel of wound-healing area. (D) The number of Bel-7402 cells in the lower chamber. Mean±SD. n=3. ^bP<0.05, ^cP<0.01 *vs* control.

Shh increased invasion and migration of Bel-7402 cells

As illustrated in Figure 3, Shh notably improved the migration of Bel-7402 cells, significantly increased area of wound-healing by greater than 41.63%. At the same time, Shh could significantly increase the number of migrating Bel-7402 cells in the lower chamber when the cells were treated with 0.13 μg/mL and 0.5 μg/mL Shh for 24 h, incremental rates were 49.99%±14.04% with 0.13 μg/mL Shh and 69.28%±20.29% with 0.5 μg/mL Shh in invasion assays. Those data demonstrated

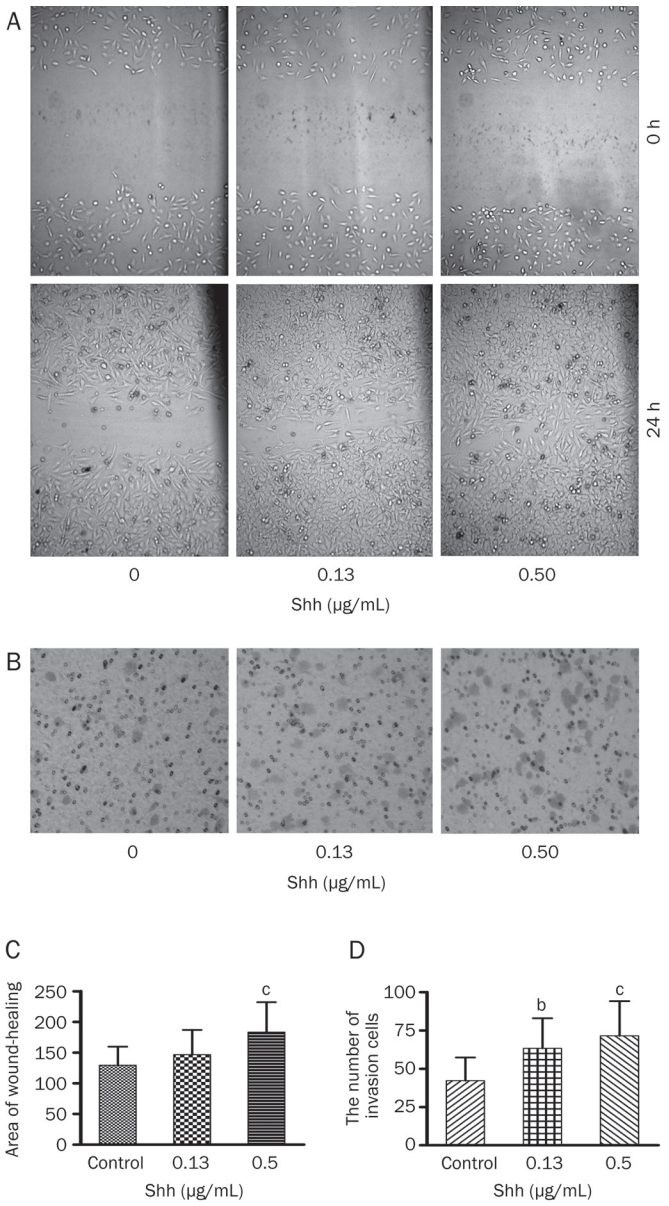

Figure 3. Shh increases invasion and migration of Bel-7402 cells. (A) Representative photographs (200×magnification) of metastatic cells treated with and without Shh 24 h after wounding from a representative experiment. (B) Representative photographs (400×magnification) of Bel-7402 cells treated with or without Shh for 24 h in invasion assay from 1 of 3 independent experiments. (C) Values of wound-healing assessed by measuring the pixel of wound area. (D) The numbers of Bel-7402 cells in the lower chamber. Mean±SD. n=3. ^bP<0.05, ^cP<0.01 *vs* control.

that Shh greatly enhanced the invasive and migratory capacity of Bel-7402 cells.

U0126 and PD98059 inhibited invasion and migration of Bel-7402 cells induced by Shh

Hh signaling pathway can lead to carcinogenesis via activation of ERK1/2. Therefore we determined whether the Hh signaling pathway promotes invasion and migration of Bel-7402 cells through p-ERK1/2. The MAPK inhibitor, U0126 and PD98059, were used in the invasion and migration assays with Bel-7402 cells *in vitro*. The results indicated that Shh notably increased the invasion and migration of Bel-7402 cells (P<0.01). U0126 significantly decrease the numbers of migratory Bel-7402 cells elevated by Shh. The inhibitory rates were 61.72%±18.75% with 5 μmol/L U0126 and 117.63%±28.90% with 10 μmol/L U0126. At the same time, U0126 notably inhibited migration of Bel-7402 cells induced by Shh, significantly decreased area of wound-healing by greater than 86.87% (Figure 4). PD98059 had similar effects with U0126 on the invasion and migration of Bel-7402 cells induced by Shh. These studies demonstrated that the U0126 and PD98059 could suppress the invasion and migration capacity of Bel-7402 cells induced by Shh.

Effects of KAAD-cyc on the expression of Gli1, p-ERK1/2, and MMP-9 proteins in Bel-7402 cells

Bel-7402 cells were cultured in serum-free media containing 1 and 4 μmol/L KAAD-cyc for 24 h. The expression of Gli1, p-ERK1/2, and MMP-9 proteins were determined by Western blot analysis. The results indicated that KAAD-cyc dramatically inhibited the expression of Gli1, p-ERK1/2, and MMP-9 proteins in Bel-7402 compared with vehicle control (Figure 5A and 5B).

Effects of Shh on the expression of Gli1, p-ERK1/2, and MMP-9 proteins in Bel-7402 cells

Bel-7402 cells were cultured in serum-free media containing 0.13 and 0.50 μg/mL Shh for 24 h. The expression of Gli1, p-ERK1/2, and MMP-9 proteins were determined by Western blot analysis. The results indicated that Shh dramatically increased the expression of Gli1, p-ERK1/2, and MMP-9 in

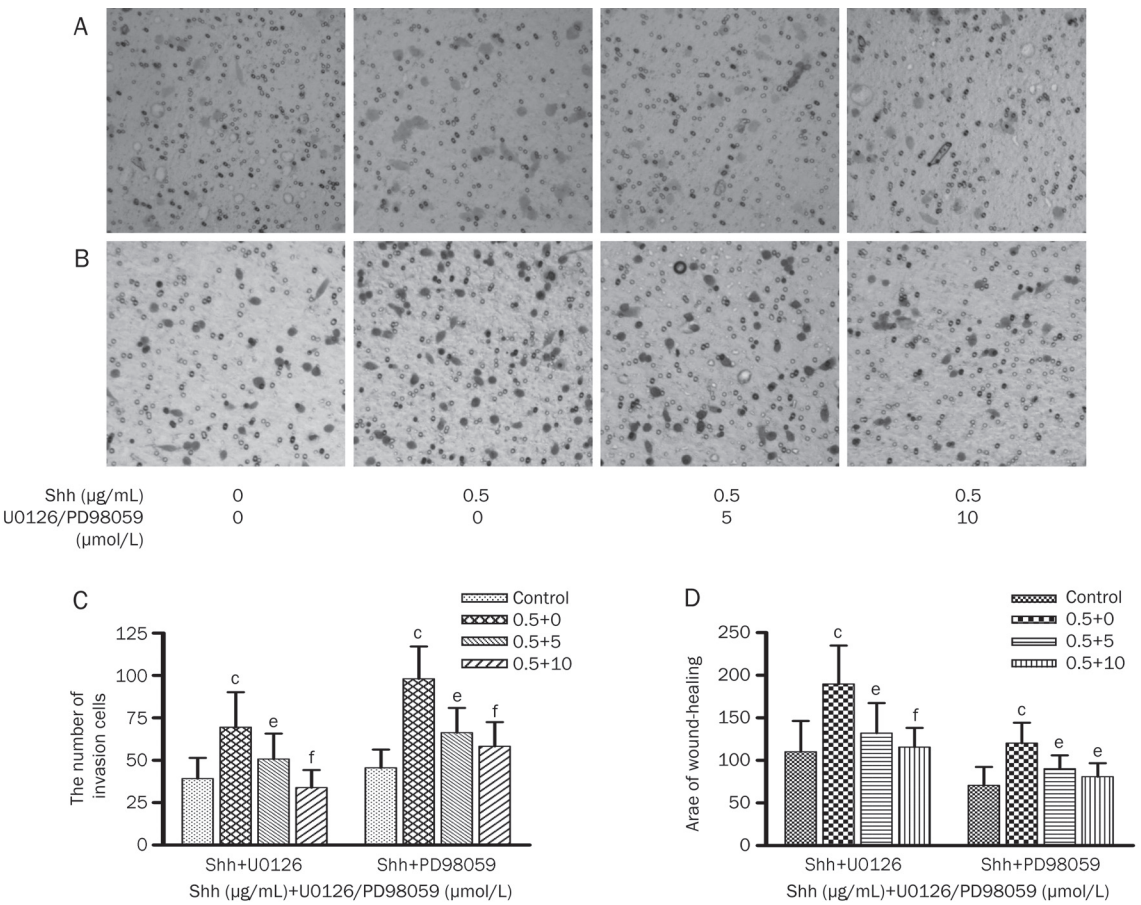

Figure 4. U0126 and PD98059 inhibit invasion and migration of Bel-7402 cells induced by Shh. (A) Representative photographs (400×magnification) of Bel-7402 cells treated with or without U0126 for 24 h after being pretreated by Shh from a representative experiment. (B) Representative photographs (400×magnification) of Bel-7402 cells treated with or without PD98059 for 24 h after being pretreated by Shh from a representative experiment. (C) The numbers of Bel-7402 cells in the lower chamber in Figure 4A and 4B, each bar represents the mean±SD of three separate experiments. (D) Values of wound-healing assessed by measuring the pixel of wound area, each bar represents the mean±SD of three separate experiments. ^{b}P<0.05, ^{c}P<0.01 *vs* control; ^{e}P<0.05, ^{f}P<0.01 *vs* Shh.

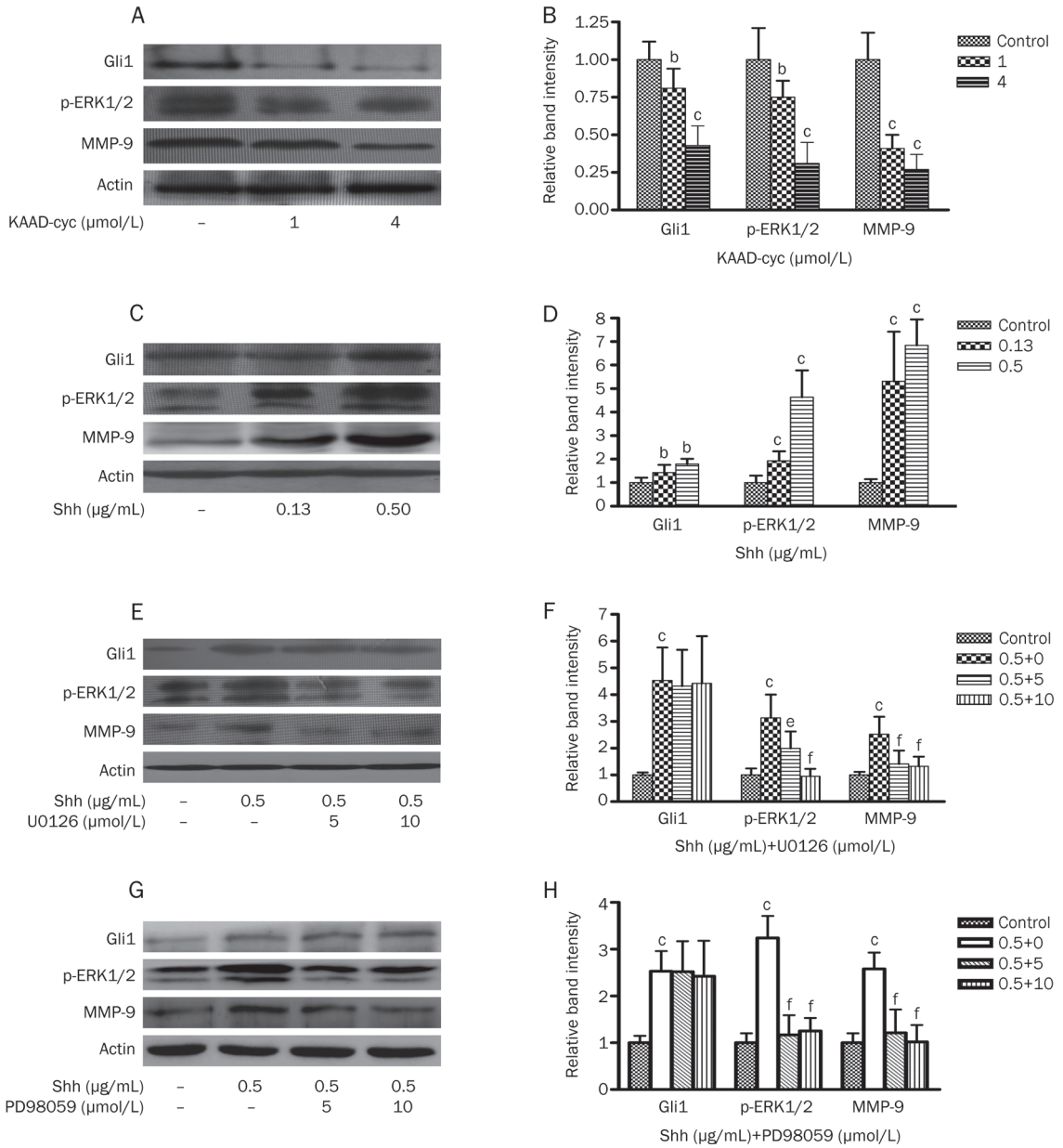

Figure 5. Effects of KAAD-cyc, Shh, U0126, or PD98059 on the expressions of Gli1, p-ERK1/2, and MMP-9 proteins in Bel-7402 cells. (A) Western blot analysis of Gli1, p-ERK1/2, and MMP-9 protein levels in cell lysates from Bel-7402 cells treated with 1 or 4 μmol/L KAAD-cyc for 24 h. (B) The values under each lane indicate relative density of the band in Figure 5A normalized to β-actin, respectively. (C) Western blot analysis of Gli1, p-ERK1/2, and MMP-9 protein levels in cell lysates from Bel-7402 cells treated with 0.13 or 0.50 μg/mL Shh for 24 h. (D) The values under each lane indicate relative density of the band in Figure 5C normalized to β-actin, respectively. (E) Western blot analysis of Gli1, p-ERK1/2, and MMP-9 protein levels in cell lysates from Bel-7402 cells pretreated by 0.50 μg/mL Shh, then treated with 5 or 10 μmol/L U0126 for 24 h. (F) The values under each lane indicate relative density of the band in Figure 5E normalized to β-actin, respectively. (G) Western blot analysis of Gli1, p-ERK1/2, and MMP-9 protein levels in cell lysates from Bel-7402 cells pretreated by 0.50 μg/mL Shh, then treated with 5 or 10 μmol/L PD98059 for 24 h. (H) The values under each lane indicate relative density of the band in Figure 5G normalized to β-actin, respectively. $^{b}P<0.05$, $^{c}P<0.01$ *vs* control; $^{e}P<0.05$, $^{f}P<0.01$ *vs* Shh.

Bel-7402 in concentration dependent manner compared with vehicle control (Figure 5C and 5D).

Effects of U0126 and PD98059 on the expression of Gli1, p-ERK1/2, and MMP-9 in Bel-7402 cells induced by Shh

After Bel-7402 cells were treated with 0.5 μg/mL Shh, then 5 or 10 μmol/L U0126 and 5 or 10 μmol/L PD98059 were added for 24 h. Western blot analysis indicated that both U0126 and PD98059 dramatically inhibited the expression of MMP-9 and p-ERK1/2 in a concentration dependent manner. However, both U0126 and PD98059 had no effects on expression of Gli1 under the same condition compared with vehicle control (Fig-

ure 5E and 5G).

Discussion

Hepatocellular carcinoma (HCC) is one of the most malignant cancers especially in Asian countries, and its poor prognosis is mainly due to metastasis after excision[52]. Currently there are no available effective treatment[53, 54]. Studies of the underlying molecular mechanism of HCC metastasis provide potential to identify new therapeutic targets. Previous evidence has demonstrated that the Hh signaling plays an important role in multiple tumor types. This signaling pathway is involved in and participates development, invasion and metastasis of HCC[34–40]. In this study, we further detected expression of Shh and Gli1 in metastasis and non-metastasis HCC liver tissues, simultaneously we used KAAD-cyc, a specific inhibitor of Hh pathway and Shh, a ligand of the Hh pathway in invasion and metastasis assays of human HCC cell line, and we confirmed the results. However, to date no report has been presented to identify a potential mechanism. Therefore we investigated the mechanisms of the Hh signaling pathway in HCC invasion and metastasis. Gli1, a transcription factor activated in the Hh pathway, significantly enhanced tumor growth and metastases of other cancers through the activation of ERK1/2[42, 45]. Overexpression of MMP-9 is also a key factor for tumor invasion and metastasis[47, 48, 55]. Moreover, the Hh signaling pathway may enhance migration and invasion of cancer cells by increasing the expression of MMP-9[49, 50].

In the present study, we found that expressions of Shh, MMP-9, and p-ERK1/2 were remarkably stronger in HCC samples with metastasis than in non-metastasis HCC liver samples. Moreover, there was a significant difference in expression of Gli1 in nuclei of cells in HCC tissue samples with metastasis compared to and HCC samples with no metastasis. Moreover, expression of Gli1 was also positively correlated to expressions of both MMP-9 and p-ERK1/2. These data suggested that the Hh signal pathway may be involved in human HCC invasion and metastasis by up-regulating the protein expression MMP-9 and p-ERK1/2.

Since the Hh signaling pathway has been associated with MAPK/ERK pathway in different cancer[43–46], furthermore our results indicate that the pathway is also notably correlated to expressions of p-ERK1/2 in HCC tissues. To confirm these results, we treated a HCC cell line, Bel-7402 cells, with KAAD-cyc, Shh, U0126, or PD98059 *in vitro*. Our results demonstrated that KAAD-cyc inhibited the invasion and migration of Bel-7402 cells and decreased the expression of Gli1, p-ERK1/2 proteins in Bel-7402, but Shh increased the expression of Gli1, p-ERK1/2 proteins. U0126 and PD98059 inhibited the invasion and metastasis of Bel-7402 cells induced by Shh, decreased the expression of Gli1 proteins, but they had no effect on the expression of Gli1. These indicate that the Hh signal pathway is involved in human HCC invasion and metastasis by up-regulating the expression of MAPK/ERK pathway, instead of the MAPK/ERK pathway inducing expression of Gli1.

Matrix metalloproteinases (MMPs) have long been associated with cancer cell invasion and metastasis. MMPs are proteolytic enzymes, their basic mechanism of action is to degrade proteins in extracellular matrix. Activation of MMPs has been detected in almost all type of human cancers, which is closely correlated to advanced tumor stage, increasing tumor invasion and metastasis. Onishi *et al* reported that the Hh signaling pathway up-regulated cell migration and invasion in human cancers by increasing expressions of MMP-9[50]. However, the relationship among the Hh signaling pathway, MAPK/ERK pathway and MMP-9 remains unclear. Our results indicate that the Hh pathway is also correlated with expressions of p-ERK1/2 and MMP-9 in HCC tissues. In Bel-7402 cellular assays, KAAD-cyc inhibited expression of MMP-9 proteins, and Shh up-regulated expression of MMP-9 proteins. Both U0126 and PD98059 were able to inhibit the expression of MMP-9 elevated by Shh. Therefore, we concluded that the Hh signaling pathway mediated the protein expression MMP-9 through MAPK/ERK pathway.

Most importantly, we have confirmed that the Hh signal pathway is involved in human HCC invasion and metastasis. We hypothesize and also deduce that the Hh signaling pathway activates the ERK pathway, subsequently, the ERK pathway up-regulates the protein expression of MMP-9, thereby mediating human HCC invasion and metastasis. These data may assist in identifying novel diagnostic markers and therapeutic targets for the treatment of highly aggressive HCC.

Acknowledgements

The study is supported by National Natural Science Foundation of China (No 30973543 and 81173075), and Anhui Provincial Natural Science Foundation (No 090413108 and KJ2012A160).

The authors thank senior technician Cheng-yi WU, Ai-wu ZHOU and Yun-fang ZHANG, technician Li-hua LIU for their excellent technical assistance.

Author contribution

Wei WEI and Jing-tao LU designed the research; Jing-tao LU, Wen-di ZHAO, and Wei HE performed the research; Jing-tao LU and Wei HE analyzed data; and Jing-tao LU wrote the paper.

Abbreviations

HCC, hepatocellular carcinoma; Hh, hedgehog; PI3K, phosphatidylinositol-3 kinase; Ptc, patched; Smo, smoothened; Gli, the glioma-associated oncogenes; KAAD-cyc, KAAD-cyclopamine; MMPs, matrix metalloproteinases; PBS, phosphate-buffered saline; DMEM, Dulbecco's modified Eagle's medium.

References

1 Aravalli RN, Steer CJ, Cressman EN. Molecular mechanisms of hepatocellular carcinoma. Hepatology 2008; 48: 2047–63.
2 Walzer N, Kulik LM. Hepatocellular carcinoma: latest developments. Curr Opin Gastroenterol 2008; 24: 312–9.
3 Parkin DM, Bray F, Ferlay J, Pisani P. Global cancer statistics, 2002.

CA Cancer J Clin 2005; 55: 74–108.
4 Chen XP, Qiu FZ, Wu ZD, Zhang ZW, Huang ZY, Chen YF, *et al*. Effects of location and extension of portal vein tumor thrombus on long-term outcomes of surgical treatment for hepatocellular carcinoma. Ann Surg Oncol 2006; 13: 940–6.
5 Tang ZY, Ye SL, Liu YK, Qin LX, Sun HC, Ye QH, *et al*. A decade's studies on metastasis of hepatocellular carcinoma. J Cancer Res Clin Oncol 2004; 130: 187–96.
6 Min L, He B, Hui L. Mitogen-activated protein kinases in hepatocellular carcinoma development. Semin Cancer Biol 2011; 21: 10–20.
7 Hsieh YH, Wu TT, Huang CY, Hsieh YS, Hwang JM, Liu JY. p38 mitogen-activated protein kinase pathway is involved in protein kinase Calpha-regulated invasion in human hepatocellular carcinoma cells. Cancer Res 2007; 67: 4320–7.
8 Martínez-López N, Varela-Rey M, Fernández-Ramos D, Woodhoo A, Vázquez-Chantada M, Embade N, *et al*. Activation of LKB1-Akt pathway independent of phosphoinositide 3-kinase plays a critical role in the proliferation of hepatocellular carcinoma from nonalcoholic steatohepatitis. Hepatology 2010; 52: 1621–31.
9 Whittaker S, Marais R, Zhu AX. The role of signaling pathways in the development and treatment of hepatocellular carcinoma. Oncogene 2010; 29: 4989–5005.
10 Chen JS, Wang Q, Fu XH, Huang XH, Chen XL, Cao LQ, *et al*. Involvement of PI3K/PTEN/AKT/mTOR pathway in invasion and metastasis in hepatocellular carcinoma: Association with MMP-9. Hepatol Res 2009; 39: 177–86.
11 Wei W, Chua MS, Grepper S, So SK. Blockade of Wnt-1 signaling leads to anti-tumor effects in hepatocellular carcinoma cells. Mol Cancer 2009; 8: 76–81.
12 Kaposi-Novak P, Lee JS, Gòmez-Quiroz L, Coulouarn C, Factor VM, Thorgeirsson SS. Met-regulated expression signature defines a subset of human hepatocellular carcinomas with poor prognosis and aggressive phenotype. J Clin Invest 2006; 116: 1582–95.
13 Horiguchi N, Takayama H, Toyoda M, Otsuka T, Fukusato T, Merlino G, *et al*. Hepatocyte growth factor promotes hepatocarcinogenesis through c-Met autocrine activation and enhanced angiogenesis in transgenic mice treated with diethylnitrosamine. Oncogene 2002; 21: 1791–9.
14 Ruizi AA, Sanchez P, Dahmane N. Gli and hedgehog in cancer: tumours, embryos and stem cells. Nat Rev Cancer 2002; 2: 361–72.
15 Goetz JA, Suber LM, Zeng X, Robbins DJ. Sonic hedgehog as a mediator of long-range signaling. Bioessays 2002; 24: 157–65.
16 Nybakken K, Perrimon N. Hedgehog signal transduction: recent findings. Curr Opin Genet Dev 2002; 12: 503–11.
17 Sasaki H, Nishizaki Y, Hui C, Nakafuku M, Kondoh H. Regulation of Gli2 and Gli3 activities by an amino-terminal repression domain: implication of Gli2 and Gli3 as primary mediators of Shh signaling. Development 1999; 126: 3915–24.
18 Stepan V, Ramamoorthy S, Nitsche H, Zavros Y, Merchant JL, Todisco A. Regulation and function of the sonic hedgehog signal transduction pathway in isolated gastric parietal cells. J Biol Chem 2005; 280: 15700–8.
19 Ingham PW, McMahon AP. Hedgehog signaling in animal development: paradigms and principles. Genes Dev 2001; 15: 3059–87.
20 Cohen MM Jr. The Hedgehog signaling network. Am J Med Genet 2003; 123A: 5–28.
21 Kump E, Ji J, Wernli M, Häusermann P, Erb P. Gli2 upregulates cFlip and renders basal cell carcinoma cells resistant to death ligand-mediated apoptosis. Oncogene 2008; 27: 3856–64.
22 Caro I, Low JA. The role of the hedgehog signaling pathway in the development of basal cell carcinoma and opportunities for treatment. Clin Cancer Res 2010; 16: 3335–9.
23 Bisht S, Brossart P, Maitra A, Feldmann G. Agents targeting the Hedgehog pathway for pancreatic cancer treatment. Curr Opin Investig Drugs 2010; 11: 1387–98.
24 Yoshikawa K, Shimada M, Miyamoto H, Higashijima J, Miyatani T, Nishioka M, *et al*. Sonic hedgehog relates to colorectal carcinogenesis. J Gastroenterol 2009; 44: 1113–7.
25 Katoh Y, Katoh M. Hedgehog signaling pathway and gastric cancer. Cancer Biol Ther 2005; 4: 1050–4.
26 Velcheti V, Govindan R. Hedgehog signaling pathway and lung cancer. J Thorac Oncol 2007; 2: 7–10.
27 Thayer SP, di Magliano MP, Heiser PW, Nielsen CM, Roberts DJ, Lauwers GY, *et al*. Hedgehog is an early and late mediator of pancreatic cancer tumorigenesis. Nature 2003; 425: 851–6.
28 Reagan-Shaw S, Cozma D, Thomas-Tikhonenko A, Ahmad N, Spiegelman VS. Role of GLI2 transcription factor in growth and tumorigenicity of prostate cells. Cancer Res 2007; 67: 10642–6.
29 Xu FG, Ma QY, Wang Z. Blockade of hedgehog signaling pathway as a therapeutic strategy for pancreatic cancer. Cancer Lett 2009; 283: 119–24.
30 Haaf AT, Bektas N, von Serenyi S, Losen I, Arweiler EC, Hartmann A, *et al*. Expression of the glioma-associated oncogene homolog (GLI)1 in human breast cancer is associated with unfavourable overall survival. BMC Cancer 2009; 25: 298–301.
31 Mukherjee S, Frolova N, Sadlonova A, Novak Z, Steg A, Page GP, *et al*. Hedgehog signaling and response to cyclopamine differ in epithelial and stromal cells in benign breast and breast cancer. Cancer Biol Ther 2006; 5: 674–83.
32 Eichenmüller M, Gruner I, Hagl B, Häberle B, Müller-Höcker J, von Schweinitz D, *et al*. Blocking the hedgehog pathway inhibits hepatoblastoma growth. Hepatology 2009; 49: 482–90.
33 Ma X, Sheng T, Zhang Y, Zhang X, He J, Huang S, *et al*. Hedgehog signaling is activated in subsets of esophageal cancers. Int J Cancer 2006; 118: 139–48.
34 Sicklick JK, Li YX, Jayaraman A, Kannangai R, Qi Y, Vivekanandan P, *et al*. Dysregulation of the Hedgehog pathway in human hepatocarcinogenesis. Carcinogenesis 2006; 27: 748–57.
35 Huang S, He J, Zhang X, Bian Y, Yang L, Xie G, *et al*. Activation of the hedgehog pathway in human hepatocellular carcinomas. Carcinogenesis 2006; 27: 1334–40.
36 Cheng WT, Xu K, Tian DY, Zhang ZG, Liu LJ, Chen Y. Role of hedgehog signaling pathway in proliferation and invasiveness of hepatocellular carcinoma cells. Int J Oncol 2009; 34:829–36.
37 Tada M, Kanai F, Tanaka Y, Tateishi K, Ohta M, Asaoka Y, *et al*. Down-regulation of hedgehog-interacting protein through genetic and epigenetic alterations in human hepatocellular carcinoma. Clin Cancer Res 2008; 14: 3768–76.
38 Kim Y, Yoon JW, Xiao X, Dean NM, Monia BP, Marcusson EG. Selective down-regulation of glioma-associated oncogene 2 inhibits the proliferation of hepatocellular carcinoma cells. Cancer Res 2007; 67: 3583–93.
39 Kim HY, Cho HK, Hong SP, Cheong J. Hepatitis B virus X protein stimulates the Hedgehog-Gli activation through protein stabilization and nuclear localization of Gli1 in liver cancer cells. Cancer Lett 2011; 309: 176–84.
40 Chen X, Lingala S, Khoobyari S, Nolta J, Zern MA, Wu J. Epithelial mesenchymal transition and hedgehog signaling activation are associated with chemoresistance and invasion of hepatoma subpopulations. J Hepatol 2010; 55: 838–45.
41 Zheng X, Yao Y, Xu Q, Tu K, Liu Q. Evaluation of glioma-associated

oncogene 1 expression and its correlation with the expression of sonic hedgehog, E-cadherin and S100a4 in human hepatocellular carcinoma. Mol Med Report 2010; 3: 965–70.

42 Philips GM, Chan IS, Swiderska M, Schroder VT, Guy C, Karaca GF, *et al*. Hedgehog signaling antagonist promotes regression of both liver fibrosis and hepatocellular carcinoma in a murine model of primary liver cancer. PLoS One 2011; 6: e23943.

43 Elia D, Madhala D, Ardon E, Reshef R, Halevy O. Sonic hedgehog promotes proliferation and differentiation of adult muscle cells: Involvement of MAPK/ERK and PI3K/Akt pathways. Biochim Biophys Acta 2007; 1773: 1438–46.

44 Schnidar H, Eberl M, Klingler S, Mangelberger D, Kasper M, Hauser-Kronberger C, *et al*. Epidermal growth factor receptor signaling synergizes with Hedgehog/GLI in oncogenic transformation via activation of the MEK/ERK/JUN pathway. Cancer Res 2009; 69: 1284–92.

45 Chang H, Li Q, Moraes RC, Lewis MT, Hamel PA. Activation of ERK by sonic hedgehog is independent of canonical hedgehog signaling. Int J Biochem Cell Biol 2010; 42: 1462–71.

46 Seto M, Ohta M, Asaoka Y, Ikenoue T, Tada M, Miyabayashi K, *et al*. Regulation of the hedgehog signaling by the mitogen-activated protein kinase cascade in gastric cancer. Mol Carcinog 2009; 48: 703–12.

47 Donadio AC, Remedi MM, Susperreguy S, Frede S, Gilardoni MB, Tang Y, *et al*. Extracellular matrix metalloproteinase inducer and matrix metalloproteinases (MMPs) as regulators of tumor-host interaction in a spontaneous metastasis model in rats. Histochem Cell Biol 2008; 130: 1155–64.

48 Cortes-Reynosa P, Robledo T, Macias-Silva M, Wu SV, Salazar EP. Src kinase regulates metalloproteinase-9 secretion induced by type IV collagen in MCF-7 human breast cancer cells. Matrix Biol 2008; 27: 220–31.

49 Wang K, Pan L, Che X, Cui D, Li C. Sonic Hedgehog/GLI signaling pathway inhibition restricts cell migration and invasion in human gliomas. Neurol Res 2010; 32: 975–80.

50 Onishi H, Kai M, Odate S, Iwasaki H, Morifuji Y, Ogino T, *et al*. Hypoxia activates the hedgehog signaling pathway in a ligand-independent manner by upregulation of Smo transcription in pancreatic cancer. Cancer Sci 2011; 102: 1144–50.

51 Huang XH, Chen JS, Wang Q, Chen XL, Wen L, Chen LZ, *et al*. miR-338-3p suppresses invasion of liver cancer cell by targeting smoothened. J Pathol 2011; 225: 463–72.

52 Thorgeirsson SS, Grisham JW. Molecular pathogenesis of human hepatocellular carcinoma. Nat Genet 2002; 31: 339–46.

53 Thomas MB, Zhu AX. Hepatocellular carcinoma: the need for progress. J Clin Oncol 2005; 23: 2892–9.

54 Grieco A, Pompili M, Caminiti G, Miele L, Covino M, Alfei B, *et al*. Prognostic factors for survival in patients with early-intermediate hepatocellular carcinoma undergoing non-surgical therapy: comparison of Okuda, CLIP, and BCLC staging systems in a single Italian centre. Gut 2005; 54: 411–8.

55 Kessenbrock K, Plaks V, Werb Z. Matrix metalloproteinases: regulators of the tumor microenvironment. Cell 2010; 141: 52–67.

Acta Pharmacologica Sinica (2012) 33: 701–709
 1671-4083/12 $32.00
www.nature.com/aps

Original Article

Prostanoid EP_1 receptor as the target of (–)-epigallocatechin-3-gallate in suppressing hepatocellular carcinoma cells *in vitro*

Juan JIN, Yan CHANG, Wei WEI*, Yi-fu HE, Shan-shan HU, Di WANG, Yu-jing WU

Institute of Clinical Pharmacology, Anhui Medical University, Key Laboratory of Anti-inflammatory and Immunopharmacology of the Education Ministry of China, Hefei 230032, China

Aim: To investigate the effects of (–)-epigallocatechin-3-gallate (EGCG), an active compound in green tea, on prostaglandin E_2 (PGE_2)-induced proliferation and migration, and the expression of prostanoid EP_1 receptors in hepatocellular carcinoma (HCC) cells.
Methods: HCC cell line HepG2, human hepatoma cell lines MHCC-97L, MHCC-97H and human hepatocyte cell line L02 were used. Cell viability was analyzed using MTT assay. PGE_2 production was determined with immunoassay. Wound healing assay and transwell filter assay were employed to assess the extent of HCC cell migration. The expression of EP_1 receptor and Gq protein were examined using Western blot assay.
Results: PGE_2 (4-40000 nmol/L) or the EP_1 receptor agonist ONO-DI-004 (400-4000 nmol/L) increased the viability and migration of HepG2 cells in concentration-dependent manners. EGCG (100 μg/mL) significantly inhibited the viability and migration of HepG2 cells induced by PGE_2 or ONO-DI-004. HepG2 cells secreted an abundant amount of PGE_2 into the medium, and EGCG (100 μg/mL) significantly inhibited the PGE_2 production and EP_1 receptor expression in HepG2 cells. EGCG (100 μg/mL) also inhibited the viability of MHCC-97L cells, but not that of MHCC-97H cells. Both EGCG (100 μg/mL) and EP_1 receptor antagonist ONO-8711 inhibited PGE_2 4 μmol/L and ONO-DI-004 400 nmol/L-induced growth and migration of HepG2 cells. Both EGCG (100 μg/mL) and ONO-8711 210 nmol/L inhibited PGE_2- and ONO-DI-004-induced EP_1 expression. EGCG and ONO-8711 had synergistic effects in inhibiting EP_1 receptor expression. PGE_2, ONO-DI-004, ONO-8711, and EGCG had no effects on Gq expression in HepG2 cells, respectively.
Conclusion: These findings suggest that the anti-HCC effects of EGCG might be mediated, at least partially, through the suppressing EP_1 receptor expression and PGE_2 production.

Keywords: hepatocellular carcinoma; epigallocatechin-3-gallate; prostaglandin E_2; prostanoid EP_1 receptor

Acta Pharmacologica Sinica (2012) 33: 701–709; doi: 10.1038/aps.2012.13

Introduction

Hepatocellular carcinoma (HCC), one of the most common malignancies worldwide[1], often arises in the background of chronic liver inflammation and cirrhosis. At this time, no effective chemotherapeutic or chemopreventive treatments are available. HCC is a growing health problem, and innovative treatment approaches are urgently needed.

(–)-Epi-gallocatechin-3-gallate (EGCG, structure shown in Figure 1), one of the most abundant bioactive components in leaves of green tea, has received increasing attention for its various physiological activities, such as antioxidant activity[2, 3] and anti-tumor properties[4–6]. The effects of EGCG on tumor cell proliferation and apoptosis have been well documented[7].

PGE_2 is the prostaglandin that is abundantly present in HCC. Studies have established the important role of the PGE_2 synthesis pathway as a potential target for the treatment and/or prevention of HCC[8, 9]. PGE_2 exerts its biological activities primarily via G-protein-coupled prostaglandin receptors ($EP_{1\text{-}4}$), which belong to the highly conserved superfamily of

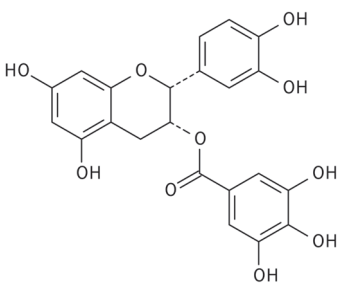

Figure 1. Chemical structure of EGCG.

* To whom correspondence should be addressed.
E-mail wwei@ahmu.edu.cn
Received 2011-10-19 Accepted 2011-02-01

7-transmembrane-spanning proteins. Among these four EP receptors, studies have shown EP_1 to be the most important in tumor development. EP_1, through activation of epidermal growth factor receptor (EGFR)/c-Met signaling, plays an important role in tumor cell invasion[10]. A selective EP_1 agonist increased the phosphorylation of EGFR, which suggests that it might enhance the invasion of tumor cells[10]. Moreover, an EP_1 antagonist reduced the viability of HCC cells and increased their apoptosis[1]. The EP_1 receptor is of major importance in colon cancer development as well. For example, in one study, EP_1 receptor deficiency inhibited colon cancer development[11]. In addition, a selective EP_1 antagonist suppressed tongue carcinogenesis in rats, notably reduced the number of tumors in UV-induced mouse skin cancer[12] and inhibited the COX-2 and PGE_2-induced migration and viability of human chondrosarcoma[13]. These reports suggest that the EP_1 receptor might play a key role in the PGE_2-induced tumor process.

Studies have demonstrated the anti-inflammatory and antioxidant activity of EGCG, which is mediated via the inhibition of COX-2[14] and microsomal prostaglandin E_2 synthase-1 (mPGES-1)[15]. Although previous studies have suggested that EGCG downregulates COX-2 and mPGES-1 expression, whether the antitumoral effects of EGCG on HCC are mediated via regulation of EP_1 and PGE_2 has not been established. We hypothesized that EGCG might exert an anti-HCC effect by virtue of its suppressive action on both PGE_2 production and EP_1 expression.

Materials and methods

Drugs

The EP_1-receptor selective antagonist ONO-8711 and EP_1-receptor selective agonist ONO-DI-004 were kindly provided by ONO Pharmaceutical Co., Osaka, Japan. EGCG and PGE_2 were purchased from Sigma (St Louis, MO, USA). EP_1-receptor-antibody and Gq-receptor-antibody were obtained from Cayman Chemical, Ann Arbor, MI, USA.

Cell culture

The human hepatoma cell line MHCC-97L and MHCC-97H was obtained from the Liver Cancer Institute of Zhongshan Hospital, Fudan University, Shanghai, China. The HepG2 cell line was obtained from the Shanghai Cell Bank of Chinese Academy of Sciences. Human hepatocyte cell line L02 was obtained from the Shanghai Institute of Cell Research. All of cell lines were cultured at 37 °C in a 5% CO_2 environment in DMEM from Gibco BRL Life Technologies Inc (Grand Island, New York, USA) supplemented with 10% fetal bovine serum (FBS, Sigma).

Cell proliferation assay

Proliferation was measured using a 3-(4,5-dimethylthiazol-2-yl)-2,5-diphenyltetrazoliumbromide (MTT) assay (EZ4U; Biomedica, Vienna, Austria). To assess the effects of PGE_2 (4×10^{-6} mol/L), ONO-8711 (210 nmol/L and 10 μmol/L), ONO-DI-004 (400 nmol/L) and EGCG (12.5, 25, 50, and 100 μg/mL) on cell proliferation, HepG2, MHCC-97L and MHCC-97H cells in an exponential growth phase were cultured at a density of 8×10^3 cells/well in a 96-well plate and incubated overnight in DMEM containing 10% FBS. The cells were then serum starved for 24 h before being treated with the compounds. After treatment with various concentrations of reagents, MTT solution (5.0 mg/mL in PBS) was added (20.0 μL/well), and the plates were incubated for another 4 h at 37 °C. The purple formazan crystals were dissolved in 150.0 μL of Dimethyl Sulfoxide (DMSO) per well. After 10 min, the plates were read on a microplate reader (American Bio-Tek) at 490 nm. The cells without drugs were used as a control. The assays were performed in three independent experiments. The inhibition of cell proliferation was determined using the following formula: inhibition of cell proliferation (%)=[1–(OD of the experimental samples/OD of the control)]×100% (n=3, mean±SD).

Transwell filter cell migration assay

Boyden chambers containing polycarbonate filters with 8 μm pore size (Costar, Bodenheim, Germany) were employed. Cells were seeded at a density of 5×10^5 cells per milliliter. To initiate the chemotaxis assay, cells (5×10^4) in 100 μL of DMEM without FCS were added to the inner chamber, and the lower chamber was filled with 600 μL of DMEM with 10% FCS, as well as PGE_2 (4×10^{-6} mol/L) or ONO-DI-004 (400 nmol/L) as an inducer of cell migration. The cells were allowed to migrate for 12 h at 37 °C in an atmosphere of 95% air/5% CO_2. Cells on the filter were first stained with hematoxylin-eosin staining, and cells that remained on the upper surface of the filter were removed using a cotton swab. The cells that migrated onto the lower surface of the filter were examined by microscope after mounting them onto a slide. A total of six random high-power microscopic fields (HPF) (100×) per filter were photographed, and the number of cells was directly counted. Experiments were carried out in triplicate and were repeated three times with consistent results.

Wound healing assay

Cell migration was examined using the wound-healing assay. HepG2 cells were cultured to a confluent monolayer in a 6-well plate at 37 °C in an atmosphere of 95% air/5% CO_2. Thereafter, a scratch (wound) was introduced in the confluent cell layer using a yellow pipette tip. The cells were washed three times with phosphate-buffered saline (PBS) to remove detached cells. The cells were then incubated with different compounds for 24 h, and pictures of a defined wound spot were made with a computer-aided phase contrast microscope at 0 and 24 h. The area of the wound in the microscopic pictures was measured using Image J software (National Institutes of Health, MD) at different time points. The relative distance of wound closure (%)=(distance at 0 h-distance at 24 h)/relative distance of control×100%.

Enzyme-linked immunosorbent assay

The HCC cell line HepG2 was plated into six-well plates and grown to 70% confluence. After washing with PBS, the cells

were treated with increasing concentrations of EGCG (0, 12.5, 25, 50, and 100 μg/mL) in serum-free DMEM for 24 h. The cell supernatants were then collected, and the PGE_2 levels were measured using a commercial PGE_2 immunoassay kit (R&D Systems, Minneapolis, MN, USA), according to the manufacturer's instructions. A PGE_2 standard was run in parallel to the supernatant samples. Each assay was performed using triplicate samples.

Western-blot analysis

The cells were treated with PGE_2 and ONO-DI-004 for 2 h with or without a 1 h pretreatment with EGCG at 100 μg/mL. After treatment for 2 h, protein was extracted from cells in RIPA lysis buffer (50 mmol/L TRIS (tris (hydroxymethyl) aminomethane)-HCl, pH 7.4, 150 mmol/L NaCl, 10 mmol/L phenylmethylsulfonyl fluoride (PMSF), 1 mmol/L ethylene diamine tetraacetic acid (EDTA), 0.1% sodium dodecyl sulfate (SDS), 1% Triton X-100, 1% sodium deoxycholate). The protein concentration was determined with the Lowry Protein Assay. A protein sample was mixed with the 5×sample buffer (4:1) (Bio-Rad, Hercules, CA) and heated in boiling water for 10 min. The proteins were resolved by sodium dodecyl-sulfate-polyacrylamide gel electrophoresis (SDS-PAGE), transferred to polyvinylidene fluoride (PVDF) membranes (Millipore, Bedford, MA), and incubated with blocking buffer [Tris-buffered saline/Tween 20 (TBST)/5% nonfat dry milk] overnight at 4 °C. Immunoblotting was performed with the mouse antibody raised against human EP_1 receptor (1:1000) or Gq protein (1:1000) followed by the appropriate horseradish peroxidase (HRP)-conjugated goat anti-mouse antibody (1:15 000). Immunodetection was performed with an enhanced chemiluminescence system (ECL, Pierce, Rockford, IL) using hydrogen peroxide and luminol as a substrate.

Statistical analysis

Biostatistical analyses were conducted using the SPSS 11.5 software package. All experiments were repeated at least three times. The results of multiple experiments are given as the mean±SEM. The non-parametric Kruskal-Wallis test was used to detect differences among the different experimental groups. A level of $P<0.05$ was accepted to indicate statistical significance.

Results

EP_1 expression in HCC cells

Previous studies showed that PGE_2 promoted tumor progression via binding to the EP_1 receptor[10, 11]. We showed that the EP_1 receptor protein was expressed in the L02, MHCC-97H, MHCC-97L, and HepG2 cell lines (Figure 2). The expression of EP_1 receptors was higher in HCC cell lines compared with human normal hepatocyte L02 cells.

PGE_2 induced HCC growth

PGE_2 is known to have a critical role in carcinogenesis. Therefore, we first detected the effect of PGE_2 on the viability of HepG2 cells. PGE_2 (0, 4, 40, 400, and 4000 nmol/L promoted

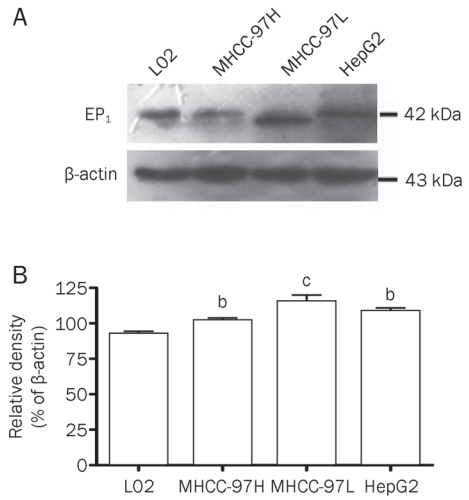

Figure 2. Expression of EP_1 receptor in HCC cells and human hepatocytes L02. (A) A representative Western blot showing the expression of EP_1 in HCC cell lines MHCC-97H, MHCC-97L, and HepG2. Human hepatocyte L02 cell line was used as control. (B) Bar graphs show quantitative evaluation of EP_1 expression by densitometry from triplicate independent experiments. Mean±SEM. $^bP<0.05$, $^cP<0.01$ compared with normal hepatocyte cell line L02.

HepG2 growth in a dose-dependent way ($P<0.05$, Figure 3A). After treatment with 4 μmol/L PGE_2 for 24, 48, and 72 h, the viability of HepG2 cells was increased (Figure 3B).

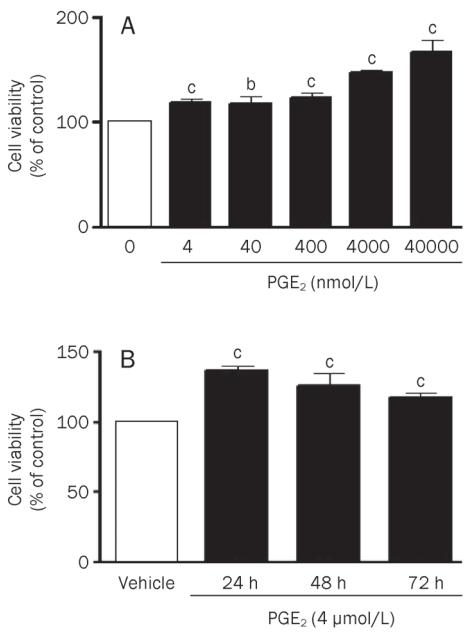

Figure 3. Effect of PGE_2 on HepG2 growth. (A) Effect of PGE_2 (0, 4, 40, 400, 4000, and 40000 nmol/L on cell viability after 24 h treatment. (B) Effect of 4 μmol/L PGE_2 on cell viability after 24, 48, and 72 h. Data were expressed as mean±SEM of two separate experiments which was performed in duplicate. $^bP<0.05$, $^cP<0.01$ compared with control group.

Effect of selective EP_1-receptor agonist and antagonist on HepG2 growth

We next measured the response of HepG2 cells to selective EP_1-receptor agonist ONO-DI-004. Cells were grown in the absence or presence of ONO-DI-004 (0, 4, 40, 400, and 4000 nmol/L), and proliferation was evaluated after 24 h. As shown in Figure 4A, both 400 nmol/L and 4 μmol/L of ONO-DI-004 significantly promoted HepG2 cell growth ($P<0.05$). We chose the 400 nmol/L of ONO-DI-004 to investigate its effect on cell viability at different time points (Figure 4B). The growth of cells was significantly increased after 48 h of stimulation by ONO-DI-004 ($P<0.01$). Subsequent experiments aimed to evaluate the potential of the selective EP_1-receptor-antagonist ONO-8711 as a chemotherapeutic compound. As shown in Figure 4C, the treatment of HepG2 cells with ONO-8711 (210 nmol/L, 1, 5, and 10 μmol/L) significantly reduced cell viability as compared with controls (cells treated with serum-free DMEM) ($P<0.01$).

EGCG inhibits PGE_2 production

After showing that PGE_2 stimulated HepG2 cell growth and knowing that mPGES expression is inhibited by EGCG[15], we aimed to determine the inhibitory effect of EGCG (12.5−100 μg/mL) on the production of PGE_2 in HCC cell lines. EGCG inhibited PGE_2 production as compared with controls (cells treated with serum-free DMEM). HepG2 cells secreted an abundant amount of PGE_2 into the growth medium, which was significantly reduced after treatment with 100 μg/mL of EGCG (Figure 5).

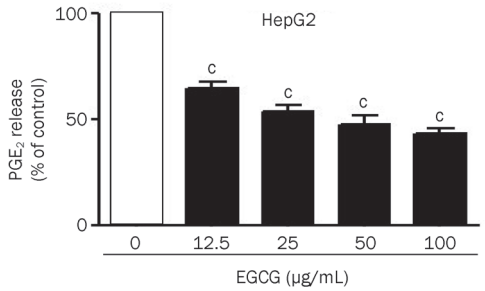

Figure 5. Effect of EGCG 12.5–100 μg/mL on production of PGE_2 by HepG2 cells after 48 h. Data were expressed as mean±SEM of two separate experiments, each of which was performed in duplicate. $^cP<0.01$ compared with control group.

EGCG inhibits HCC cell growth

First, we aimed to investigate the mechanisms by which EGCG exerts its anti-tumor activity. HCC cell lines HepG2, MHCC-97L and MHCC-97H were treated with EGCG (12.5–100 μg/mL) for 24 or 48 h. As shown in Figure 6, at a concentration of 50 μg/mL, the reduction of cell viability was significant in MHCC-97L and HepG2 cells ($P<0.01$), but MHCC-97H cell growth had no change. The extent of viability-reduction differed between HCC cell lines. In addition, EGCG might inhibit MHCC-97H cell migration or invasion or induce cell apoptosis but not cell growth. The exact mechanism would need to be further determined.

EGCG inhibits selective EP_1 receptor agonist-induced growth of HepG2 cells

Our results suggested that EGCG inhibited PGE_2 expression and HepG2 cell growth. We next tested the effect of EGCG (100 μg/mL) on PGE_2- and ONO-DI-004-induced cell growth. As shown in Figure 7, EGCG 100 μg/mL significantly inhibited PGE_2- and ONO-DI-004-induced growth of HepG2 cells ($P<0.01$).

EGCG inhibits selective EP_1 receptor agonist-induced migration of HepG2 cells

We next investigated how PGE_2, ONO-DI-004 and ONO-8711 influenced the migratory behavior of HepG2 cells by performing wound healing assays. Consistent with their role as positive regulators of cell growth, cells treated with PGE_2 or ONO-DI-004 closed the wound faster than the control, and EGCG and ONO-8711 inhibited cell migration. PGE_2 and ONO-DI-004 had an additive effect on cell migration (Figure 8A, 8B).

We further investigated the inhibitory effects of EGCG on PGE_2- and ONO-DI-004-induced migration using transwell filter assays. EGCG (100 μg/mL) significantly inhibited HepG2

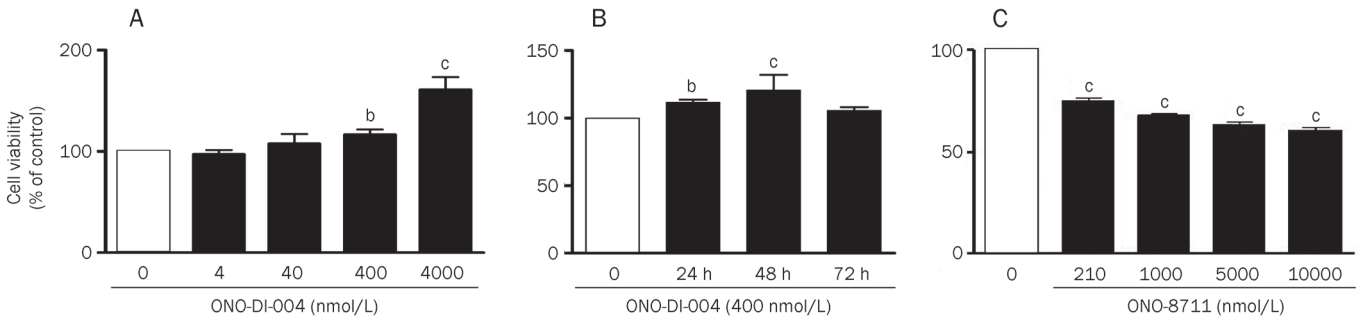

Figure 4. Selective EP_1 receptor agonist ONO-DI-004 and antagonist ONO-8711 on viability of HepG2 cells. (A) Effect of ONO-DI-004 (0, 4, 40, 400, and 4000 nmol/L on cell viability after 24 h. (B) Effect of 400 nmol/L of ONO-DI-004 on cell viability after 24, 48, and 72 h. (C) Effect of 210 nmol/L, 1, 5, and 10 μmol/L of ONO-8711 on viability of HepG2 cells after 24 h. Data were expressed as the relative inhibitory ratio in untreated cells and the mean±SEM of two separate experiments, each of which was performed in duplicate. $^bP<0.05$, $^cP<0.01$ compared with control group.

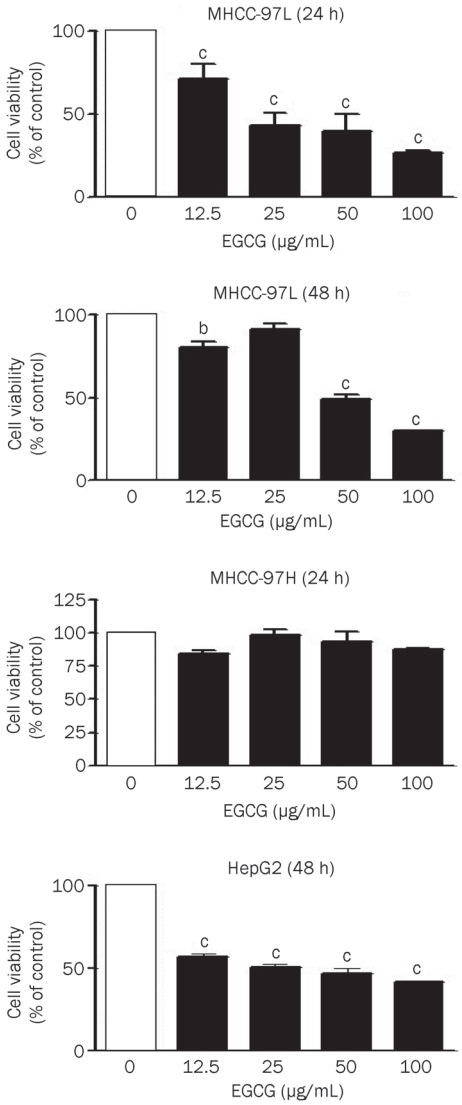

Figure 6. Inhibitory effect of EGCG (0, 12.5, 25, 50, and 100 μg/mL) on the growth of HepG2 cells, MHCC-97L and MHCC-97H cells after 24 or 48 h. Data were expressed as mean±SEM of two separate experiments which was performed in duplicate. $^{c}P<0.01$ compared with untreated group.

cell migration induced by PGE_2 (4 μmol/L) or ONO-DI-004 (400 nmol/L) ($P<0.01$, Figure 8C).

EGCG inhibits EP_1 expression in HepG2 cells

We further examined whether EP_1 receptor expression was altered after treatment with EGCG in HepG2 cells by Western blot assay. As shown in Figure 9A, when the cells were treated with PGE_2 or ONO-DI-004, an increase was observed in the expression of EP_1 receptors, which were inhibited by EGCG. In general, EP_1 receptors are coupled to Gq proteins, which are important for EP_1 signaling. Therefore, we also tested the expression of Gq proteins. There was no significant suppression of Gq expression after treatment with EGCG or ONO-8711 (Figure 9A). The results suggested that EGCG inhibited proliferation and migration of HepG2 induced by

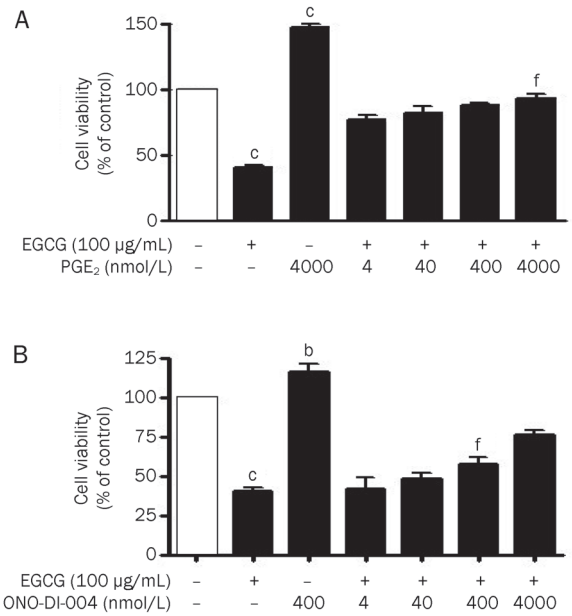

Figure 7. Inhibitory effects of EGCG 100 μg/mL on PGE_2 (A) and ONO-DI-004 (B)-induced growth of HepG2 cells. Data were expressed as the mean±SEM of two separate experiments, each of which was performed in duplicate. $^{b}P<0.05$, $^{c}P<0.01$ *vs* untreated group. $^{f}P<0.01$ *vs* single PGE_2- or ONO-DI-004-treated groups, respectively.

PGE_2, partially by suppressing the expression of the EP_1 receptor but not the Gq protein. We tested the effect of ONO-8711 or EGCG on PGE_2- and ONO-DI-004-induced EP_1 expression (Figure 9B). We found that both ONO-8711 and EGCG inhibited the PGE_2- and ONO-DI-004-induced EP_1 expression. PGE_2 and ONO-DI-004 had an synergistic effect on EP_1 expression.

Discussion

The increased expression of COX-2 and concomitant increased production of PGE_2 are considered to be a major cause of the pathological changes seen in cancers. Studies have indicated that COX-2-mediated production of PGE_2 increases cancer cell growth, which can be suppressed by several COX-2 inhibitors[16, 17]. Because of the unfavorable cardiovascular safety profile of selective COX-2 inhibitors, there is an interest in using PG receptor-specific compounds as novel agents in the prevention and treatment of certain cancers[18]. PGE_2 exerts its biological activities primarily via $EP_{1\text{-}4}$ receptors. Indeed, the EP_1 receptor has previously been shown to play a key role in the progression of various carcinomas, including colon cancer and skin cancer[10, 12, 18, 19]. Suppression of synthesis of PGE_2 and expression of its receptors is a compelling rationale in the treatment of HCC. Since the effects of EGCG on the migration and proliferation of HCC as induced by PGE_2 and EP_1 agonists was unknown, we decided to investigate this topic.

EGCG exerts an inhibitory effect in many cancers, such as prostate cancer[20, 21] and liver cancer[22]. Previous studies have shown that EGCG decreased the expression of COX-2[23] and mPGES[15]. However, the exact mechanism of the inhibi-

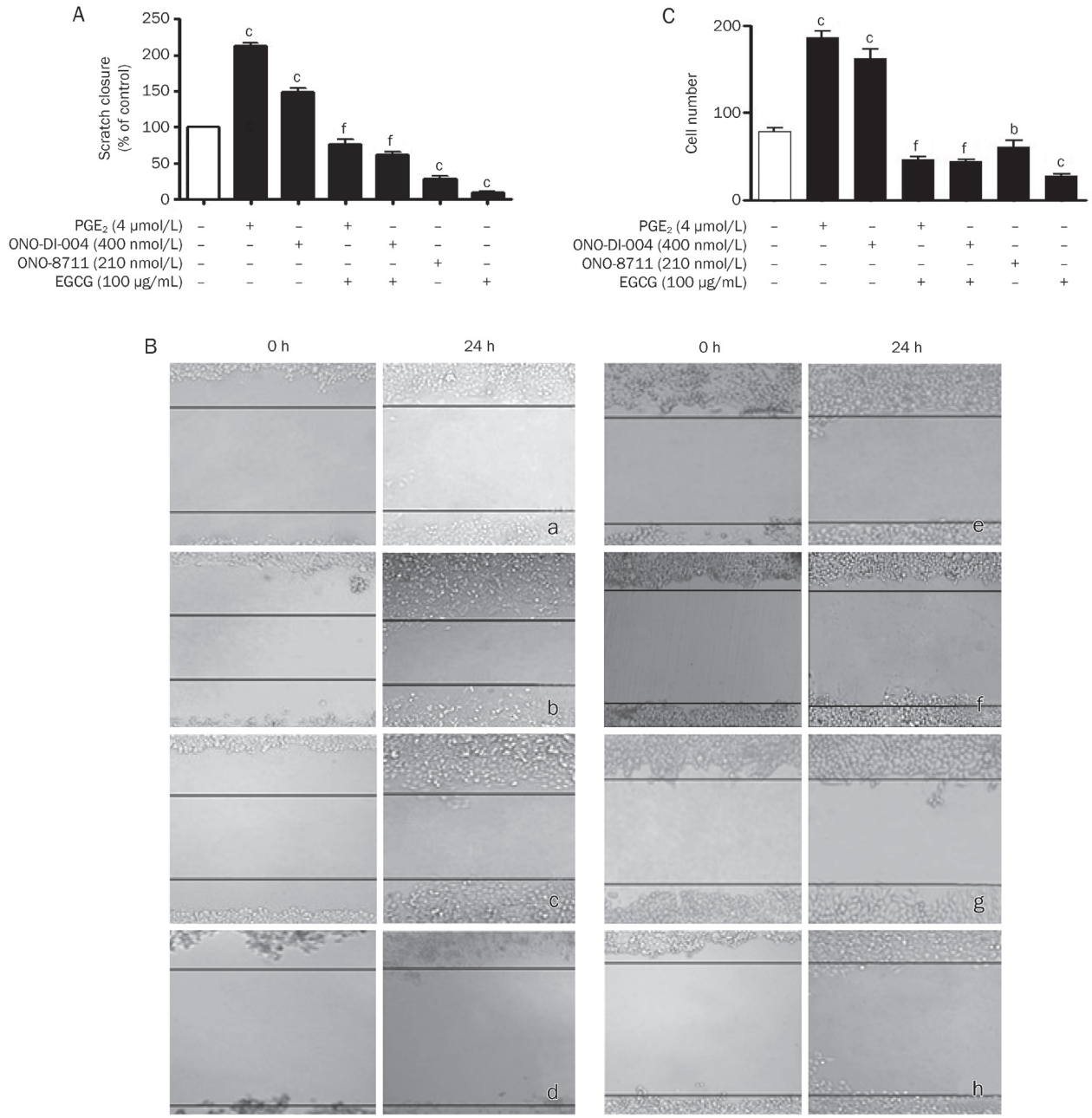

Figure 8. Inhibitory effects of EGCG and ONO-8711 on PGE_2- and ONO-DI-004-induced migration of HepG2 cells. (A) Effect of EGCG (100 μg/mL) and ONO 8711 210 nmol/L on PGE_2- and ONO-DI-004-stimulated scratch closure. (B) Representative photographs of wound-healing assay. (a) control; (b) PGE_2 (4 μmol/L); (c) ONO-DI-004 (400 nmol/L); (d) ONO-8711 (210 nmol/L); (e) ONO-8711+PGE_2; (f) EGCG (100 μg/mL); (g) EGCG+ONO-DI-004; (h) EGCG+PGE_2. The black line was used to mark the range of the scratches. (C) Effect of EGCG (100 μg/mL) and ONO 8711 (210 nmol/L) on PGE_2- and ONO-DI-004-stimulated cell migration. Data shown are expressed as the mean±SEM of two separate experiments, each of which was performed in duplicate. $^cP<0.01$ compared with untreated group. $^fP<0.01$ *vs* single PGE_2- or ONO-DI-004-treated group, respectively.

tory effect of EGCG on HCC cells is not well understood. We examined HCC cell proliferation after treatment with EGCG. After incubation with 50 or 100 μg/mL of EGCG, a significant reduction in cell proliferation in HepG2 and MHCC-97L cells, but not MHCC-97H cells was observed (Figure 6). To evaluate the effect of EGCG on PGE_2 production in HCC cells, we detected PGE_2 expression in HepG2 cells. As shown in Figure 5, EGCG decreased PGE_2 expression in a dose-dependent way. We found that EGCG produced a strong inhibitory effect on the growth of HCC cells and significantly downregulated PGE_2 production.

Previous studies demonstrated that PGE_2 binding to the

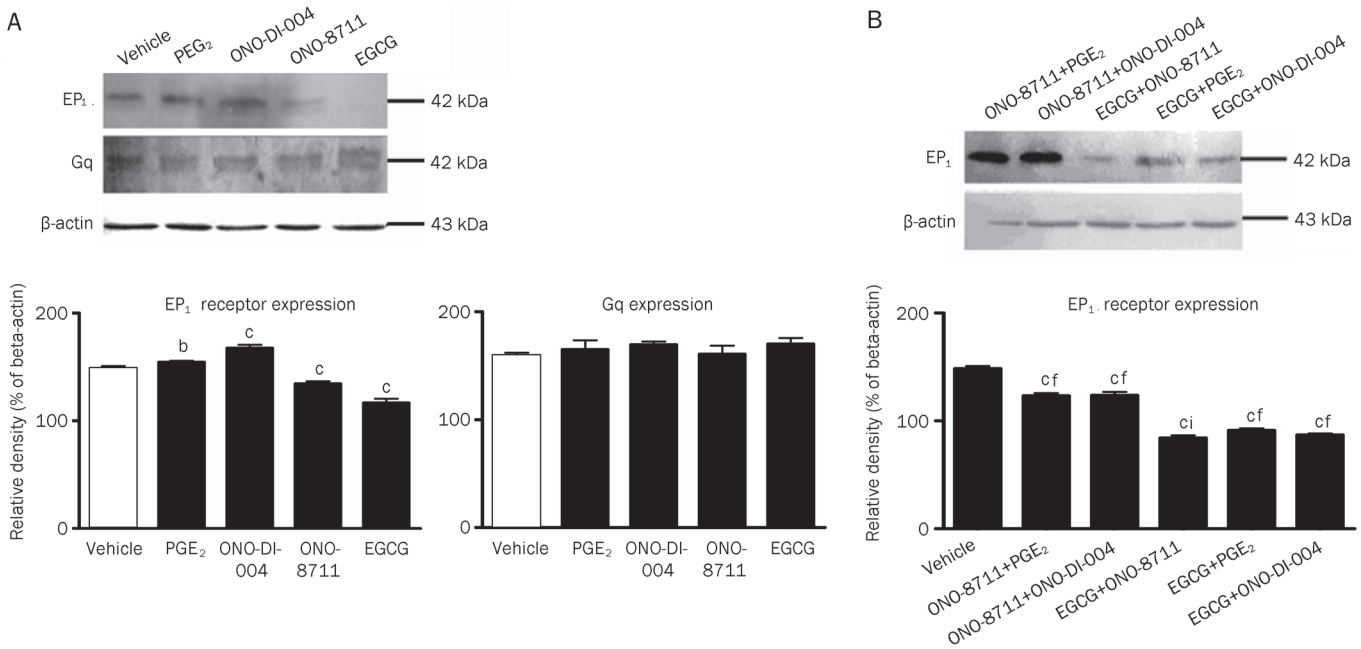

Figure 9. EGCG inhibited EP_1 receptor expression in human HepG2 cells. Effect of PGE_2 4 μmol/L, ONO-DI-004 400 nmol/L, ONO-8711 210 nmol/L, and EGCG 100 μg/mL alone on EP_1 receptor expression (A) and Gq expression (B). (C) EGCG and ONO-8711 on PGE_2 and ONO-DI-004-induced EP_1 receptor expression. The data were expressed as mean±SEM of three independent experiments. $^bP<0.05$, $^cP<0.01$ compared with control groups. $^fP<0.01$ *vs* single PGE_2- or ONO-DI-004- treated group, respectively. $^iP<0.01$ *vs* single EGCG- or ONO-8711-treated group, respectively.

EP_1 receptor up-regulated survivin, which accelerated HCC cell growth and metastasis[19], but the important role of EP_1 receptors in tumor progression remained to be elucidated. To specifically determine whether the EP_1 receptor is functionally active in HCC cells, we used a selective EP_1 receptor agonist and antagonist to analyze their effects on cell viability and migration.

Previous studies showed that the EP_1 receptor antagonist AH6809 inhibited anchorage-independent cell growth and reduced the viability of HCC cells[24]; however, ONO-8711 significantly inhibited breast cancer and HCC development, presumably via induction of apoptosis[1, 25]. Our data showed that the selective EP_1 receptor agonist ONO-DI-004 dramatically increased cell viability and migration in HCC cells in a dose-dependent manner and that the EP_1 receptor antagonist ONO-8711 exerted an inhibitory effect. In addition, ONO-8711 significantly inhibited PGE_2-induced HepG2 cell migration. Furthermore, we detected the effect of PGE_2 and the selective EP_1 receptor agonist on EP_1 expression by Western blot assay. The results showed that both of them up-regulated EP_1 receptor expression. Taken together, these data provide direct evidence that EP_1 expression as well as proliferation and migration of HCC cells are increased by both PGE_2 and the selective EP_1 receptor agonist. By contrast, the selective EP_1 receptor antagonist inhibited PGE_2-induced cell migration. These findings demonstrate that the EP_1 receptor appears to be the predominant receptor that regulates PGE_2-induced HCC cell growth and metastasis.

Our study focuses on the inhibitory effect of EGCG on PGE_2 and EP_1 receptor agonist-induced HCC development. First, we observed that both PGE_2 and the EP_1 receptor agonist stimulated HCC progression. To elucidate the effects of EGCG on PGE_2/EP_1 agonist-induced tumor development, we investigated cell proliferation, migration and EP_1 receptor expression. Cell proliferation and migration were significantly reduced by EGCG at 100 μg/mL compared with the control ($P<0.01$). In PhIP-induced breast cancers, COX-2 and PGE_2 are closely related to estrogen biosynthesis through the aromatase gene (CYP), and these members may be involved in mammary gland carcinogenesis through the EP_1 receptor[26]. COX-2 acts as an oncogene under certain circumstances, leading to the production of PGE_2 which could then act in a paracrine or autocrine way to induce signaling via EP receptors, in particular the EP_1 receptor[27]. In our study, we found that expression of the EP_1 receptor was significantly decreased in the HCC cell line HepG2 after treatment with EGCG (Figure 9). EP_1 receptors are coupled to Gq proteins, but no significant difference in Gq protein expression was observed after treatment with EGCG or ONO-8711. The level of Gq expression was unchanged in our cell system, suggesting that although no significant change occurred in Gq production, the activity of Gq might be already changed or that the level of Gq expression may depend on specific cell types. The exact mechanism should be further studied. We are attempting to determine whether the activity of the Gq protein changed upon treatment with specific chemicals or whether the level of Gq expression was changed in other cell lines.

In conclusion, EP_1 receptors were expressed at a higher

level in HCC cells compared with normal human hepatocytes. EGCG significantly inhibited PGE_2/EP_1 agonist-induced HCC development through suppression of cell viability and migration. We also found that EGCG demonstrated prominent inhibition of PGE_2 synthesis and EP_1 receptor expression. These findings suggest that EGCG may be effective in managing HCC and may help in the development of new therapeutic strategies for both the prevention and treatment of HCC.

Acknowledgements

This work was supported by the National Natural Science Foundation of China (No 30973543 and No 30572356), and by the Scientific Research Foundation of Anhui Medical University (No 2008kj13).

The authors acknowledge ONO Pharmaceutical Co. in Japan for providing the selective EP_1 receptor agonist and antagonist. The authors especially thank Yuri SHEIKINE for rearranging and correcting the manuscript.

Author contribution

Wei WEI designed research. Juan JIN and Yan CHANG performed research and wrote the manuscript; Yi-fu HE contributed new reagents or analytic tools. Shan-shan HU, Di WANG, and Yu-jing WU performed research.

References

1 Breinig M, Rieker R, Eiteneuer E, Wertenbruch T, Haugg AM, Helmke BM, *et al*. Differential expression of E-prostanoid receptors in human hepatocellular carcinoma. Int J Cancer 2008; 122: 547–57.

2 Frei B, Higdon JV. Antioxidant activity of tea polyphenols *in vivo*: evidence from animal studies. J Nutr 2003; 133: 3275S–84S.

3 Khan N, Afaq F, Saleem M, Ahmad N, Mukhtar H. Targeting multiple signaling pathways by green tea polyphenol (–)-epigallocatechin-3-gallate. Cancer Res 2006; 66: 2500–5.

4 Fassina G, Vene R, Morini M, Minghelli S, Benelli R, Noonan DM, *et al*. Mechanisms of inhibition of tumor angiogenesis and vascular tumor growth by epigallocatechin-3-gallate. Clin Cancer Res 2004; 10: 4865–73.

5 Thangapazham RL, Singh AK, Sharma A, Warren J, Gaddipati JP, Maheshwari RK. Green tea polyphenols and its constituent epigallocatechin gallate inhibits proliferation of human breast cancer cells *in vitro* and *in vivo*. Cancer Lett 2007; 245: 232–41.

6 Ju J, Hong J, Zhou JN, Pan Z, Bose M, Liao J, *et al*. Inhibition of intestinal tumorigenesis in Apcmin/+ mice by (–)-epigallocatechin-3-gallate, the major catechin in green tea. Cancer Res 2005; 65: 10623–31.

7 Yang CSL, Lambert JD, Hou Z, Ju J, Lu G, Hao X. Molecular targets for the cancer preventive activity of tea polyphenols. Mol Carcinog 2006; 45: 431–5.

8 Liu W, Nakamura H, Tsujimura T, Cheng J, Yamamoto T, Iwamoto Y, *et al*. Chemoprevention of spontaneous development of hepatocellular carcinomas in fatty liver Shionogi mice by a cyclooxygenase-2 inhibitor. Cancer Sci 2006; 97: 768–73.

9 Kern MA, Haugg AM, Koch AF, Schilling T, Breuhahn K, Walczak H, *et al*. Cyclooxygenase-2 inhibition induces apoptosis signaling via death receptors and mitochondria in hepatocellular carcinoma. Cancer Res 2006; 66: 7059–66.

10 Han C, Michalopoulos GK, Wu T. Prostaglandin E_2 receptor EP_1 transactivates EGFR/MET receptor tyrosine kinases and enhances invasiveness in human hepatocellular carcinoma cells. J Cell Physiol 2006; 207: 261–70.

11 Kawamori T, Kitamura T, Watanabe K, Uchiya N, Maruyama T, Narumiya S, *et al*. Prostaglandin E receptor subtype EP(1) deficiency inhibits colon cancer development. Carcinogenesis 2005; 26: 353–7.

12 Tober KL, Wilgus TA, Kusewitt DF, Thomas-Ahner JM, Maruyama T, Oberyszyn TM. Importance of the EP(1) receptor in cutaneous UVB-induced inflammation and tumor development. J Invest Dermatol 2006; 126: 205–11.

13 Liu JF, Fong YC, Chang CS, Huang CY, Chen HT, Yang WH, *et al*. Cyclooxygenase-2 enhances alpha2beta1 integrin expression and cell migration via EP1 dependent signaling pathway in human chondrosarcoma cells. Mol Cancer 2010; 9: 43.

14 Sanchez-Huerta V, Gutierrez-Sanchez L, Flores-Estrada J. (–)-Epigallocatechin 3-gallate (EGCG) at the ocular surface inhibits corneal neovascularization. Med Hypotheses 2011; 76: 311–3.

15 Andreas K, Haupl T, Lubke C, Ringe J, Morawietz L, Wachtel A, *et al*. Antirheumatic drug response signatures in human chondrocytes: potential molecular targets to stimulate cartilage regeneration. Arthritis Res Ther 2009; 11: R15.

16 Leng J, Han C, Demetris AJ, Michalopoulos GK, Wu T. Cyclooxygenase-2 promotes hepatocellular carcinoma cell growth through Akt activation: evidence for Akt inhibition in celecoxib-induced apoptosis. Hepatology 2003; 38: 756–68.

17 Wendum D, Masliah J, Trugnan G, Flejou JF. Cyclooxygenase-2 and its role in colorectal cancer development. Virchows Arch 2004; 445: 327–33.

18 Hull MA, Ko SC, Hawcroft G. Prostaglandin EP receptors: targets for treatment and prevention of colorectal cancer? Mol Cancer Ther 2004; 3: 1031–9.

19 Bai XM, Jiang H, Ding JX, Peng T, Ma J, Wang YH, *et al*. Prostaglandin E2 upregulates survivin expression via the EP1 receptor in hepatocellular carcinoma cells. Life Sci 2010; 86: 214–23.

20 Chung LY, Cheung TC, Kong SK, Fung KP, Choy YM, Chan ZY, *et al*. Induction of apoptosis by green tea catechins in human prostate cancer DU145 cells. Life Sci 2001; 68: 1207–14.

21 Lu YP, Lou YR, Xie JG, Peng QY, Liao J, Yang CS, *et al*. Topical applications of caffeine or (–)-epigallocatechin gallate (EGCG) inhibit carcinogenesis and selectively increase apoptosis in UVB-induced skin tumors in mice. Proc Natl Acad Sci U S A 2002; 99: 12455–60.

22 Shirakami Y, Shimizu M, Adachi S, Sakai H, Nakagawa T, Yasuda Y, *et al*. (–)-Epigallocatechin gallate suppresses the growth of human hepatocellular carcinoma cells by inhibiting activation of the vascular endothelial growth factor-vascular endothelial growth factor receptor axis. Cancer Sci 2009; 100: 1957–62.

23 Ahmed S, Rahman A, Hasnain A, Lalonde M, Goldberg VM, Haqqi TM. Green tea polyphenol epigallocatechin-3-gallate inhibits the IL-1 beta-induced activity and expression of cyclooxygenase-2 and nitric oxide synthase-2 in human chondrocytes. Free Radic Biol Med 2002; 33: 1097–105.

24 Cusimano A, Fodera D, Lampiasi N, Azzolina A, Notarbartolo M, Giannitrapani L, *et al*. Prostaglandin E2 receptors and COX enzymes in human hepatocellular carcinoma: role in the regulation of cell growth. Ann N Y Acad Sci 2009; 1155: 300–8.

25 Kawamori T, Uchiya N, Nakatsugi S, Watanabe K, Ohuchida S, Yamamoto H, *et al*. Chemopreventive effects of ONO-8711, a selective

prostaglandin E receptor EP(1) antagonist, on breast cancer development. Carcinogenesis 2001; 22: 2001–4.

26 Nakatsugi S, Ohta T, Kawamori T, Mutoh M, Tanigawa T, Watanabe K, *et al*. Chemoprevention by nimesulide, a selective cyclooxygenase-2 inhibitor, of 2-amino-1-methyl-6-phenylimidazo[4,5-b]pyridine (PhIP)-induced mammary gland carcinogenesis in rats. Jpn J Cancer Res 2000; 91: 886–92.

27 Liu CH, Chang SH, Narko K, Trifan OC, Wu MT, Smith E, *et al*. Overexpression of cyclooxygenase-2 is sufficient to induce tumorigenesis in transgenic mice. J Biol Chem 2001; 276: 18563–9.

Acta Pharmacologica Sinica (2012) 33: 710–716
 1671-4083/12 $32.00
www.nature.com/aps

Original Article

Stereoselective binding of mexiletine and ketoprofen enantiomers with human serum albumin domains

Da SHI[1, #], Yin-xiu JIN[2, #], Yi-hong TANG[3, #], Hai-hong HU[1], Si-yun XU[1], Lu-shan YU[1], Hui-di JIANG[1], Su ZENG[1, *]

[1]Department of Drug Metabolism and Pharmaceutical Analysis, College of Pharmaceutical Sciences, Zhejiang University, Hangzhou 310058, China; [2]Taizhou University, Taizhou 317000, China; [3]Shanghai Institute of Technology, Shanghai 201418, China

Aim: To investigate the stereoselective binding of mexiletine or ketoprofen enantiomers with different recombinant domains of human serum albumin (HSA).

Methods: Three domains (HSA DOM I, II and III) were expressed in *Pichia pastoris* GS115 cells. Blue Sepharose 6 Fast Flow was employed to purify the recombinant HSA domains. The binding properties of the standard ligands, digitoxin, phenylbutazone and diazepam, and the chiral drugs to HSA domains were investigated using ultrafiltration. The concentrations of the standard ligands, ketoprofen and mexiletine were analyzed with HPLC.

Results: The recombinant HSA domains were highly purified as shown by SDS-PAGE and Western blotting analyses. The standard HSA ligands digitoxin, phenylbutazone and diazepam selectively binds to DOM I, DOM II and DOM III, respectively. For the chiral drugs, *R*-ketoprofen showed a higher binding affinity toward DOM III than *S*-ketoprofen, whereas *S*-mexiletine bound to DOM II with a greater affinity than *R*-mexiletine.

Conclusion: The results demonstrate that HSA DOM III possesses the chiral recognition ability for the ketoprofen enantiomers, whereas HSA DOM II possesses that for the mexiletine enantiomers.

Keywords: mexiletine; ketoprofen; human serum albumin; protein binding; stereoselectivity; ultrafiltration technique; *Pichia pastoris* GS115 cells

Acta Pharmacologica Sinica (2012) 33: 710–716; doi: 10.1038/aps.2012.8

Introduction

Human serum albumin (HSA) is the most abundant protein in human blood plasma, accounting for about half of the blood serum protein. After systemic absorption, most drugs undergo some degree of reversible binding to HSA[1]. The two enantiomers of a chiral drug may bind to HSA with different affinities, resulting in different free fractions. Over 50% of the drugs in current clinical use are chiral, and the majority of synthetically derived chiral drugs are administered as mixtures of the constituent stereoisomers (most commonly the racemate)[2]. In addition to stereoselective metabolism, stereoselective protein binding might also be responsible for the differences in pharmacokinetics between enantiomers[3–5]. Studies on the mechanism of stereoselective binding to HSA may better explain the different pharmacokinetics between enantiomers.

HSA has a limited number of high-affinity binding sites for drugs[6]. Fragments of HSA produced by chemical or enzymatic cleavage have been used to define the exact high-affinity binding sites for several ligands[7–10]. However, this method is limited by the finite number of cleavage sites in HSA, and chemical cleavage may destroy the structure of the binding site. Because HSA is composed of three quasi-independent domains, DOM I, DOM II, and DOM III[1], a new method based on the cloning and expression of these three independent domains was first introduced by Dockal M[11]. Several studies have successfully employed recombinant HSA domains to identify the specific binding sites of several drugs, including warfarin, ochratoxin A, propofol and halothane[12–15]. The use of recombinant HSA fragments in a binding study with warfarin enantiomers demonstrated that the recombinant domains may also be a useful tool to reveal the stereoselective binding properties of chiral drugs[16]. In this study, we constructed three recombinant HSA domains to investigate the stereoselective binding properties of ketoprofen and mexiletine.

Ketoprofen and mexiletine are both chiral drugs and are currently used as racemates. The stereoselective binding of

# These three authors contributed equally to this work.
* To whom correspondence should be addressed.
E-mail zengsu@zju.edu.cn
Received 2011-08-10 Accepted 2012-01-15

ketoprofen enantiomers to human serum albumin was discovered in 1980[17]. In 1990, Verbeeck *et al* determined that ketoprofen bound extensively to HSA (above 99%)[18], and that this binding may be related to the enantioselective disposition of ketoprofen *in vivo*. In the past several decades, studies on the stereoselective binding of ketoprofen to HSA have reached a consensus that ketoprofen mainly binds to site II of HSA and does so in a stereoselective manner[19–21]. However, contradictory stereoselective binding results have been obtained under different experimental conditions[17, 18, 22–24]. Studies using the method based on recombinant HSA domains may complement other binding studies to better understand the stereoselective binding properties of ketoprofen to HSA. Mexiletine is 70% bound to serum protein[25], and the stereoselective disposition of mexiletine in man was first studied in 1986[26]. *In vitro* studies using serum protein from healthy subjects indicated that mexiletine bound to serum protein in a stereoselective manner[27]. Because serum protein is made up of HSA and other proteins such as α-acid glycoprotein, the mechanism of stereoselective binding between mexiletine and HSA needs to be further studied. However, little progress has been made in identifying either binding sites in HSA or the chiral binding mechanism. In this study, the stereoselective properties of the binding between chiral drugs (mexiletine and ketoprofen) and HSA were investigated using purified recombinant HSA domains.

Materials and methods

Cloning

This protocol was a modification of previously published methods[11, 12]. In brief, the gene segments coding for the HSA domains (the domains contained the following amino acids: HSA DOM I, 1–197; HSA DOM II, 189–385; and HSA DOM III, 381–585) were amplified by polymerase chain reaction (PCR) using the pBS-HSA plasmid as the template. The forward and reverse primers (Table 1) were designed to incorporate *Eco*R I and *Not* I sites, respectively.

The PCR products were digested overnight and then ligated into the pPIC9 vector (Invitrogen), resulting in the recombinant vectors pPIC9-HSA DOM I, pPIC9-HSA DOM II, and pPIC9-HSA DOM III. The recombinant vectors were transformed into *E coli* DH5α for amplification and subsequent DNA sequence analysis. The identified recombinant plasmids were linearized with *Sal* I and transformed into competent *Pichia pastoris* GS115 cells (Invitrogen). The transformants were screened for viability in the absence of glucose and histidine. The positive recombinants were confirmed by PCR and DNA sequencing.

Table 1. Sequence of primers.

Primers	Sequence
Domain I	
Forward primer	ggcggaattcgatgcacacaagag
Reverse primer	atttgcggccgctctctgtttggc
Domain II	
Forward primer	agcagaattcgggaaggcttcgtct
Reverse primer	ataatgcggccgcctgaggctcttc
Domain III	
Forward primer	agacgaattcgtggaagagcctcag
Reverse primer	tatagcggccgcttataagcctaa

Expression and purification

The recombinants were grown on YPD medium and then transferred to BMGY medium for induction with methanol. Methanol with a final concentration of 1% was added every 24 h to maintain induction. All incubations were performed at 28 °C on an orbital shaker at 250 r/min. Supernatant samples were collected every 12 h for SDS-PAGE and Western blot analysis.

The protein was purified using the modified procedure described by Matsushita S[14]. All steps of the purification procedure were performed at 4 °C. The supernatants were harvested at 72 h after induction, followed by filtration through a 0.45 μm filter. Purification was performed by precipitation with 85% $(NH_4)_2SO_4$. The resulting samples were passed through a preequilibrated Blue Sepharose column (Amersham). After washing with 50 volumes of buffer 1 (50 mmol/L KH_2PO_4, pH 7.0), elution was performed with buffer 2 (50 mmol/L KH_2PO_4, 1.5 mol/L KCl, pH 7.0). The isolated protein samples were extensively dialyzed against Sorensen's phosphate buffer. The protein concentrations were measured by the Bradford method.

Western blot analysis

The purified protein samples were eluted by adding an equal volume of loading buffer and then running them on 12% SDS-PAGE gels. The separated proteins were then transferred to PVDF membranes. The membranes were incubated in the presence of goat anti-human serum albumin polyclonal antibody (Beckman). Exposure to the primary antibody was followed by incubation with a horseradish peroxidase (HRP)-conjugated secondary anti-goat IgG antibody (Sanying Biotechnology). The blots were developed using an enhanced chemiluminescence detection system (ECL) (Amersham) according to the manufacturer's instructions.

Ultrafiltration

The binding properties of the three recombinant domains with the standard ligands ketoprofen and mexiletine were investigated by ultrafiltration using a Microcon centrifugation system (America, Millipore) that utilized a filter membrane with a 30-kDa cutoff at 37 °C. Phenylbutazone, diazepam and digitoxin, each of which binds to a specific site in HSA, were chosen as the standard ligands. Aliquots of 500 μL of each HSA domain with standard ligands were centrifuged at 7000×*g* for 5 min. For ketoprofen and mexiletine, the centrifugations were performed at 7500×*g* for 10 min and 10000×*g* for 15 min, respectively. The ultrafiltrate (150 μL) was collected

and prepared as described above.

Nonspecific filter membrane binding was evaluated in protein-free phosphate-buffered saline (PBS). The mixture was transferred to the ultrafilter without incubation, followed by ultrafiltration at 2000x*g* for 5 min at 37 °C. The samples in PBS buffer with or without ultrafiltration were directly injected into an HPLC system.

The percentage adsorbed by the ultrafilter is calculated using the following formula:

$$P\%=1-A_{ultrafiltrate}/A_{PBS}$$

$A_{ultrafiltrate}$, drug peak area in the ultrafiltrate; A_{PBS}, drug peak area in PBS buffer.

Sample preparation

The ultrafiltrates for the standard ligands (phenylbutazone, diazepam and digitoxin) were directly injected into the HPLC system. For ketoprofen, *R*-flurbiprofen was used as the internal standard. Ketoprofen was activated with 1% triethylamine and 2% thionyl chloride (both in methylene chloride) and then reacted with *S*-(–)-1-(1-naphthyl) ethylamine (*S*-NEA) (Sigma) to generate diastereoisomeric amides[28]. For mexiletine, *R*-esmolol was used as the internal standard, and the chiral derivatization was performed at 35 °C for 10 min with 2,3,4,6-tetra-*O*-acetyl-β-*D*-glucopyranosyl isothiocyanate (GITC) (Sigma)[29].

HPLC analysis

The concentrations of the standard ligands, ketoprofen and mexiletine, were analyzed by HPLC. HPLC was performed on an Agilent 1100 system consisting of a G1311A pump, a G1315A (DAD) UV detector, a manual injector and ChemStation software. An Agilent Zorbax C18 (250 mm×4.6 mm, 5 μm) column was used. An aliquot of 20 μL of each sample was injected and analyzed at room temperature (Table 2).

Results

Cloning expression and purification

After induction with methanol, the supernatants of the pPIC9-HSA DOM I, pPIC9-HSA DOM II, and pPIC9-HSA DOM III transformants were analyzed by SDS-PAGE and Western blot. A single band was present at approximately 23 kDa, as shown in Figure 1, in accordance with the previously reported molecular masses of 22860, 22519, and 23383 Da for of HSA DOM I, HSA DOM II, and HSA DOM III, respectively[11]. The recombinant domains were also identified by Western blot with an anti-human HSA antibody, as shown in Figure 2. The results confirmed that the recombinant HSA domains were successfully expressed and secreted into the supernatant.

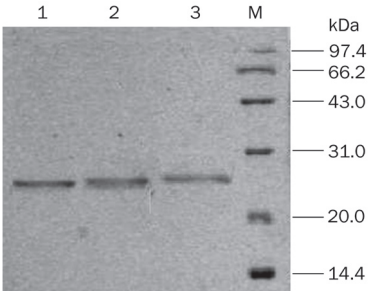

Figure 1. Analysis of the expression products by SDS-PAGE. (1) HSA DOM III; (2) HSA DOM II; (3) HSA DOM I. The positions of the molecular weight standards are indicated in the right-most lane.

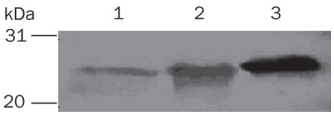

Figure 2. Analysis of the expression products by Western blot. (1) HSA DOM I; (2) HSA DOM II; (3) HSA DOM III. The positions of the molecular weight standards are indicated in the left-most lane.

To prevent the secreted foreign proteins from being degraded by the KEX-2 proteases present on the membrane of *Pichia pastoris*, tryptone was added to the culture, providing excess substrate for these proteases. Because higher concentrations of methanol might inhibit the expression of the target proteins, the final concentration of methanol was less than 1%. As shown in Figure 3, the expression levels of the recombinant domains peaked at 72–96 h at a concentration of 210–275 mg/L. Consequently, the supernatants were harvested at 72 h for purification.

Although negligible levels of nonspecific proteins were detected by SDS-PSGE and Western blot, there were large amounts of mineral salts and metabolites in the supernatants. Impurities such as pigments, amino acids and carbohydrates may strongly inhibit the binding of the ligands with the recombinant protein fragments, resulting in a decreased protein binding rate. Blue Sepharose affinity chromatography was employed as the central step in the purification procedure. The Blue Sepharose column exhibited highly specific binding with the recombinant domains, as demonstrated by

Table 2. The estabolished HPLC methods.

Drug	Mobile phase (*v/v*)	Flow rate (mL/min)	Detection (nm)
Phenylbutazone	Water-methanol (25:75)	0.7	238
Diazepam	Water-methanol (25:75)	0.7	242
Digitoxin	Water-acetonitrile (55:45)	1	220
Ketoprofen	Phosphate buffer (0.01 mol/L, pH 4.5)-acetonitrile (40:60)	0.8	250
Mexiletine	Phosphate buffer (0.02 mol/L, pH 5.5)-acetonitrile (75:25)	0.9	214

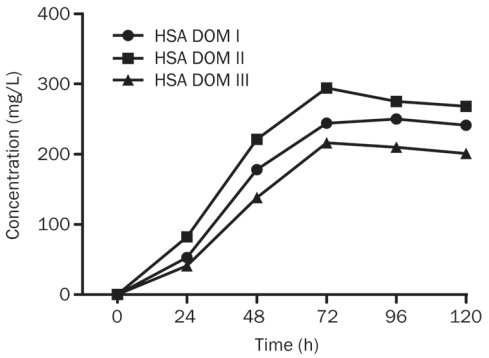

Figure 3. The protein expression in recombinant *P pastoris* at different time points.

the fact that the purity of the domain preparation was greater than 98% in a previous study[11]. The purification efficiencies with or without precipitation were also compared. The recovery without precipitation is lower than that with precipitation (data not shown). These results indicated that the purification should be performed with precipitation. As shown in Figure 4, the secreted protein segments were highly purified and concentrated after purification.

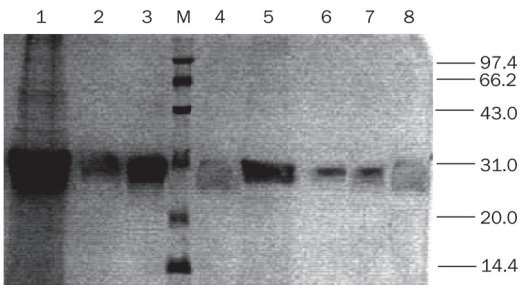

Figure 4. Analysis of the expression, precipitation and purification products by SDS-PAGE. (1) Precipitation of HSA DOM II; (2) Expression products of HSA DOM III; (3) Purification products of HSA DOM II; (4) Expression products of HSA DOM I; (5) Precipitation of HSA DOM I; (6) Purification products of HSA DOM I; (7) Purification products of HSA DOM III; (8) Expression products of HSA DOM III.

Confirmation of nonspecific filter binding

As shown in Table 3, the average nonspecific adsorption percentages under different concentrations were 3.53% for ketoprofen and 2.63% for mexiletine. These results indicated that the ultrafiltration system was suitable for studying the binding of ketoprofen and mexiletine to HSA.

Table 3. The nonspecific adsorption of ketoprofen and mexiletine with ultrafilter (n=3).

Drug	Spiked amount (μg/mL)	P (%)	P (%)
Ketoprofen	1.0	3.77	3.53±0.50
	5.0	3.86	
	50.0	2.95	
Mexiletine	0.5	2.25	2.63±1.57
	5.0	1.28	
	50.0	4.36	

Binding with standard ligands

It was widely accepted that the three recombinant domains possessed the three principal binding sites of HSA: the warfarin site (site I) in DOM II, the diazepam site (site II) in DOM III and the digitoxin site (site III) in DOM I[6]. In the present study, the binding properties of HSA and the three HSA domains with phenylbutazone, diazepam and digitoxin, each of which represents a standard ligand for HSA, were investigated. As shown in Figure 5, phenylbutazone bound to DOM II with greater affinity than to DOM I and showed no affinity to DOM III. Diazepam bound to DOM III with high selectivity. Digitoxin mainly bound to DOM I but also slightly bound to DOM II and DOM III. The results indicated that the primary binding sites of digitoxin, phenylbutazone and diazepam were on DOM I, DOM II, and DOM III, respectively. However, there may be low-affinity sites on DOM I for phenylbutazone and on DOM II and DOM III for digitoxin.

The binding abilities of the HSA domains were lower than

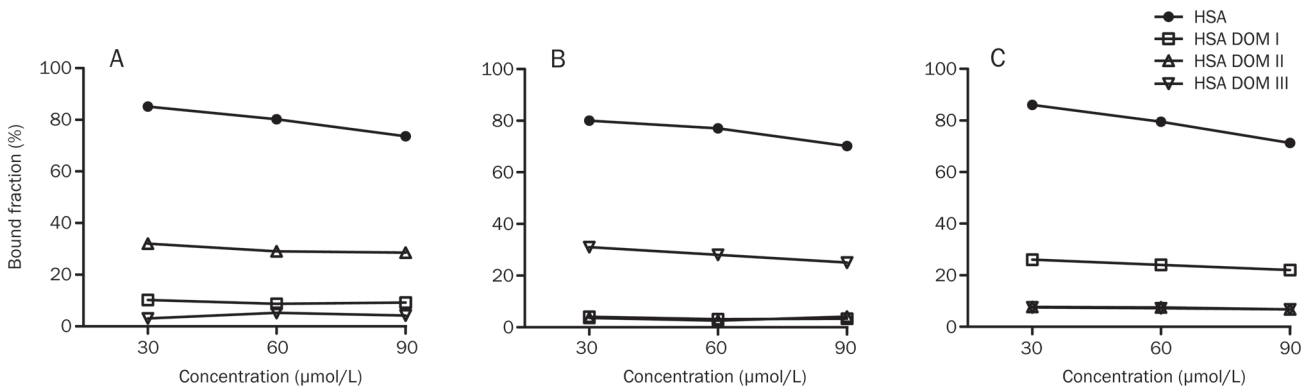

Figure 5. The protein binding of phenylbutazone (A), diazepam (B) and digitoxin (C) in 60 μmol/L HSA, HSA DOM I, HSA DOM II, and HSA DOM III.

those of rHSA, in agreement with the results of a previous report[14] in which the site II marker DNSS bound with greater affinity to rHSA (62.4%±5.4%) than to domain III (38.9%±7.8%). The importance of the integrated three-dimensional structure may account for this phenomenon, as the interdomain interactions may maintain the stability of the ligand binding sites.

Binding with the enantiomers of chiral drugs

Contradictory results for the binding of ketoprofen enantiomers to HSA have been obtained in several studies[17, 19, 24, 30]. Zou *et al* [24] reported that the *S*-enantiomers bind to HSA more strongly than the *R*-enantiomers do. According to Dubois *et al*[19], *R*-ketoprofen bound more strongly than *S*-ketoprofen, whereas Guo *et al* [31] found that ketoprofen had little stereoselectivity with respect to binding to HSA. The binding of ketoprofen to DOM III showed remarkable stereoselectivity at the concentration of albumin found in plasma (5.2 μmol/mL), as *R*-ketoprofen exhibited a significantly higher binding affinity than *S*-ketoprofen (P=0.0209). The bound fractions for *R*-ketoprofen and *S*-ketoprofen were 35.5%±4.6% (n=3) and 20.5%±5.5% (n=3), respectively (Figure 6).

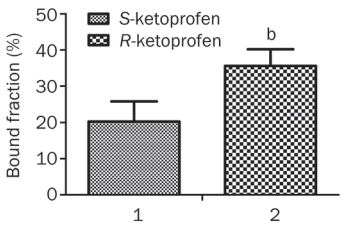

Figure 6. The binding of *S*-ketoprofen (1) and *R*-ketoprofen (2) (1.25 μmol/mL) to HSA DOM III (5.2 μmol/mL) (n=3).

For mexiletine, the primary binding site on HSA was site I in DOM II. Enantioselectivity was also observed for mexiletine enantiomers but was the opposite of that for ketoprofen. The binding of mexiletine enantiomers to HSA was significantly stereoselective, with the bound fractions of *S*-mexiletine and *R*-mexiletine being 44.35%±1.9% (n=3) and 32.9%±2.1% (n=3), respectively (P=0.0022)[31]. The stereoselective trend was the same with the HSA domains. As shown in Figure 7, *S*-mexiletine [bound fraction of 55.3%±14.6% (n=3)] bound to DOM II with a slightly greater affinity than *R*-mexiletine [bound fraction of 45.9%±17.7% (n=3)]. However, the stereoselectivity of the binding of mexiletine was not statistically significant, with a P value of 0.3404.

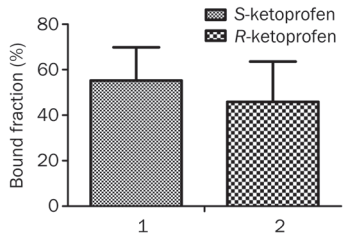

Figure 7. The binding of *S*-mexiletine (1) and *R*-mexiletine (2) (1.15 μmol/mL) to HSA DOM II (4.9 μmol/mL) (n=3).

Discussion

HSA binding with ketoprofen enantiomers

Ketoprofen, a chiral non-steroidal anti-inflammatory drug (NSAID) of the 2-aryl propionate family, is currently marketed and used as a racemate. *S*-ketoprofen possesses most of the beneficial pharmacological activity[32], whereas the *R*-enantiomer is considered to be an impurity or a pro-drug: approximately 10% of the *R*-enantiomer undergoes chiral inversion upon oral administration[33]. Ketoprofen bound extensively to HSA (above 99%)[18] in a stereoselective manner[34], which may be related to the enantioselective disposition of ketoprofen *in vivo*[35, 36]. Ketoprofen was reported to bind to HSA at site I and site II; the main binding site was site II (the high affinity binding site) in domain III[19–21]. In this study, the bound fraction for ketoprofen racemate was in accordance with the results of the study by Matsushita[14] (bound fraction of 64.0%±5.4% for the ketoprofen racemate). These results indicated that the recombinant HSA domains produced in our study were highly purified and exhibited great activity.

The stereoselective HSA binding of ketoprofen has been identified by several studies[17, 22–24, 30]. However, contradictory results have been obtained under different experimental conditions. Dubois *et al*[19] found that the enantioselective binding of ketoprofen enantiomers to HSA depended on drug and protein concentrations. Enantioselectivity was observed in HSA at 1 g/L, but the opposite enantioselectivity was observed at 40 g/L. At the concentration of HSA in plasma (40 g/L), R-ketoprofen bound more strongly than the *S*-isomer, and the k values of site II for *S*-ketoprofen were less than half of those for *R*-ketoprofen. Similar findings were obtained in our study, where the higher binding ability of *R*-ketoprofen to DOM III was detected at a similar physiological concentration. The method based on recombinant HSA domains may give a direct and thorough view of the stereoselective binding of chiral drugs.

HSA binding with mexiletine enantiomers

Mexiletine, an orally effective class 1 antiarrhythmic agent with a chiral center, is also used therapeutically as a racemate. The stereoselective disposition of mexiletine in humans was first revealed by Grech-Belanger *et al*[26], who noted that the area under concentration-time curve (AUC) of *S*-mexiletine was always significantly higher (P<0.01) and that the rate of renal clearance was significantly lower (P<0.05)[3] than that of the other enantiomer. It was reported that mexiletine was 70% bound to serum protein in healthy subjects[25], and therefore, the differences observed between the pharmacokinetics of the enantiomers may be due largely to differences in their serum protein binding affinities.

As the stereoselective binding site and the mechanism of the binding of mexiletine enantiomers to HSA remain unknown,

recombinant HSA domains were used in this study. This study represents the first attempt to identify the primary binding site of mexiletine to HSA, and it was determined that this binding site may be site I in DOM II. The bound fraction ratio of *S*-enantiomer to *R*-enantiomer on DOM II was 1.2, a value that was in accordance with stereoselective binding to recombinant HSA (ratio is 1.34). The nonsignificant difference between *S*-mexiletine and *R*-mexiletine with respect to binding to DOM II may due to the large errors. Thus, more data should be gathered in future studies to confirm the stereoselectivity.

An *in vitro* binding study of mexiletine enantiomers further revealed that the serum binding of mexiletine could be accounted for primarily by binding to HSA and/or AGP[25]. The binding of mexiletine enantiomers to AGP was examined in our previous study[31], and the binding to AGP was also found to be stereoselective, with a bound fraction of 37.3%–24.1% for the *R*-enantiomer and a bound fraction of 31.1%–21.0% for the *S*-enantiomer. Although these results demonstrated opposite stereoselectivities for the binding to AGP and the binding to HSA, the stereoselective binding of the *S*-enantiomer to HSA may predominate in the plasma. Because the *S*-enantiomer possessed a slightly higher binding affinity for HSA DOM II, it had higher values for pharmacokinetic parameters, including the AUC[26], the terminal elimination half-life[3], and smaller values for parameters including renal clearance[26] and steady-state volume of distribution[3] than the *R*-enantiomer. These results confirmed the relationship between the HSA DOM binding of the mexiletine enantiomers and their pharmacokinetic properties.

The application of recombinant HSA domains

Recombinant HSA domains, first introduced in 1999[11], have been used in several studies as powerful tools for ligand binding studies. To pinpoint the essential structural elements for the formation of the warfarin binding site on HSA, Dockal *et al* further constructed a defined set of five recombinant proteins[12]. Matsushita *et al*[14] analyzed the function of three recombinant HSA domains and considered DOM I to be a potential protein carrier for drug delivery. The same recombinant HSA domains were employed by Il'ichev *et al*[13] to gain insight into the localization of binding sites and the nature of binding interactions between ochratoxin A and HSA. Liu *et al*[15] utilized recombinant HSA domains to identify the main binding sites of two general anesthetics, propofol and halothane. Further analyses of the architecture of binding sites characterized the general anesthetic structure-activity relationship.

All of the above studies suggest that the recombinant HSA domains might be a suitable platform for the characterization of ligand binding. However, there has only been a single study applying the recombinant HSA domains to stereoselective binding research. Twine *et al*[16] constructed two domain fragments of HSA corresponding to domains 1 and 2 (D12) and domains 2 and 3 (D23) and used these HSA fragments to study the binding of warfarin enantiomers to HSA. The results demonstrated that the fragments of HSA retained the ability to discriminate between pairs of warfarin enantiomers. In the present study, we performed stereoselective binding research using ketoprofen and mexiletine enantiomers and three recombinant HSA domains. This study complements other binding studies by revealing the binding properties of ketoprofen enantiomers to HSA. As the stereoselective binding of mexiletine to serum protein has not been well investigated, the nature of binding interactions between mexiletine enantiomers and HSA is further characterized in this study. The mexiletine binding sites are primarily found in DOM II, with an increased preference for the *S*-enantiomer.

In summary, we produced three highly purified recombinant HSA domains (HSA DOM I, HSA DOM II, and HSA DOM III), each of which had a specific ligand binding site. The recombinant domains were then employed to investigate the different chiral binding properties of the ketoprofen and mexiletine enantiomers. The results demonstrate that the method based on the recombinant HSA domains may have great potential to increase the understanding of the stereoselective binding properties of chiral drugs.

Acknowledgements

This project was supported by the State Key Development Program for Basic Research of China (Grant No 2011CB710800) and National Major Projects for Science and Technology Development of the Ministry of Science and Technology of China (No 2012ZX09506001-004).

Author contribution

Su ZENG designed the study. Da SHI, Yin-xiu JIN, and Yi-hong TANG performed the experiments. Hai-hong HU and Si-yun XU contributed analytic tools. Lu-shan YU and Hui-di JIANG analyzed the data. Da SHI, Yin-xiu JIN, Yi-hong TANG, and Su ZENG wrote the paper.

References

1 He XM, Carter DC. Atomic structure and chemistry of human serum albumin. Nature 1992; 358: 209–15.
2 Caner H, Groner E, Levy L, Agranat I. Trends in the development of chiral drugs. Drug Discov Today 2004; 9: 105–10.
3 Igwemezie L, Kerr C, McErlane K. The pharmacokinetics of the enantiomers of mexiletine in humans. Xenobiotica 1989; 19: 677–82.
4 Hong Y, Tang Y, Zeng S. Enantioselective plasma protein binding of propafenone: mechanism, drug interaction, and species difference. Chirality 2009; 21: 692–8.
5 Sun DL, Huang SD, Wu PS, Li J, Ye YJ, Jiang HD. Stereoselective protein binding of tetrahydropalmatine enantiomers in human plasma, HSA, and AGP, but not in rat plasma. Chirality 2010; 22: 618–23.
6 Chuang VTG, Otagiri M. Stereoselective binding of human serum albumin. Chirality 2006; 18: 159–66.
7 Reed RG, Feldhoff RC, Clute O, Peters Jr T. Fragments of bovine serum albumin produced by limited proteolysis. Conformation and ligand binding. Biochemistry 1975; 14: 4578–83.
8 Bos OJM, Fischer MJE, Wilting J, Janssen LHM. Drug-binding and other physicochemical properties of a large tryptic and a large peptic

fragment of human serum albumin. BBA-Protein Struct M 1988; 953: 37–47.
9 Bos OJM, Remijn JPM, Fischer MJE, Wilting J, Janssen LHM. Location and characterization of the warfarin binding site of human serum albumin: A comparative study of two large fragments. Biochem Pharmacol 1988; 37: 3905–9.
10 Bos O, Labro J, Fischer M, Wilting J, Janssen L. The molecular mechanism of the neutral-to-base transition of human serum albumin. Acid/base titration and proton nuclear magnetic resonance studies on a large peptic and a large tryptic fragment of albumin. J Biol Chem 1989; 264: 953.
11 Dockal M, Carter DC, Ruker F. The three recombinant domains of human serum albumin. Structural characterization and ligand binding properties. J Biol Chem 1999; 274 : 29303–10.
12 Dockal M, Chang M, Carter DC, Rüker F. Five recombinant fragments of human serum albumin — tools for the characterization of the warfarin binding site. Protein Sci 2000; 9: 1455–65.
13 Il'ichev YV, Perry JL, Rüker F, Dockal M, Simon JD. Interaction of ochratoxin A with human serum albumin. Binding sites localized by competitive interactions with the native protein and its recombinant fragments. Chem-Biol Interact 2002; 141: 275–93.
14 Matsushita S, Isima Y, Chuang VTG, Watanabe H, Tanase S, Maruyama T*, et al.* Functional analysis of recombinant human serum albumin domains for pharmaceutical applications. Pharm Res 2004; 21: 1924–32.
15 Liu R, Meng Q, Xi J, Yang J, Ha CE, Bhagavan NV*, et al.* Comparative binding character of two general anaesthetics for sites on human serum albumin. Biochem J 2004; 380: 147.
16 Twine S, Gore M, Morton P, Fish B, Lee A, East J. Mechanism of binding of warfarin enantiomers to recombinant domains of human albumin. Arch Biochem Biophys 2003; 414: 83–90.
17 Rendic S, Albic-Kolbah T, Kajfez F, Sunjic V. Stereoselective binding of (+) and (–)-alpha-(benzoylphenylpropionic) acid (ketoprofen) to human serum albumin. Farmaco, Edizione Scientifica 1980; 35: 51–9.
18 Verbeeck R, Blackburn J, Loewen G. Clinical pharmacokinetics of nonsteroidal anti-inflammatory drugs. Clin Pharmacokinet 1983; 8: 297.
19 Dubois N, Lapicque F, Abiteboul M, Netter P. Stereoselective protein binding of ketoprofen: effect of albumin concentration and of the biological system. Chirality 1993; 5: 126–34.
20 Sakai T, Maruyama T, Imamura H, Shimada H, Otagiri M. Mechanism of stereoselective serum binding of ketoprofen after hemodialysis. J Pharmacol Exp Ther 1996; 278: 786.
21 Zhivkova ZD, Russeva VN. Stereoselective binding of ketoprofen enantiomers to human serum albumin studied by high-performance liquid affinity chromatography. J Chromatogr B 1998; 714: 277–83.
22 Hayball PJ, Nation RL, Bochner F, Newton JL, Massy-Westropp RA, Hamon DPG. Plasma protein binding of ketoprofen enantiomers in man: method development and its application. Chirality 1991; 3: 460–6.
23 Lapicque F, Muller N, Payan E, Dubois N, Netter P. Protein binding and stereoselectivity of nonsteroidal anti-inflammatory drugs. Clin Pharmacokinet 1993; 25: 115.
24 Zou H, Wang H, Zhang Y. Stereoselective binding of warfarin and ketoprofen to human serum albumin determined by microdialysis combined with HPLC. J Liq chromatogr R T 1998; 21: 2663–74.
25 Kwok D, Kerr C, McErlane K. Pharmacokinetics of mexiletine enantiomers in healthy human subjects. A study of the *in vivo* serum protein binding, salivary excretion and red blood cell distribution of the enantiomers. Xenobiotica 1995; 25: 1127–42.
26 Grech-Belanger O, Turgeon J, Gilbert M. Stereoselective disposition of mexiletine in man. Brit J Clin Pharmaco 1986; 21: 481.
27 McErlane K, Igwemezie L, Kerr C. Stereoselective serum protein binding of mexiletine enantiomers in man. Res Commun Chem Pathol Pharmacol 1987; 56: 141.
28 Jin YX, Tang YH, Zeng S. Analysis of flurbiprofen, ketoprofen and etodolac enantiomers by pre-column derivatization RP-HPLC and application to drug-protein binding in human plasma. J Pharmaceut Biomed 2008; 46: 953–8.
29 Jin YX, Zeng S. Determination of mexiletine enantiomers in human serum albumin after derivatization with GITC by RP-HPLC. Chinese Pharmaceutical Journal 2007. Chinese.
30 Guo CC, Tang YH, Hu HH, Yu LS, Jiang HD, Zeng S. Analysis of chiral non-steroidal anti-inflammatory drugs flurbiprofen, ketoprofen and etodolac binding with HSA. J Pharmaceut Anal; 1: 184–90.
31 Jin YX. Enantioselective binding of chiral drugs, mexiletine and ketoprofen, to plasma proteins. Thesis for master degree. Zhejiang University. 2006. p 24–31. Chinese.
32 Hutt A, Caldwell J. The importance of stereochemistry in the clinical pharmacokinetics of the 2-arylpropionic acid non-steroidal anti-inflammatory drugs. Clin Pharmacokinet 1984; 9: 371–3.
33 Rudy AC, Liu Y, Brater C, Hall SD. Stereoselective pharmacokinetics and inversion of (*R*)-ketoprofen in healthy volunteers. J Clin Pharmacol 1998; 38: 3S.
34 Jamali F, Brocks D. Clinical pharmacokinetics of ketoprofen and its enantiomers. Clin Pharmacokinet 1990; 19: 197.
35 Grubb N, Rudy D, Brater D, Hall S. Stereoselective pharmacokinetics of ketoprofen and ketoprofen glucuronide in end-stage renal disease: evidence for a 'futile cycle' of elimination. Br J Clin Pharmacol 1999; 48: 494–500.
36 Bannwarth B, Lagrange F, Péhourcq F, Llanas B, Demarquez J. (*S*)-ketoprofen accumulation in premature neonates with renal failure who were exposed to the racemate during pregnancy. Br J Clin Pharmacol 1999; 47: 459–60.